UC Irvine

UC Irvine Electronic Theses and Dissertations

Title

Exploring Structure-Function Relationships and Redox Partner Interactions in Heme Enzymes

Permalink

https://escholarship.org/uc/item/5cr4b9nt

Author

Chreifi, Georges

Publication Date

2016

Copyright Information

Peer reviewed|Thesis/dissertation

UNIVERSITY OF CALIFORNIA,
IRVINE

Exploring Structure-Function Relationships and Redox Partner Interactions in Heme Enzymes

DISSERTATION

submitted in partial satisfaction of the requirements
for the degree of

DOCTOR OF PHILOSOPHY

in Biological Sciences

by

Georges Chreifi

Dissertation Committee:
Chancellor's Professor Thomas L. Poulos, Chair
Professor Celia W. Goulding
Professor Melanie J. Cocco

2016

DEDICATION

To my beloved Lindsay, who gave everything to support me on this journey

and to my parents, for all the sacrifices you made

I couldn't have done this on my own

TABLE OF CONTENTS

LIST OF FIGURES

this study

LIST OF TABLES

ACKNOWLEDGMENTS

CURRICULUM VITAE

Georges Chreifi, Ph.D.

Education

University of California, Irvine Irvine, CA
Ph.D., Biological Sciences June 2016
- Dissertation: *Exploring Structure-Function Relationships and Redox-Partner Interactions in Heme Enzymes.*
  Advisor: Thomas L. Poulos.
- Notable Award: Howard A. Schneiderman Fellowship, June 2015

Concordia University Montreal, Canada
B.S., Biochemistry June 2011

Research Experience

University of California, Irvine Irvine, CA

PhD. Student - Poulos Research Group September 2012 - August 2016
- Project 1: The *Leishmania major* heme peroxidase system serves as a model to better understand protein-protein interactions and the relationship between enzyme structure and catalytic activity. I performed a full kinetic analysis of the system, including measurement of association rate constants and steady-state kinetics, determination of the rate-limiting step, and the role of specific amino acids on redox partner association and dissociation.

- Project 2a: Under or over-production of nitric oxide (NO) *in vivo* can have deleterious consequences. Analogues of tetrahydrobiopterin, a cofactor of nitric oxide synthase, were synthesized by collaborators in an effort to regulate NO production. I co-crystallized each compound with endothelial NOS to determine their binding modes and provide a guide for the design of future inhibitors or activators.

- Project 2b: Ongoing collaboration with synthetic chemistry group to design potent, isoform selective and blood-brain barrier permeable Nitric oxide synthase substrate bioisostere inhibitors for the treatment of melanoma and of neurodegenerative diseases, including Alzheimer's, Parkinson's and Lou Gehrig's.

- Project 3: The parasite *Leishmania major* causes the tropical disease Leishmaniasis. The reactive nitrogen species peroxynitrite, produced in host macrophages by the irreversible collision between nitric oxide and superoxide, is highly destructive to organisms *in vivo*. The structure of a novel heme enzyme from *L. major* involved in peroxynitrite detoxification is hypothesized as a potential therapeutic target. I determined the crystal structure of the enzyme for the first time, revealing an intriguing Histidine-Cysteine heme coordination and paving the way for determining the chemistry and mechanism for the future design of inhibitors.

- Project 4: X-ray free electron laser was used to capture the first reaction intermediate of yeast cytochrome c peroxidase to determine the structure and protonation state of active site residues before any reduction of the heme. Structural results were combined with measurements of the kinetic solvent isotope effect involved in the transition state to establish a well corroborated reaction mechanism and validate the usefulness of XFELs.

- Project 5: Cytochrome P450s are most famous for their role in xenobiotic detoxification. Most of what we know about the details of P450 structure and chemistry has been elucidated by studying bacterial P450s. Recent findings from our laboratory have shown a structural basis for the long hypothesized effector role of the iron-sulfur binding redox partner in the P450cam model system. This finding has caused a paradigm shift in our views of how P450s work. I have been using a similar structural and biochemical approach on bacterial P450cin to solve the crystal structure of P450cin in complex with its FMN-containing redox partner Cindoxin by using site-specific chemical crosslinking coupled to mass spectrometry analysis.

Research Associate - Poulos Research Group   June 2011 - September 2012
- Project: To better understand the flow of electrons within the neuronal nitric oxide synthase reductase domain from NADPH to the FAD and FMN cofactors. Rate constants for the charge transfer between $NADP^+$ and $FADH_2$ in NOS were determined for the first time.

Teaching and Mentoring Experience

University of California, Irvine   Irvine, CA

Teaching Assistant, Biochemistry   Summer 2013, Winter 2014, Summer 2014
- Taught this biochemistry course **3** times.
- Coordinated with lecturer to increase student comprehension and help them reach course objectives.
- Also independently led 6 discussion groups of 60 students each, tailored to help students develop a deeper understanding of biochemistry concepts.
- Used active learning techniques to keep students engaged, including clicker questions to apply the material learned, group activities to solve problems, and encouraging student interaction and discussion.

    "During lecture, Georges will walk around the lecture hall to make sure all the students get their questions answered. He's friendly and always approachable"

    "He has the knowledge to help guide students into understanding biochemical concepts"

Teaching Assistant, Biochemistry Laboratory   Winter 2014 and Spring 2014
- **Independently** ran two 20-student laboratories.
- Hands-on teaching of gene expression vector design, protein purification, protein quantification assays, enzymology, UV/Vis spectrophotometry, and X-ray crystallography basics.
- Also taught proper lab report and scientific writing.
- Supervised skill-training activities, evaluated student performance and provided individual feedback.

    "Very detailed and helpful. Gives you information you need without spoon feeding it to you. Lets you think about problems."

    "Makes an effort to actually teach students, is patient and encourages us to come to our own conclusions."

    "He is enthusiastic and easy to approach with problems, he doesn't hesitate to assist in lab procedures and seems fair at teaching the class objectives"

Teaching Assistant, Molecular Biology   Spring 2014 and Summer 2014
- Taught this molecular biology course **twice**.
- Coordinated with lecturer and helped design a 6-week molecular biology learning module that I independently taught to groups of 30-70 students each.
- Learned to communicate effectively in order to improve student learning.

Guest Lecturer, Biochemistry   July 2013
- Invited to teach a lecture on protein purification to two separate groups of 250 undergraduate biology students.
- Motivated and encouraged students interested in graduate school by sharing my own experience as a graduate student doing research in Biological sciences.

Undergraduate and Graduate Research Advisor   May 2012 – June 2016
- Trained and mentored **5** undergraduate student researchers and **2** graduate students in laboratory research in molecular biology, biochemistry, and X-ray crystallography.
- One student won the UCI Dean's Award for Excellence in Research.

Publications

1. **Chreifi G**, Baxter EL, Doukov T, Cohen AE, McPhillips SE, Song J, Meharenna YT, Soltis SM, Poulos TL. Crystal structure of the pristine peroxidase ferryl center and its relevance to proton-coupled electron transfer. *PNAS* 2016 Feb 2;113(5):1226-31.

2. Fields JB, Hollingsworth SA, **Chreifi G**, Heyden M, Arce AP, Magaña-Garcia HI, Poulos TL, Tobias DJ."Bind and Crawl" Association Mechanism of Leishmania major Peroxidase and Cytochrome c Revealed by Brownian and Molecular Dynamics Simulations. *Biochemistry* 2015 Dec 15;54(49):7272-82.

3. **Chreifi G**, Hollingsworth SA, Li H, Tripathi S, Arce A, Magaña-Garcia HI, and Poulos TL. Enzymatic Mechanism of Leishmania major Peroxidase and the Critical Role of Specific Ionic Interactions. *Biochemistry* 2015 Jun 2;54(21):3328-36.

4. Mukherjee P, Li H, Sevrioukova I, **Chreifi G**, Martásek P, Roman LJ, Poulos TL, Silverman RB. Novel 2,4-disubstituted pyrimidines as potent, selective, and cell-permeable inhibitors of neuronal nitric oxide synthase. *J Med Chem.* 2015 Feb 12;58(3):1067-88.

5. Li H, Jamal J, Plaza C, Pineda SH, **Chreifi G**, Jing Q, Cinelli MA, Silverman RB, Poulos TL. Structures of human constitutive nitric oxide synthases. *Acta Crystallogr D Biol Crystallogr.* 2014 Oct; 70(Pt 10):2667-74.

6. **Chreifi G**, Li H, McInnes CR, Gibson CL, Suckling CJ, Poulos TL. Communication Between the Zinc and Tetrahydrobiopterin binding sites in Nitric Oxide Synthase. *Biochemistry* 2014 July 1;53(25):4216-23.

7. Kang S, Tang W, Li H, **Chreifi G**, Martásek P, Roman LJ, Poulos TL, Silverman RB. Nitric oxide synthase inhibitors that interact with both heme propionate and tetrahydrobiopterin show high isoform selectivity. *J Med Chem.* 2014 May 22; 57(10):4382-96.

8. Cinelli MA, Li H, **Chreifi G**, Martásek P, Roman LJ, Poulos TL, Silverman RB. Simplified 2-aminoquinoline-based scaffold for potent and selective neuronal nitric oxide synthase inhibition. *J Med Chem.* 2014 Feb 27; 57(4):1513-30.

9. Huang H, Li H, Yang S, **Chreifi G**, Martásek P, Roman LJ, Meyskens FL, Poulos TL, Silverman RB. Potent and selective double-headed thiophene-2-carboximidamide inhibitors of neuronal nitric oxide synthase for the treatment of melanoma. *J Med Chem.* 2014 Feb 13; 57(3):686-700.

10. Jing Q, Li H, **Chreifi G**, Roman LJ, , Martásek P, Poulos TL, Silverman RB. Chiral linkers to improve selectivity of double-headed neuronal nitric oxide synthase inhibitors. *Bioorg Med Chem Lett.* 2013 Oct 15;23(20):5674-9.

11. Li H, Jamal J, **Chreifi G**, Venkatesh V, Abou-Ziab H, Poulos TL. Dissecting the kinetics of the NADP(+)FADH2 charge transfer complex and flavin semiquinones in neuronal nitric oxide synthase. *J Inorg Biochem.* 2013 Jul;124:1-10.

Fellowships and Awards

Howard A. Schneiderman Fellowship Award, University of California, Irvine   June 2015

The $5,000 Schneiderman fellowship is the highest honor granted to only two graduate students annually by the UC Irvine Ayala School of Biological Sciences in recognition of excellence in research and outstanding work in Biological Sciences.

Travel Grant, University of California, Irvine   April 2014

Recipient of a travel grant to present my research results at the American Society for Biochemistry and Molecular Biology conference in San Diego, CA.

Technical Experience

Molecular Biology:	DNA primer design, restriction enzyme digestion, recombinant DNA work, vector cloning, subcloning, site-directed mutagenesis, DNA ligation, PCR, agarose gel electrophoresis, DNA sequencing.
Protein Expression:	Developed recombinant protein expression protocols for optimal yields in various *E. coli* strains, including BL21(DE3), JM109(DE3).
Protein Purification:	Optimized protocols to achieve crystal quality purity using techniques such as SDS-PAGE, salt fractionation, ultra-filtration, and various column chromatography techniques, including metal affinity, ion exchange, hydrophobic interaction, and gel filtration (FPLC using ÄKTA instrumentation) chromatography.
Biochemistry, enzymology, and proteomics:	Design and optimization of enzyme activity assays to measure catalytic activity, ligand/inhibitor binding affinity and characterize protein-protein interactions in electron transfer systems. Techniques used include aerobic and anaerobic absorbance and fluorescence stopped-flow spectroscopy for measurement of rapid kinetics, further characterization using single and double beam UV-Vis spectrophotometers, and measurement of binding kinetics by biolayer interferometry (using Fortebio BLItz). Experience with site-specific crosslinking of peptides/proteins and mass spectrometry techniques such as MALDI-TOF, GC/MS, LC/MS-MS.
Structural biology:	Structure-based drug design, high throughput protein crystal screening using the TTP Labtech Mosquito and Art Robbins Crystal Gryphon protein crystallography dispensers. Experienced with sitting and hanging drop vapor diffusion, batch and free-interface diffusion setups. Synchrotron data collection and in-house (Rigaku MicroMax-007F) X-ray diffraction analysis, data processing, refinement and structure solution using single and multiple anomalous dispersion, and molecular replacement for phasing. Experienced with crystallography software for processing diffraction data, model building, refinement, graphics visualization and animation, including HKL-2000, MOSFLM, XDS, CCP4, Phenix, Coot, PyMol and UCSF Chimera.

Presentations

UCI-Ewha Research Symposium
Irvine, CA
Poster presentation
January 25 2016
Designed and created figures, tables and text for a poster presentation. Communicated research and results to an audience in the field of pharmaceutical sciences.

West Coast Protein Crystallography Workshop XXII   Monterey, CA
Poster presentation   April 2015
Designed and created figures, tables and text for a poster presentation. Communicated research and results to experts in X-ray crystallography.

American Society for Biochemistry and Molecular Biology EB 2014 Conference   San Diego, CA
Poster presentation   April 2014
Designed and created figures, tables and text for a poster presentation. Communicated research and results to a broad audience, many of which were not experts in my field.

References

Dr. Thomas L. Poulos
Chancellor's professor of Biochemistry, Chemistry and Pharmaceutical Sciences
University of California, Irvine
(949) 824-7020
poulos@uci.edu

Dr. Celia Goulding
Professor of Molecular Biology, Biochemistry and Pharmaceutical Sciences
University of California, Irvine
(949) 824-0337
celia.goulding@uci.edu

Dr. Melanie Cocco
Professor of Molecular Biology, Biochemistry and Pharmaceutical Sciences
University of California, Irvine
(949) 824-4487
mcocco@uci.edu

ABSTRACT OF THE DISSERTATION

Exploring Structure-Function Relationships and Redox Partner Interactions

in Heme Enzymes

By

Georges Chreifi

Doctor of Philosophy in Biological Sciences

University of California, Irvine, 2016

Professor Thomas L. Poulos, Chair

While ubiquitous in the biological realm, heme enzymes exhibit numerous functions, including protecting organisms against reactive oxygen species, detoxifying xenobiotics and neuronal signaling. The specific function of a heme enzyme is tuned by the structure of the protein that binds the prosthetic group. This relationship between heme and protein is why heme enzymes have long served a foundational role in probing structure-function relationships in biology. The aim of this dissertation is to gain additional insights into heme enzyme structure-function relationships, as well as to gain a better understanding of heme enzyme active site chemistry and the interactions between the enzymes and their redox partners. We have done this by studying four different heme enzyme systems: i) a cytochrome c peroxidase from *Leishmania major* dubbed *Leishmania major* Peroxidase (LmP), ii) a speculative peroxynitrite isomerase, also from *L. major* dubbed pseudoperoxidase (LmPP), iii) a cytochrome P450 monooxygenase from *Citrobacter braakii* called P450cin, and iv) several mammalian nitric oxide synthase (NOS) isoforms. We determined the precise catalytic mechanism LmP, including the intriguing rate-limiting step of catalysis at steady-state and the importance of proton transfer in the catalytic

cycle. We also captured the X-ray crystal structure of the first catalytic intermediate with an iron center unreduced by electrons. This pristine structure, taken together with kinetics, corroborates our mechanistic conclusions. In the process, we validated the usefulness of X-ray free electron lasers as a powerful tool to probe the structure of enzymes that contain transition metals. We probed the association of LmP with its redox partner LmCytc and discovered the existence of a non-catalytic binding site. For our second system, we have solved the crystal structure of a novel LmPP and proposed a hypothetical mechanism that awaits testing. Although we were unable to reach our goals for our third system, we established a protocol to address the crystallization of the P450cin-Cdx complex. For our fourth system, we explored the precise and sensitive balance of forces that stabilize the structure and thus function of NOS, which is maintained by an elegant synergistic relationship between the Zn^{2+}, cofactor, and substrate binding sites. We finish by describing collaborative work attempting to design potent, isomer selective and bioavailable inhibitors to treat neurodegenerative diseases.

INTRODUCTION

Chapter 1

1.1 Introduction to heme proteins

Metalloproteins are involved in a countless number of cellular reactions where they play a central role in the biochemistry of living systems. One of the most widely studied metal containing cofactors is iron protoporphyrin IX, more commonly called heme. A fascinating property of heme containing proteins and enzymes is that they are involved in a multitude of very diverse functions, most famously in dioxygen transport or storage by hemoglobin and myoglobin, in biological electron transfer such as cytochrome c in the electron transport chain, and in various biological catalysis, including oxygenases such as cytochrome P450s, many peroxidases, and nitric oxide synthases (NOS). The sheer chemical diversity produced by the coupling of a heme group to a protein is so vast that new functions are being discovered every year in numerous, diverse organisms. The fact that the same cofactor is involved in such a diversity of functions proves that heme proteins exemplify the importance of the relationship between structure and function in biology, and has prompted countless research groups and resources to try to better understand the structural and functional intricacies that define heme function and catalysis. What we have found is that the 3-dimensional protein environment around the active site is always exquisitely fine-tuned to effect a different function, and that slight changes in structure can result in vast changes in function. At the chemistry level, understanding the basics of heme biochemistry is an extremely beneficial venture, since it can help us understand the mechanisms of important biochemical transformations that occur across all life. A better understanding of the protein environment has even allowed some groups to

engineer heme enzymes to catalyze novel reactions,[1] which is a testament to the endless potential of coupling the heme group to a specific protein environment. This dissertation, therefore, centers on the relationship between structure and function in heme enzymes and in providing a deeper understanding of the fascinating and exquisite details of heme active site chemistry. We will therefore look at four fascinating heme enzyme systems that demonstrate the diversity and distinctiveness of heme catalysis: the heme peroxidase, a putative heme peroxynitrite isomerase, a cytochrome P450 monooxygenase, and nitric oxide synthase.

1.2 Heme peroxidases

We have repeated *ad nauseam* that the same heme group is ubiquitous in nature, yet is used to achieve very different biological functions, but stressing this point is important because of the central role heme proteins have played in our understanding of structure-function relationships in biology. We first look at heme peroxidases since they have very often stood out as ideal heme enzymes for these types of studies because they form significantly more stable intermediates that have long lifetimes when compared to other heme enzymes, making them easier to capture and study using biophysical methods. Anecdotally, heme peroxidases have served such a breakthrough role in understanding heme chemistry that much of the terminology used for peroxidase intermediates, such as compound I and II, has been applied to other heme enzymes that have less stable, shorter-lived intermediates, some of which have never even been captured by biophysical techniques in other heme enzymes, but have only been inductively hypothesized.

Peroxidase structure and enzymology

Oxidative heme enzymes perform their biological function by storing oxidizing equivalents as higher oxidation states of iron and organic radicals, and peroxidases have historically served a special role in this area. These enzymes catalyze the conversion of H_2O_2 to H_2O. Structurally, they are expressed as single polypeptide chains, generally about 30-40 kDa in size and possess a heme binding site stabilized by a single His imidazole that ligates the iron at the proximal side of the heme, with the distal side being open to coordinate H_2O_2. Cytochrome c peroxidase (CcP) produced by *Saccaromyces cerevisiae* (baker's yeast) was the first heme peroxidase crystal structure to be determined,[2] and has generally been one of the most studied peroxidases in the quest to probe structure-function relationship in heme enzymes, as well as in elucidating the fundamental mechanisms of interprotein electron transfer (ET).[3] Its physiological function is to protect the organism against oxidative stress by breaking down H_2O_2, a harmful reactive oxygen species (ROS), into harmless components. CcP therefore catalyzes the chemical transformation of one equivalent of H_2O_2 into two equivalents of H_2O by using two reducing equivalents from yeast cytochrome c (Cytc), a small, well conserved heme protein whose primary physiological function is electron transfer.

1    $CcP(Fe^{III};Trp) + H_2O_2 \longrightarrow CmpI(Fe^{IV}=O;Trp^{\cdot+}) + H_2O$

2    $CmpI(Fe^{IV}=O;Trp^{\cdot+}) + Cytc(Fe^{II}) \longrightarrow CmpII(Fe^{IV}=O;Trp) + Cytc(Fe^{III})$

3    $CmpII(Fe^{IV}=O;Trp) + H^+ \rightleftharpoons CmpII(Fe^{III}-OH;Trp^{\cdot+})$

4    $CmpII(Fe^{III}-OH;Trp^{\cdot+}) + Cytc(Fe^{II}) + H^+ \longrightarrow CcP(Fe^{III};Trp) + Cytc(Fe^{III}) + H_2O$
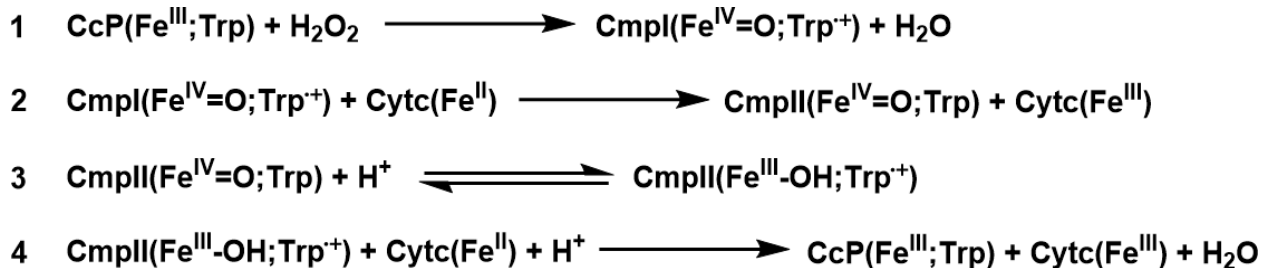
Figure 1.1 – CcP reaction mechanism

Figure 1.1 depicts the generally accepted CcP reaction mechanism, which begins with the CcP heme iron in the ferric (Fe^{III}) state. Binding of H_2O_2 is followed by heterolytic fission of the O-O bond, releasing the first molecule of H_2O and forming the first reactive intermediate termed Compound I (CmpI). CcP CmpI has been confirmed to be composed of a ferryl-oxo complex ($Fe^{IV}=O$) and a radical on the indole ring of Trp191 ($Trp^{\cdot+}$).[4-5] In the second step, the substrate cytochrome c binds the peroxidase and delivers one electron to CmpI, which reduces the Trp191 radical and forms CmpII.[6-12] An intramolecular electron transfer from Trp191 reduces Fe^{IV} to Fe^{III}.[13-14] Another molecule of cytochrome c then binds and delivers a second electron as a final step and reduces the Trp191 radical, restoring the enzyme back to its resting state and allowing the cycle to repeat.

Peroxidase Classification

Non-mammalian heme peroxidases have been classified into three main classes.[15] Class I peroxidases are located inside the cell, and CcP is the most famous example. Class II peroxidases are extracellular enzymes mainly produced by some species of fungi. Class III peroxidases are also extracellular, but mainly expressed by plants. Horseradish peroxidase (HRP) is a well studied example of a Class III peroxidase. CcP was initally considered an outlier in comparison to most other heme peroxidases, such as HRP, for two main reasons. First, CmpI in most other heme peroxidases has a porphyrin-π cationic radical[16] instead of an amino acid radical such as Trp191 in CcP, and second, because CcP was the only well studied peroxidase that uses Cytochrome c (Cytc) as a reducing substrate. Fastforward to the year 2005, when a mitochondrial heme peroxidase produced by the protozoan *Leishmania major* (a parasite that causes the disease leishmaniasis) was discovered.[17] This *L. major* peroxidase was originally

thought to be a functional hybrid of *S. cerevisiae* CcP and *P. sativum* ascorbate peroxidase (APX), and was named LmAPX. Work done in our laboratory eventually showed that the enzyme is structurally and functionally very similar to CcP and it was thus renamed LmP. LmP was also found to use Cytc from the same organism as a reducing substrate (LmCytc),[18] and has now become the most extensively studied non-yeast CcP.[19-20] What is more interesting is that LmP appears to be one of the first heme peroxidases to mimic the rather unique CcP mechanism. EPR work has shown that CmpI in LmP is indeed a Trp cationic radical, analogous to Trp191 in CcP, and that the stability of the intermediate is similar.[21] Furthermore, the structure of the LmP-LmCytc complex are quite similar,[22] albeit with some important differences that we will discuss in a later chapter.

What remains unclear is whether the two mechanisms are entirely analogous, and especially whether the first electron transfer reduces the Trp radical like in CcP, or the ferryl-oxo complex ($Fe^{IV}=O$), and these are questions that we take on in Chapter 2.

Differences between CcP and LmP

We now shift our focus on the differences between the CcP and LmP systems. Despite some similarities, several properties differentiate LmP from CcP. First, unlike CcP, the LmP reaction follows classic Michaelis-Menten kinetics and the reaction rate is highly dependent on electrostatic interactions. Indeed, while CcP activity increases with increasing ionic strength at any given substrate concentration,[14] LmP activity steadily decreases with increasing ionic strength (Figure 1.2). This shows the importance of ionic strength on protein-protein interactions and complex formation, and the potential role of specific inter-complex interactions.
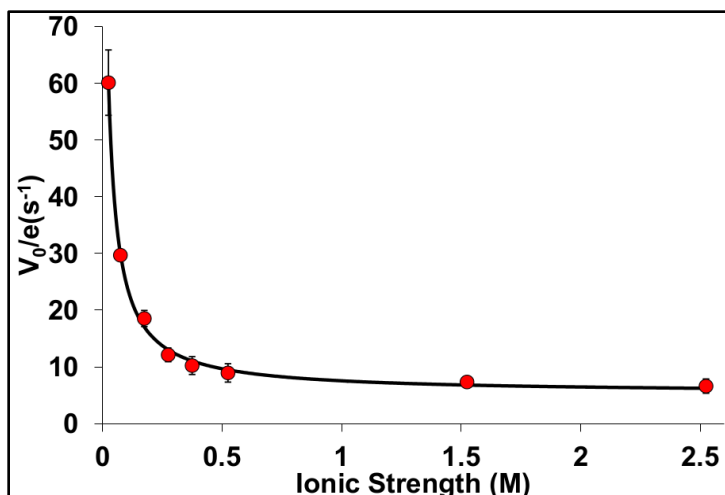
Figure 1.2 – LmP turnover as a function of ionic strength
Lmcytc oxidation by LmP as a function of increasing ionic strength. For each measurement, 180 mM H_2O_2 were added to a reaction mixture containing 50 nM LmP and 10 μM LmCytc in 25 mM phosphate buffer pH 6.5. The ionic strength was controlled by adding the necessary amounts of KCl and LmCytc oxidation was monitored at 558 nm for 1 min.

Second, while CcP relies mainly on non-bonded contacts to stabilize complex formation (Figure 1.3A),[23] the LmP-LmCytc complex is stabilized by specific elecstrostatic interactions. The most notable of these interactions is the ion pair generated by Arg24 of LmCytc, which upon complex formation, undergoes a conformational change and forms two strong H-bonds with Asp211 of LmP, sequestering them both from contact with the solvent (Figure 1.3B). Asp211 itself is a central residue: it is only 4.1 Å away from the LmCytc heme iron in the complex, is the first residue in the proposed electron transfer pathway on the way to the LmP heme, and its backbone carbonyl oxygen stabilizes the binding of a K^+ ligand. Previous studies have shown that the function of the K^+ ligand that binds LmP is to stabilize: 1) the protein structure near the active site and 2) the spin state of the heme iron required for enzymatic activity.[24] Previous site-directed mutagenesis studies on Arg24 have shown a large decrease in LmCytc binding affinity (K_M) and overall enzymatic activity,[22] confirming the key role of this ion pair, although the exact reasons are not fully understood. We also tackle this interaction in Chapter 2.
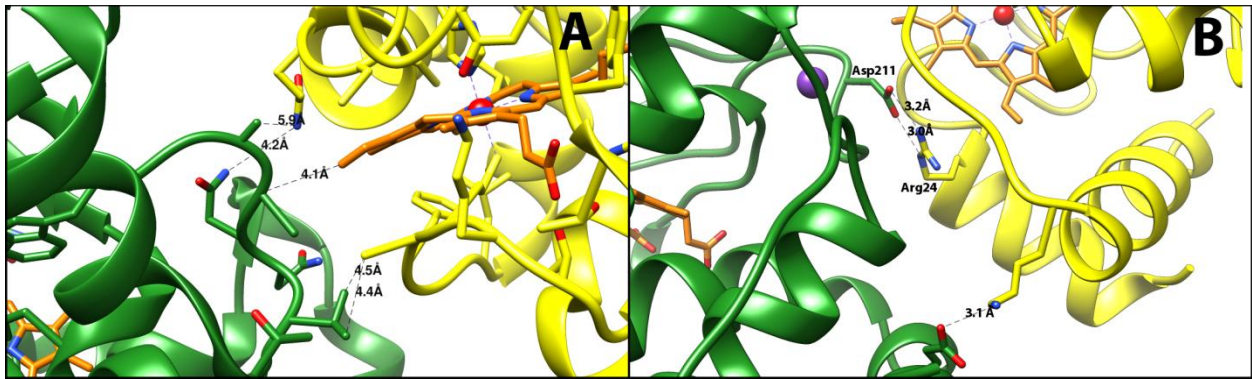
Figure 1.3 – Active sites of CcP and LmP in a complex with their physiological cytochromes c.
(A) CcP-Cytc complex. (B) LmP-LmCytc complex. For both panels, the peroxidase is depicted in green, the cytochrome c in yellow, and heme in orange. H-bonds are depicted as dashed lines with distance in Angstroms. This figure was generated using UCSF Chimera.[25]

Biomedical Relevance of LmP

The fact that this peroxidase is one of few identified in human pathogens initially gave biomedical relevance to peroxidase study, with the hope that inhibiting its activity might increase the organism's sensitivity to oxidative stress (especially since *Leishmania* lacks catalase and selenium containing glutathione peroxidases).[19] Unfortunately, this therapeutic option has been invalidated. Although LmP knockouts did increase sensitivity to exogenously added H_2O_2, the organism was shown to compensate by instead inducing the over-expression of non-selenium glutathione peroxidase and other anti-oxidative enzymes to increase survival under oxidative stress, (and even become more virulent!).[26] These results have essentially eliminated LmP as a potential therapeutic target.

Statement of Purpose

So why are we interested in studying yet another heme peroxidase? The main reason is that understanding the similarities and differences of this system in comparison with CcP can provide really interesting and useful insights into heme enzyme structure and chemistry and

allows us to better understand how heme enzymes from different biological systems achieve and stabilize higher oxidation states.

1.3 Cytochrome P450

Dioxygen (O_2) is known to play two main roles in biological organisms. First, as a terminal electron acceptor (e.g. in the electron transport chain), and second, as a reagent used by oxygenases to catalyze a variety of oxidation reactions. There are two main types of oxygenases, monooxygenases and dioxygenases, which are aptly named based on the number of oxygen atoms that are incorporated into the substrate. (Figure 1.4)

Monooxygenase: $\quad$ C−H + O_2 + H_2 $\longrightarrow$ C−OH + H_2O

Dioxygenase: $\quad$ C−H + O_2 $\longrightarrow$ C−OH $\parallel$ O
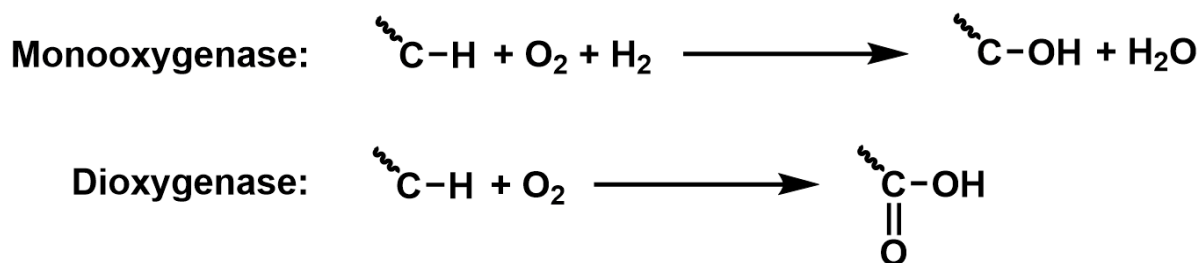
Figure 1.4 –The two oxygenase categories

Cytochrome P450 is a monooxygenase, and its history is quite interesting. In 1958, Garfinkel[27] and Klingenberg[28] independently discovered a red pigment in pig and rat liver microsomes that displayed a rather unusual absorption peak at 450 nm in the presence of CO, although not much more was known at the time. It wasn't until 1964 that Omura and Sato found a pigment from rabbit liver with the same spectroscopic properties and identified it as a heme protein. [29] Even though its function was still unknown, it was nonetheless named Cytochrome P450, with the "P" standing for pigment, and the "450" alluding to the signature Soret absorption peak at 450 nm induced by CO binding to the ferrous heme. Since then, these fascinating enzymes have been identified in breathtaking numbers in all biological kingdoms, including in

animals, plants, archea, bacteria and more recently even in viruses.[30] As of April 2016, over 35,000 P450s have been identified, including 57 in human beings,[31] making P450s one of the largest enzyme superfamilies.

P450s are most well known for their role in drug metabolism, where they act as a first point of contact for the drug, which gets hydroxylated. The incorporation of a hydroxyl group increases the polarity and thus the solubility of the compound, which allows other enzymes in the detoxification pathway to further modify it and eliminate it. P450s are also involved in steroid biosynthesis, antibiotic biosynthesis, vitamin production and cholesterol metabolism.[32] All P450s must receive two electrons from NADH or NADPH *via* other redox-active proteins. The microsomal P450s use a single NADPH-Cytochrome P450 reductase protein that contains a flavin adenine dinucleotide (FAD) and flavin mononucleotide (FMN) cofactors, where electrons flow from NADPH, to FAD, to FMN, and finally to P450. On the other hand, most bacterial and mitochondrial P450 systems involve cofactors in separate proteins, and often an iron-sulfur protein is involved instead of the FMN flavoprotein, meaning that electrons flow from NAD(P)H, to FAD, to an iron-sulfur protein, and finally to P450. This is not always the case however, since the multitude of P450 ET systems are very diverse. For instance, in the P450$_{BM3}$ system from the gram-positive *Bacillus megaterium*, all of the redox-active cofactors are expressed in a multi-domain single polypeptide, resulting in a very efficient hydroxylase.[33]

Altogether, P450s are capable of catalyzing the oxidative conversion of more than one million substrates.[34-35] Of these conversions, P450 monooxygenases are most famous for their ability to activate one of the oxygen atoms of dioxygen and incorporate it into an inert hydrocarbon. Even more remarkable is its ability to perform this hydroxylation both regio- and stereoselectively, all of which is done without oxidizing the protein itself. These features have earned it the nickname "nature's blowtorch". The fact that P450s are able to activate dioxygen, a molecule with low kinetic reactivity at ambient temperatures and pressures, is also an impressive feat. This remarkable ability is conferred by the heme iron, which is able to overcome this kinetic barrier by binding dioxygen in the ferrous oxidation state to form a ferrous-O_2 (or ferric-O_2^-) complex. Once bound, P450 catalysis is modulated by the nature of the heme proximal ligand, which is the thiolate anion of a cysteine residue.[36] Together with the residues that surround the active site pocket on the distal side of the heme, the thiolate nature of the axial ligand plays a crucial role in O_2 activation by what has been called the "push/pull" effect (Figure 1.5).[37-41] This mechanism describes the driving forces behind the heterolytic cleavage of the O-O bond and stabilization of the CmpI intermediate, which occur for two main reasons. First, the thiolate provides electron density to "push" the iron to a higher oxidation state, while distal residues form a H-bonding network that "pull" the outer oxygen of the peroxide, stretching the O-O bond, favoring cleavage of the bond and reduction of the outer oxygen to water.
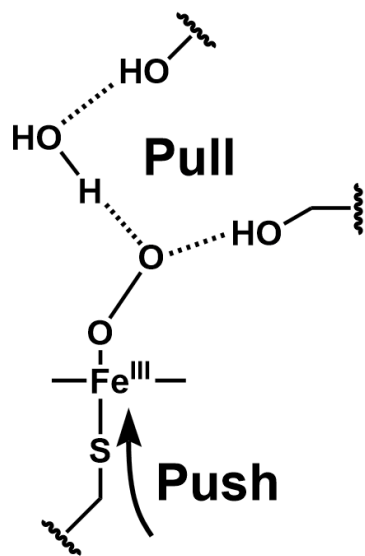
Figure 1.5 – The push-pull mechanism of O-O bond cleavage
The thiolate nature of the axial ligand "pushes" electron density to stabilize a higher iron oxidation state. At the same time, H-bonding between the outer oxygen of the peroxide and protein side-chains "pull" the O-O bond apart.

Mechanism

The overall P450 reaction mechanism has been characterized and is well known (Figure 1.6). At resting state, the P450 heme is hexacoordinated, in a low spin state, with a water in the sixth axial position (A). Binding of a substrate in the active site pocket displaces the water, shifting the heme to a high spin pentacoordination, and increasing the redox potential of the heme iron (B). This allows electrons flowing from NAD(P)H to reduce the ferric iron to ferrous (C), which in turn allows O_2 to bind and form a ferric-superoxo complex (D). A proton-coupled electron transfer (PCET) event reduces the superoxo to peroxo and simultaneously protonates it to form a hydroperoxo (E). The push/pull effect then stabilizes the formation of CmpI (F). Subsequent hydroxylation of the substrate by CmpI occurs by a 2-step "oxygen rebound mechanism".[42] First, the substrate C-H bond is homolytically cleaved to generate a carbon radical and CmpII (G). Then, the carbon radical is recombined with the hydroxyl to form the final hydroxylated substrate (H). The substrate is finally released, allowing H_2O to coordinate the heme and return the enzyme to its resting state.

11
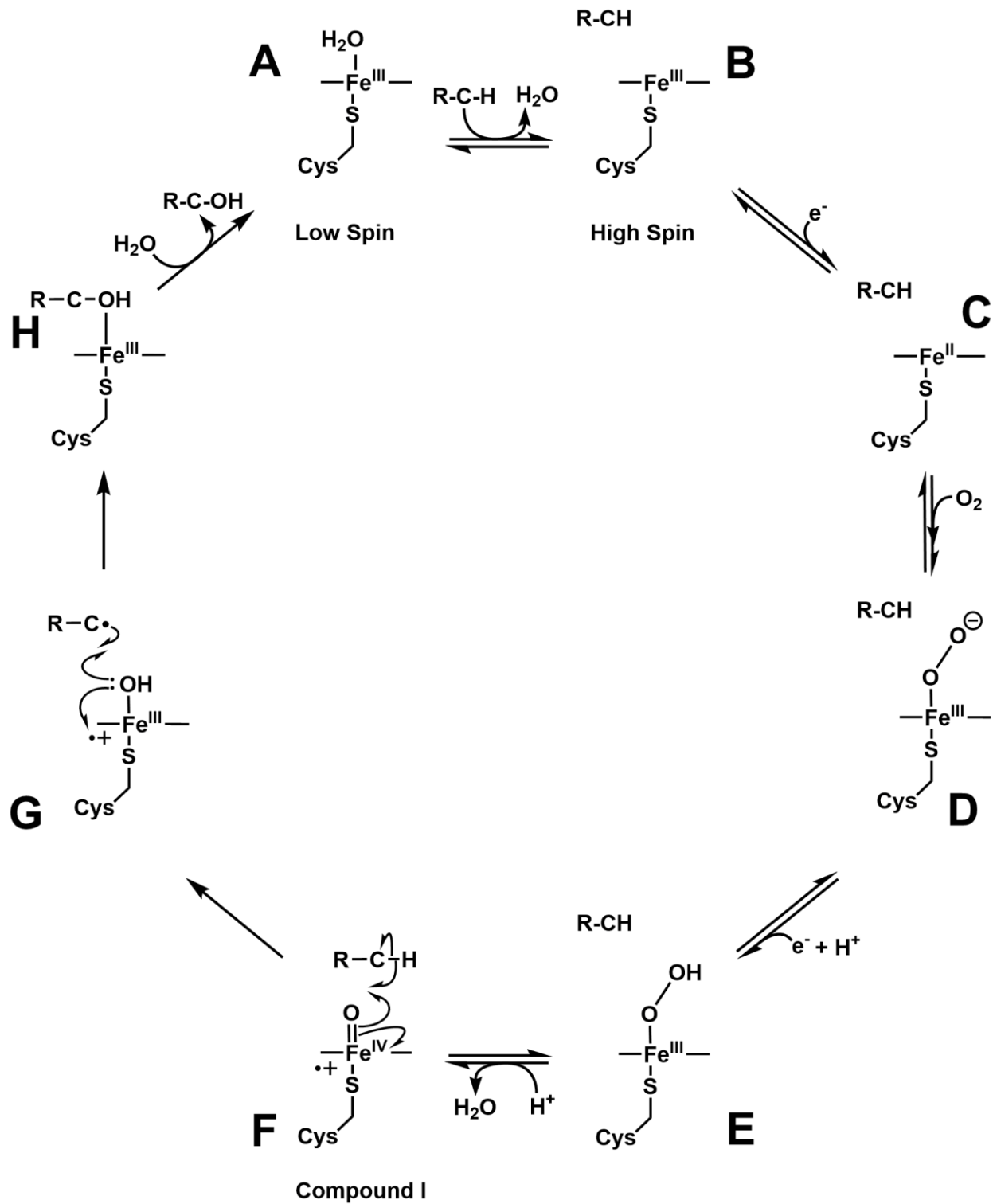
Figure 1.6 – The P450 reaction mechanism

12

P450s are expressed as a single polypeptide chain, and are usually between 40-50 kDa in size. Most eukaryotic P450s are tethered to the inner mitochondrial membrane or to the endoplasmic reticulum membrane via an N-terminal hydrophobic tail, making them difficult to recombinantly express and purify in large quantities. For this reason, bacterial systems were mainly used as models to probe the P450 mechanism in eukaryotes. P450cam from *Pseudomonos putida* is arguably the most well studied P450 to date, and has served as the main model from which most P450 chemistry has been elucidated, having been the first one to be sequenced,[43-44] well characterized[45] and crystallized.[46-47]

P450cam catalyzes the regio- and stereoselective hydroxylation of camphor to generate 5-*exo*-hydroxycamphor (Figure 1.7), thus allowing the pseudomonad to solubilize camphor and use it as a carbon source. The P450cam system uses two separate redox-active proteins to transfer electrons, the FAD binding Putidaredoxin reductase (PdR), and the Fe_2S_2 binding Putidaredoxin (Pdx). One intriguing aspect that appears to be unique to the P450cam system is that the second ET (Step D→E in Figure 1.6) has been shown to be specific to Pdx, and that no other redox partner is able to deliver this electron.[48-50] Our aim is to study whether P450cam is truly unique in that aspect, or if another P450 system could behave similarly, which we discuss in Chapter 6.
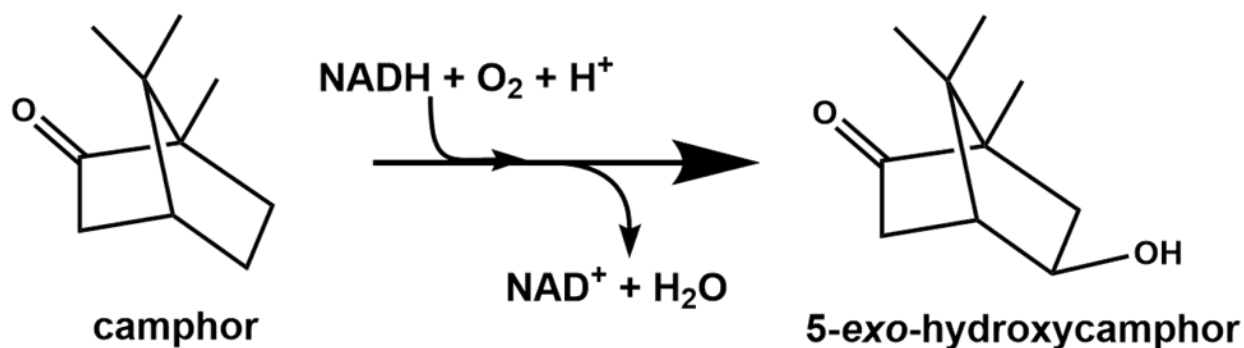
Figure 1.7 – **P450cam hydroxylates camphor to 5-*exo*-hydroxycamphor.**
As a monooxygenase, only one O atom is used in the reaction, the other is reduced to H_2O.

1.4 Nitric Oxide Synthase

Nitric oxide (NO) is an important signaling molecule whose small size and high reactivity make it particularly effective as a biological messenger. This small free radical is also one of few known gaseous signaling molecules and has been the subject of considerable research in the biomedical sciences because of its involvement in a large variety of physiological functions. For instance, NO release in the vascular endothelium promotes smooth muscle relaxation and vasodilation, whereas in the central nervous system, it is involved in neuronal signaling.[51] NO also serves as a cytotoxic agent in the immune system where it reacts with superoxide (O_2^-) to form peroxynitrite ($ONOO^-$), a reactive nitrogen species used in a response to an invading pathogen.[52-53] The main producers of NO in cells are heme enzymes called nitric oxide synthases (NOSs). NOS catalyzes the 2-step oxidation of L-arginine to L-citrulline, releasing NO in the process.[54] In the cell, NO production initiates a signaling cascade that begins when NO binds to the heme of guanylyl cyclase, acting as a positive regulator that activates the enzyme, converting GTP to cyclic GMP and transducing a signal.[55]

Mammals express three different NOS isoforms that produce NO in these different tissues: neuronal (nNOS), endothelial (eNOS), and inducible (iNOS).[56] All three isoforms share the same domain architecture, composed of two main domains, the N-terminal oxygenase domain and C-terminal reductase domain. This arrangement is similar to bacterial cytochrome $P450_{BM3}$,[33] where the oxygenase and flavin domains are fused in a single polypeptide chain, and therefore allows NOS to be self-sufficient and function without needing electrons from external redox partners. This fusion is different from what we see in the mammalian microsomal P450 system, where the heme and flavins are expressed in two separate proteins, namely P450 and

P450 reductase.[57-58] The NOS N-terminal oxygenase domain is where the heme group is located

(we also call it the heme domain), along with a nearby binding site for the cofactor (6R-)5,6,7,8-

tetrahydrobiopterin (H_4B),[59] and is where NO catalysis occurs. In solution, NOS forms a dimer

from two identical polypeptide chains, and the dimer interface is formed between the two

oxygenase domains. This homodimer is required for activity, since monomeric NOS does not

bind H_4B or substrate.[60] The NOS dimer is stabilized by a Zn^{2+} ion coordinated to four

symmetry-related Cys residues exactly along the dimer 2-fold axis.[61-62] The NOS C-terminal

reductase domain provides the binding sites for NADPH, FAD and FMN.[63] It is interesting to

note that NOS was initially identified as a flavoprotein[64] before being recognized as a heme

enzyme,[65-66] and that the crystal structures of both domains have been solved in isolation,[61, 67-71]

but no structure with both domains is yet known. Electron flow in NOS is similar to the P450

system, which proceeds from NADPH to FAD then to FMN, and finally reaching the heme

catalytic center. NOS differs from P450s in that it is activated by Ca^{2+}-calmodulin (CaM)

binding to a helical linker region located between the heme and reductase domains, which

activates NOS catalysis.[72] Figure 1.8 shows what happens when CaM binds to NOS: a

conformational change allows the FMN subdomain of one subunit to bind to the heme domain of

the other subunit, meaning that electrons flow from one subunit to the other,[73] which explains

why NOS is only active as a homodimer. *In vivo*, CaM binding to nNOS and eNOS is regulated

by cellular Ca^{2+} levels.[74] As for iNOS, CaM exhibits an extremely high binding affinity, making

it bound even at low intracellular Ca^{2+} concentrations.[75]
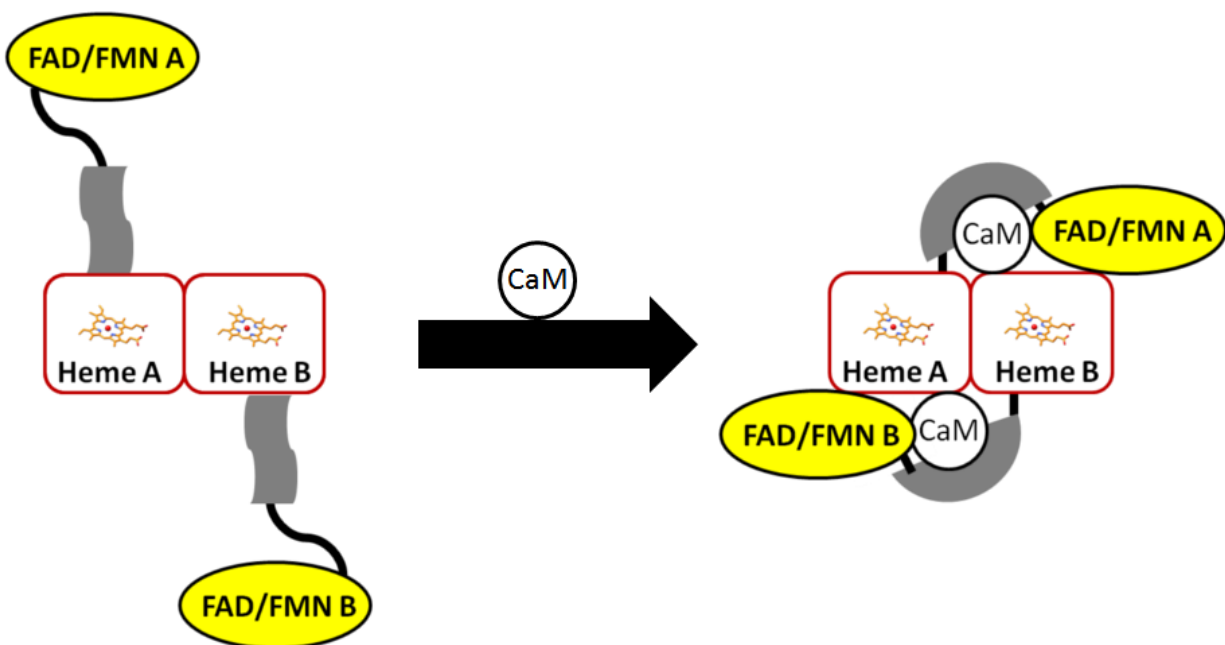
Figure 1.8 – Cartoon drawing of NOS regulation by CaM
Binding of CaM to the linker region causes a conformational change that connects the reductase domain of one chain to the heme of the other chain, thus allowing electron transfer between the FMN and heme groups of opposing chains.

NOS chemistry

Like the much studied cytochrome P450s, the NOS heme is pentacoordinated, with a cysteine thiolate serving as the proximal ligand that coordinates the iron. CO binding to the reduced heme also produces the characteristic 450 nm absorption. As expected from the theme of this dissertation, what differentiates the function of the two systems is the structural architecture of the active site, which, in the case of NOS, is geared to stabilize binding of L-Arginine, and its conversion to L-citrulline. As we have just seen, the NOS catalytic reaction requires the co-factor H_4B. Since NOS is active as a homodimer, a total of two H_4B molecules bind at the dimer interface, about 15 Å away from the Zn^{2+} site, and each H_4B interacts directly with one of the hemes. The role of H_4B is unique in NOS. While in other enzymes, H_4B undergoes a two-electron redox cycle and dissociates, H_4B binding in NOS is permanent, where it serves as a one electron donor in the reaction, forming a cationic radical species that is reduced

by the end of each catalytic cycle. Thus, H_4B in NOS is regenerated after each NO synthesis cycle and never dissociates.[76-78]

L-Arginine   **Nω-Hydroxy-L-Arginine**   **L-Citrulline**   **Nitric Oxide**

Figure 1.9 – NOS catalysis: two-step oxidation of L-arginine to L-citrulline and NO
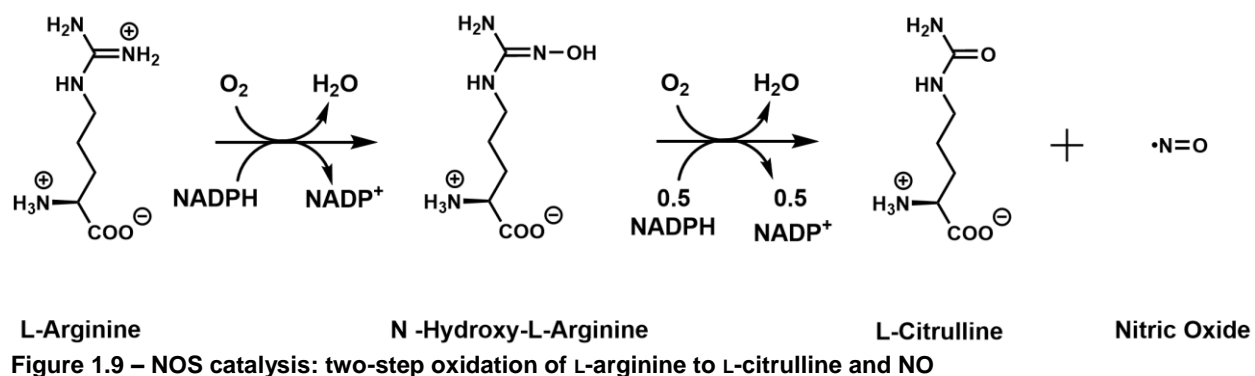
NOS catalysis proceeds in a two step mechanism. First, L-arginine is hydroxylated to N^ω-L-hydroxyarginine (L-NHA), then L-NHA is oxidized to citrulline and NO (Figure 1.9).[79-80] Mechanistically, the first step (Figure 1.10, steps A to C) is analogous to substrate hydroxylation by P450cam (Figure 1.6). A detailed mechanism for the second step, however, has been elusive and two main mechanisms for the oxidation of L-NHA have been proposed so far. The most likely of the proposed mechanisms is described in Figure 1.10, steps D to H. Starting from (D), Electrons originating from H_4B reduce the ferric-superoxo (Fe^{III}-O_2^-) to ferric-peroxo(Fe^{III}-O_2^{2-}), which generates a H_4B cationic radical (E). Then, a nucleophilic attack by the peroxide causes formation of one of the C-O bonds (F). The proximal oxygen of the peroxide then abstracts a proton from the nitrogen atom of L-NHA, generating L-Citrulline and NO^- (G). In the final step, the H_4B radical is reduced by obtaining an electron from the ferrous NO complex, thus regenerating H_4B for another cycle and allowing the release of NO from ferric heme (H).
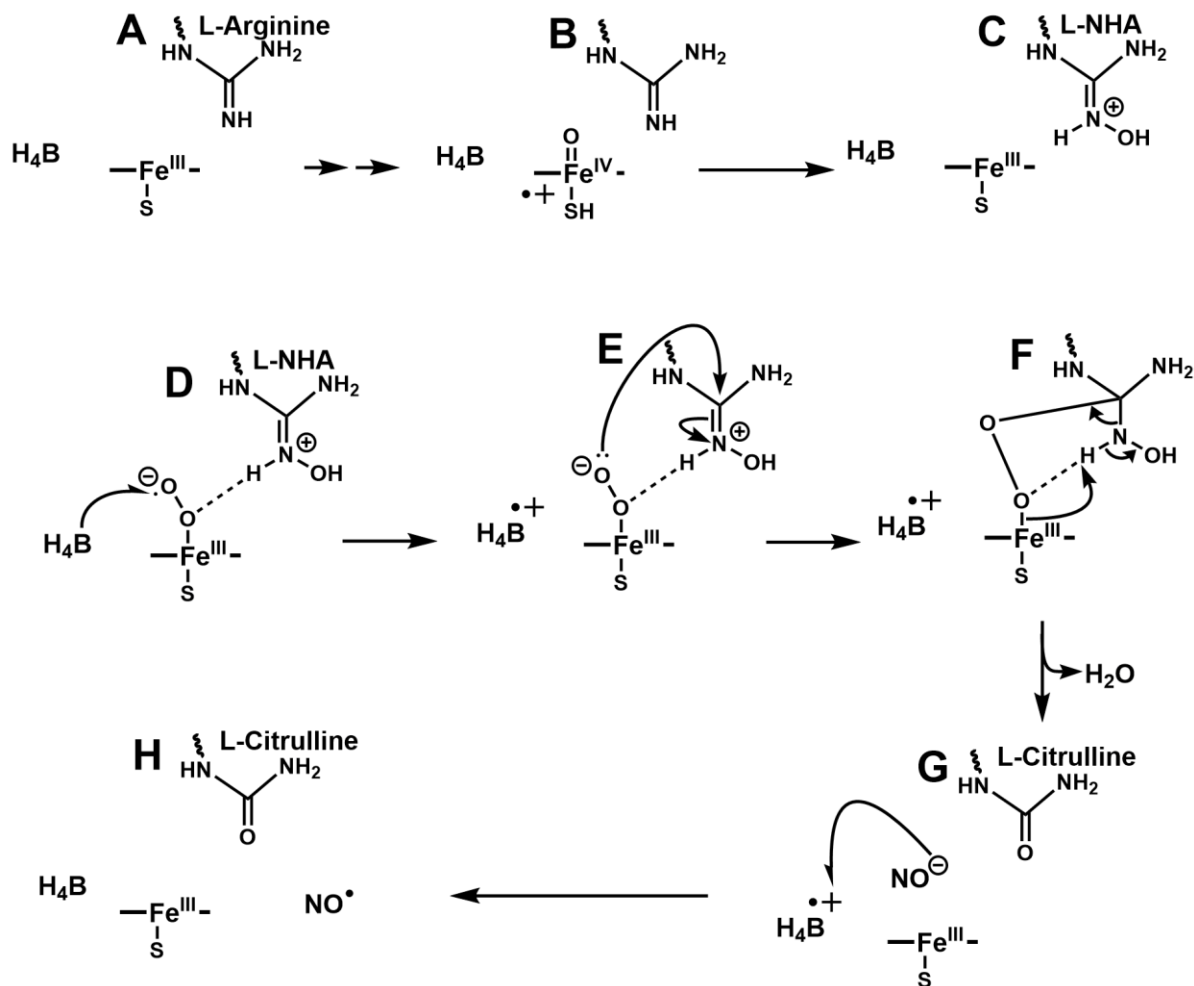
Figure 1.10 – Conversion of L-Arginine to L-Citrulline *via* L-NHA intermediate
The mechanism of hydroxylation of L-Arginine by NOS (steps A to C) proceeds via CmpI formation, just like in P450s. The most likely mechanism for oxidation of L-NHA involves the formation of an iron-peroxo complex which abstracts a proton of the N^ω of L-NHA, generating L-Citrulline and NO^- in the process. Electrons from the NO^- are then hypothesized to regenerate the H_4B cofactor, allowing release of the NO radical from the heme.

Cytotoxicity of NO

Although NO plays a vital role as a second messenger, the small molecule appears to also be a neurotoxin when overexpressed in brain cells. Being an extremely reactive molecule, uncontrolled NO production can wreak havoc in a variety of ways, including nitrating important enzymes, lipids, DNA, and by depleting intracellular levels of detoxifying enzymes such as glutathione.[81] Overexpression of neuronal NO has therefore been implicated in the pathology of several neurodegenerative diseases and conditions such as as brain ischemia,[82] septic shock,[83]

18

seizures,[84] migraines,[85] Alzheimer's disease,[86] Parkinson's disease,[87] and ALS,[88] and even in the growth of melanoma tumors.[89] Improper nNOS regulation is not the only deleterious condition, as even iNOS overexpression in the immune system has been linked to cancer development,[90] and bacterial NOS has been implicated in increased virulence and antibiotic resistance.[91-92] This large body of evidence has made NOS inhibition, and nNOS in particular, a very active research field in the hope to find a potent cure for these ailments.[93-95]

Even though nNOS inhibition is a promising strategy for the treatment of neurodegenerative diseases, there are several obstacles associated with nNOS inhibitor design. Unwanted inhibition of iNOS can affect the immune system and inhibition of eNOS can cause hypertension.[96-97] Therefore, for any inhibitor to have great therapeutic potential, it must not only be potent, but also have much greater selectivity for nNOS than the other isoforms. The problem is that the NOS active site architecture in all three isoforms is very similar[94, 98] and, therefore, the first obstacle to designing good nNOS inhibitors is that they must be isoform selective. Most nNOS inhibitors are designed as structural mimics of the native substrate, L-Arginine, but the problem with such inhibitors is that they have many basic amines and are highly polar which means they have poor blood-brain barrier permeability, and thus are not useful as real life therapeutics. Therefore, the second obstacle to designing a good nNOS inhibitor is blood-brain barrier permeability.

Chapters 8 to 12 will describe some of the efforts undertaken through an ongoing collaboration between the Silverman and Poulos groups by taking a stucture-based inhibitor design approach to try to develop potent and selective nNOS inhibitors. This fruitful

collaboration has resulted in the production of a large library of mammalian nNOS inhibitors,[99-100] with both research groups having contributed as follows. The Silverman group designed and synthesized the inhibitors, and performed most of the inhibitor assays to determine inhibitor potency and isoform selectivity. The Poulos group, with Dr. Huiying Li spearheading this side of the project, focused on the structural side of the work by using the prepared inhibitors to solve the X-ray crystal structures of nNOS and eNOS, with each of these inhibitors bound in the active site. These NOS-inhibitor complexes provide the structural basis behind the measured inhibitory potencies, and reveal the binding modes of these inhibitors in the active site. They also provide helpful guidance to improving the design of future inhibitors to increase potency and specificity. I was a co-author in several of the manuscripts that were published as a result of this collaboration, and my contribution was to solve the crystal structures of eNOS in complex with the inhibitors in order to structurally address the specificity issue and guide the design of future inhibitors to have reduced specificity for eNOS.

1.5 Description of the dissertation chapters

To recap, the central uniting theme in this dissertation is the heme group, whose role is studied in different systems in order to elucidate a deeper understanding of the structure-function relationships that biological systems use to drive life. We begin our discussion with *L. major* peroxidase, by first examining its entire kinetic profile and step-by-step mechanism in Chapter 2. In Chapter 3, we probe the catalytic mechanism of CmpI formation in CcP and LmP, as well as measure and characterize the solvent deuterium isotope effect in the reduction of CmpII. Chapter 4 describes our examination of the protein-protein interactions of LmP and LmCytc in a collaboration with Scott A. Hollingsworth of the same research group using a combination of

computational and experimental methods. In Chapter 5, we take a look at a novel heme enzyme, also from *L. major* and that appears quite similar, but that does not physiologically catalyze the reduction of H_2O_2. This enzyme, dubbed pseudoperoxidase, instead appears to detoxify the reactive nitrogen species peroxynitrite. In chapter 6, we shift gears to discuss our ongoing efforts to determine whether Cdx is more than just a redox partner in the cytochrome P450cin system. Our final system studied is NOS. In Chapter 7, we discover a previously unknown communication between the H_4B and Zn^{2+} sites that highlights a new aspect of the delicate structure of the NOS dimer. Finally, Chapters 8 to 12 describe my involvement in the Silverman-Poulos collaboration to design potent, selective and bioavailable nNOS inhibitors as a therapeutic solution for a series of neurodegenerative diseases. Throughout this entire discussion, an emphasis is placed on the role of the heme and the interaction between heme and protein as we gain numerous insights on the nature of heme catalysis.

ENZYMATIC MECANISM OF LEISHMANIA MAJOR PEROXIDASE AND THE CRITICAL ROLE OF SPECIFIC IONIC INTERACTIONS

Chapter 2

Summary

In this chapter, we try to work out the entire LmP mechanism and whether it is truly analogous to CcP. In the process, we uncover interesting insights about the enzyme, including the important role of specific ionic interactions and an intriguing rate-limiting step at steady-state. We have used steady-state and single turnover kinetics to better understand the overall mechanism of LmP catalysis. We find that while the activity of CcP greatly increases with ionic strength, k_{cat} for LmP remains relatively constant at all ionic strengths tested. Therefore, unlike CcP, where dissociation of oxidized Cytc is limiting at low ionic strength, association/dissociation reactions are not limiting at any ionic strength in LmP. We conclude that in LmP, the intramolecular electron transfer reaction, $Fe^{IV}=O;Trp$ to $Fe^{III}-OH;Trp^{\cdot+}$, is limiting at all ionic strengths. Unlike CcP, LmP depends on key intermolecular ion pairs to form the electron transfer competent complex. Mutating these sites causes the initial rate of association to decrease by two orders of magnitude and a substantial lowering of k_{cat}. The drop in k_{cat} is due to a switch in the rate-limiting step of the mutants from intramolecular electron transfer to the rate of association in forming the LmP-LmCytc complex. Overall, we show that while LmP and CcP form very similar complexes and exhibit similar activities, they substantially differ in how activity changes as a function of ionic strength. This difference is primarily due to the heavy

reliance of LmP on highly specific intermolecular ion pairs, while CcP relies mainly on nonpolar interactions.

New concepts?

- *Stopped-flow spectroscopy:* A technique used to study rapid kinetics where separate reactants are pushed into a mixing chamber before the absorbance is measured.

- **Steady-state kinetics:** In a simple enzyme scheme $E + S \rightleftharpoons ES \rightleftharpoons E + P$, steady-state is achieved when the rate of formation of the ES complex is equal to its rate of decay.

- **Single turnover:** Measurement of the initial encounter of an enzyme and substrate before any product or intermediates have formed.

- k_{cat}**:** Also called the turnover number, represents the maximal rate of conversion of substrate to product.

- K_M**:** Michaelis-Menten constant, the substrate concentration at which the reaction rate is half of its maximum value. K_M is often used as an approximation of the binding affinity of a substrate to an enzyme.

- *Rate-limiting step:* The slowest step of a reaction which determines its overall rate.

INTRODUCTION

Heme peroxidases play important roles in plant and fungal biosynthetic processes, and of the many plant and fungal peroxidases that have been studied, *S. cerevisiae* CcP has received special attention. As we saw in chapter 1, one property that has made enzymes like CcP attractive for detailed biophysical studies is that many heme peroxidases form distinct intermediates that are spectroscopically identifiable and relatively stable. This has enabled most of the intermediates in the generally accepted yeast CcP mechanism to be characterized.

Despite the similarities between CcP and LmP, there are important differences which we need to pay attention to in this chapter. First, steady-state assays have shown that with yeast CcP, activity first increases with increasing ionic strength, up to around 150 mM, but then remains constant, or even decreases at higher ionic strength.[14] LmP activity steadily decreases with increasing ionic strength (see figure 1.2). In addition, the steady-state kinetics of LmP are comparatively simple and most consistent with a single binding site for LmCytc, while with yeast CcP, it now is well established that there is a second site that is populated at low ionic strength.[14, 101] Furthermore, we have seen that the complex that forms between CcP and Cytc does not have specific ionic interactions at the interface,[23] while the LmP-LmCytc complex depends on specific electrostatic interactions,[22] including a key ionic interaction between LmP Asp211 and LmCytc Arg24, located at the binding interface. The role of this ion pair was initially probed by site-directed mutagenesis and steady-state Cytc oxidation assays, which revealed that replacing Arg24 with Ala increases K_M by 2-fold and decreases k_{cat} by 30-fold.[21] A decrease in affinity was expected, but such a large decrease in k_{cat} was not, since at saturating levels of LmCytc, k_{cat} might be expected to approach wild type levels. In this chapter, we probe

the intermolecular interactions in the LmP-LmCytc complex in more detail with additional mutations, steady-state kinetics, and stopped-flow spectroscopy. In addition, we establish an overall mechanism for the oxidation of LmCytc by LmP based on steady-state and single turnover kinetics, ionic strength dependence, and mutagenesis results.

EXPERIMENTAL PROCEDURES

Cloning and site-directed mutagenesis

The wild type LmP construct expressed without the N-terminal hydrophobic tail as Δ34LmP was supplied by Dr. Subrata Adak and was cloned into pET28a vector containing a Kan^R gene and a N-terminal 6X-Histidine tag as pET28a/Δ34LmP. The cytochrome c gene from L. major was expressed and purified as previously described.[20] LmP and LmCytc mutants were prepared by PCR using the TaKaRa PrimeSTAR polymerase kit, and each gene was fully sequenced to ensure the fidelity of the PCR reaction.

Protein Expression and Purification

Expression and purification of wild type and mutant LmP were carried out as follows: each plasmid was transformed in Escherichia coli BL21(DE3) cells and plated onto LB agar with kanamycin(50 μg/mL). A single colony was used to inoculate each 5 mL of 2xYT starter culture (50 μg/mL kanamycin). The culture was incubated for 8 hours at 37 °C and 220 rpm agitation. Each liter of TB medium (kanamycin 50 μg/mL) was inoculated with 2 mL of 2xYT starter culture. The cells were grown at 37 °C with 210 rpm agitation in a New Brunswick Scientific C25KC incubator until an OD600 of 0.8-1.0 was obtained. Cells were then induced with 0.5 mM isopropyl β-D-thiogalactoside and 0.4 mM δ-aminolevulinic acid, and a new dose of kanamycin

was added. Post-induction cells were then incubated for 24hrs at 25°C and 100 rpm, after which they were harvested by centrifugation and stored at −80°C. Cells were resuspended in Buffer A (50 mM potassium phosphate, pH 7.5, 1 mM PMSF, 150 mM KCl). Cells were lysed by passing through a microfluidizer at 18k psi (Microfluidics International Co). The soluble fraction was isolated by centrifugation at 17,000 rpm and 4°C for 1hr. The crude extract was then loaded onto a Ni^{2+}-nitrilotriacetate column previously equilibrated with 10 column volumes (CV) of buffer A. The column was washed with 10 CV of 10 mM L-Histidine in buffer A before elution with a 10 to 75 mM L-Histidine linear gradient in buffer A. Fractions were pooled according to an $R_z(A_{408}/A_{280}) > 1.3$ and concentrated in a 10,000 molecular weight cut-off Amicon concentrator at 4°C, and then loaded onto a Superdex 75 column (HiLoad 16/60, GE Healthcare) controlled by an FPLC system and pre-equilibrated with buffer B (50 mM potassium phosphate, pH 7.0 and 5% glycerol). Fractions were pooled according to the following criteria: an $R_z(A_{408}/A_{280}) > 1.5$ and spectroscopic observation of fully formed Compound I upon addition of stoichiometric amounts of hydrogen peroxide. Sample homogeneity was determined by SDS-PAGE. Expression and purification of wild type and mutant LmCytc were previously described.[20]

Steady-State Kinetics

All spectrophotometric steady-state activity measurements were performed at room temperature on a Cary 3E or Cary 300 UV/Visible spectrophotometer. LmCytc was reduced by adding excess sodium dithionite and incubated on ice for 30 mins. The dithionite was then removed by passing through an Econo-Pac 10DG desalting column (Bio-Rad) pre-equilibrated with 25 mM potassium phosphate, pH 6.5. All concentrations were determined using the appropriate molar extinction coefficients (ε_{558} of 29 mM^{-1} cm^{-1} for reduced LmCytc, ε_{408} of 113.6

mM^{-1} cm^{-1} for LmP, ε_{240} of 0.0436 mM^{-1} cm^{-1} for H$_2$O$_2$), and the rates of LmCytc oxidation were calculated using a $\Delta\varepsilon_{558}$ of 19.4 mM^{-1} cm^{-1}. All activity measurements were performed in 25 mM potassium phosphate pH 6.5 buffer and the ionic strength was increased by adding specific amounts of KCl. The reaction was initiated by the addition of H$_2$O$_2$ (0.18 mM) and the oxidation of ferrous LmCytc was monitored at 558 nm. All initial velocities were corrected for the enzyme-free reaction between ferrous LmCytc and H$_2$O$_2$, which accounted for about 15 % of the enzyme catalyzed rate. Data were fit according to the following hyperbolic equation:

$$\frac{V_{max} \times [LmCytc]}{K_M + [LmCytc]}$$

Stopped-Flow Kinetics

All stopped-flow kinetic measurements were performed using an SX.18MV stopped-flow spectrometer (Applied Photophysics) with a dead time of ~1.0 ms and using a protocol previously established on CcP.[8, 102] Single-wavelength absorptions were measured using a photomultiplier detector. Ferric LmCytc was reduced and prepared with the same method used in the steady-state activity assays. CmpI was formed by adding stoichiometric amounts of H$_2$O$_2$ and a spectrum was taken to ensure complete formation of CmpI. LmCytc and CmpI were loaded into separate 2.5 mL syringes and injected into the two separate drive syringes of the stopped-flow instrument. All measurements were carried out in the highest ionic strength buffer used in the steady-state activity assays: 25 mM potassium phosphate, pH 6.5 and 150 mM KCl. We used a final concentration of LmCytc of 0.3 µM and were able to observe at least 85 % of the reaction in every experiment. Just as in the yeast CcP system, a greater than 10-fold excess of LmP could not be used, and therefore pseudo-first-order kinetics could not be measured. We therefore calculated the second-order rate constant k$_1$ by fitting the kinetic traces measured at 420 nm

using the software provided with the stopped-flow instrument (Applied Photophysics) and the following standard single exponential equation:

$$A_{420} = C_1 \, e^{-k_{obs}t} + b$$

where C is the amplitude term, k_{obs} is the observed rate constant for the decay of oxidizing LmCytc and b is an off-set value.

Crystal Preparation

The LmP D211R protein sample used for crystallization was generated by thrombin digestion. A 50:1 weight ratio of LmP:thrombin was used, and incubated at 25 °C for 2 hours. The digested sample was then loaded onto a Ni^{2+}-nitrilotriacetate column previously equilibrated with buffer A, and eluted with 5 mM imidazole in buffer B. The protein sample was then concentrated to 6 mg/mL in buffer B using a 10,000 MWCO Amicon concentrator. Crystals were grown at room temperature in 10 % PEG MME 5,000 (w/v), 0.1 M MES:NaOH pH 6.5, 7.5 mM Praseodymium^{III} Acetate Hydrate, and 5 % DMSO in a hanging drop vapor diffusion setup. Two different crystal morphologies grew in under 24 hrs. The first were thin plates, about 100 μm in length while crystals with the second morphology others were hexagonal prisms, about 100-150 μm in length (Figure 2.1). Both freshly grown crystals were harvested after 24 hrs and passed stepwise through a cryo-protectant solution containing 30 % glycerol (v/v) for 4 hrs at 4°C, before being flash cooled with liquid nitrogen.
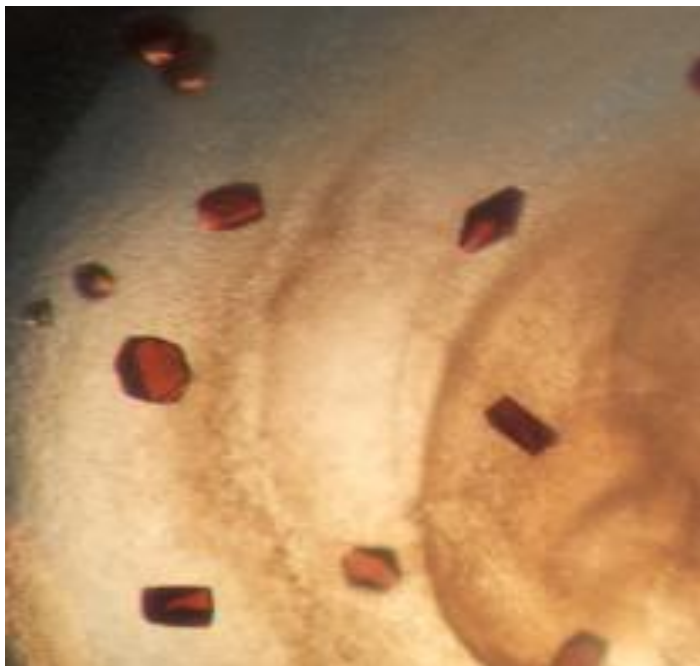
Figure 2.1 – LmP crystals
Hexagonal prisms of about 100-150 μm in length

X-ray Diffraction Data Collection, Processing, and Structure Refinement

Cryogenic (100 K) X-ray diffraction data were collected remotely at the Advanced Light Source (ALS) facility using the data collection control software Blu-Ice[103] and a crystal mounting robot. An ADSC Q315r CCD detector at beamlines 8.2.1 and 8.2.2 was used for data collection. Raw data frames were indexed and integrated using iMOSFLM,[104] and scaled using SCALA(AIMLESS).[105] The LmP(D211R) structure was solved by molecular replacement using Phaser[106] and the wild type LmP structure (PDB entry 3RIV). The initial difference Fourier maps were then calculated and the models were refined using PHENIX.[107] The refined structures were validated in COOT[108] before deposition in the RCSB Protein Data Bank. The crystallographic data collection and structure refinement statistics are summarized in Table 2.1 with PDB accession codes included.

PDB entry	5AL9	5ALA
radiation source	ALS BL 8.2.1	ALS BL 8.2.2
space group	C2	P212121
unit cell dimensions [a,b,c]	142.44, 57.86, 36.62	45.88, 79.18, 179.19
data resolution (highest-resolution shell) (Å)	36.51-1.37 (1.44-1.37)	47.71-2.73 (2.83-2.73)
X-ray wavelength (Å)	1.00	1.00
total no. of observations (highest-resolution shell)	154623	71264
no. of unique reflections (highest-resolution shell)	61602 (8933)	18116 (2365)
completeness (%) (highest-resolution shell)	98.3 (98.1)	99.9 (100)
R_{merge} (highest-resolution shell)	0.100 (0.898)	0.854 (1.286)
I/σ (highest-resolution shell)	5.7 (1.5)	18.5 (1.4)
$CC_{1/2}$ (highest-resolution shell)	0.988 (0.397)	0.752 (0.697)
redundancy (highest-resolution shell)	2.5 (2.0)	3.9 (4.1)
B factor, Wilson plot (Å^2)	12.32	67.63
R_{work}/R_{free}	0.1848/0.2037	0.2092/0.2823
no. of protein atoms	2183	4349
no. of heteroatoms	77	153
no. of waters	278	80
disordered residues	(A) 301-303	(A)301-303 (B) 301-303
root-mean-square deviation for bond lengths (Å)	0.024	0.016
root-mean-square-deviation for bond angles (°)	1.12	1.28

Table 2.1 – Crystallographic Data and Refinement Statistics

RESULTS

Mechanism of CmpI reduction in LmP

Although LmP exhibits similar Cytc oxidation rates and forms a very stable cationic Trp radical,[21] it has yet to be established whether the overall mechanism is analogous to CcP. It therefore makes sense to start our work by determining if the mechanism of CmpI reduction in LmP is the same. We have done this by using the same stopped-flow protocols established for CcP[8, 102] to determine if the cationic Trp radical in CmpI or Fe^{IV} is reduced first by LmCytc, as it is in CcP. To follow the reduction of Fe^{IV} in CmpI, it is first necessary to determine isosbestic points between reduced and oxidized LmCytc so as to ensure that any potential absorbance change is due to a reduction of Fe^{IV} in CmpI and not in the oxidation state of the LmCytc iron. The isosbestic point determination experiment was done by anaerobically titrating sodium dithionite into ferric cytochrome c and measuring a full diode array spectrum after each addition.

Figure 2.2A shows the spectrum obtained. We should also ensure that LmP has different isosbestic points, which we have done by similarly titrating H_2O_2 into ferric LmP and measuring full spectra each time. The LmCytc isosbestic at 436 nm was chosen as optimal to observe a potential LmP Fe^{IV} reduction. Using too much LmCytc in the experiment increases the risk of reducing CmpII. To avoid this, a 2-fold excess of LmP CmpI over ferrous LmCytc was used in order to isolate the first electron transfer step and prevent reduction of CmpII. Furthermore, the experiment had to be done at high ionic strength in order to observe the entire reaction within a stopped-flow instrument dead-time of ~1 ms. Figure 2.2B shows the reaction between 0.6 µM LmP CmpI and 0.3 µM ferrous LmCytc in 25 mM potassium phosphate buffer pH 6.5 containing 150 mM KCl. The 420 nm kinetic trace confirms that 93% of the LmCytc was oxidized during the reaction, yet the small absorbance change at 436 nm accounts for only 12%, suggesting that $Trp^{\cdot+}$ must have been reduced and not Fe^{IV}.
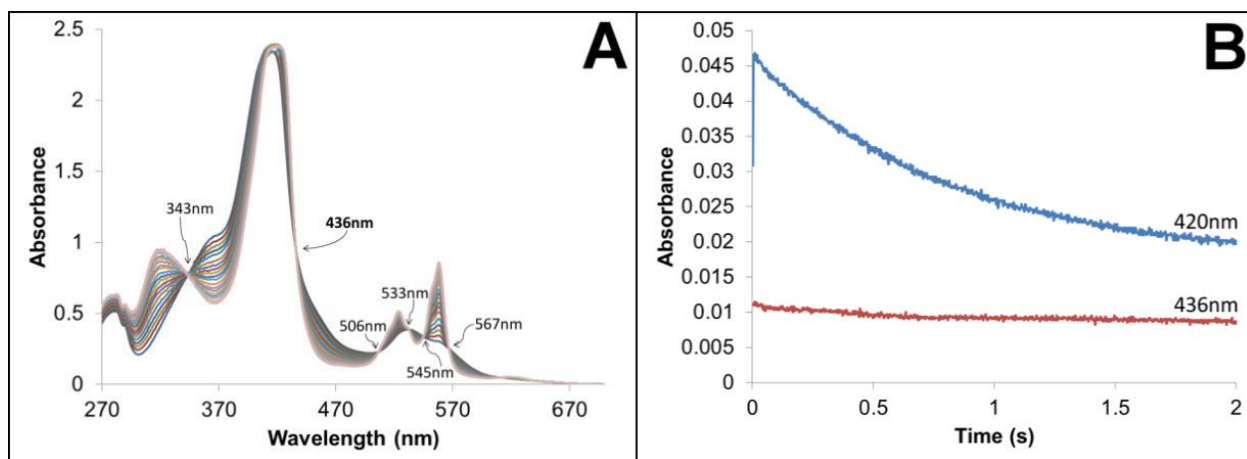
Figure 2.2 – (A) Anaerobic titration spectra of LmCytc by sodium dithionite. (B) Stopped-flow kinetic traces monitored at 420 and 436 nm. 0.6 µM LmP(CpdI) was mixed with 0.3 µM LmCytc in a buffer containing 25 mM potassium phosphate (pH 6.5) and 150 mM KCl at 25 °C.

Even though the stopped-flow experiment provides strong evidence that the Trp is reduced first, we performed an independent experiment to corroborate the results. This was done

by measuring the UV/Vis spectra of the following 3 reaction mixtures, which were incubated for 10 mins at 4°C using a 2-fold excess LmP over LmCytc, (Figure 2.3):

(A) CmpI + LmCytc^{II}

(B) CmpI + LmCytc^{III}

(C) LmP + LmCytc^{III}

The approach taken in this experiment takes advantage of the fact that LmP at resting state and CmpI exhibit distinct absorption spectra, while the oxidation state of the Trp has no effect on visible absorption spectra. A reduction of Fe^{IV} would therefore exhibit a distinct spectrum while reduction of Trp would result in no spectral change. What we observe is that while the recorded spectra of (A) and (C) do not superpose, (A) and (B) superpose well and exhibit very similar features, each of which are typical of an LmP CmpI spectrum, including a heme Soret peak at the 418 nm and characteristic α and β bands at 560 nm and 531 nm, respectively. These results provide additional spectral confirmation that the first electron transfer reduces the Trp$^{\cdot+}$ radical and not Fe^{IV}. We can therefore confidently conclude that the order of electron transfer for LmP is the same as in CcP.
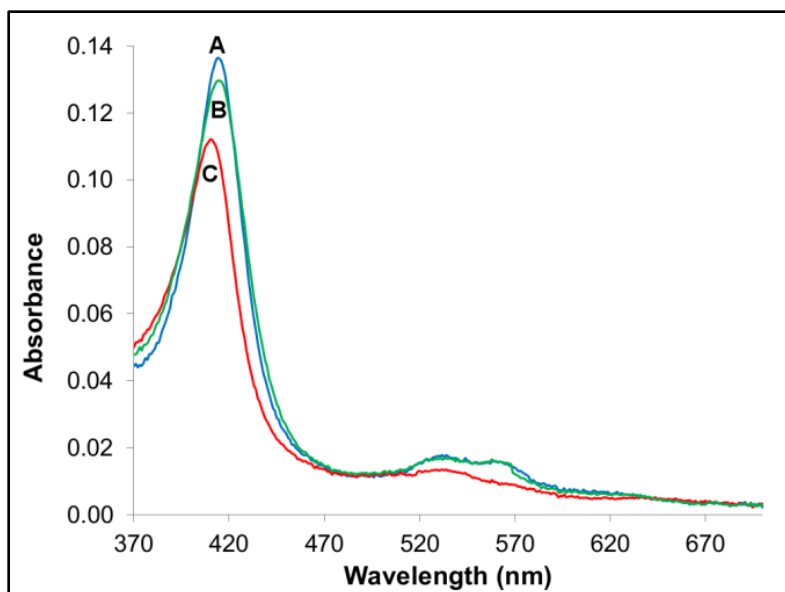
Figure 2.3 – Spectral superpositions
UV/Vis spectrum of reaction mixture containing: (A) CmpI + LmCytc^{II}, (B) CmpI + LmCytc^{III}, and (C) LmP + LmCytc^{III}

Mechanism of LmCytc oxidation by LmP

Figure 2.4 outlines a more detailed steady-state mechanism of CcP oxidation by Cytc. Previous work on CcP15 has shown that the off-rate (k_{-1} in Figure 2.4) should not be limiting at high ionic strength and that the rate-limiting step is generally agreed to be intramolecular ET reduction of Fe^{IV} by the active site Trp to give Fe^{III}-OH;Trp$^{.+}$ (k_4 in Figure 2.4). Is that also the case for LmP? To find out, we probed the kinetics of the wild type LmP system using a combination of single turnover and steady-state kinetics (Figure 2.5 and Table 2.2).
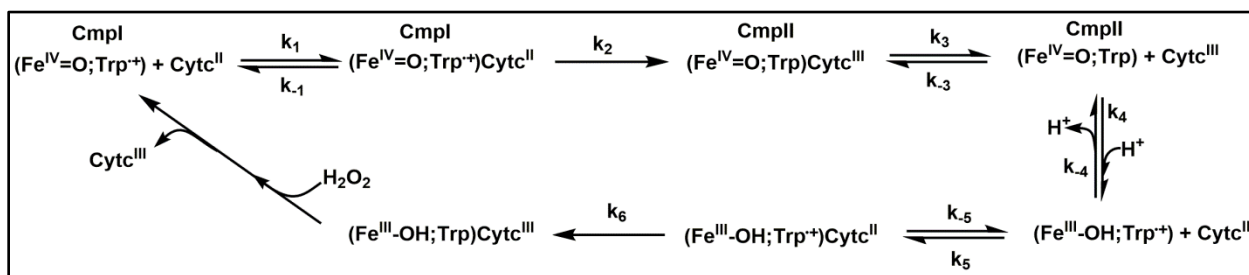
Figure 2.4 – Steady-state kinetic model of LmP catalysis adapted from Miller.[14]

All single turnover stopped-flow experiments were carried out by mixing LmCytc (Fe^{II}) kept at a constant concentration of 0.6 µM with changing concentrations of LmP CmpI, ranging in excess from 1.2 µM to 4.0 µM in a high ionic strength buffer containing 25 mM potassium phosphate, pH 6.5 and 150 mM KCl. CmpI reduction is a second-order reaction, with a bimolecular rate constant of 2.7×10^7 M^{-1} s^{-1}. To see whether complex formation is limiting for the wild type (WT-WT) complex, we can compare the single turnover results to the steady-state assays. The comparison is done by first generating a standard curve (k_{obs} as a function of increasing LmP CmpI concentration) and by calculating a pseudo-first-order rate constant at a given LmCytc concentration. For instance, at 10 μM LmCytc, we get a k_{calc} of 265 s^{-1}. We then compare this value to the measured V_o/e from steady-state assays at the same 10 μM LmCytc concentration, which is only 61.6 s^{-1}, revealing a 5-fold lower rate measured by the steady-state assays. The same 5-fold difference is observed at all other LmCytc concentrations, which suggests that the initial association event between LmP and LmCytc is not limiting, even at high ionic strength, and that we are therefore measuring the rate of a different event in our steady-state experiments.

Figure 2.5 – LmP-LmCytc Kinetics

(A) superposed plots of V_o/e vs LmCytc concentration for the wild type complex show the effect of increasing ionic strength. The ionic strength was ncreased by adding specific quantities of KCl to the reaction buffer. Blue diamonds, no KCl added; red squares, 25 mM KCl, greentriangles, 50 mM KCl; purple crosses, 75 mM KCl; blue crosses, 150 mM KCl. (B) Plot of first-order k_{obs} asa function of LmP CmpI concentration obtained from single turnover stopped-flow experiments for the wild type complex in buffer with 150 mM KCl. (C) Superposed plots of V_o/e vs LmCytc concentration for the charge-reversal mutants in buffer with 150 mM KCl. In each case, saturation was not achieved. For panels A and C, the data were fit to the Michaelis-Menten equation. (D) Superposed plots of first-order k_{obs} as a function of LmP CmpI concentration obtained from single turnover stopped-flow experiments for the charge-reversal mutants in buffer with 150 mM KCl. For panels C and D, red circles represent LmP(D211R)-LmCytc(WT); green triangles, LmP(WT)-LmCytc(R24D); and blue squares, LmP(D211R)-LmCytc(R24D).

[KCl] (mM)	LmP(WT)-LmCytc(WT)			LmP(D211R)-LmCytc(WT)		
	k_{cat} (s^{-1})	K_M (μM)	k_1 (M^{-1} · s^{-1})	k_{cat} (s^{-1})	K_M (μM)	k_1 (M^{-1} · s^{-1})
0	409 ± 9	4.1 ± 0.3		9.1 ± 0.3	6.8 ± 0.7	
25	418 ± 17	5.3 ± 0.6				
50	531 ± 35	13 ± 2.1				
75	610 ± 10	26 ± 0.8				
150	531 ± 74	83 ± 17	2.7×10^7	22 ± 2.7	131 ± 19	1.5×10^5
[KCl] (mM)	**LmP(WT)-LmCytc(R24D)**			**LmP(D211R)-LmCytc(R24D)**		
	k_{cat} (s^{-1})	K_M (μM)	k_1 (M^{-1} · s^{-1})	k_{cat} (s^{-1})	K_M (μM)	k_1 (M^{-1} · s^{-1})
0	15 ± 1.0	11 ± 1.9		11 ± 0.8	16 ± 2.7	
25						
50						
75						
150	40 ± 14	182 ± 74	2.2×10^5	19 ± 3.9	89 ± 87	2.1×10^5

Table 2.2 – Steady-State and Single Turnover Kinetic Parameters
Kinetic data were obtained in 25 mM potassium phosphate buffer pH 6.5 at 25 °C. The ionic strength was increased by adding specific quantities of potassium chloride. Steady-state parameters were calculated by fitting the Michaelis-Menten equation where saturation was possible.

Another interesting finding from steady-state kinetics (Table 2.2) is that K_M increases from 4.1 μM to 83 μM as ionic strength increases, but k_{cat} at saturation remains relatively unchanged, varying from 409 s^{-1} at low ionic strength to 531 s^{-1} in 150 mM KCl. This stands in stark contrast to CcP behavior as a function of ionic strength: with a measured k_{cat} in CcP that increases 400-fold from low to high ionic strength,[14] the moderate variation observed with LmP becomes insignificant, and most likely due to standard error (especially since saturation becomes more elusive at higher the ionic strengths).

Overall, the insensitivity of k_{cat} to increasing ionic strength in LmP suggests that the rate-limiting process is one that is independent of ionic strength, and therefore cannot be either complex association or dissociation (k_1 or k_{-3} and k_{-1} or k_3 in Figure 2.4, respectively). This leaves only two other options: intermolecular ET from LmCytc Fe^{II} to the LmP Trp208 radical (k_2) or intramolecular reduction of Fe^{IV}=O by Trp208 (k_4 in Figure 2.4). The rate-limiting process is unlikely to be intermolecular ET, as previous work on the CcP-Cytc system measured a very rapid ET event,[109] with a rate constant of 2×10^6 s^{-1}. The structures at the intermolecular

interface and contact distances are so similar in LmP that there is no reason to expect much difference in the intermolecular ET rate. The LmCytc heme contacts LmP at the same location as in CcP (Figure 2.6A and B). This means that the ET pathway and distance between the Cytc and Trp radical is the same in both LmP and CcP.
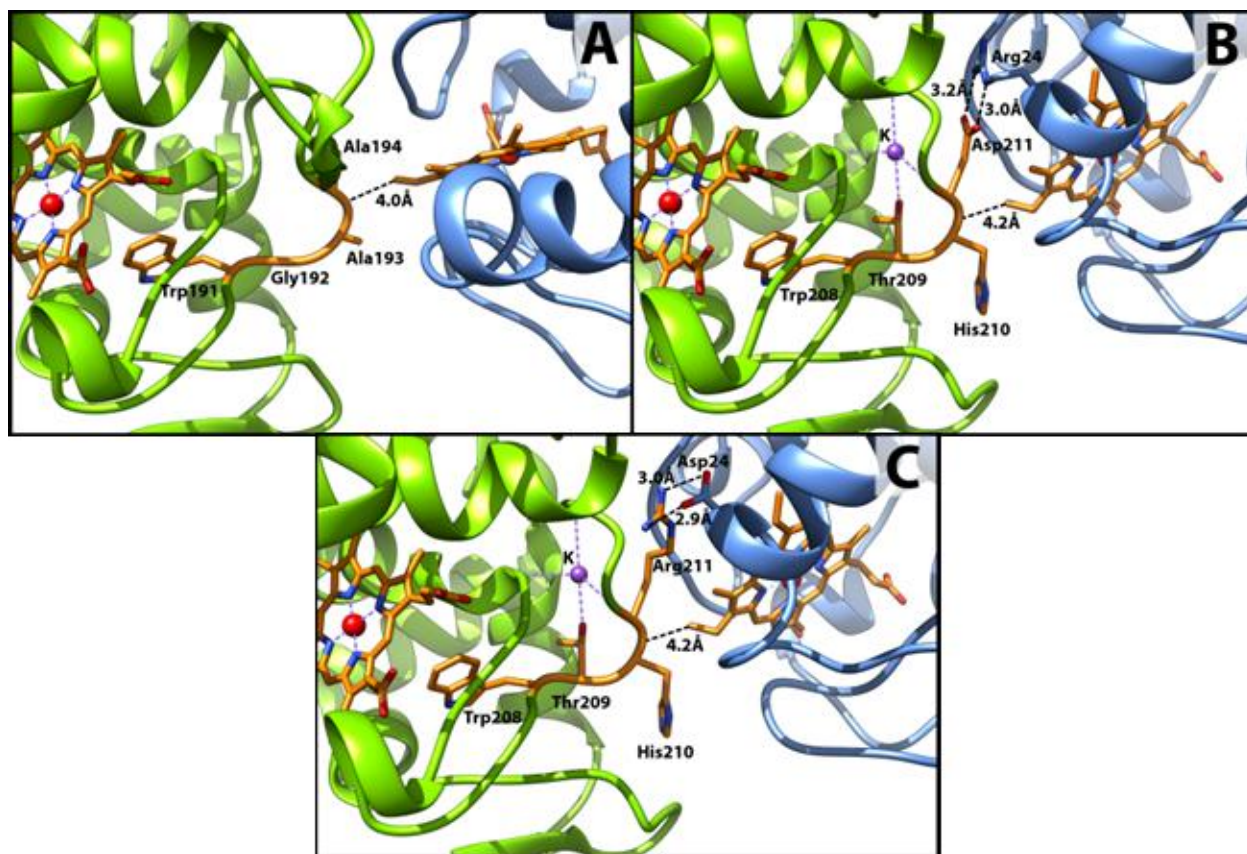
Figure 2.6 – Structural interfaces of complexes
(A) CcP-Cytc, (B) LmP-LmCytc, and (C) LmP-LmCytc with the possible orientation of the D211R and R24D side chians. Contact distances are nearly identical for both LmP and CcP, making the ET pathway and distances between the Cytc heme and Trp radical (Trp191 in CcP and Trp208 in LmP) the same.In the LmP complex, Arg24 and Asp211 form an excellent bifurcated H-bond with ideal geometry. While the charge-reversal mutant (C) may allow electrostatic interactions between the two groups, good hydrogen bonding geometry is not possible. All figures in this chapter were generated using UCSF Chimera.[25]

By process of elimination, we can therefore be confident that the rate-limiting step at steady-state in the LmP mechanism is the intramolecular reduction of Fe^{IV}=O by Trp208, which also means that the LmP system behaves similarly to wild type CcP at high ionic strength, where

the rate-limiting process is most likely intramolecular reduction of $Fe^{IV}=O$ by Trp (k_4 in Figure 2.4). At low ionic strength, however, the systems differ substantially, since for LmP, the rate-limiting step does not change, whereas for CcP, the rate-limiting step is generally agreed to be dissociation of the complex.[14, 109] To briefly summarize, the rate-limiting step in the yeast system changes from product dissociation at low ionic strength to intramolecular ET at high ionic strength while for LmP, the rate-limiting step remains intramolecular ET at all ionic strengths.

Disrupting the D211-R24 electrostatic interaction

In earlier work from our laboratory, it was shown that the LmCytc R24A mutant exhibited a large drop in k_{cat} and large increase in K_M. 21 The LmP D211R mutant exhibited similar changes in activity (Figure 2.7 and Table 2.2). These results show that either changing electrostatic complementarity at the center of the complex or disrupting a specific ion pair is responsible for the loss in activity. To determine the importance of electrostatic complementarity, we also generated the LmP D211R and LmCytc R24D charge-reversal mutants. Electrostatic complementarity is maintained at the center of this charge-reversal complex, but simple modeling (Figure 2.6C) shows that the mutant Asp24 in LmCytc would not be able to form optimal H-bonding interactions with the mutant side chain Arg211 in LmP. Furthermore, since the backbone carbonyl oxygen of the native Asp211 stabilizes binding of a K^+ ligand in wild type LmP, we wanted to ensure that the metal binding site was not affected by the presence of a positively charged Arg residue replacing the native Asp. We therefore determined the X-ray crystal structure of the LmP D211R mutant to a resolution of 1.37 Å (PDB entry 5AL9), and the electron density shows either partial occupancy of the native K^+ ion, or full

occupancy of a Na$^+$ ion (Figure 2.7A), confirming that metal binding was preserved and allows us to use kinetic data obtained with the mutant.
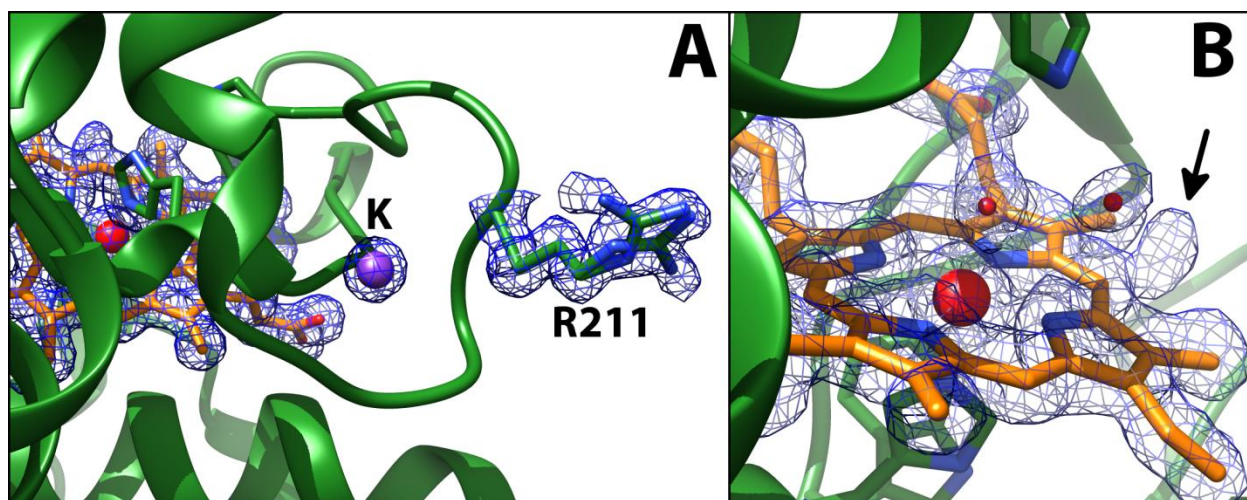
Figure 2.7 – (A) Crystal structure of LmP D211R mutant in the C2 space group with the 2F_o-F_c electron density map contoured at 1.0σ. The strong density supports binding of the metal ligand. (B) Active site heme of LmP D211R mutant with the 2F_o-F_c electron density map contoured at 1.0 σ. The strong lobe of electron density near the δ-meso carbon (indicated by the arrow) supports covalent binding of a diatomic molecule. For both panels, protein LmP is colored green and heme in orange.

Although the mutant structure is identical to the wild type structure, we did find one unexpected difference. The mutant crystallized in two different space groups: C2 with one molecule per asymmetric unit (the hexagonal prisms mentioned in the experimental section) and P2$_1$2$_1$2$_1$ with two molecules per asymmetric unit (the thin 2-dimensional plates). Diffraction data for the C2 form extend to 1.37Å but only to 2.73Å for P2$_1$2$_1$2$_1$. In two different crystals of the C2 form, we observed a very large lobe of positive difference density near the heme, consistent with a diatomic molecule covalently linked to δ-meso carbon (Figure 2.7B). This is not observed in the P2$_1$2$_1$2$_1$ form. At present, we have no suitable explanation for what is clearly a covalently modified heme. We speculate that synchrotron radiation could possibly have reduced the iron, thus enabling an oxy complex to form, followed by further reduction to peroxy, ultimately leading to a CmpI-like intermediate. This might generate sufficient oxidizing power to generate a

heme radical that then reacts with buffer components. We observed something similar in a mutant of CcP where the distal pocket active site Trp cross-linked with an engineered Tyr residue in an iron-dependent redox process,[110] clearly indicating that redox mediated oxidative chemistry can occur in crystals during x-ray exposure, even at cryogenic temperatures.

Kinetics of single and double charge-reversal mutant complexes were compared to the wild type complex (Table 2.2). In all cases, CmpI reduction was found to be second-order, with bimolecular rate constants k_1 of 1.5 x 10^5 M^{-1} s^{-1} for LmP(D211R)-LmCytc(WT), 2.2 x 10^5 M^{-1} s^{-1} for LmP(WT)-LmCytc(R24D), and 2.1 x 10^5 M^{-1} s^{-1} for the double charge-reversal mutant complex LmP(D211R)-LmCytc(R24D). The clear pattern emerges from the data, revealing that each rate constant measured by single turnover for the mutants is 2-orders of magnitude slower relative to the WT-WT complex. Such a large decrease in association rate constant warrants an examination of the turnover kinetics at saturation. Steady-state assays showed that all mutants were active in all combinations, but with large decreases in k_{cat} and increases in K_M (Table 2.2). This also means that for the double charge reversal complex (D211R-R24D), restoring simple charge complementarity is not sufficient to recover activity. It is more likely that specific H-bonding geometry is required.

Since it was not possible to capture the full rate of LmCytc oxidation by stopped-flow at low ionic strength, we focused our analysis on the high ionic strength results. For all mutants that disrupt the D211-R24 electrostatic interaction, we calculated pseudo-first-order k_{calc} at a given LmCytc concentration using our measured k_1 from stopped-flow experiments and compared these values to V_o/e measurements from steady-state kinetics (Table 2.3), just like we did with

wild type in the previous section. What we find is excellent agreement for all measurements. For instance, if we take the D211R-R24D mutant, k_{calc} = 2.08 s⁻¹ at 10 μM LmCytc is practically identical to the 2.14 s⁻¹ measured from steady-state kinetics. Taken together, these experiments suggest that the rate of association becomes limiting for these mutants, at least at high ionic strength, while, as noted in the previous section, the rate-limiting step for the WT-WT complex is intramolecular ET from Trp208 to Fe^{IV}=O (k_4 in Figure 2.4). Because the mutants do not saturate at high ionic strength (Figure 2.5C), estimates of K_M have large errors and thus are unfortunately not very accurate.

[LmCytc] (μM)	LmP(WT)-LmCytc(WT)		LmP(D211R)-LmCytc(WT)	
	k_{calc} (s⁻¹)	V_o/e (s⁻¹)	k_{calc} (s⁻¹)	V_o/e (s⁻¹)
5	133	31.1 ± 5.5	0.76	0.83 ± 0.13
10	265	61.6 ± 11	1.51	1.59 ± 0.04
20	530	107 ± 0.8	3.02	2.88 ± 0.16
25	663	120 ± 3.1	3.78	3.52 ± 0.18
30	795	143 ± 42	4.53	4.12 ± 0.05
[LmCytc] (μM)	LmP(WT)-LmCytc(R24D)		LmP(D211R)-LmCytc(R24D)	
	k_{calc} (s⁻¹)	V_o/e (s⁻¹)	k_{calc} (s⁻¹)	V_o/e (s⁻¹)
5	1.08	1.11 ± 0.10	1.04	0.97 ± 0.11
10	2.15	2.12 ± 0.14	2.08	2.14 ± 0.05
20	4.3	3.82 ± 0.06	4.16	3.28 ± 0.04
25	5.38	4.88 ± 0.00	5.2	4.38 ± 0.42
30	6.45	5.64 ± 0.05	6.24	4.38 ± 0.02

Table 2.3 – Comparison of Calculated Pseudo-First-Order k_{calc} Values Based on Single Turnover Data and Measured V_o/e Values from Steady-State Experiments

DISCUSSION

The results from this study show that the mechanism outlined in Figure 2.4 initially developed for CcP[14] explains the LmP data as well. The main difference is that in CcP, the rate-limiting step changes as a function of ionic strength. At low ionic strength, the CcP-Cytc complex is so strong, dissociation of the complex becomes limiting, and a second weaker site must be taken into account.[14] At higher ionic strength, CmpII reduction becomes limiting. With

LmP, k_{cat} is not very sensitive to ionic strength, strongly suggesting some process other than association or dissociation is limiting. This points to an intramolecular process, and since CmpI reduction in CcP is much faster than CmpII reduction, it is very likely that k_4 (Figure 2.4) is always limiting in LmP.

Although consistent with the available data and the extensive amount of work carried out on CcP, CmpII reduction is a complex process.[111] The active site Trp191 in CcP is essential for all electron transfer steps and it is known that there is an equilibration between Trp191 and the heme iron (k_4/k_{-4} in Figure 2.4),[112] suggesting that the electron reducing both CmpI and CmpII is transferred to $Trp^{\cdot+}$. Since ET from Cytc to $Trp^{\cdot+}$ is very fast in CmpI reduction, reduction of $Trp^{\cdot+}$ in CmpII should also be fast. It then must be the Trp-to-Fe^{IV}=O ET process (k_4 Figure 2.4) that is limiting. However, since the Trp is so close to the heme iron, one might ask why would an ET event be so slow? Reduction of Fe^{IV}=O to Fe^{III}-OH requires protonation of the ferryl O atom and thus is a proton-coupled ET reaction, which could considerably slow the reaction. Relevant to this discussion is that the k_4/k_{-4} equilibrium (Figure 2.4) between Fe^{IV}=O and Trp is pH dependent,[112] with Fe^{IV}=O;Trp favored at high pH and Fe^{III}-OH;$Trp^{\cdot+}$ favored at low pH, which is consistent with the requirement of ferryl O atom protonation coupled to ferryl reduction. Within the active site pocket of CcP and LmP, the distal His and Arg are obvious possible proton donors. A recent neutron diffraction study shows that the distal His52 in CcP CmpI is protonated at pH 6,[113] and thus could possibly serve as the source of the required proton in the k_4/k_{-4} (Figure 2.5) equilibrium. Also consistent with the distal His (His68 in LmP) being involved in ferryl reduction is that LmP activity is highest at pH 6.5 and decreases about two-fold at pH 8.0.[18]

This analysis and the potential role of His52 in reduction of the ferryl center is also relevant to the mechanism of CmpI formation. Owing to His52 being protonated in the neutron diffraction structure, an alternative mechanism for CmpI formation has been proposed,[113] which differs substantially from the traditional view[114] that His52 shuttles a proton from the iron-linked O atom of H_2O_2 to the distal peroxide O atom, thus promoting heterolytic cleavage of the O-O bond. However, crystals for neutron diffraction were grown at pH 6.0 which is near the pK_a of His, plus the inherently stronger N-D bond should favor protonation of His52. Moreover, density functional calculations[115] indicate that the ferryl O atom carries a partial negative charge, which is expected to favor protonation of His52 in CmpI. Thus, the neutron diffraction structure is fully consistent with the generally accepted mechanism of CmpI formation[114] and its later modification to include solvent in the proton transfer process.[116] More work has been done to expand on this discussion in Chapter 3.

Conclusions

The mutagenesis results show that LmP is far more sensitive to modification of the interface than CcP. With CcP, many mutants exhibit an increase in k_{cat} at low ionic strength because some mutants increase the rate of product dissociation.[14] The most dramatic effect in CcP is with charge- reversal mutants that create electrostatic clashes at the interface.[117] CcP relies more on nonpolar interactions, while LmP relies on the specific ion pairing between Asp211 in LmP and Arg24 in LmCytc. Despite such large differences, both enzymes carry out the peroxidation of Cytc at similar rates, and the structure of the complexes are remarkably similar. For detailed enzymatic studies, however, LmP offers some advantages owing to the relatively simple steady-state kinetics, the simple dependence on ionic strength, and the lack of

any evidence for a second LmCytc binding site. The main unknown in both systems is the intramolecular ET reaction from the active site Trp to $Fe^{IV}=O$ (k_4 in Figure 2.4) which, as we discussed earlier, is most probably rate-limiting in LmP. Unfortunately, this reaction has proven quite difficult to study in CcP. Because LmP kinetics are more straightforward, it may allow for a more detailed probing of CmpII reduction and of the Trp-to-Fe^{IV} ET reaction. We will pursue this further in Chapter 3.

CRYSTAL STRUCTURE OF THE PRISTINE PEROXIDASE FERRYL CENTER AND ITS RELEVANCE TO PROTON-COUPLED ELECTRON TRANSFER

Chapter 3

Summary

Using X-ray crystallography to capture reactive intermediates in metalloproteins, such as CmpI in peroxidases, has historically been riddled with difficulties. We propose a rather novel solution: X-ray free electron lasers (XFELs). We also challenge conclusions made from a recent work that proposes a different mechanism of CmpI formation based on a neutron diffraction structure (which also does not reduce Fe^{IV}). The problem at hand is that X-ray-generated hydrated electrons rapidly reduce Fe^{IV}, which undermines conclusions made based on traditional X-ray crystallography. Obtaining an intact or "pristine" crystal structure of CmpI therefore requires very short exposure times, many crystals, and even then, some reduction is unavoidable. The new generation of XFELs are capable of generating intense X-rays on the 10s of femtosecond time scale, which makes this technique ideal for structure determination with no metal reduction or X-ray damage. We thus report the 1.5 Å crystal structure of CcP CmpI using data obtained with the Stanford Linear Coherent Light Source (LCLS). This structure is consistent with previous structures obtained by using vastly more complicated data collection protocols. Of particular importance is the active site water structure that can mediate the proton

transfer reactions required for both CmpI formation and reduction of CmpII $Fe^{IV}=O$ to Fe^{III}-OH. The structures indicate that a water molecule is ideally positioned to shuttle protons between an iron-linked oxygen and the active site catalytic His52. We therefore have carried out both computational and kinetic studies to probe the reduction of $Fe^{IV}=O$. Kinetic solvent isotope experiments show that the transfer of a single proton is critical in the peroxidase rate-limiting step, which, as we have discussed in Chapter 2, is very likely the proton-coupled reduction of $Fe^{IV}=O$ to Fe^{III}-OH. We also find that the pK_a of the catalytic His substantially increases in CmpI, indicating that this active site His is the source of the proton required in the reduction of $Fe^{IV}=O$ to Fe^{IV}-OH.

New concepts?

- **XFEL:** Electrons are accelerated in a long (~2km) particle accelerator at nearly the speed of light. The electrons are then introduced into magnetic fields with a curved trajectory. The high energy and shimmering results in the emission of X-ray radiation in extremely short and intense flashes.

- **KSIE:** Even though isotopes have the same chemical reactivity, bonds to lighter isotopes vibrate faster, and therefore will break faster. If the rate-limiting step of a reaction involves the transfer of a proton from solvent, then measuring the activity in deuterated solvent should exhibit an isotope effect.

- **Proton inventory:** A solvent isotope effect experiment that can reveal the number of protons involved in the rate-limiting step. The relationship between velocity and deuterium content indicates the number of sites involved. A linear relationship indicates a single proton, a quadratic curve indicates two protons, a cubic curve indicates three protons, etc...

- **Neutron Diffraction:** Free neutrons are used instead of X-rays to determine the crystal structure of a protein. The main advantage is that since neutrons interact directly with atomic nuclei

(instead of the electrons), the protonation state of various ionizable groups can be directly determined.

INTRODUCTION

CcP CmpI (Figure 3.1A) has played a central role in understanding heme catalytic intermediates. Peroxidases, and especially CcP, have long played a central role in metalloenzymology owing to the relative ease of trapping and characterizing highly reactive intermediates. Of particular importance is CmpI, which we have discussed at length in previous chapters. The first structure of a peroxidase[2] suggested a mechanism of CmpI formation wherein the catalytic His52 shuttles a proton from the iron-linked peroxide O atom to the distal peroxide O atom, thus promoting heterolytic fission of the O-O bond.[114] This mechanism was later modified to include a water molecule (Figure 3.1A)[118] that mediates the transfer of protons between the peroxide and His52. This modification makes the mechanism more energetically feasible since His52 is too far ($\approx$3.6 Å) from the iron-linked peroxide for direct proton transfer. Crystal structures of CmpI support this water-modified mechanism. The required water bridges the $Fe^{IV}O$ oxygen atom and His52, and is perfectly positioned to serve a role in proton transfer.[119-120] However, a major problem with using crystallography to study high potential centers like $Fe^{IV}=O$ is that X-ray generated photo-electrons can readily reduce metal centers in metalloprotein crystals. For some time, mechanistic conclusions were based on the incorrect assumption that the metal redox state remains unchanged during X-ray data collection. The discrepancy between spectroscopic studies and crystal structures of the ferryl $Fe^{IV}O$ has been quite prominent, but a proper understanding of the structural features is critically important for not only peroxidases, but also for cytochrome P450 and nitric oxide synthase mechanisms.[121] A majority of spectroscopic methods are most consistent with a short $Fe^{IV}=O$ double bond, while a number of crystal structures are consistent with a $Fe^{IV}-O$ single bond, leading to the incorrect conclusion that ferryl O atom is protonated to give $Fe^{IV}-OH$.[122] More careful low radiation dose

composite data collection protocols, coupled with single crystal spectroscopy of CmpI [119-120] have partially resolved this problem and these more recent structures agree with the extensive spectroscopic data supporting $Fe^{IV}=O$. While peroxidase CmpI is relatively stable, it is impossible to completely prevent X-ray damage and it would be highly desirable to eliminate the X-ray induced reduction of metal centers altogether. Until very recently, the only feasible way of obtaining such a structure was with neutron diffraction and a 2.5 Å resolution neutron diffraction structure of CcP CmpI has recently been solved.[113] Neutron diffraction offers a major advantage as it allows visualization of hydrogen atoms, thus enabling enzymatically important H-bond donor/acceptor relationships to be precisely determined. However, the experimental constraints for neutron diffraction such as crystal size, hydrogen-deuterium exchange, and the limited facilities for neutron diffraction have greatly limited its application. A second approach is to obtain X-ray data using the new generation of X-ray free electron lasers (XFELs), which produce X-ray pulses on the 10s of fs timescale. The extremely short, bright pulses allow diffraction to take place before significant radiation damage occurs. This is particularly advantageous for the determination of catalytically relevant structures of metalloproteins, as diffraction is completed before atomic rearrangements occur around the metal center. Given the historical significance of CcP, we have solved the 1.5 Å crystal structure of yeast CcP CmpI obtained from XFEL data collected at the Stanford Linac Coherent Light Source (LCLS). While this structure together with the neutron diffraction and other CmpI structures are consistent with the mechanism shown in Figure 3.1A, Casadei et al.[113] propose a substantially different mechanism based on the observation that the distal His52 is protonated in CmpI and that the H-bond donor/acceptor relationship does not support a water-mediated proton transfer mechanism, but rather direct proton transfer from peroxide to His52 (Figure 3.1B). Relevant to the discrepancy between the

mechanisms in Figure 3.1A and 3.1B is the pK_a of His52. This is important, since, as we discussed in Chapter 2, the proton-coupled electron transfer (PCET) reduction of CmpII (Figure 3.1C) is rate-limiting in peroxidase catalysis[123] and a protonated His52 could directly participate in proton transfer to the ferryl O atom during reduction of $Fe^{IV}=O$. Therefore, we have also done computational and kinetic solvent isotope experiments that examine the pKa of His52 and address the importance of proton transfer in CmpII reduction. For the experimental work, we have used LmP rather than CcP due to the advantages of LmP, with simplified kinetics, a k_{cat} that is independent of ionic strength, and unlike CcP, a single binding site for Cytc. As a result, the interpretation of kinetic results is more straightforward with LmP.

A. Traditional Mechanism
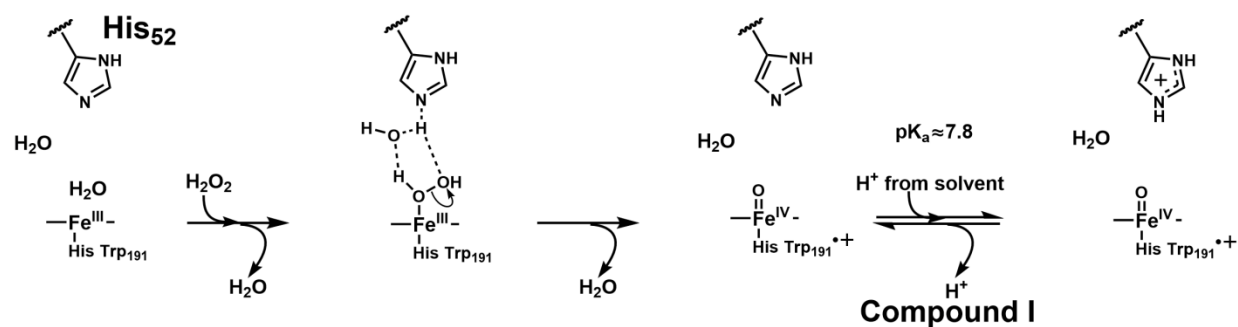
B. Modified Mechanism Based on Neutron Diffraction
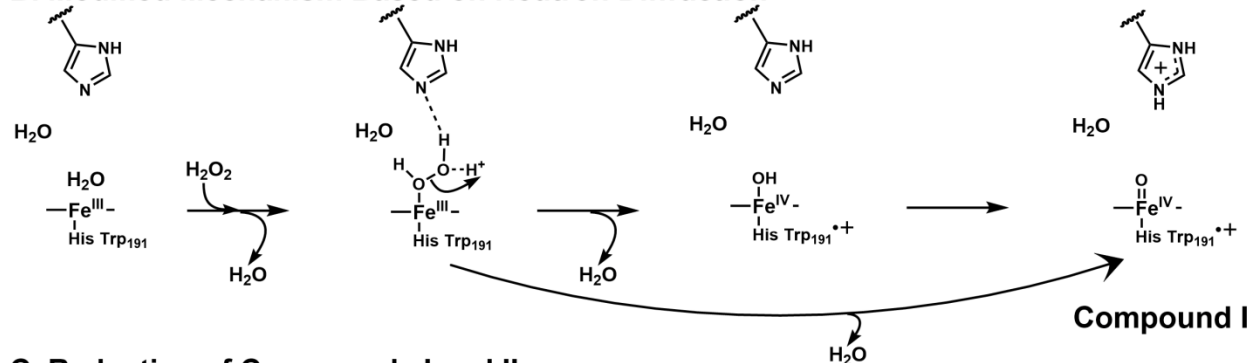
C. Reduction of Compounds I and II
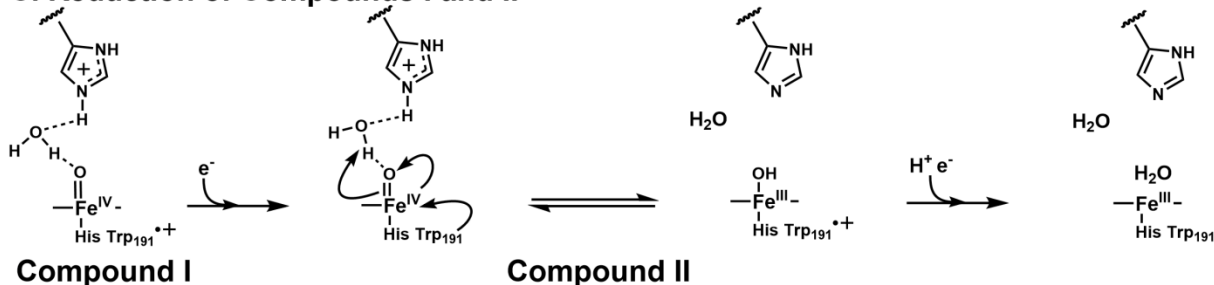
Figure 3.1 – Peroxidase Mechanism

(A) Traditional "water-modified" mechanism of CmpI formation. In this mechanism, peroxide first coordinates the heme iron, followed by proton transfer to the distal peroxide O atom via an ordered water molecule and the distal His52. The protonation state of the distal His depends on the His pKa. Our computational experiments indicate that the pKa substantially increases in CmpI.

(B) Modified mechanism based on the observation that His52 in CcP CmpI is protonated in the neutron diffraction structure (Casadei et al.[113]). Formation of CmpI proceeds via two possible routes, one of which involves the Fe^{IV}-OH intermediate.

(C) Mechanism of CmpII reduction, which includes a proton-coupled electron transfer event resulting in a net transfer of a proton from the distal His to the ferryl O atom.

EXPERIMENTAL PROCEDURES

Protein Expression, Purification, and Crystallization.

The N184R mutant of CmpI was produced and crystallized as previously reported.[124] Briefly, 10 µL sitting drops containing 400 µM protein, 22% (4S)-2-Methyl-2,4-Pentanediol

(MPD), and 50 mM Tris-phosphate, pH 6.0, were seeded and incubated at 4 °C for a few days. Freshly grown crystals were soaked in 10 mM H_2O_2, 35% MPD and 50 mM Tris-phosphate, pH 6.0. Crystals ranging between 150 μm and 1 mm in length were harvested onto Hampton-style cryoloops, flash frozen, and stored in an SSRL cassette. LmP and LmCytc used in KSIE experiments were expressed and purified as described in Chapter 2 and the published work.[123]

Data Collection

Data were collected at the X-ray Pump Probe (XPP) end station at LCLS in December 2013 and in June 2014 under a stream of liquid nitrogen. Crystals were mounted on a goniometer using the Stanford Automated Mounting system[125] and diffraction patterns were collected on a Rayonix MX325 detector as described previously.[126] The helical data collection mode was used in which each crystal was translated and rotated after each exposure[126] so that multiple radiation damage free diffraction images were obtained from each crystal. During the December 2013 beam time, a total of 96 still images were collected from 9 crystals. Crystals were exposed to a 3 μm x 3 μm X-ray beam at photon energy of 9.49 keV with a pulse length of 25 fs. Crystals were translated by 50 μm and rotated by 0.5° between exposures. During the June 2014 experiment, 275 stills were collected from 25 crystals using a 15 μm x 15 μm beam at photon energy of 9.43 keV and a pulse length of 40fs. Crystals were translated by 60 μm and rotated by 0.5° between exposures.

Experiment	December 2013	June 2014
Radiation Source	LCLS XPP hutch	LCLS XPP hutch
Crystals exposed	9	25
Images collected	96	275
Images indexed	46	217
X-ray Wavelength (Å)	1.30591	1.31319
Photon energy (keV)	9.436	9.494
Pulse energy	14.465	14.415
Crystal to detector distance (mm)	143.6	143.1
Pulse length (fs)	25	40
Electron beam energy	14.465	14.415

Table 3.1 – Data collection statistics

Crystallographic Data Processing

Data were indexed and integrated separately for each experiment using nXDS[127] with profile fitting turned off, and the minimum Ewald offset correction set to 0.1. Reflections from both experiments were scaled together with XSCALE, and intensities were converted to structure factor amplitudes using XDSCONV. 253 images out of a total of 371 collected images were used in the final dataset. Molecular replacement was performed using MOLREP[128] with data between 18 Å and 1.5 Å. A low radiation dose structure of cytochrome c peroxidase Compound I obtained at SSRL beamline 9-2 (pdb ID code 3M23),[120] from which the heme was removed, was used as a starting structure for molecular replacement. The MR structure was refined for 10 cycles at 1.5 Å using the program REFMAC[129] after which the heme was modeled in. Several more rounds of refinement were performed with all restraints on the iron removed, including the Fe-N and Fe-O restraints. Processing and refinement statistics are shown in Tables 3.1 and 3.2.

PDB code	5EJX	5EJT
Total images collected	371	360
Images indexed	253	360
Reflections used	600891	722513
Unique Reflections	65592	60803
Completeness	97.80%	100
I/σ	3.33	14.5
CC$_{1/2}$	61.70%	30
R$_{work}$/R$_{free}$	23.4/26.1	15.3/17.7 or 14.4/17.3
Space Group	19	19
a, b, c (Å)	107.47, 74.99, 51.25	107.32, 75.19, 51.15
α, β, γ (°)	90, 90, 90	90, 90, 90
Resolution Range (Å)	18 - 1.5	39-1.55

Table 3.2 – Crystallographic refinement statistics

Annealed Crystal Structure

We have shown previously that the CmpI spectrum in the crystal (Figure 3.3A) is identical to the solution spectrum and that significant reduction does not occur until a dose of ≈0.1MGy[120] as calculated by RADDOSE.[130] However, at a 7-8 MGy dose, the spectrum dramatically changes ("high dose" spectrum in Figure 3.3A) and the Fe-O distance increases to 1.9 Å (Figure 3.3B). To further probe the nature of the X-ray reduced species, data were collected at 2 different positions on a 0.2 x 0.2 x 0.15 mm^3 CmpI crystal at 13000 eV on BL12-2, resulting in an absorbed dose of 7.8 MGy, which ensures complete reduction. The visible spectrum of the crystal was measured at BL9-1 and showed significant photoreduction. The crystal was then annealed by blocking the cryostream for 10 seconds. Gas bubbles were observed leaving the crystal during the warming of the crystal. The visible spectrum of the crystal was measured again, and surprisingly demonstrated some ferryl features. The crystal was exposed for an additional 1000 seconds at 13000 eV with a 200 μm X-ray beam on beamline BL9-1. The absorbed dose for the exposure was calculated to be 0.8 MGy, resulting in a cumulative absorbed dose of 8.6 MGy for the crystal. The crystal was annealed again, and the measured visible

spectrum retained ferryl features. Finally, a 360 degrees dataset with 10 seconds per degree was collected to a resolution of 1.55 Å. A calculated additional 2.87 MGy was absorbed by the crystal, resulting in a cumulative dose of 11.5 MGy. The dataset was processed by the SSRL's 'autoxds' script using XDS,[131] POINTLESS and AIMLESS,[132] using the AIMLESS $CC_{1/2}>30\%$ criteria for a resolution cutoff. The previous Compound I structure (3M23) was also used to initiate refinement using BUSTER.[133] Data collection and refinement statistics are listed in Tables 3.1 and 3.2.

Computational Methods

Two procedures were used for estimating the *pKₐ* of the catalytic distal His in both ferric resting state CcP (2CYP) and CcP Compound I (3M23). In both cases, protein charges were assigned using the Amber ff99SB forcefield. Heme parameters, including the oxyferryl oxygen atom, were taken from density functional calculations by Harris and Loew.[134] The first method utilized the H++ webserver (http://biophysics.cs.vt.edu/index.php), which is a simplified user-friendly adaption of MEAD.[135] This approach uses a continuum dielectric model to calculate the electrostatic difference in work required to change the protonation state of a titratable group in solvent compared to the lower dielectric milieu within the protein.

The second approach is based on the methods initially developed by Warshel et al.[136] and later adapted for Amber by Mongan et al.[137] Here, the free energy required to deprotonate a titratable group in the protein ($\Delta G_{protein}$) is compared to the same calculation free in solution (ΔG_{water}) and the $\Delta\Delta G = (\Delta G_{protein} - \Delta G_{water})$ is used to calculate the *pKₐ* of the protein-bound group. The constant pH protocols using a Generalized Born implicit solvent model as

implemented in Amber 12 were used. Provided with Amber 12 are the free energy calculations for all standard titratable amino acids free in solution, which leaves only the $\Delta G_{protein}$ to be calculated. This is achieved by a Monte Carlo sampling of the Boltzman distribution of the two possible protonation states during a molecular dynamics run. In our case, a Monte Carlo step was performed every 100 fs over a 2 ns MD run and the pH was set to 7.0. Since explicit solvent was not used, we found, consistent with previous results,[138] that the protein can adopt unrealistic conformations. Therefore, a 1.0 kcal/mol restraint was placed on backbone atoms. The output provides the fraction of time the titratable group spends in any one of the two protonation states, which is directly related to $\Delta G_{protein}$ from which $\Delta\Delta G$ can be calculated. The pK_a in the protein is readily calculated from $pKa_{protein} = pKa_{water} + \Delta\Delta G(1/2.03kT)$.

Kinetic Solvent Isotope Effects

All kinetic experiments were performed at room temperature on a Cary 300 UV/Vis spectrophotometer. For these experiments, LmCytc was reduced by adding a small excess of fresh sodium ascorbate and incubating on ice for 1 hour. All LmCytc solutions used were ensured to contain no more than 2% LmCytc^{III}. Deuterated buffers for KSIE experiments were prepared in 99.9% D_2O (EMD Millipore), and pD was adjusted according to the following relationship: $pD = pH_{obs} + 0.38$. LmP and LmCytc stock solutions were highly concentrated using 10,000 MWCO Amicon concentrators (Millipore) to ensure minimal protium contribution to deuterated buffers, and were equilibrated in D_2O buffer before each activity measurement. All concentrations were determined using the appropriate molar extinction coefficients (ε_{558} of 29 mM$^{-1} \cdot$ cm^{-1} for reduced LmCytc, ε_{408} of 113.6 mM$^{-1} \cdot$ cm^{-1} for LmP, and ε_{240} of 0.0436 mM^{-1} cm^{-1} for H_2O_2), and LmCytc oxidation rates were calculated using a $\Delta\varepsilon_{558}$ of 19.4 mM$^{-1} \cdot$ cm^{-1}.

The reaction was initiated by the addition of H_2O_2 (0.15 mM), and $LmCytc^{II}$ oxidation was monitored at 558 nm. K_M and k_{cat} measurements were done in 25 mM potassium phosphate (KH_2PO_4/K_2HPO_4), pH 6.8 and in the same deuterated buffer at pD 6.8. Data were fit according to the following hyperbolic term:

$$\frac{V_{max} \times [LmCytc]}{K_M + [LmCytc]}$$

pH/pD dependent assays were done in 5 mM KH_2PO_4/K_2HPO_4 buffer at pH/pD 6.0, 7.0 and 8.0, and a final reaction mixture containing 0.5 nM LmP and 30 μM LmCytc.

RESULTS

Crystal Structures

The X-ray damage-free XFEL structure of CcP CmpI is shown in Figure 3.2 and is identical to a previous low dose structure solved by our laboratory obtained by a composite data collection protocol that required several crystals, each exposed for no more than 10 seconds.[120] The solvent structure is especially important given that even partial reduction of CmpI alters the active site solvent architecture, possibly due to the change in charge on the heme iron and to the associated changes in the local electrostatic environment. The ordered solvent directly H-bonded to both the ferryl O atom and to His52 is important to consider when discussing mechanism. Consistent with the low dose structures, the Fe-O bond length is 1.7 Å, and thus is best described as $Fe^{IV}=O$, while the Arg48 and Trp51 are in hydrogen bond contact with the ferryl oxygen (Figure 3.2B). In earlier studies, we showed that the Trp191 radical is stable in the crystalline state,[139] and we assume that in our present structure the Trp191 radical is fully formed. We find no changes in structure around Trp191, which is perhaps not unexpected since it has been

demonstrated that the local electrostatic environment has been carefully tuned to stabilize a Trp cationic radical.[121]
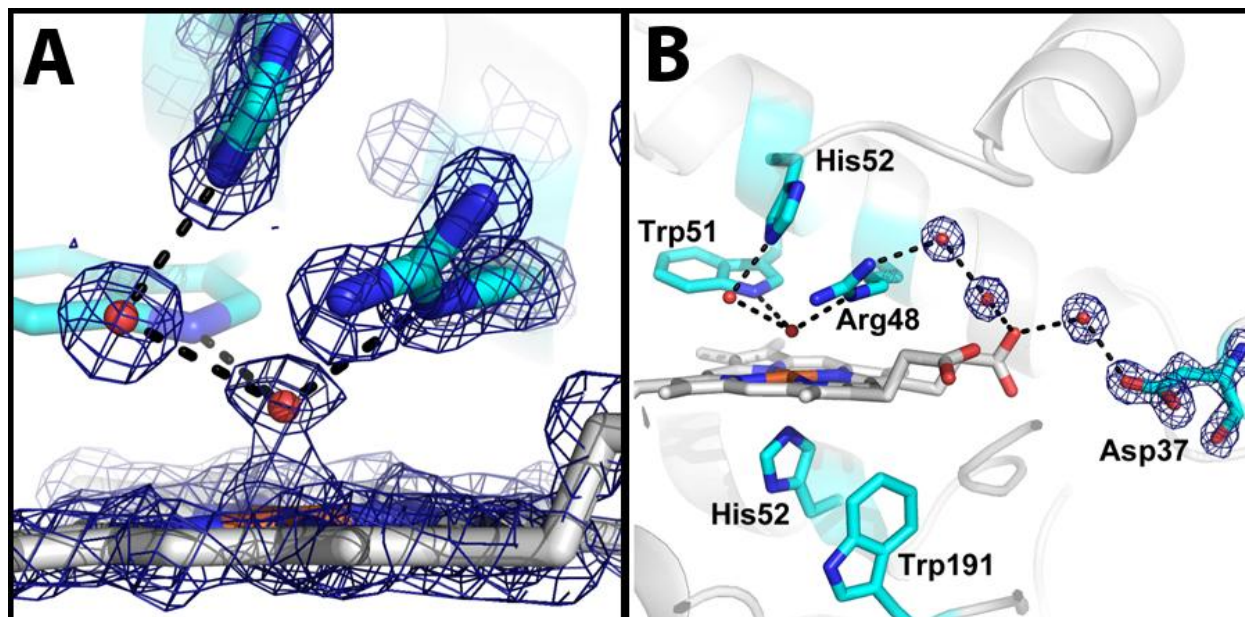
Figure 3.2 – XFEL CmpI structure
$2F_o$-F_c electron density map of the XFEL CmpI structure contoured at 2.0σ. The dashed lines indicate H-bonding interactions which are less than 3.0 Å. The Fe^{IV}-O bond length is 1.7 Å (A) Close-up view of the ferryl center (B) Extensive H-bonded network connecting the ferryl O atom to the surface of the enzyme.

In our previous work, we found that the Fe-O bond length increases linearly with X-ray dose as Fe^{IV}=O is reduced by the X-ray beam.[120] The final high dose X-ray structure had a Fe-O bond length of 1.9 Å, but the redox state of the iron was uncertain. Figure 3.3 shows the single crystal spectrum obtained from crystals before and after extensive X-ray exposure. The spectral features of the X-ray reduced crystal are similar to the solution spectrum of dithionite reduced CcP. Even so, a water/hydroxide only 1.9 Å from the iron would be very unusual for Fe^{II} heme, while Fe^{III}-OH would be more consistent with the known solution properties of heme proteins. Unfortunately, it is not possible to compare the solution and crystal spectra since CcP is unstable at the pH levels required to form Fe^{III}-OH. When the crystal is annealed by briefly warming and then cooling back to liquid nitrogen temperatures, followed by collection of a 1.55 Å data set, the

water density moves to a distance of 2.3 Å from the iron and the electron density becomes much weaker (Figure 3.3). The weaker electron density is indicative of low occupancy and/or higher thermal motion which would be consistent with 5-coordinate Fe^{II} or Fe^{III} or, possibly, a mixture of both. It is therefore very likely that the high dose structure (Figure 3.3C) represents a cryo-trapped Fe^{III}-OH or, possibly, Fe^{II}-OH$_2$. This also suggests that previous structures of CmpI or II with a long Fe-O bond are Fe^{III} or Fe^{II} and not Fe^{IV}.
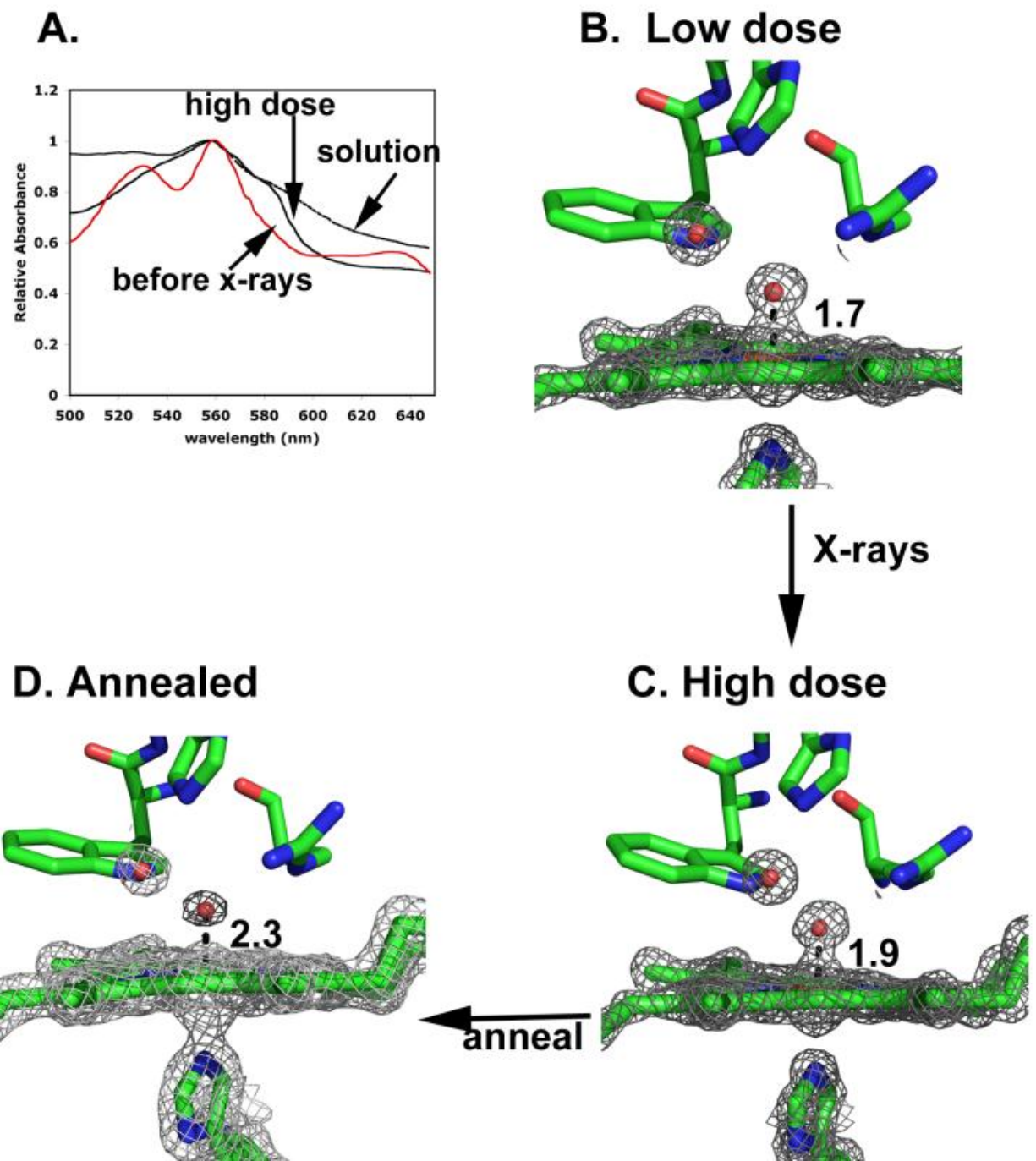
Figure 3.3 – Spectra and structure of CmpI as a function of X-ray dose
(A) Single crystal spectra of CmpI before and after extensive (7.8 MGy) X-ray exposure and the solution spectrum of CcP reduced anaerobically with dithionite. (B) $2F_o$-F_c maps of the low dose and (C) high dose CmpI structures taken from our previous work.[120] (D) 1.5Å structure of a high dose crystal after annealing. All maps were contoured at 2.0σ.

pKa of Catalytic Distal His

The neutron diffraction structure of CcP CmpI shows that the distal His52 is protonated in CmpI, but is unprotonated in the resting Fe^{III} state. Based on these observations, Casadei et al.[113] have proposed a mechanism for CmpI formation (Figure 3.1B) that differs substantially from the generally accepted mechanism (Figure 3.1A).[114, 118, 140] The main difference is that the mechanism in Figure 3.1B requires a proton from some external source and Fe^{IV}-OH as a transient intermediate in CmpI prior to movement of the proton from the ferryl hydroxide to His52, thus generating Fe^{IV}=O. There are at least three problems with this mechanism. First, the transient existence of Fe^{IV}-OH is unlikely given that EXAFS (extended X-ray absorption fine structure) and resonance Raman studies show that the pK_a of the ferryl O atom in ferryl systems with an axial His ligand is ≤ 4.[122, 141] Second, Casadei et al.[113] reject the water mediated mechanism of CmpI formation (Figure 3.1A) proposed by Vidossich et al.[118] based on a faulty assumption that H-bond donor/acceptor relationships observed in the neutron diffraction structure of CmpI proves their model. However, it is in fact the H-bonding pattern in the transition state and not CmpI that is relevant, so the conclusion that the H-bonding pattern of the ordered water in CmpI is not consistent with a water-mediated proton transfer mechanism is not sound. Third, the peroxide iron-linked O atom is about 3.6 Å from His52, which is far too long for direct H-bonding and proton transfer. As shown by the computational work of Vidossich et al.,[118] a water-mediated proton transfer mechanism as depicted in Figure 3.1A is energetically more feasible and is consistent with the CmpI X-ray crystal structures since the water molecule H-bonded to both His52 and the ferryl O atom is ideally positioned to mediate proton transfer.

Method	pK_a resting state	pK_a CmpI
H++/MEAD	5.4	7.4
Constant pH	5.1	7.8

Table 3.3 – Calculated pK$_a$ values of His52

One simple explanation for why His52 is observed to be protonated in the neutron diffraction structure is that the pKa of His52 increases in CmpI. This is reasonable since the crystals were grown at pH 6, so one might expect a significant fraction of His52 to be protonated if the pKa were 7 or higher. As outlined in the Experimental Procedures section, we used two computational procedures to estimate the pK_a of His52 in both the resting Fe^{III} state and in CmpI. Both methods give a substantial increase in the pK_a of His52 (Table 3.3) from $\approx$ 5.1 - 5.4 in the ferric resting state to $\approx$ 7.6 - 7.8 in CmpI, consistent with the neutron diffraction structure where the crystals were grown at pH 6.[113] These results are also consistent with resonance Raman studies[142-143] where a group, most likely the distal His, with a pK_a near 8.8[144] effects the $Fe^{IV}{=}O$ stretching frequency of horseradish peroxidase CmpII *via* changes in H-bonding strength to the ferryl O atom. The increase in pK_a can be readily rationalized by the structures and the charges on the heme atoms derived from density functional calculations. In the resting Fe^{III} state, there is little dielectric shielding between His52 and the heme iron. This, together with the nearby Arg48, surrounds His52 with an electropositive environment that depresses the His52 pK_a relative to a His free in solution. In CmpI, however, the partial negative charge on the ferryl O atom increases the basicity of His52, which is why a protonated His52 is observed in the neutron diffraction structure[113] and is not due to an unknown source of protons as depicted in Figure 3.1B.

Kinetic Solvent Isotope Effects

Despite the problematic mechanistic conclusions based on the neutron diffraction structure,[113] that His52 is observed to be protonated is a critically important finding relevant to the reduction of CmpII (Figure 3.1C). To recap this portion of the mechanism, in the first electron transfer step to CmpI, Cytc delivers an electron to the Trp radical to give CmpII. The reduction of CmpII involves internal electron transfer from Trp to $Fe^{IV}=O$ to give the Trp radical and Fe^{III}-OH. As shown in Figure 3.1C, protonation of the ferryl O atom during reduction of CmpII requires transfer of the His52 proton *via* ordered solvent. As we concluded in Chapter 2, this step is thought to be rate-limiting for CcP at high ionic strength,[14, 109] while for the closely related LmP, this step was found to be limiting at all ionic strengths.[123] If CmpII reduction is limiting and solvent plays an important role in proton transfer, as suggested by the CmpI structures, then one might predict a considerable kinetic solvent isotope effect (KSIE).

The KSIE studies were carried out with LmP and LmCytc rather than with CcP. We saw in Chapters 1 and 2 that LmP is also a CcP and forms the same stable Trp radical,[21] and the crystal structure of the LmP-LmCytc complex[22] is very similar to the CcP-Cytc complex.[23] We also saw that LmP differs from CcP, mainly by exhibiting simpler kinetics since k_{cat} for LmP is relatively insensitive to ionic strength,[123] while k_{cat} for CcP increases substantially with ionic strength.[14] This is generally thought to be the result of a change in rate-limiting step in CcP where product dissociation is limiting at low ionic strength while reduction of CmpII is limiting at high ionic strength. An additional complication with CcP is the presence of a second low affinity site for Cytc at low ionic strength.[14, 101] Given that the rate-limiting step for LmP appears not to change with ionic strength and that there is no indication of a second Cytc binding site, we

focused on LmP for detailed KSIE studies.
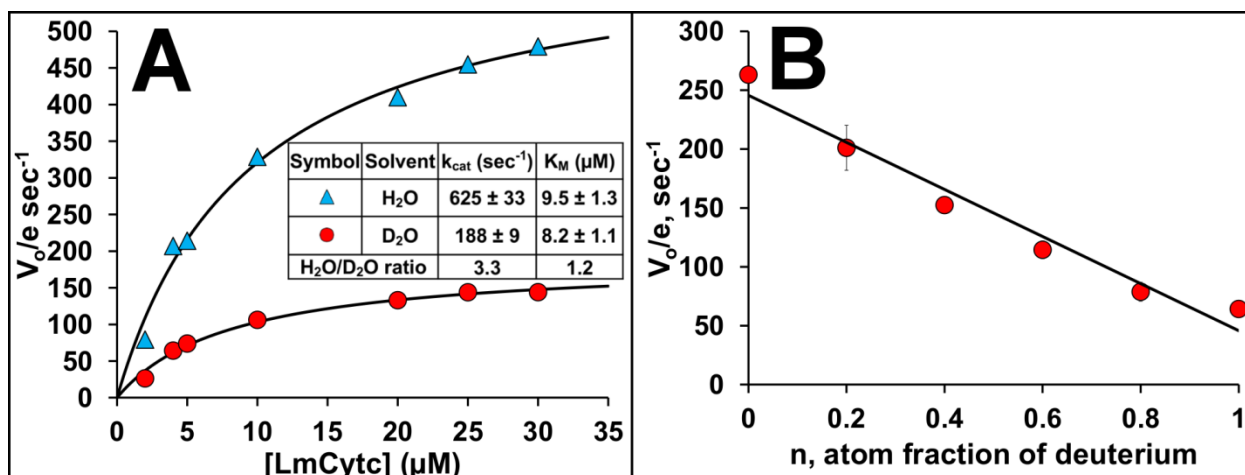
Figure 3.4 – Kinetic solvent isotope effects
(A) Comparison of the LmP reaction in H_2O and D_2O together with k_{cat} and K_M determinations using fits of these plots to the Michaelis-Menten equation. (B) Proton inventory plot of rate vs. fraction of D_2O.

As shown in Figure 3.4A, the KSIE is 3.3 with no effect on K_M, clearly indicating that proton transfer is critical in the rate-limiting step. We also determined the KSIE as a function of pH and found that the KSIE increases slightly as the pH increases, to a maximum of 4.4 at pH 7.0 (Table 3.4), with maximum activity peaking near pH 7.0 and then decreasing at pH 8.0. These observations are consistent with previous studies.[18] A plot of rate *vs* fraction of D_2O (proton inventory, Figure 3.4B) shows a linear relationship, indicating that a single proton is involved in the rate-limiting step.

pH/pD	D_2O	H_2O	H_2O/D_2O ratio
	V_o/e (s^{-1})		
6.0	58.9 ± 3	175 ± 7	3.0 ± 0.3
7.0	76.2 ± 6	338 ± 8	4.4 ± 0.4
8.0	66.2 ± 7	261 ± 10	3.9 ± 0.6

Table 3.4 – KSIE as a function of pH/pD
All measurements were made in 5 mM potassium phosphate buffer (KH_2PO_4/K_2HPO_4) titrated to the appropriate pH/pD according to the following relationship: $pD = pH_{obs} + 0.38$.

CONCLUSIONS

The present work, together with a wealth of data on peroxidase catalysis support the water-modified traditional peroxidase mechanism of CmpI formation highlighted in Figure 3.1B. This conclusion includes the recent data provided by the neutron diffraction structure determined by Casadei et al.[113] One factor that was previously omitted and that is critical to a correct interpretation of the mechanism is that His52 protonation observed in the CmpI neutron diffraction structure[113] is almost certainly due to an increase in the His52 pK_a. This increase in the His52 pK_a has important implications for CmpII reduction. Reduction of $Fe^{IV}=O$ to Fe^{IV}-OH requires both electron and proton transfer, which our KSIE studies suggest is rate-limiting. As depicted in Figure 3.1C, His52 is the ideal source of the required proton. Once the iron is reduced to Fe^{III}, the pK_a returns to the resting state value of $\approx$ 5.1 - 5.4. Our new CmpI structure is consistent with this mechanism and with previous crystallographic work based on complicated composite data protocols, which validates the earlier studies.[119-120] Our work also illustrates the utility of using the new generation of XFELs to carry out traditional crystal structure determinations with the obvious advantage of no X-ray damage or reduction of metal centers, thus providing an accessible and beneficial tool in structural biology for probing short-lived intermediates in enzyme catalysis.

"BIND AND CRAWL" ASSOCIATION MECHANISM OF LEISHMANIA MAJOR PEROXIDASE AND CYTOCHROME C REVEALED BY BROWNIAN AND MOLECULAR DYNAMICS SIMULATIONS

Chapter 4

Summary

In this chapter, we take a step away from the LmP active site and investigate the interaction between LmP and LmCytc. The association of LmP and LmCytc, which is known from kinetics measurements to be very fast ($\sim 10^8$ $M^{-1} \cdot s^{-1}$), does not involve major conformational changes, and as discussed in Chapter 3, is dominated by electrostatic interactions, especially the one between LmP Asp211 and LmCytc Arg24. In a collaboration between the Poulos and Tobias laboratories, Scott Hollingsworth and James Fields used Brownian dynamics simulations to investigate the mechanism of formation of the LmP-LmCytc complex. The simulations confirm the importance of electrostatic interactions involving the negatively charged Asp211 residue at the LmP active site, but also reveal the role of negatively charged residues in helix A of LmP in complex formation that was previously unrecognized. We solved the crystal structure of the D211N mutant of LmP, showing it is essentially identical to that of wild type LmP, and reinforcing the notion that it is the loss of hydrogen bonding at the interface, and not a change in structure, that reduces the association rate of the D211N (or D211R) variant of LmP. The Brownian dynamics simulations further show that complex

formation occurs via a "bind and crawl" mechanism, in which LmCytc first docks to a location on helix A that is far from the active site, forming an initial encounter complex, and then moves along helix A to the active site. An atomistic molecular dynamics simulation confirms the helix A binding site. Are the simulations accurate? We performed steady-state activity assays and stopped-flow kinetics measurements to confirm the role of helix A charges in the association mechanism.

The work described in this chapter was primarily designed by James Fields and Scott Hollingsworth in a Poulos-Tobias collaboration. I am a co-author on the mansucript that was published as a result of this collaboration, and my contribution included solving the crystal structure of the LmP D211N mutant, and performing the experimental stopped-flow and steady-state assays to validate the computational results. This chapter makes use of the text and images from our published work. For additional details on the computational work, please refer to the published manuscript.[145]

New Concepts?

- **Brownian Dynamics:** Computational simulation technique in which protein molecules are treated as rigid bodies in an implicit solvent. The technique is used to describe the motion and trajectories of a protein and its interactions as a single particle.

- **Molecular Dynamics:** Another computational simulation technique which describes protein interactions at the atomic level.

- **Probability Isosurface:** A 3-dimensional surface for the center of mass of an object that represents the probability of finding it in a specific location during the simulation.

INTRODUCTION

LmP and LmCytc form an inter-protein electron transfer (ET) complex to scavenge hydrogen peroxide in order to protect the parasitic *Leishmania* from the oxidative response of the infected host.[26] ET complexes require a precise combination of both specificity and efficiency. On one hand, such complexes must include a degree of specificity where the complex binding surfaces complement each other through hydrophobic and/or electrostatic interactions. On the other hand, the complexes must be dynamic, associating and disassociating quickly, for rapid ET and turnover to occur. If the redox partners form too tight a complex, rapid turnover cannot be achieved. ET between two proteins can be broken up into three simplified steps: (i) formation of the complex; (ii) electron transfer reaction; (iii) dissociation and separation of the complex. Here, we focus on the first step for the LmP-LmCytc system and, particularly, on the question of whether or not it actually comprises two steps, namely, the formation of an initial encounter complex, followed by local sampling of the binding interface that leads ultimately to the formation of a relatively tight ET complex.

We have confirmed in Chapter 2 that the LmP and CcP ET mechanisms are analogous and we have briefly discussed some of the structural differences between the two redox-partner complexes. Although CcP and LmP carry out the same redox chemistry,[18] we have seen strong evidence that the mechanisms of their associations with their cytochrome c redox partners are different. To recap, LmP obeys Michaelis-Menten kinetics,[18, 22, 123] while CcP does not.[146] Also, while K_M steadily increases with increasing ionic strength, k_{cat} is effectively independent of ionic strength in LmP.[123] This is quite different from CcP, where k_{cat} steadily increases with ionic strength until a maximum near 150 mM salt.[14] This behavior in CcP has been attributed to a

change in rate-limiting step at low ionic strength from product dissociation to intramolecular ET at high ionic strength. For LmP, the rate-limiting step remains intramolecular ET at all ionic strengths.[123] The larger increase in K_M with ionic strength in LmP is due to the greater dependence on intermolecular ion pairing, while CcP depends more on nonpolar interactions. The latter observations suggest that electrostatic interactions drive the formation of the LmP-LmCytc ET complex, whereas nonpolar interactions drive the formation of the CcP-Cytc complex. This hypothesis is supported by inspection of the crystal structures of the respective ET complexes. In the LmP complex, LmP D211 and LmCytc R24 form a salt bridge at the center of the binding interface and LmP E49 forms an ion pair with LmCytc K98 at the periphery of the interface.[22] In contrast, there are close contacts between nonpolar side chains (e.g., CcP A193 and Cytc V28) but no ion pairs at the CcP-Cytc interface.[23] Not only does the CcP-Cytc complex lack the inter-protein ion pairs found in the LmP-LmCytc complex, but calorimetric studies show that the ΔH of association is –2.1 kcal/mol, while –TΔS is –6.0 kcal/mol.[147] Although initial complex formation may well be driven by complimentary electrostatic surfaces, the predominance of the entropic term in the association free energy indicates that the stability of the CcP-Cytc complex is dominated primarily by nonpolar interactions.

In this study, my colleagues have used Brownian dynamics (BD) simulations to investigate the mechanism of LmP-LmCytc complex formation. The initial association reaction is often very difficult to dissect experimentally since the detailed rate constants are near diffusion controlled. BD simulations, in which protein molecules are treated as rigid bodies with atomically detailed interactions in an implicit solvent, have been employed extensively to model the formation of many ET protein complexes, thus providing molecular level details on the initial

association reaction that are often experimentally inaccessible.[148-167] In the case of the LmP-LmCytc system, comparison of the individual and co-crystal structures reveals no major conformational changes and only minimal reorientations of side chains at the interface upon complex formation. Thus, rigid-body BD simulations should be capable of accurately describing the association of LmP and LmCytc. We validated the BD simulations of the formation of the LmP-LmCytc complex by comparing computed second-order association rates with measured association rate constants determined from single turnover experiments. Finally, we carried out BD simulations of the formation of the CcP-Cytc complex to gain insights into the differences in the mechanisms of association of LmP and CcP with their respective cytochromes c.

EXPERIMENTAL PROCEDURES

Brownian Dynamics and Molecular Dynamics

All computational techniques were performed by my colleagues and experimental details can be found in the published work.[145]

Steady-state Activity Assays

Spectrophotometric steady-state activity assays monitoring the oxidation of reduced LmCytc were performed at 25 °C on a Cary 3E UV−visible spectrophotometer (Varian/Agilent). Reduction of LmCytc was performed by the addition of granules of sodium dithionite followed by an incubation period of 30 min on ice. Excess remaining sodium dithionite was then removed by passing the reduced sample through an Econopac 10DG desalting column (Bio-Rad) previously equilibrated with 50 mM potassium phosphate (pH 6.5). The eluate was then concentrated in a 10,000 molecular weight cutoff centricon at 4 °C. The concentration of reduced

LmCytc was determined using the previously determined molar extinction coefficient ($\Delta\varepsilon_{558}$) of 29 mM^{-1} · cm^{-1}.[18] The assay spanned 2 hours, during which time negligible amounts of LmCytc spontaneously oxidized. The LmP concentration was determined using the Soret molar extinction coefficient ($\Delta\varepsilon_{408}$ = 113.6 mM^{-1} · cm^{-1}).[21] The hydrogen peroxide concentration was also measured using the molar extinction coefficient ($\Delta\varepsilon_{240}$ = 0.0436 mM^{-1} · cm^{-1}).

In each experiment, the reaction buffer consisted of 25 mM potassium phosphate (pH 6.5) and the ionic strength was increased to 150 mM via the addition of KCl. For each experiment, the reaction was initiated by adding 0.18 mM hydrogen peroxide and the absorbance change was monitored at 558 nm for 1 min. The turnover number was calculated using the previously determined $\Delta\varepsilon_{558}$ of 19.4 mM^{-1} · cm^{-1}.[18]

The data were analyzed by fitting to the Michaelis−Menten equation:

$$\frac{V_{max} \times [\text{LmCytc}]}{K_M + [\text{LmCytc}]}$$

Stopped-Flow Kinetics

Stopped-flow kinetic measurements were performed as described in Chapter 2 and in previous work.[123] Compound I reduction was second-order, and the bimolecular rate constant k_1 was calculated by fitting the kinetic traces using the software provided with the stopped-flow instrument (Applied Photophysics) according to the following standard single-exponential equation:

$$A_{420} = Ce^{-k_{obs}t} + b$$

where C is the amplitude term, k_{obs} is the observed rate constant for the decay of oxidizing LmCytc, and b is an offset value. The association rate constant k_1 was determined as the slope of a fit of the (linear) concentration dependence of k_{obs}.

Crystal Preparation

The LmP D211N protein sample was prepared for crystallization as described in Chapter 2 and in the published work.[123] Crystals were grown at room temperature in 10% (w/v) PEG 5000 MME, 0.1 M MES-NaOH (pH 6.5), and 7.5 mM praseodymium[III] acetate hydrate in a hanging drop vapordiffusion setup. Freshly grown crystals were harvested after 24 hours and passed stepwise through a cryoprotectant solution containing 30% (v/v) glycerol for 4 hours at 4 °C. Crystals were then flash-cooled with liquid nitrogen.

X-ray Diffraction Data Collection, Processing, and Structure Refinement.

Cryogenic (100 K) X-ray diffraction data were collected remotely at the Advanced Light Source (ALS) facility, using the data collection control software BluIce,[103] and a crystal mounting robot. An ADSC Q315r detector at beamline 12.3.1 was used for data collection. Raw data frames were indexed, integrated, and scaled using XDS.[131] The LmP D211N structure was determined by molecular replacement using phaser[106] and the wild type LmP structure (PDB entry 3RIV).[21] The initial difference Fourier map was then calculated, and the model was refined using REFMAC.[129, 168] Water molecules were also modeled using REFMAC and checked in COOT.[108] The TLS (translation−liberation−screw rotation model)[169] protocol was implemented in the final stage of refinement with each chain as one TLS group, and the refined structure was validated in COOT. Coordinates and structure factors were deposited in the RCSB Protein Data Bank. Crystallographic data collection and structural refinement statistics are summarized in Table 4.1.

PDB entry	5AMM
Radiation source	ALS BL 12.3.1
Space group	$P2_12_12_1$
Unit cell dimensions a, b, c (Å)	46.25, 78.31, 160.98
Data resolution (Å) (highest-resolution shell)	50.0 - 2.09 (2.17 - 2.09)
X-ray wavelength (Å)	1.01
Total no. of observations (highest shell)	69311 (6417)
No. of unique reflections (highest-resolution shell)	34997 (3268)
Completeness (%) (highest-resolution shell)	99.15 (94.86)
Rmerge (highest-resolution shell)	0.02603 (0.5488)
I/sigma (highest-resolution shell)	18.69 (1.35)
$CC_{1/2}$ (highest-resolution shell)	0.999 (0.477)
Redudancy (highest-resolution shell)	2.0 (2.0)
B factor, Wilson plot ($Å^2$)	44.34
Number of protein atoms	4254
Number of heteroatoms	90
Number of waters	95
Disordered residues	(A) 301-303 (B) 301-303
R_{work}/R_{free}	0.1842/0.2445
Root-mean-squared deviation for bond lengths (Å)	0.016
Root-mean-squared deviation for bond angles (°)	1.7

Table 4.1 – Crystallographic Data and Refinement Statistics

RESULTS AND DISCUSSION

The importance of helix A in the Formation of the LmP−LmCytc Complex.

A probability isosurface for the center of mass of LmCytc around wild type LmP obtained from BD trajectories initiated from the cocrystal structures is shown in Figure 4.1A. The most prominent feature in the isosurface coincides with the position of the center of mass of LmCytc in the cocrystal structure (Figure 4.1B). Thus, the BD simulations of the cocrystal structures recapitulate the binding of LmCytc to the LmP active site, as established in the crystal structure of the complex. In the probability isosurface shown in Figure 4.1A, there is a second, relatively small feature corresponding to an interaction between LmCytc and helix A of LmP, which will be discussed in more detail below.
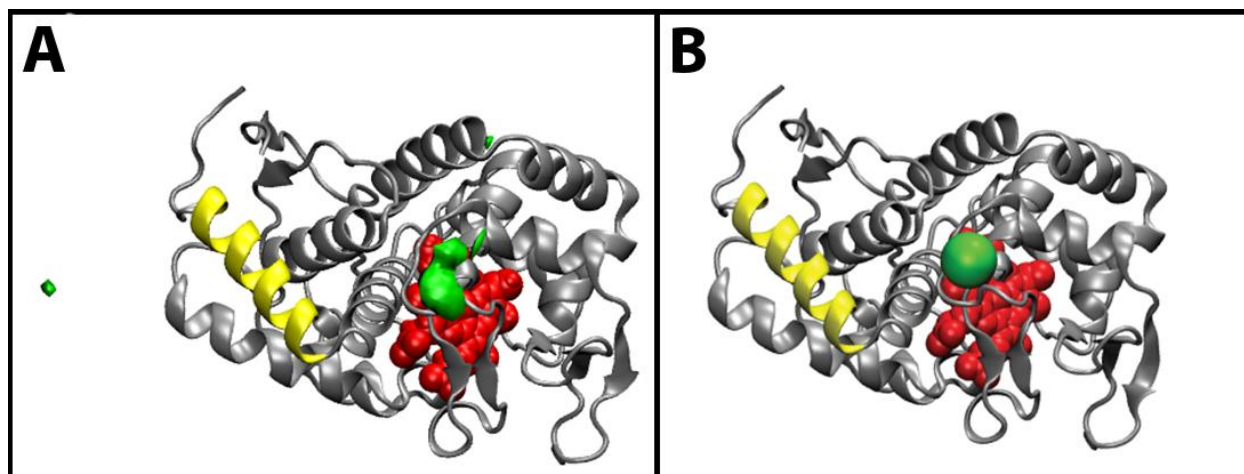
Figure 4.1 – BD simulations of LmP-LmCytc complex at 50 mM ionic strength
Helix A is drawn as a yellow ribbon, the heme is depicted as red van der Waals spheres and probability isosurfaces for the LmCytc center-of-mass calculated from BD simulations are drawn in green and contoured at a value of 2.2 × 10^{-3} . (A) BD simulation initiated from the co-crystal structures. Two features appear in the isosurface, the larger of which corresponds to LmCytc binding to the active site of LmP and a smaller feature indicating LmCytc interacting with Helix A. (B) Position of the center-of-mass of LmCytc in the co-crystal structure. Here, only one large feature appears at the active site. Unless indicated, molecular graphics images in this chapter were drawn using PyMol.[170]

The second-order association rate computed from the BD trajectories of the wild type cocrystal structures at an ionic strength of 50 mM (NaCl), $(4.3 \pm 0.1) \times 10^8$ M^{-1} s^{-1} (Table 4.2), is in good agreement with experimentally measured association rate constant k_1 of 4.5×10^8 M^{-1} s^{-1}, determined by a single turnover assay with 50 mM KCl in the reaction buffer (Table 4.3).[123] While the k_{cat} for LmP is independent of ionic strength, the K_M increases substantially, thereby resulting in a decrease in k_{cat}/K_M value as ionic strength increases.[123] Consistent with this observation, increasing the ionic strength from 50 to 150 mM in the BD simulations reduces the second-order association rate by 1 order of magnitude (Table 4.2), in good agreement with the experimental data (Table 4.3 and Figure 4.2).

LmP variant	ionic strength (mM)	BD rate (M–1 s–1)
wild type	50	$(4.3 \pm 0.1) \times 10^8$
	150	$(3.8 \pm 0.4) \times 10^7$
D211N (AS)	50	$(3.3 \pm 0.4) \times 10^7$
	150	$(5.1 \pm 1.5) \times 10^6$
D47N (HA)	50	$(2.1 \pm 0.1) \times 10^8$
	150	$(4.6 \pm 1.4) \times 10^6$
E49Q (HA)	50	$(1.3 \pm 0.1) \times 10^8$
	150	$(2.8 \pm 1.0) \times 10^6$
D50N (HA)	50	$(1.6 \pm 0.1) \times 10^8$
	150	$(2.8 \pm 1.0) \times 10^6$
E54Q (HA)	50	$(1.8 \pm 0.1) \times 10^8$
	150	$(4.1 \pm 1.3) \times 10^6$
D47A/D50A/E54A (HA)	150	$(6.9 \pm 1.8) \times 10^6$

Table 4.2 – Second-order association rates of LmP and LmCytc from BD simulations
AS denotes that the mutation is at the active site of LmP. HA denotes that the mutation is in helix A of LmP.

Enzyme	KCl added, mM	k_{cat}, s^{-1}	K_M, μM	k_1, M^{-1} s^{-1}
Wild Type	0	$409 \pm 9^{\dagger}$	$4.1 \pm 0.3^{\dagger}$	
	50	$531 \pm 35^{\dagger}$	$13 \pm 2.1^{\dagger}$	$4.5 \times 10^{8\dagger}$
	150	$531 \pm 74^{\dagger}$	$83 \pm 17^{\dagger}$	$2.7 \times 10^{7\dagger}$
D211N	0	$34.5 \pm 0.8^*$	$23 \pm 1.3^*$	
	150			$5.3 \times 10^{6*}$
D47A/D50A/E49A	0	$372 \pm 10^*$	$7 \pm 0.6^*$	
	150	$162 \pm 10^*$	$31 \pm 8.6^*$	$1.4 \times 10^{7*}$

Table 4.3 – Kinetic parameters obtained from steady-state assays of LmCytc oxidation by LmP
[†]Values previously reported and shown in Chapter 2
*Kinetic traces and fits are shown in Figure 4.2
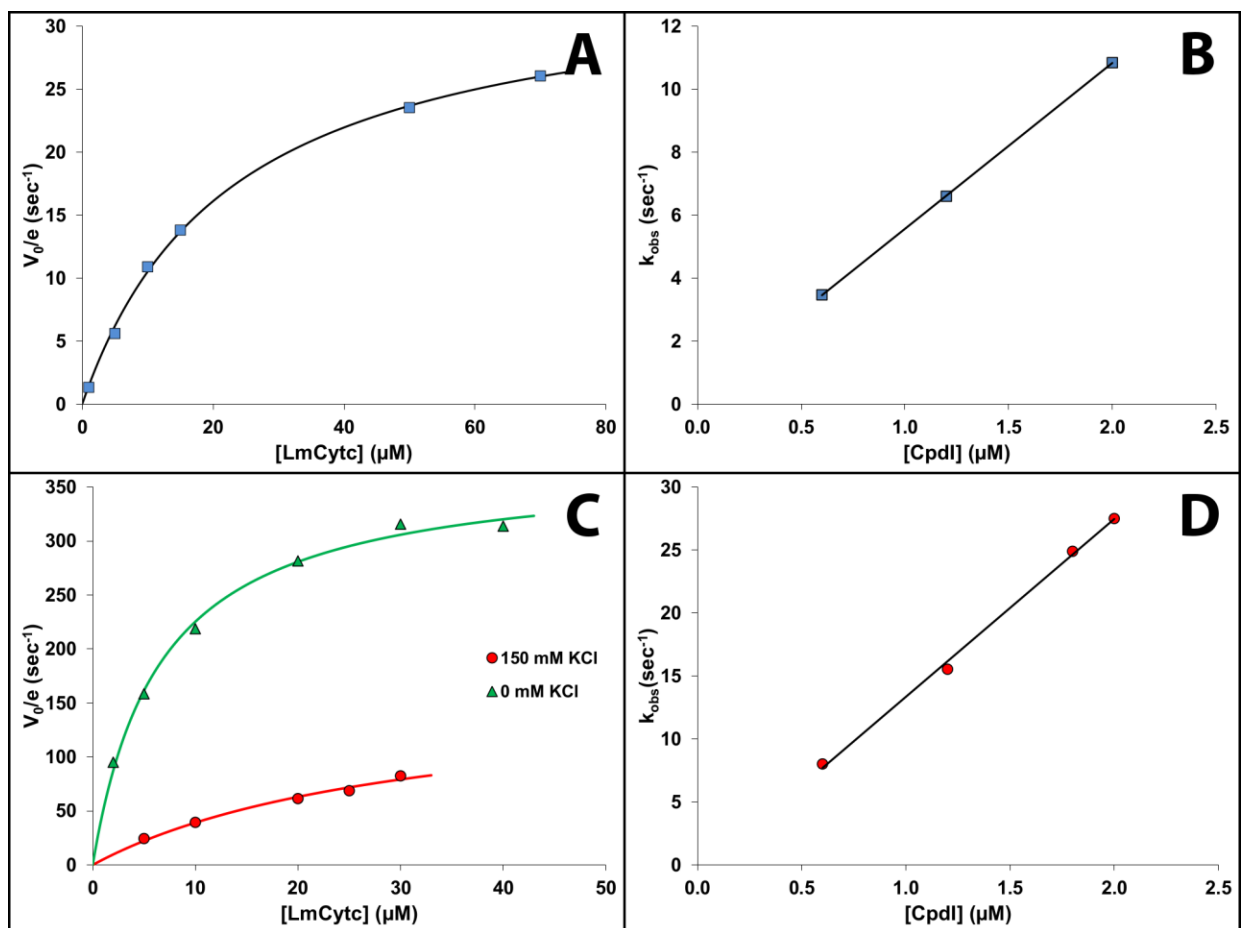
Figure 4.2 – Steady-state and single turnover results for the LmP mutants
(A) V_o/e vs LmCytc concentration for LmP D211N in 25 mM potassium phosphate buffer, pH 6.5. (B) Plot of first-order k_{obs} as a function of LmP CmpI concentration obtained from single turnover stopped-flow experiment for LmP D211N. (C) Superposed V_o/e vs LmCytc concentration for triple helix A mutant LmP D47A/D50A/E54A in 25 mM potassium phosphate buffer, pH 6.5. The measurements depicted by the green triangles had no KCl added, while the red circles were measured in a reaction buffer containing an additional 150 mM KCl. The data in panels (A) and (C) were fit to the Michaelis-Menten equation. (D) Plot of first-order k_{obs} as a function of CmpI concentration obtained from single turnover stopped-flow experiment for LmP D47A/D50A/E54A. The reaction buffers used for all stopped-flow experiments was supplemented with 150 mM KCl.

We next wanted to examine the role of electrostatic interactions, and thus considered several charge neutralizing mutations in LmP. When Asp211, which is located at the active site binding interface, is mutated to Asn *in silico*, binding with LmCytc Arg24 is disrupted. This is evident from the lack of a feature at the active site in the probability isosurface shown in the middle column of Figure 4.3A. The D211N mutation results in a substantial reduction in both the BD association rate (Table 4.2) and in the experimental k_1 (Table 4.3) at an ionic strength of 150

mM. Notice that the good agreement between the BD predicted and experimentally measured consequences of the D211N mutation provides further validation of the BD simulations as a tool to examine protein-protein interactions in this system .

Figure 4.3 – Probability isosurfaces comparing LmP mutants to wild type
(A) BD simulations initiated from the co-crystal structures; (B) BD simulations initiated from the individual structures
All probability isosurfaces were contoured at a value of 2.2 × 10^{-3} and depicted in green.

Computational results showed that the most significant interaction between LmCytc and D211N LmP occurs in the vicinity of helix A of LmP (Figure 4.3A, middle column). Helix A contains several negatively charged residues (Asp47, Glu49, Asp50 and Glu54) that protrude away from the active site interface (Figure 4.4). We eliminated these negatively charged side chains on helix A in the D50N, D47N, E49Q, E54Q, and D47N/D50N/E54Q variants, and the resulting simulations show a reduction in the level of binding of LmCytc to the active site of

LmP (Figure 4.3A, right column). Another interesting observation is that with the exception of E49Q, all of the charge neutralizing D to N and E to Q mutations also reduce the level of interaction of LmCytc with helix A of LmP. Overall, the computed association rates were significantly lower than that of the wild type for all of the helix A D to N and E to Q mutants (Table 4.2).
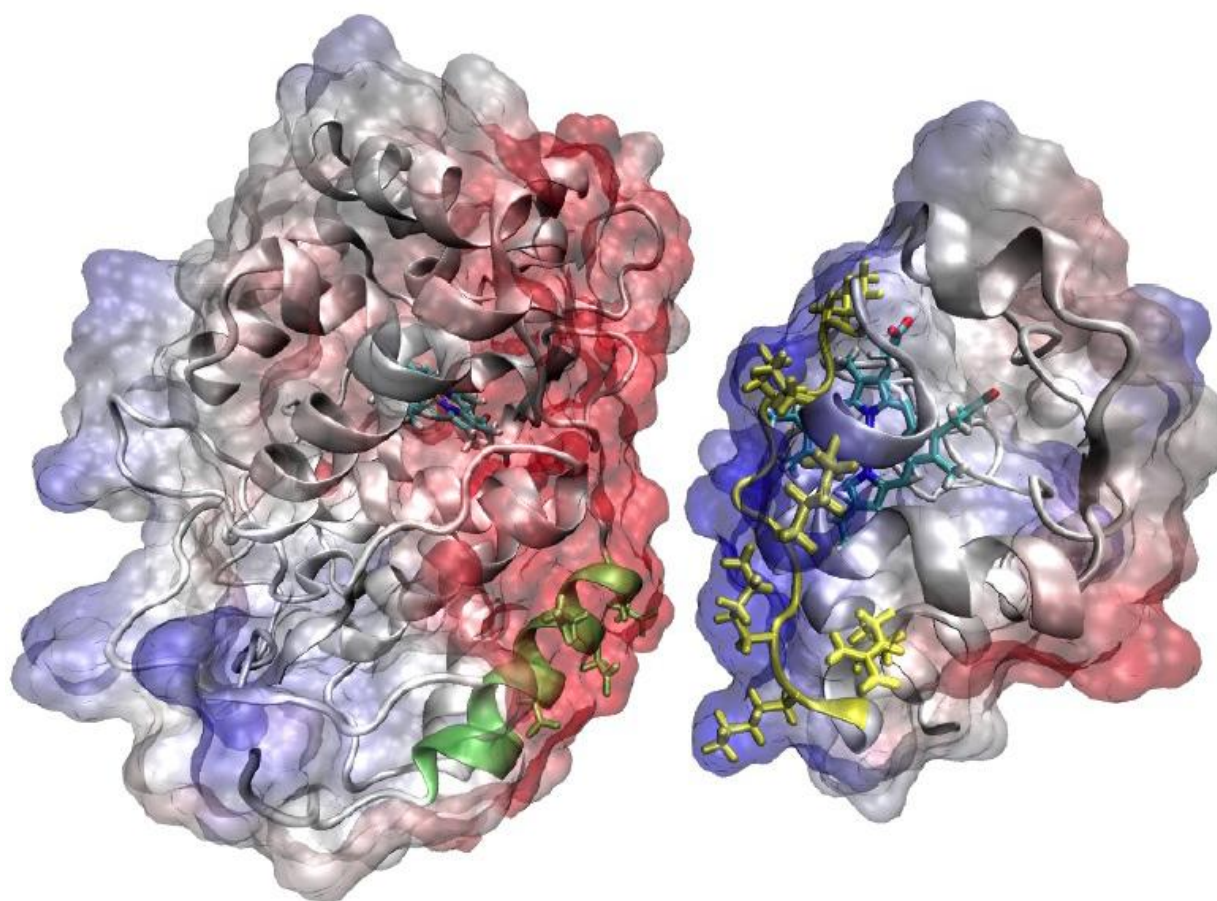
Figure 4.4 – Overview of the LmP-LmCytc system
The LmP-LmCytc complex as determined by Jasion et al.[22] is shown where LmP (left) and LmCytc (right) have been separated to highlight the highly complimentary electrostatic surfaces. The backbone of each protein is shown in cartoon representation and electrostatic potentials are displayed on transparent solvent-accessible surfaces where negative potential is red and positive is blue. The backbone of helix A of LmP is colored green. Negatively charged side chains on helix A of LmP are shown in green licorice and positively charged side chains of LmCytc at the binding interface are shown in yellow licorice.

The importance of the helix A charges was confirmed experimentally by steady-state assays of the LmP D47A/D50A/E54A triple mutant. At an ionic strength of 150 mM, the measured k_1 for the triple mutant is ~19 times lower than that of wild type LmP (Table 4.3). The ~6-fold reduction in the second-order association rate of the triple mutant versus that of the wild type computed from the BD trajectories (Table 4.2) agrees qualitatively with the reduction observed experimentally. Once again, the BD simulations have revealed a real transient feature that was not previously obvious based on the structure and kinetics of the complex.

Structure of the D211N Mutant of LmP.

LmP shares a common feature with many other peroxidases in that it has a structurally important cation binding site near the proximal side of the heme (Figure 4.5B). In LmP, this is either K^+ or Na^+ and the carbonyl O atom of D211 provides one of the ligands. Because we were concerned that the D211N mutation might cause structural perturbations around the cation site, we determined the crystal structure of the D211N mutant. As shown in Figure 4.5B, the cation site remains fully occupied and there are no significant structural perturbations. Therefore, any change in the measured kinetics is due solely to the mutation and not to structural changes. The D211N structure used in the BD simulations, which was prepared by *in silico* mutation before the D211N crystal structure was determined, is essentially identical to the crystal structure (Figure 4.5A).
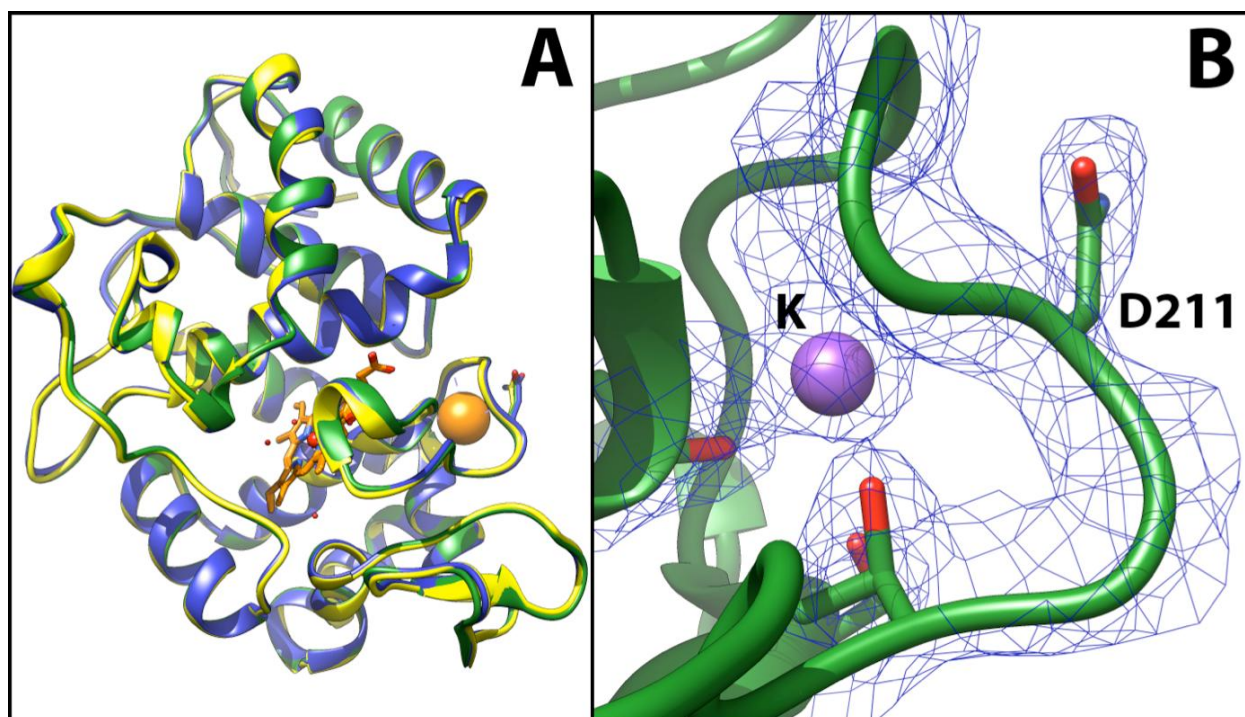
Figure 4.5 – Crystal structure of the LmP D211N mutant
(A) Superposition of the α-carbon backbones of the wild type LmP (blue), the LmP D211N (green) mutant, and the LmP D211N *in silico* mutant used for the BD simulation; (B) K$^+$ ion binding site, with the $2F_o$ - F_c density map contoured at 1.0σ. Molecular graphics in this figure were made using UCSF Chimera.[25]

A Key Role for Helix A in the Formation of the LmP−LmCytc Complex.

In the cocrystal structures, the side chain conformations in the two proteins are optimized at the binding interface to support formation of a tight ET complex. In the individual structures, the conformations of the side chains at the binding interface are slightly different and are presumably more representative of the conformations of the proteins when they first encounter one another in solution, before the formation of the tight ET complex. Thus, BD simulations initiated from the individual structures permit us to sample configurations of the initial encounter complex and determine which interactions bring the two proteins together initially. The probability isosurface obtained from BD trajectories of the individual wild type structures is shown in Figure 4.3B (left column). In contrast to the case of the wild type cocrystal structures

(Figure 4.3A, left column), there are no features in the isosurface near the LmP active site for the individual wild type structures. This suggests that minor adjustments of the conformations of side chains at the binding interface are required for the formation of the tight ET complex. The tiny feature near the N-terminal end of helix A of LmP in the isosurface from the simulations of the cocrystal structures (Figure 4.3A, left column) is significantly enhanced in the isosurface from the simulations of the individual structures (Figure 4.3B, left column). The broadness of this feature in the case of the individual structures is indicative of local sampling of LmCytc around helix A of LmP. The existence of the feature near helix A suggests that interactions at the binding interface that are required for the formation of the final complex are not necessary to bring the proteins together initially. This hypothesis is supported by the persistence of the helix A feature in the isosurfaces obtained from both sets of simulations of the D211N mutant (middle column of panels A and B of Figure 4.3), which do not display a feature in the isosurface near the active site in either set of simulations (cocrystal or individual structures).

The key role for negative charges on helix A suggested by the BD simulations of the cocrystal structures of mutants in which helix A charges were neutralized is reinforced by simulations of the corresponding mutants of the individual structures. The helix A feature is absent in the isosurfaces from the simulations of the D50N, E49Q, and D47N/D50N/E54Q variants initiated from the individual structures (Figure 4.1A and Figure 4.6B, second and fourth columns). The helix A feature is present but shifted significantly away from its position in the isosurfaces of both the wild type and active site D211N mutant in the D47N and E54Q variants (Figure 4.6B, first and third columns). Thus, consistent with the simulations initiated with the cocrystal structures, the simulations initiated from the individual structures predict that

81

interactions of LmCytc with helix A of LmP are altered by elimination of negative charges on helix A.

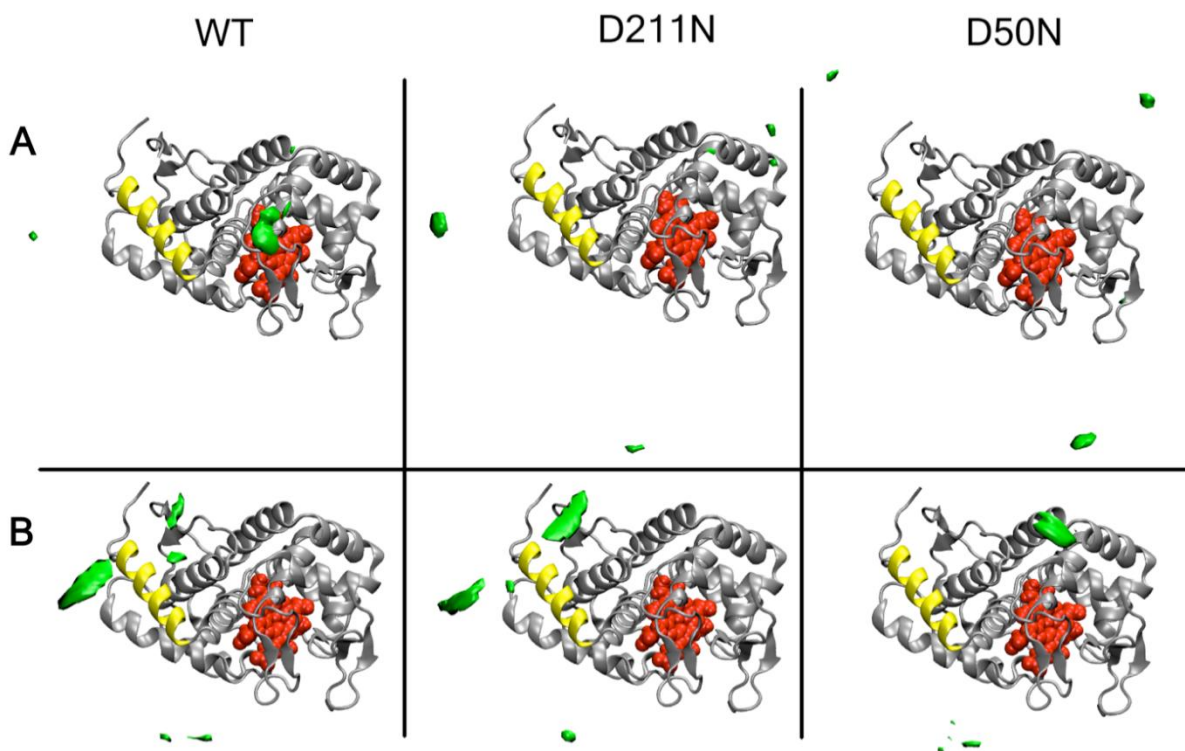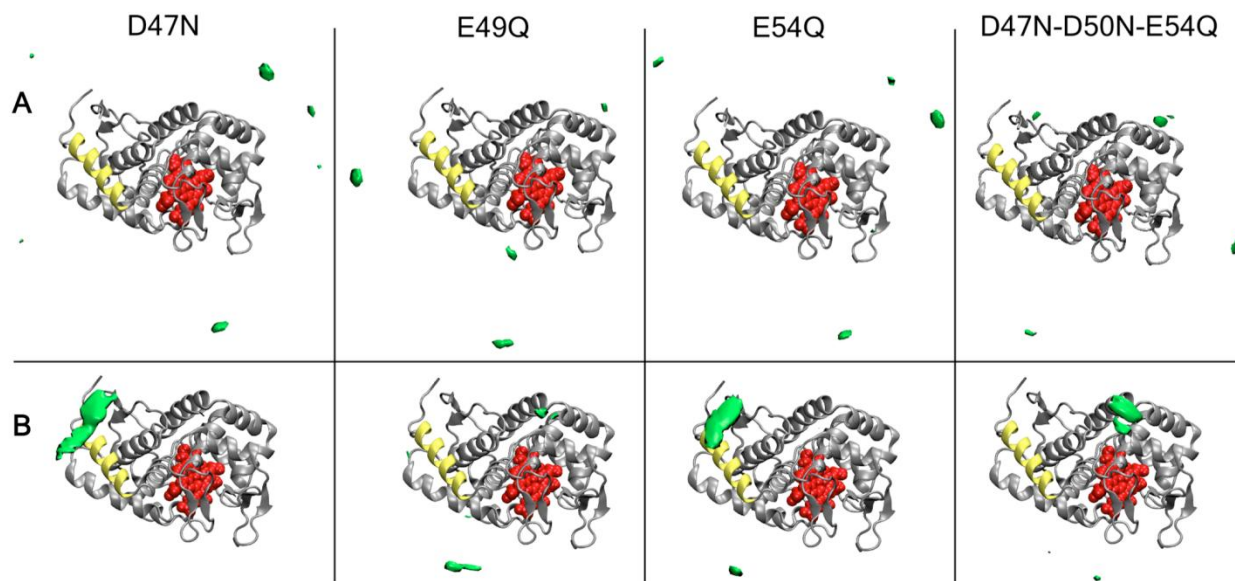**Figure 4.6 –Probability isosurfaces comparing LmP helix A mutants**
(A) BD simulations initiated from the co-crystal structures; (B) BD simulations initiated from the individual structures
All probability isosurfaces for the LmCytc center-of-mass were contoured at a value of 2.2×10^{-3} and depicted in green.

The two-step "Bind and Crawl" Mechanism

The BD simulations initiated from the cocrystal structures exposed two binding sites for LmCytc on wild type LmP, one at the active site and the other near helix A of LmP (Figure 4.1A). BD simulations initiated from the individual structures, in which the side chain conformations are not optimized for active site binding, show persistent interactions between LmCytc and helix A of wild type LmP (Figure 4.3B, left column). The observation that LmCytc binds to both the active site and helix A of LmP raises the question of whether helix A competes with the active site for LmCytc or whether binding to helix A is a prelude to binding to the active site. Visual inspection of the BD trajectories reveals that LmCytc first binds to helix A and then travels down helix A toward the cocrystal interface, stopping at the end of the helix before jumping from the end of the helix to the interface where it begins local sampling of the active

site region of LmP. By tracking the LmCytc center of mass in the BD trajectories that were initiated from the cocrystal structures, we found that LmCytc binding to the active site was preceded by binding to helix A in ~70% of the reactive trajectories.

The BD trajectories suggest that helix A plays two roles in the formation of the complex, one as the initial point of contact for LmCytc on LmP and the second as a runway to guide LmCytc to the ET interface. On the basis of the BD trajectories, we propose that the formation of the LmP−LmCytc ET complex proceeds, as suggested previously,[22] *via* a two-step "bind and crawl" mechanism in which LmCytc first binds to helix A and subsequently migrates to the active site, with concomitant changes in the conformations of side chains at the binding interface allowing the formation of a tight complex.

Molecular Dynamics Simulation of Encounter Complex Formation.

To examine the importance of helix A in more detail, my collaborators performed an MD simulation in order to observe changes at the atomic level. A configuration from a BD simulation of the wild type proteins initiated from the individual structures, in which LmCytc is close to helix A of LmP, was selected as the starting point. The two proteins were then moved farther from each other along the separation vector connecting their geometric centers to the point where their respective surfaces were 15 Å apart. Upon initiation of the simulation, LmCytc returned rapidly (within 2 ns) to helix A near its location in the configuration selected from the BD simulation. Once bound to helix A, LmCytc began to travel down the helix toward its location in the cocrystal structure. The movement down the helix, depicted in successive snapshots in Figure 4.7, was completed in 20 ns, reaching the closest approach to the cocrystal structure at

approximately 50 ns. At that point, LmCytc reached the end of the helix and remained there without jumping to the active site interface for the remainder of the 100 ns MD simulation.
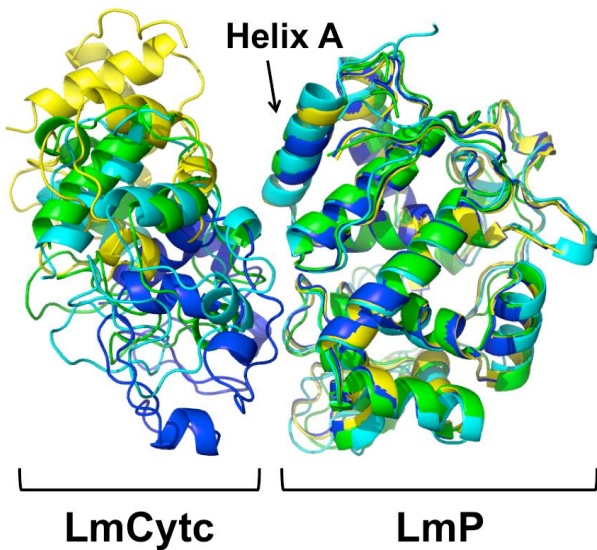
Figure 4.7 – MD simulations snapshots
Snapshots after 6 ns (green) and 50 ns (cyan) from the MD simulation of LmP and LmCytc initiated with LmCytc docked onto helix A and then displacing it by 15 Å. For comparison, the positions of the two proteins in the co-crystal structure are shown in dark blue while the initial BD configuration is shown in yellow.

The motion of LmCytc relative to LmP was also monitored by measuring the distance between the C_ζ atom of Arg24 of LmCytc and the C_γ atom of Asp211 of LmP, which is approximately 6 Å in the cocrystal structure. This distance reaches its maximal value of ~38 Å when LmCytc first binds to helix A of LmP and is gradually reduced to its minimal value of ~15 Å as LmCytc is guided toward the active site interface along helix A. The root-mean-square deviations (rmsds) of the backbone C_α and side chain C_β atoms remained in the range of 1.75−2 Å for LmP and 1−1.75 Å for LmCytc during the latter half of the MD simulation. The low values of the rmsds are consistent with the observation that the conformations of both proteins are very similar in the crystal structures of the individual proteins and the structure of the complex.[22] The main difference is that, in the complex, Arg24 of LmCytc is in a different rotameric state that

84

allows it to form a salt bridge with Asp211 in LmP, whereas in the individual structure of LmCytc, Arg24 forms an intramolecular salt bridge with LmCytc Glu101. We posit that the change in the rotameric state of Arg24 is a crucial step along the way from the initial encounter complex, where LmCytc is docked onto helix A of LmP, to the active ET complex. The intramolecular salt bridge remained intact during a large portion of the MD simulation, and this likely explains why the LmCytc Arg24−LmP Asp211 distance remained >15 Å throughout the simulation.

Effect of Helix A Mutations on Kinetics.

To assess the role of helix A on activity, we measured both steady-state and single turnover kinetics for the helix A triple mutant, D47A/D50A/E54A. The k_{cat} for the triple mutant is approximately the same as that of WT LmP, and as with WT LmP, k_{cat} is independent of ionic strength and is not limited by formation of the LmP−LmCytc complex or dissociation of the product. Instead, the rate-limiting process remains intramolecular ET from the LmP active site Trp to $Fe^{IV}=O$. We next used stopped-flow spectroscopy to measure the rate of LmCytc oxidation by LmP CmpI. As in our previous work,[123] an excess of CmpI over LmCytc was used to ensure that only reduction of the Trp radical was measured. The rate of this process is ~50% slower in the mutant (Table 4.3). These results are consistent with the BD and MD simulations and support the view that helix A plays an important role in forming the initial encounter complex.

BD Simulations Show That Yeast Cytc Does Not Associate with Helix A of CcP.

The combination of BD and MD simulations suggests that the charges on helix A play a vital role in the association of LmP and LmCytc. Three of the four charges found on helix A of LmP are not present in helix A of CcP. The lack of charges on helix A makes the CcP system a useful control for further validation of the role of helix A charges in the formation of LmP−LmCytc encounter complexes. Cytc around CcP, initiated using the structures of the proteins in their ET complex, is depicted in Figure 4.8A. For comparison, the location of the center of mass of Cytc in the structure of the complex is indicated in Figure 4.8B. There are several small features distributed broadly over the surface of CCP, but in contrast to the case of LmP (Figure 4.3A and B, left column), there are no features near the N-terminal end of helix A of yeast CCP. Thus, it is apparent that the helix A charges are required for the formation of the initial encounter complex in which LmCytc is docked onto helix A of LmP.
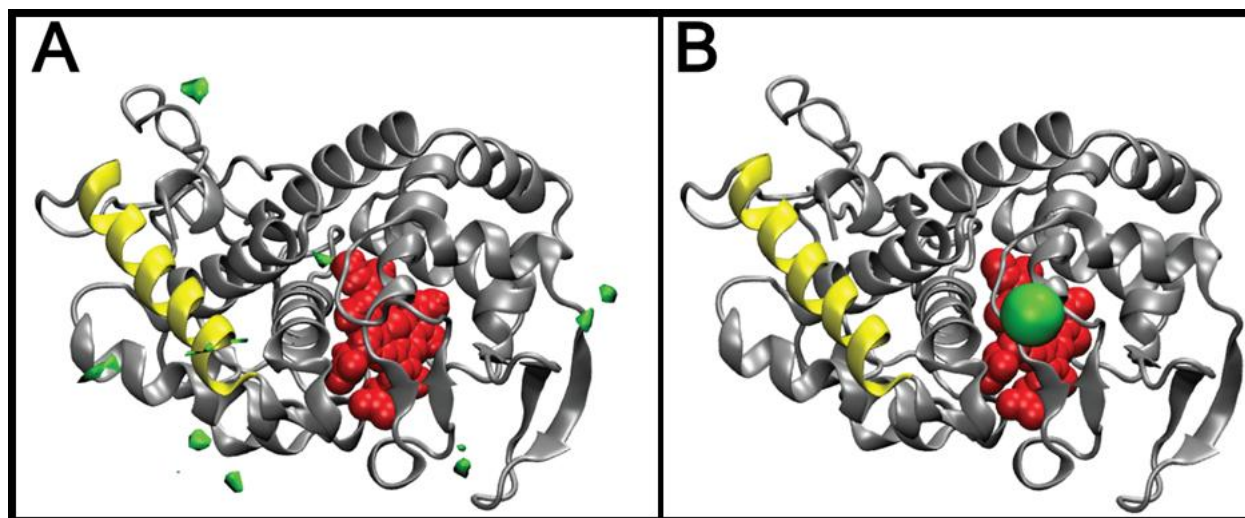
Figure 4.8 – BD simulations of yeast CcP-Cytc complex
Helix A is drawn as a yellow ribbon, the heme is depicted as red van der Waals spheres and probability isosurfaces for the Cytc center-of-mass calculated from BD simulations are drawn in green and contoured at a value of 2.2×10^{-3}. (A) BD simulation initiated from the co-crystal structures. There are several features distributed over the surface of CcP, but none indicating a strong interaction of Cytc with helix A. (B) Position of the center-of-mass of LmCytc in the co-crystal structure. Here, only one large feature appears at the active site.

The second-order association rates computed from our BD trajectories of the yeast CcP−Cytc system at ionic strengths of 100 and 300 mM, $(1.65 \pm 0.02) \times 10^9$ and $(0.414 \pm 0.012) \times 10^9$ M^{-1} s^{-1}, respectively, are in good agreement with the corresponding experimental values, 2.95×10^9 and $(0.22 \pm 0.01) \times 10^9$ M^{-1} s^{-1}, respectively.[111, 152] Our rates are lower than the values 6.71×10^9 and 0.856×10^9 M^{-1} s^{-1}, respectively, which were computed previously by Gabdoulline and Wade using a similar BD approach, and also agree well with the experimental values.16 Moreover, at first glance, the probability isosurface shown in Figure 4.8A is dramatically different from an isosurface of the Boltzmann factor calculated on the basis of electrostatic interaction energies (orange surface in Figure 5d from Gabdoulline and Wade[152]). According to the latter, Cytc has a broad distribution of configurations on the side of CcP that contains the active site, which is clearly not evident in the probability isosurface shown in our Figure 4.8A. However, when we lower the value at which we contour the probability isosurface by a factor of 10 (i.e., to 2.2×10^{-4}), we also observe a broad distribution of Cytc around the active site surface of CcP. The differences between our rates and those computed by Gabdoulline and Wade presumably reflect differences in the details of the BD simulation protocols used in the two studies.

Conclusions

This study provides an example of how computational approaches can provide novel insights into the mechanism of an important protein−protein interaction that were not at all obvious from previous experimental work, including crystal structures. Indeed, the computational effort guided the experimental work, and together, the simulations and experiments revealed new aspects of the dynamics of the initial encounter complex formed by

LmP and LmCytc. The calculated rates for both wild type and mutant LmP agree very well with experimental rates, thereby validating the BD approach. The most important new insight into the LmP−LmCytc system, predicted by the simulations and confirmed by the experiments, is the unexpected role of helix A of LmP. The dynamic picture that emerges from these studies is that LmCytc rapidly forms an initial encounter complex with helix A of LmP and then "crawls" toward the ET active site. The encounter complex is transient, with no specific intermolecular ion pairing, but rather an interaction between two large and electrostatically complementary surfaces that ensures very rapid complex formation. However, the final ET active complex does require specific interactions such as the LmP Asp211−LmCytc Arg24 ion pair. The probability of this ion pair forming upon initial complex formation is low, which implies that the system is designed to rapidly form a non-specific interaction with helix A that reduces the search for the ET active complex from a relatively slow three-dimensional search to a more rapid two-dimensional search. This ensures that complex formation and dissociation are not rate-limiting, which is exactly what we observe experimentally. The interplay between computational and experimental approaches used here should prove useful in applications to many other systems in which complementary electrostatic surfaces play a major role in complex formation.

PROTECTION AGAINST NITROSATIVE STRESS BY LEISHMANIA MAJOR HEME PSEUDOPEROXIDASE

Chapter 5

Summary

While the discovery of a CcP in a parasite initially gave biomedical relevance to CcP study, LmP proved to be a poor therapeutic target. We now take a look at a recently identified LmP cousin, also a heme protein from *Leishmania major*, that has been hypothesized to detoxify the reactive nitrogen intermediate peroxynitrite (instead of H_2O_2). Until recently, no other heme-containing enzymatic defense against peroxynitrite had been identified in Leishmania species, and the initial results provided hope for a novel therapeutic target. The absence of structural corroboration provided an obstacle to progress for this system, but we have revived the work by successfully solving the 1.76 Å crystal structure of LmPP.

New Concepts?

- **Promastigote:** One of the morphological forms in the *Leishmania* life-cycle, most common when the parasite is in the insect host, prior to infection. Leishmania possess a single flagellum, which is visible in the promastigote form.[171]

- **Amastigote:** Another morphological form in the *Leishmania* life-cycle. This form is most common when the parasite is in an infected mammalian host macrophage. The flagellum is not visible in the amastigote form.[171]

INTRODUCTION

The dangers of peroxynitrite

Peroxynitrite ($ONOO^-$) is the product of the reaction between nitric oxide (NO) and superoxide (O_2^-) radicals. In cells, peroxynitrite formation competes with superoxide dismutase (SOD) for O_2^-. However, reactions between radicals occur by radical-radical coupling and are usually very fast. In fact, the rate constant for the formation of peroxynitrite is $\sim 10^{10}$ M^{-1} s^{-1},[172] which is approximately 10 times faster than reported SOD activity of about 2×10^9 M^{-1} s^{-1}. [173] Peroxynitrite formation from NO and O_2^- radicals also has a ΔG of -22 kcal kcal $\cdot$ mol^{-1},[174] equivalent to the hydrolysis of two molecules of ATP. This essentially means that peroxynitrite formation is irreversible and outcompetes SOD for O_2^-, which can be very deleterious *in vivo*. Since it is the product of radical-radical coupling, peroxynitrite is not a free radical, but has 2 additional unpaired electrons on its terminal peroxide oxygen. Peroxynitrite is also quite stable at high pH ($pK_a = 6.8$)[175], because it predominantly adopts a *cis* conformation (Figure 5.1),[176-179] which allows the negative charge to be delocalized and results in a 3.5 kcal $\cdot$ mol^{-1} higher stability than the trans conformation (30 kcal $\cdot$ mol^{-1} barrier).[176] Protonation of peroxynitrite to peroxynitrous acid (ONOOH) stabilizes the negative charge, thus reducing the barrier to 13 kcal $\cdot$ mol^{-1},[180] and promotes its decay to nitrate with a ΔG of - 36 kcal$\cdot$$mol^{-1}$ at a rate constant of 1.3 s^{-1} at 25 °C.[175]

Peroxynitrite is, therefore, highly reactive *in vivo*, as it is both a 2-electron oxidant and a strong nucleophile. As such, it is able to oxidize and nitrate a large number of biological molecules, including iron−sulfur centers, zinc fingers and other transition metal centers.[181-183] It is also able to induce cysteine sulfhydryl hydroxylation,[175, 184-185], phenol nitration,[186] tyrosine nitration,[187-188]

DNA base nitration,[189-190] and lipid peroxidation.[191] Overall, peroxynitrite is a potent molecule used by the immune system to defend against invading pathogens.
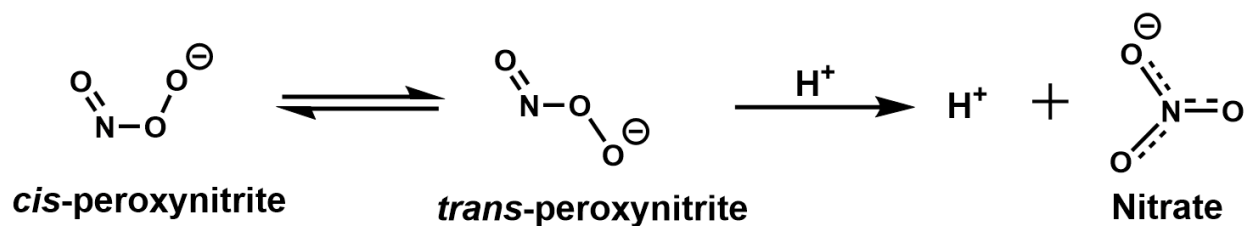
Figure 5.1 – The *cis* and *trans* conformations of peroxynitrite and its decay to nitrate at lower pH.

We have already described the *Leishmania* parasite at length. We know that it is the causative agent of leishmaniasis, a tropical disease that infects a host through the bite of a sand fly. From a biological standpoint, it is interesting to understand how this parasite is able to survive under the oxidative burst generated by the infected host's immune system. The host's activated macrophages produce high concentrations of reactive oxygen and nitrogen intermediates such as H_2O_2, $O_2^{\cdot-}$, $NO^{\cdot}$ and $ONOO^-$.[53, 192-193] Until very recently, there was no known mechanism of peroxynitrite detoxification in *Leishmania* species, but this recently changed with the identification and characterization of an LmP like heme enzyme produced by *Leishmania major*, but whose hypothetized function is peroxynitrite detoxification.[194] Due to its similarity to LmP (~14% sequence identity and ~40% conserved residues) but inability to turn over H_2O_2, it was named a pseudoperoxidase (LmPP).

Is the function of this enzyme truly to detoxify peroxynitrite? Although there are only three previously published works[194-196] that describe the results of studies done on this enzyme, we are still able to draw four main conclusions that collectively strengthen this hypothesis. First, steady-state experiments reveal that decay of $ONOO^-$ in the presence of LmPP is linear, time and enzyme dependent.[194] Second, binding of $ONOO^-$ to the heme iron has been captured by

91

stopped-flow spectroscopy: addition of ONOO$^-$ causes a blue shift in the Soret absorption band from 423nm to 415nm,[194-195] and the binding rate constant was found to be linearly dependent on ONOO$^-$ concentration.[195] Optical, EPR and resonance Raman spectroscopies show that ONOO$^-$ shifts the heme from a low-spin to a high-spin state, while H_2O_2 has no effect.[194] These three observations suggest that ONOO$^-$ is not just non-specifically nitrating the enzyme, but that it is directly interacting with the heme iron, thus causing the Soret absorption to shift. Third, *in vivo* immunofluorescence microscopy showed that the enzyme is localized in the flagellar pocket in the promastigote stage, but becomes localized on the surface of the cell in amastigotes,[194] the latter being the predominant form the parasite adopts after infecting a mammalian host. Western blotting also revealed an eightfold higher expression of LmPP in amastigotes.[194] Both of these results suggest that the function of LmPP is more crucial after the parasite has infected a mammalian host. Fourth, *in vivo* LmPP knockout (KO) mutant cells were shown to be five times more sensitive to SIN-1 (3-morpholinosydnonimine, a ONOO$^-$ donor) than wild type cells, while KO cells exposed to H_2O_2 showed similar results than wild type cells.[194] *In vivo* infection experiments showed that 40% of KO cells were killed after 24h incubation with pre-treated unstimulated macrophages (they only produce O_2^-), while wild type cells were not affected at all, and that inhibition of NO production inhibited the killing of KO cells, suggesting that either NO or ONOO$^-$ is involved in the death of the KO cells.[194] Taken together, these results strongly suggest that the function of LmPP is to break down peroxynitrite, although the exact mechanism by which this occurs is not understood.

Homology studies with LmP reveal that LmPP is quite similar, albeit with key differences in the active site. Understanding LmPP catalysis is dependent on a better

understanding of active site topology. Extensive site-directed mutagenesis experiments were done to determine the proximal and distal heme ligands.[196] Spectroscopic results suggested that the most likely candidates were a proximal His206 and distal Cys107. Since the structure of LmPP was not known, our first goal was to solve its crystal structure in order to shed light on the mechanism of LmPP catalysis.

EXPERIMENTAL PROCEDURES

Cloning and site-directed mutagenesis

The wild type LmPP construct without the N-terminal hydrophobic tail (Δ48LmPP) was obtained from Dr. Subrata Adak and cloned into the pET28a vector containing a Kan^R gene and a C-terminal 6X-Histidine tag as pET28a/Δ48LmP between the NdeI and XhoI restriction sites.

Protein Expression and Purification

Expression and purification of LmPP were carried out in a protocol similar to LmP: each plasmid was transformed in Escherichia coli BL21(DE3) cells and plated onto LB agar with kanamycin (50 μg/mL). A single colony was used to inoculate each 5 mL of 2xYT starter culture (50 μg/mL kanamycin). The culture was incubated for 8 hours at 37 °C and 220 rpm agitation. Each liter of TB medium (kanamycin 50 μg/mL) was inoculated with 2 mL of 2xYT starter culture. The cells were grown at 37 °C with 210 rpm agitation in a New Brunswick Scientific C25KC incubator until an OD_{600} of 0.8-1.0 was obtained. Cells were then induced with 0.5 mM isopropyl β-D-thiogalactoside and 0.4 mM δ-aminolevulinic acid, and a new dose of kanamycin was added. Post-induction cells were then incubated for 24hrs at 25°C and 100 rpm, after which they were harvested by centrifugation and stored at −80°C. Cells were resuspended in Buffer A

(50 mM potassium phosphate, pH 7.8, 1 mM PMSF, 5 mM β-mercaptoethanol and 100 mM KCl). Cells were lysed by passing through a microfluidizer at 18k psi (Microfluidics International Co). The soluble fraction was isolated by centrifugation at 17,000 rpm and 4°C for 1hr. The crude extract was then loaded onto a Ni^{2+}-nitrilotriacetate column previously equilibrated with 10 column volumes of buffer A. The column was washed with 10 CV of buffer A, 10 CV of 5 mM L-Histidine in buffer A, and eluted with a linear gradient of 5 to 100 mM L-Histidine in buffer A. Fractions were pooled according to an $R_z(A_{423}/A_{280}) > 1.2$ and dialyzed against buffer A for 8 hours. Thrombinolysis was done with 50:1 weight ratio of LmPP:thrombin and incubated at 25 °C for 2 hrs. The digested sample was then re-loaded onto a regenerated Ni^{2+}-nitrilotriacetate column previously equilibrated with buffer A, and eluted with 5 mM imidazole in buffer A. The protein sample was then dialyzed against buffer B (50 mM potassium phosphate pH 5.2, 2 mM DTT and 50 mM KCl) for 8 hrs. The dialzyed protein was loaded on an SP sepharose (HiTrap, GE healthcare) column preequilibrated with buffer B. The column was then washed with 10 CV of up to 150 mM KCl in buffer B, and eluted with a 150 - 400 KCl gradient in buffer B. Fractions with an Rz > 1.3 were pooled and concentrated in a 10,000 molecular weight cut-off Amicon concentrator at 4°C, and then loaded onto a Superdex 75 column (HiLoad 16/60, GE Healthcare) controlled by an FPLC system and pre-equilibrated with buffer C (50 mM potassium phosphate, pH 7.0, 2 mM DTT and 5% glycerol). Fractions were pooled according to an $R_z > 1.4$. Sample homogeneity was confirmed by SDS-PAGE.

Crystal growth

Protein used for crystallization was concentrated to 14 mg/mL in buffer C using a 10,000 MWCO Amicon concentrator. Crystals were grown at room temperature in 10 % PEG 6,000

(w/v), 5% 2-methyl-2,4-pentanediol (MPD), 0.1 M HEPES pH 7.5 in a hanging drop vapor diffusion setup. Freshly grown crystals were harvested after 24 hrs and passed stepwise through a cryo-protectant solution containing 30 % glycerol (v/v) for 4 hrs at 4°C, before being flash cooled with liquid nitrogen.

X-ray Diffraction Data Collection, Processing, and Structure Refinement

Cryogenic (100 K) X-ray diffraction data were collected remotely at the Stanford Synchrotron Radiation Lightsource (SSRL) facility using the data collection control software Blu-Ice and a crystal mounting robot. Data were collected using a Rayonix MX325 charge coupled device (CCD) detector at beamline 14-1. Multi-wavelength anomalous disperson (MAD) data were collected at two wavelengths near the Fe absorption edge using the inverse beam protocol. Raw data frames were indexed and integrated using iMOSFLM,[104] and scaled using SCALA(AIMLESS).[105] The phase information and initial difference Fourier maps were determined from the MAD data using the PHENIX AutoSol wizard.[197] The initial model was then built using the PHENIX AutoBuild wizard[198] and unmodelled residues were then built in manually using COOT[108] and refined against a high resolution data set using PHENIX.[107] The refined structures were validated in COOT. The crystallographic data collection and structure refinement statistics are summarized in Table 5.1.

Data collection and refinement statistics

Radiation source	SSRL BL 14-1
Space group	P $4_1 2_1 2$
Unit cell dimensions a, b, c (Å)	63.68, 63.68, 152.49
Data resolution (Å) (highest-resolution shell)	48.88 (1.827 - 1.764)
X-ray wavelength (Å)	1.18076
Total no. of observations (highest shell)	573101 (51197)
No. of unique reflections (highest-resolution shell)	31236 (3100)
Completeness (%) (highest-resolution shell)	98.22 (94.03)
R_{merge} (highest-resolution shell)	0.7103 (3.476)
I/σ (highest-resolution shell)	73.11 (1.74)
$CC_{1/2}$ (highest-resolution shell)	0.998 (0.297)
Redudancy (highest-resolution shell)	18.0 (16.5)
B factor, Wilson plot ($Å^2$)	34.91
Number of protein atoms	2211
Number of heteroatoms	43
Number of waters	181
Disordered residues	49-55, 273-278, 340-341
R_{work}/R_{free}	0.1957/0.2184
Root-mean-squared deviation for bond lengths (Å)	0.007
Root-mean-squared deviation for bond angles (°)	1.05

Table 5.1 – Crystallographic Data and Refinement Statistics

Stopped-Flow kinetics

Peroxynitrite stocks synthesized from acidified nitrite and hydrogen peroxide were purchased as an aqueous solution from Millipore, aliquoted and stored at -80 °C until right before the experiment. The stock solution was diluted to working concentrations using 5 mM NaOH, and the peroxynitrite concentration was determined spectrophotometrically using the extinction coefficient ε_{302} = 1.705 mM^{-1} cm^{-1}.

All stopped-flow kinetic measurements were performed using an SX.20MV stopped-flow spectrometer (Applied Photophysics) with a dead time of ~1.0 ms. Single-wavelength absorptions were measured using a photomultiplier detector. One stopped-flow drive syringe was loaded with wild type LmPP at various concentrations in 100 mM potassium phosphate buffer, pH 6.0 and the other drive syringe with the peroxynitrite solution in 5 mM NaOH.

As with other stopped-flow data, the second-order rate constant k_1 was calculated by fitting the kinetic traces measured at 302 nm using the software provided with the stopped-flow instrument (Applied Photophysics) and the following standard single exponential equation:

$A_{302} = C_1 \, e^{-k_{obs}t} + b$

where C is the amplitude term, k_{obs} is the observed rate constant for the decay of peroxynitrite and b is an off-set value.

RESULTS AND DISCUSSION

Physical and spectroscopic characteristics

The wild type Δ48LmPP/pET28a construct expressed in large quantities (~60 mg of protein per liter of TB) in BL21(DE3) cells. The final purified protein was polyhistidine tag-free, with an R_z (A_{423}/A_{280}) value of 1.44, ran at approximately 33 kDa on the SDS-PAGE gel (Figure 5.2A), and was measured at 33.4 kDa by MALDI-TOF mass fingerprinting. The resting state UV-visible spectrum of LmPP is typical of hexacoordinate low-spin heme, with the Soret band at 423 nm, the α and β bands at 570 nm and 542 nm, respectively and a split soret δ band at at 359 nm (Figure 5.2B).
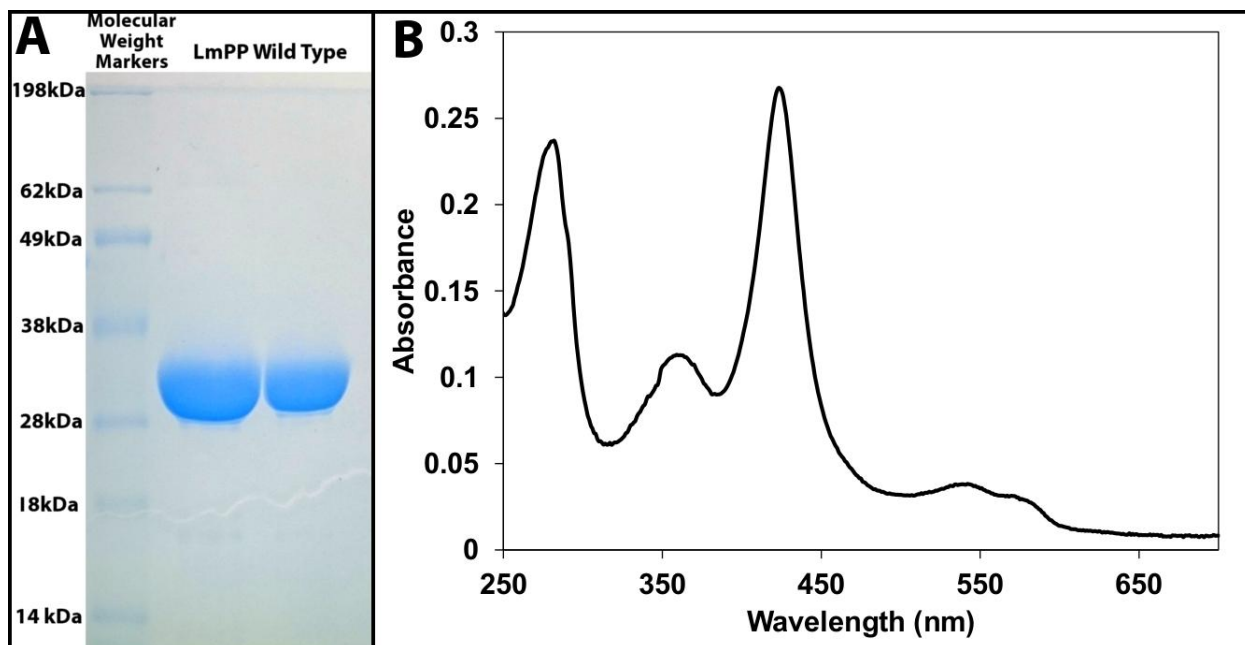
Figure 5.2 – (A) SDS-PAGE of purified wild type LmPP. (B) UV/Vis spectrum of wild type LmPP at pH 7.0.

Crystal Structure

The structure of wild type LmPP was solved to 1.76 Å, revealing a rather uncommon Cysteine/Histine coordination involving His206 at the proximal side and Cys107 at the distal side of the heme(Figure 5.3A), as predicted by Saha et al.
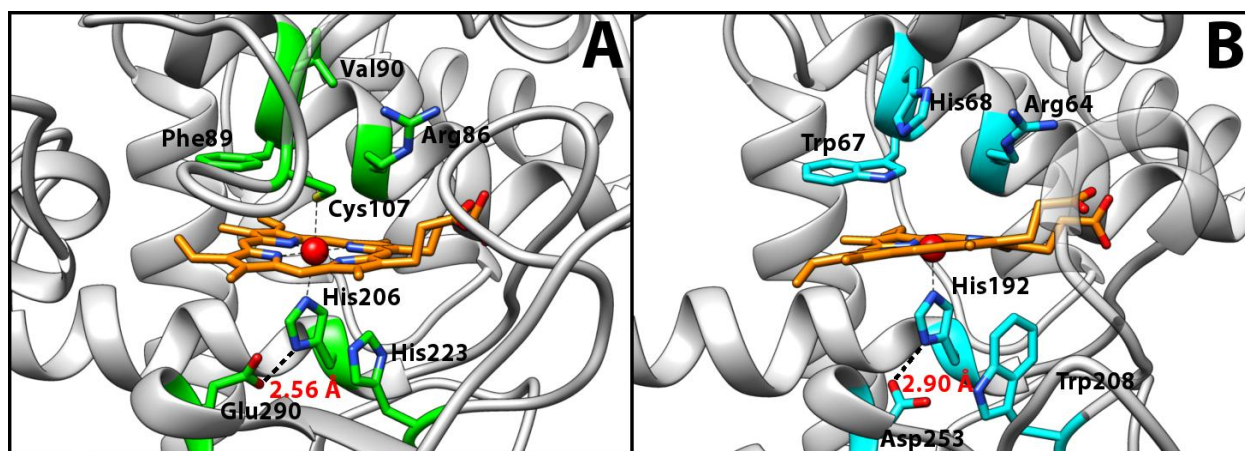
Figure 5.3 – (A) Active site structure of wild type LmPP. (B) Active site structure of wild type LmP (PDB entry 3RIV). All molecular graphics in this chapter were made using UCSF Chimera.[25]

98

Is LmPP structurally a peroxidase? At initial glance, LmPP appears to be a typical heme peroxidase, albeit with slight adjustments. Figure 5.4A is a superposition of the α-carbon backbone of LmPP on LmP, which shows that the 3-dimensional fold of the novel structure is nearly identical to LmP, with the exception of a few surface loops. However, similarities between the two enzymes end upon closer inspection. At the active site, LmPP lacks the proximal Trp that forms a radical in CmpI of LmP and CcP, which is replaced by His223 (Figure 5.3A). On the distal side of the heme, the crucial catalytic His discussed in Chapter 3 that stabilizes binding of H_2O_2, formation of CmpI and reduction of CmpII in peroxidases is replaced with Val90 in LmPP. An additional heme contacting loop not present in LmP that contains the coordinating Cys107 residue occupies a large portion of the distal side of the heme, leaving little space for a small molecule to bind. At the surface, charges of residues involved in LmCytc recognition (helix A) and binding (D211, E49) are positively charged, and suggest that interaction with LmCytc (also positively charged surface) is likely impossible.
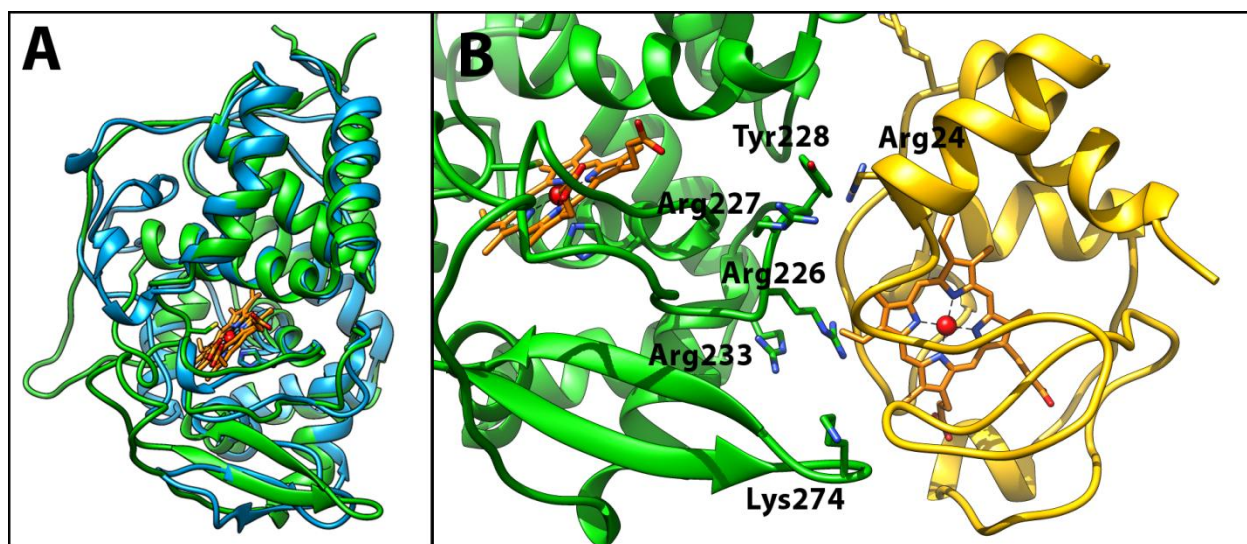
Figure 5.4 – (A) Superposition of α-carbon backbones of LmPP and LmP (B) Hypothetical *in silico* model of LmCytc binding to LmPP as it normally would in LmP. The model was adapted from the LmP-LmCytc complex structure (PDB entry 4GED). LmP is depicted in cyan, LmPP in green and LmCytc in yellow.

Using the LmP-LmCytc complex structure as a starting point, we have modeled a hypothetical complex between LmPP and LmCytc (Figure 5.4B), which shows where LmCytc would bind if it were binding to LmP, clearly showing the clashes. The crucial Arg24 of LmCytc discussed in Chapters 2 and 4 has no Asp to interact with, and would instead come sterically clash with LmPP Tyr228. In addition four positively charged LmPP side chains, Arg226, Arg227 Arg233 and Lys274 are extending into the solvent, preventing any other positively charged molecule from coming in close contact near this position (Figure 5.4B). Helix A discussed in Chapter 4 is also present in LmPP, but does not retain the crucial negatively charged Asp47, Glu49, Asp50 and Glu54. Instead, the analogous residues in LmPP helix A are Ser69, Cys71, Lys72 and Phe76, in respective order.

Potential Mechanism

Overall, the fact that LmPP ferric iron is coordinatively saturated at resting state does not leave much indication as to the mechanism/function. One hypothesis is that a substrate induced conformational change could release the Cys107 loop, and allow it to bind in the distal pocket. On the proximal side, Glu290 replaces the traditional Asp residue known to tune the redox potential of the heme and stabilize the heterolytic cleavage of the O-O bond and formation of CmpI.[199] Interestingly, the longer Glu side chain results in a shorter H-bond interaction with the His amine (2.56 Å), which most likely increases the imidazolate character of the proximal ligand compared to traditional peroxidases where the H-bond distance ranges between 2.80 Å and 3.0 Å (2.90 Å in LmP, Figure 5.3B). This feature suggests a potential role in the function of LmPP that involves the stabilization of a higher oxidation state of iron, perhaps a CmpI or CmpII like intermediate. Furthermore, work done on myoglobin mutants have shown that mutation of the

distal active site His increases the catalytic rate of peroxynitrite isomerization to nitrate.[200] Also relevant to this discussion is work done by Yi et al. involving nitrite binding to the myoglobin H64V/V67R double mutant.[201] Interestingly, this double mutant active site is analogous to the wild type LmPP active site Val90 and Arg86. The myoglobin double mutant was shown to stabilize the O-binding mode of nitrite to the heme iron instead of N-binding.[201] This is important because ONOO⁻, which can only initially bind LmPP in the O-binding mode, could be stabilized by H-bonding with distal Arg86. Based on their work, we can propose a hypothetical mechanism for LmPP as a peroxynitrite isomerase (Figure 5.5). First, ONOO⁻ donates a pair of nonbonding electrons to the ferric (Fe^{III}) heme of LmPP to form a Fe^{III}-OONO coordination complex, which subsequently displaces the Cys107 axial ligand that can obtain a proton either from the solvent or from protonated peroxynitrous acid (A). Electronic rearrangement produces CmpII ($Fe^{IV}=O$) and nitrite radical (B). The higher iron oxidation state is stabilized by the strong imidazolate property of the proximal ligand, while the nitrite radical is stabilized in the active site pocket by H-bonding interactions with Arg86 and the ferryl-oxo. The nitrite radical donates its electron to form a bond with the iron-coordinated oxygen, reducing the Fe^{IV} back to Fe^{III} (C). The nitrate can now leave the active site, allowing Cys107 to recoordinate the iron and restore the enzyme back to its resting state.
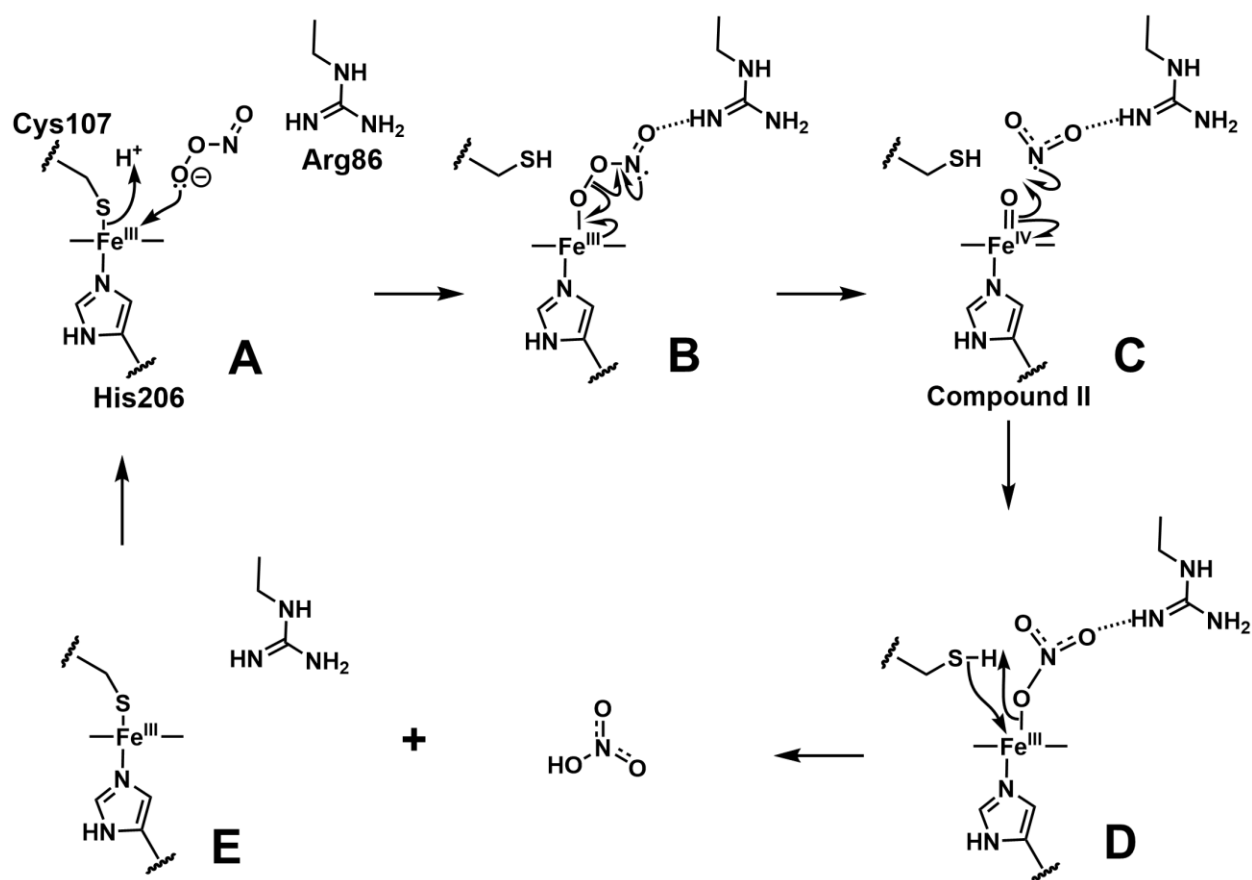
Figure 5.5 – Hypothetical mechanism A for the conversion of peroxynitrite to nitrate by LmPP

This mechanism explains why H_2O_2 is unable to displace the axial cysteine. The more electron rich outer oxygen atom of $ONOO^-$ is a stronger nucleophile, making it able to displace the coordinated cysteine. Also, the pK_a of peroxynitrous acid (ONOOH) is 6.8, while that of H_2O_2, is 11.8,[202] making it quite unfavorable for a cysteine thiol with a pK_a of 8.2 to deprotonate H_2O_2.

This mechanism also suggests a potential role for the distal Cys ligand: to restrict other reactive molecules from access to the active site and to tune the substrate specificity to peroxynitrite. Molecules such as H_2O_2 are especially unwanted since the absence of the distal His prevents heterolytic cleavage of the O-O bond and stabilization of CmpI formation, as we discussed in

Chapter 3. Binding of H_2O_2 in the absence of a reductant would therefore most likely inactivate the enzyme.

Thiols are preferential targets of peroxynitrite by a hydroxylation mechanism,[203] suggesting a possible alternate mechanism to the one we proposed, where the thiol would be hydroxylated first. However, this mechanism is not well corroborated for two main reasons. First, previous work has shown that the C107A mutant is able to catalyze the reaction,[196] and second, the enzyme is able to return to resting state after reaction with peroxynitrite in the absence of reducing agent, which would be impossible if the Cys was being modified.[194-195]

Testing the hypothesis

Preliminary experiments using peroxynitrite stock purchased from Millipore and synthesized from acidified nitrite and hydrogen peroxide gave very unfavorable results. The decay rate constant of 800 μM ONOO⁻ is the same with or without 4 μM LmPP (~0.8 s⁻¹), and adding up to 30 μM LmPP only results in a slightly higher rate constant of about 1.2 s⁻¹ (Figure 5.6A). Even more disconcerting is the fact that contrary to previous results,[194-195] reaction with peroxynitrite exhibits no shift in the soret peak, suggesting no direct interaction with the heme iron (Figure 5.6B). The reason for this discrepancy between previous work and our assays is still unclear and we are currently collaborating with the other research group in an effort to unravel this mystery.
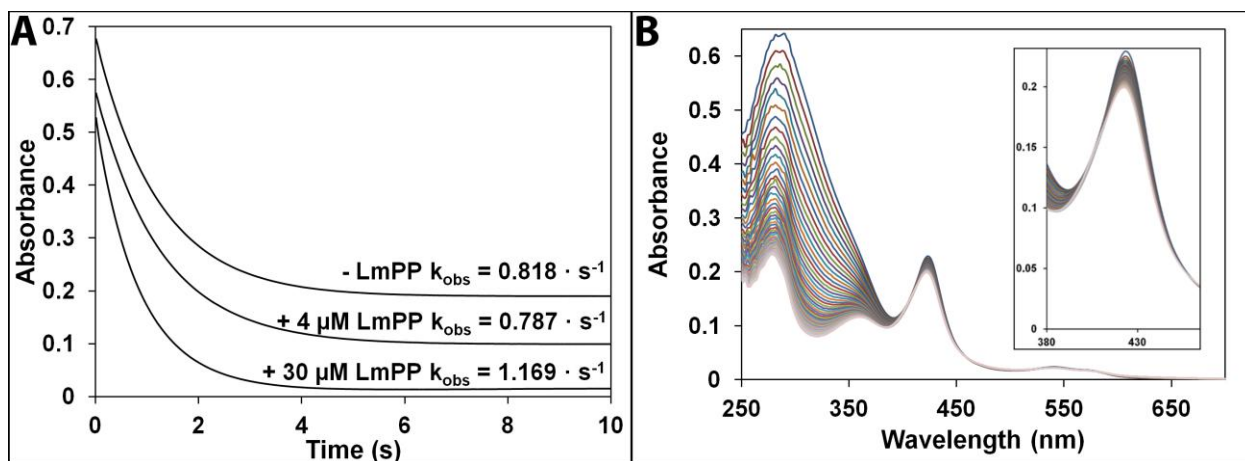
Figure 5.6 – Reaction of ONOO⁻ with wild type LmPP. Panel A shows the decay of 800 µM ONOO⁻ at 302 nm in 50 mM phosphate buffer pH 6.0 for different reaction mixtures: without enzyme, with 4.0 µM LmPP and with 30 µM LmPP. Panel B shows the reaction of 800 µM ONOO⁻ and 8.0 µM wild type LmPP in 50 mM phosphate buffer pH 6.0.

Future directions

At this stage, it is still unclear whether this mechanism is accurate and preliminary results point in the negative direction. Regardless, any evidence in support of the mechanism will largely depend on two factors. First, that the distal cysteine is able to dissociate, and second, that the intermediate formed is a CmpII ferrylnitrito radical complex (Fe^{IV}=O--˙NO_2). A crystal structure of the LmPP C107A mutant is in the works, as well as one with nitrite bound, to see if the active site can sterically allow the binding of a small molecule in the presence of the cysteine ligand. If a direct interaction with the heme iron can be observed, capturing and characterizing the proposed CmpII intermediate could be done by freeze-quench experiment, where the enzyme would be mixed with a solution of peroxynitrite, and rapidly sprayed into liquid ethane (89 K). The freeze-quenched samples could then be subjected to a variety of techniques, such as Mössbauer spectroscopy, to confirm the oxidation state of the iron and its direct environment.

Conclusions

We have discussed the structural characterization of a novel heme enzyme from the *L. major* parasite that seems to be implicated in its defense against the immune system of the infected host. LmPP was previously shown to be overexpressed and surface localized in amastigotes, and knockouts have resulted in increased sensitivity to peroxynitrite but not peroxide. To determine the enzymatic mechanism, we have solved the crystal structure of the wild type enzyme and found it has a Cys/His ligated heme, with a proximal Glu that could stabilize a higher iron oxidation state, and a distal pocket with Val and Arg residues analogous to Myoglobin mutants that were engineered to catalyze the isomerisation of peroxynitrite to nitrate. Based on this, we have proposed a possible role for the coordinated distal Cys as responsible for tuning the substrate specificity to peroxynitrite and to protect the active site from other molecules that react with transition metals. The proposed mechanism remains to be tested, but the findings are exciting nonetheless and provide a powerful guide for future experiments.

ELUCIDATING REDOX PARTNER INTERACTIONS IN THE P450CIN-CINDOXIN ELECTRON TRANSFER COMPLEX

Chapter 6

Summary

P450s are fascinating monoxygenases that are able to activate molecular oxygen and incorporate a hydroxyl group into inert hydrocarbons. Decades of research on the model P450cam system from *P. putida* have revealed most of the intricacies that define P450 catalysis, and the recent solution of the crystal structure of the P450cam-Pdx complex has provided a structural basis for its role as an effector and for the uniqueness of this system. Our research group is interested in determining if other P450s and their redox partners share this exciting feature. We have therefore turned our attention to P450cin, an enzyme that regio and stereo selectively hydroxylates 1,8-cineole, a eucalyptus oil, to produce (R)6-α-hydroxycineole. Based on our group's recent experience and success with site-specific crosslinking of redox partners, we have undertaken the task to crystallize the P450cin-Cdx covalent complex. Although unsuccessful, the work done has still allowed us to establish a powerful method for determining the potential docking sites and orientations of unknown complexes by using site-directed crosslinking of random surface mutants, combined with conventional mass spectrometry techniques.

New Concepts?

Site-specific crosslinking: Molecular technique that involves engineering specific residues on two recombinant proteins and chemically reacting them with a molecular linker to covalently attach them together.

In order to allow access to various substrates to the active site, P450s need to be very flexible, and are generally found to alter between two main conformations.[204-208] While substrate-free, the enzyme is in an "open" conformation (Figure 6.1A), with both the F and G helices extending outwards, leaving a large open channel that allows substrate access to the active site. When the substrate binds, the enzyme shifts to a "closed" comformation (Figure 6.1B), in which the F and G helices, as well as the F/G loop that connects them, undergo a large conformational change to anchor down the substrate in the active site and restrict access.
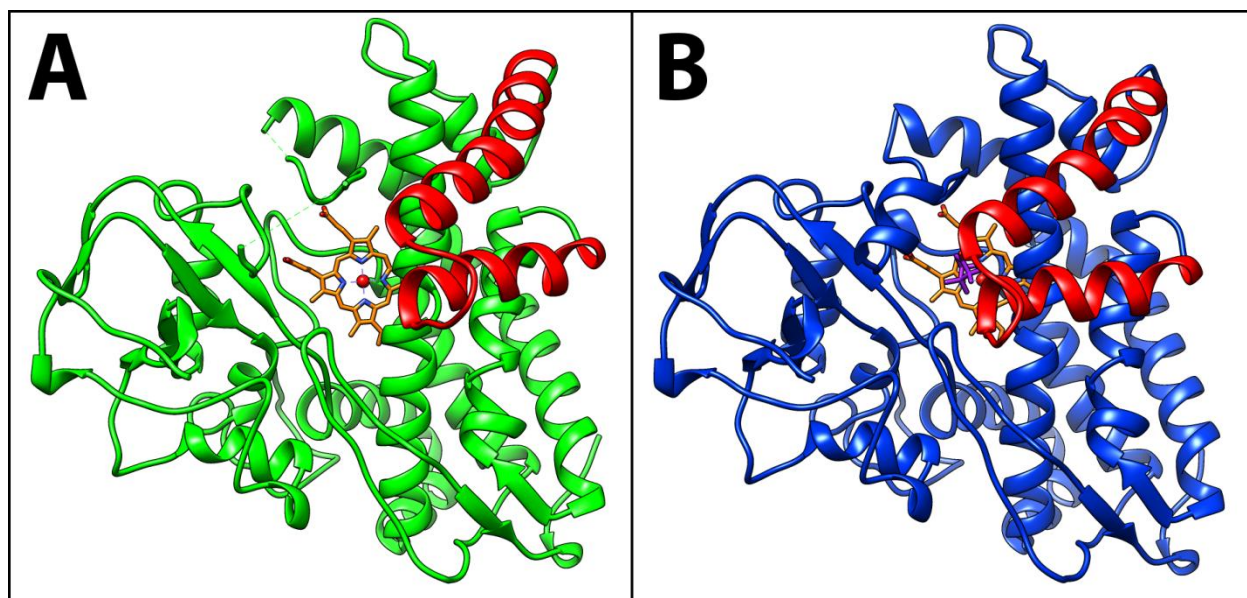
Figure 6.1 – **P450cam two main conformations** (A) Substrate-free (open) conformation depicted in green (PDB entry 3L62) (B) Substrate-bound closed conformation depicted in blue (PDB entry 3L63). For both panels, the F, G helices and F/G loop are depicted in red, camphor in purple and heme in orange. All molecular graphics depicted in this chapter were made using UCSF Chimera.[25]

We have discussed in the introductory chapter how the P450cam system uses two separate redox-active proteins to transfer electrons, the FAD binding Pdr, and the Fe_2S_2 binding Pdx, and that the P450cam system has a unique second ET (Step D→E in Figure 1.6) that has been shown to be specific to Pdx, and that no other redox partner is able to deliver this electron.[48-50]. A very large body of evidence using different methods has collectively suggested

that the required specificity for Pdx is likely due to an effector role, where its binding to P450cam induces structural changes.[209-216] It took nearly five decades to obtain a concrete structural basis for this, when the crystal structure of the oxidized and reduced P450cam-Pdx complex were solved in our laboratory by using a covalent cross-linking approach.[217] The structure revealed that Pdx binding to P450cam shifts the enzyme to the open conformation, which exposes the active site to solvent, allowing protons to protonate the ferric-O_2^-, a required step of the PCET event (Step D→E in Figure 1.6). Whether the source of the protons is a water-mediated H-bond network that forms in the open conformation or simply solvent protons that can only gain access to the active site in the open conformation, the unavoidable conclusion is that the active site must be open for cleavage of the O-O bond and conversion to product to occur.

What remains unclear is if P450cam is entirely unique in this regard, or if other P450s share this specificity. Our group has hypothesized that a similar P450 should also have at least two properties that are similar to P450cam. First, it must be the only P450 expressed by the organism, and second, the three redox partner genes should be expressed on the same tightly regulated operon. One such interesting P450, produced by the soil bacteria *Citrobacter braakii*, was identified and characterized relatively recently.[218] It was first found growing under eucalyptus trees due to its ability to use eucalyptus oil, 1,8-cineole, as a main carbon source. The P450 responsible for the metabolism of 1,8-cineole was thus called P450cin, and catalyzes the regio- and stereoselective hydroxylation of 1,8-cineole to (R)6-α-hydroxycineole (Figure 6.2B).[218] Electron flow in the P450cin system travels from NAD(P)H to the FAD binding Cindoxin reductase (CdR) to the FMN binding Cindoxin (Cdx), to P450cin (Figure 6.2A).[160] The middle redox partner, Cdx, is even more intriguing because it is the only known system to date

that uses a separate FMN binding redox protein instead of Fe_2S_2, and also because the use of an FMN redox partner itself is more analogous to mammalian P450 systems. Our group has therefore focused on characterizing this system in order to find deeper insights into redox partner binding and selectivity in the P450s. So far, the structure of P450cin[204] and Cdx[160] have been solved in isolation, and the active site of P450cin has been extensively probed using site-directed mutagenesis and BD/MD computational techniques.[160, 219] All of the work done thus far has shown that P450cin does alter between substrate-free open conformation and substrate-bound closed conformation.[204] Based on our group's success using covalent crosslinking chemistry to crystallize the P450cam-Pdx complex,[217] we have taken the same approach with P450cin-Cdx, starting with the model generated by BD/MD simulations.[160] The crosslinking chemistry involves using bis-maleimeide crosslinkers, which covalently attach reduced cysteine thiols (Figure 6.3).
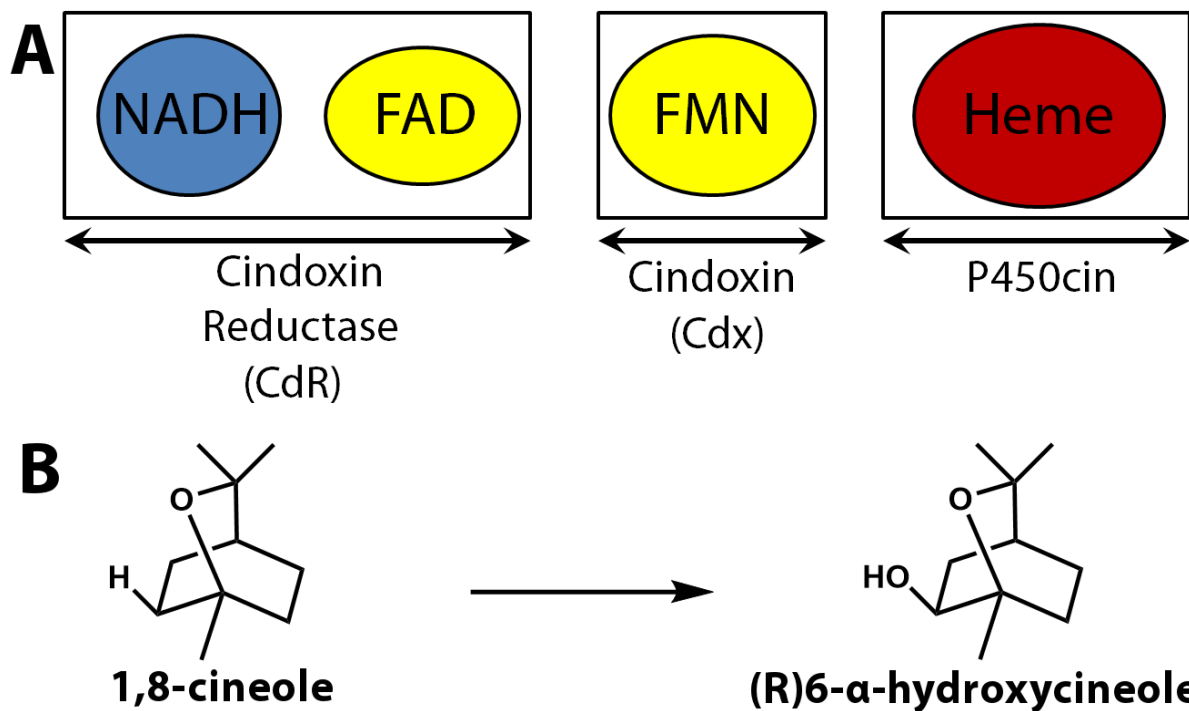
Figure 6.2 – **The P450cin system**
(A) Electrons flow in the P450cin system from NAD(P)H, to CdR, to Cdx, and finally to P450cin (B) P450cin catalyzes the regio- and stereoselective hydroxylation of 1,8-cineole to (R)6-α-hydroxycineole.
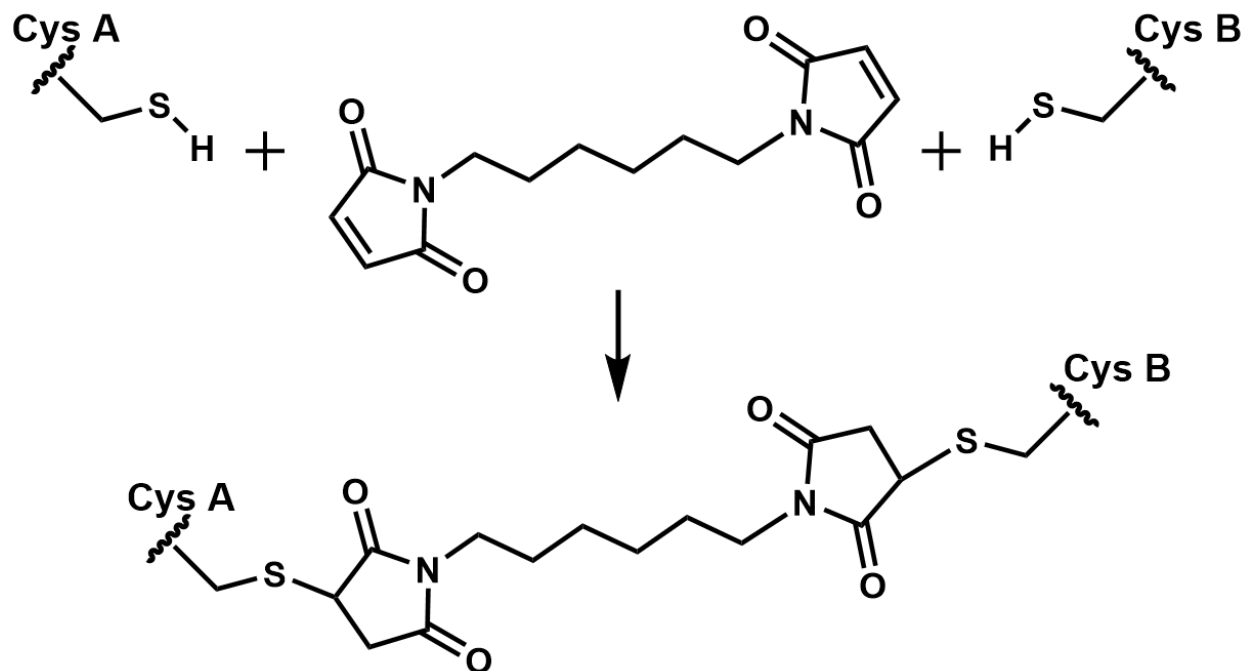
Figure 6.3 – **Bismaleimide crosslinking between two Cysteine residues**

EXPERIMENTAL PROCEDURES

Cloning and site-directed mutagenesis

Two different P450cin and Cdx constructs were used. The first P450cin construct was cloned in the pCWori vector containing an Amp^R gene between the NdeI and XhoI restriction sites as pCWori/P450cin. The second construct contained an additional C-terminal thrombin restriction site followed by a 6X-Histidine tag and was thus pCWori-His/P450cin. The first Cdx construct was cloned into pET22b vector with a C-terminal 6X-Histidine tag. The second construct was cloned into pCWori-His similar to P450cin as pCWori-His/Cdx. All mutations were done using the TaKaRa PrimeSTAR premix DNA polymerase or the Agilent PfuTurbo DNA polymerase kits.

Protein Expression and Purification

For both P450cin constructs, each plasmid was transformed in Escherichia coli BL21(DE3) cells and plated onto LB agar with ampicillin (100 μg/mL). A single colony was used to inoculate each 5 mL of 2xYT starter culture (100 μg/mL kanamycin). The culture was incubated for 16 hours at 37 °C and 220 rpm agitation. Each liter of TB medium (ampicillin 100 μg/mL) was inoculated with 2 mL of 2xYT starter culture. The cells were grown at 37 °C with 220 rpm agitation in a New Brunswick Scientific C25KC incubator until an OD$_{600}$ of 1.2-1.4 was obtained. Cells were then induced with 0.5 mM isopropyl β-D-thiogalactoside and 0.4 mM δ-aminolevulinic acid, and a new dose of ampicillin was added. Post-induction cells were then incubated for 24hrs at 20°C and 80 rpm, after which they were harvested by centrifugation and stored at −80°C. Cells were resuspended in Buffer A (20 mM potassium phosphate, pH 7.4, 1 mM PMSF, 2 mM DTT and 2 mM 1,8-cineole). Cells were lysed by passing through a

microfluidizer at 18k psi (Microfluidics International Co). The soluble fraction was isolated by centrifugation at 17,000 rpm and 4°C for 1hr. The crude extract was then loaded onto a DEAE-sepharose column previously equilibrated with 10 column volumes of buffer A. The column was washed with 10 CV of buffer A, 10 CV of 50 mM KCl in buffer A, and eluted with 300 mM KCl in buffer A. Colored fractions were pooled and dialyzed against 4L of buffer A for 8 hours, and then reloaded on a fresh DEAE-sepharose column previously equilibrated with 10 column volumes of buffer A. The column was washed with 10 CV of 100 mM KCl in buffer A and eluted with a linear gradient of 100-400 mM KCl in buffer A. Colored fractions were pooled and dialyzed against 4L of buffer A for 8 hour. 31% (w/v) of ammonium sulfate was added to the protein sample, which was stirred on ice for 30 mins, and then centrifuged at 12,000 rpm for 30 mins. The soluble fraction was then loaded onto a phenyl sepharose column previously equilibrated with 31% (w/v) $(NH_4)_2SO_4$ in buffer A. The column was then washed stepwise with 30%, 20%, and 10% (w/v) $(NH_4)_2SO_4$ in buffer A, and eluted with 5% (w/v) $(NH_4)_2SO_4$ in buffer A. Fractions with an $R_z(A_{392}/A_{280}) > 1.3$ were pooled and concentrated in a 30,000 molecular weight cut-off Amicon concentrator at 4°C, and then loaded onto a Superdex 75 column (HiLoad 16/60, GE Healthcare) controlled by an FPLC system and pre-equilibrated with buffer B (20 mM potassium phosphate, pH 7.4, 2 mM 1,8-cineole and 5% glycerol). Fractions were pooled according to an $R_z > 1.32$. Sample homogeneity was confirmed by SDS-PAGE.

Crosslinked complex purification

The reaction mixture was filtered using a 0.22 μm filter and loaded on a Ni^{2+}-nitrilotriacetate column pre-equilibrated with 10 column volumes of buffer C (20 mM potassium phosphate, pH 7.4, 2 mM 1,8-cineole, 2 μM FMN, 50 mM KCl and 5% glycerol). The column

was washed with up to 20 mM imidazole and eluted with 40 mM imidazole. The sample was then loaded on a Q-sepharose column previously equilibrated with buffer C. Binding to the column was very strong. The column was washed with up to 200 mM KCl in buffer C and eluted with a linear gradient of 200-500 mM KCl in buffer C. Final sample homogeneity was confirmed by SDS-PAGE.

Crosslinking protocol

Crosslinking reactions were set up with a 5:1 or 10:1 ratio of Cdx:P450cin, which gave similar yields, in 20 mM potassium phosphate buffer, pH 7.4 with 50 mM KCl, 2 μM FMN, 2 mM 1,8-cineole. The reaction was started by the addition of 0.02 - 0.5 mM of bismaleimide crosslinker. The reaction mixture was then placed at 4 °C on a rotator for 13 hours. Reaction yields were measured qualitatively containing the yields of complex were measured qualitatively by SDS-PAGE.

RESULTS AND DISCUSSION

Covalent crosslinking

The first approach for generating surface Cysteine mutants for bismaleimide crosslinking mutants was based on the BD/MD generated model of the complex. Figure 6.4 shows an *in silico* model of the hypothetical complex and the location of the mutations. We started with Cdx Cys135 and P450cin Cys67 (Figure 6.4A). The two cysteines in are 11.9 Å apart, which should be accessible to maleimide crosslinkers of similar or even greater chain length.
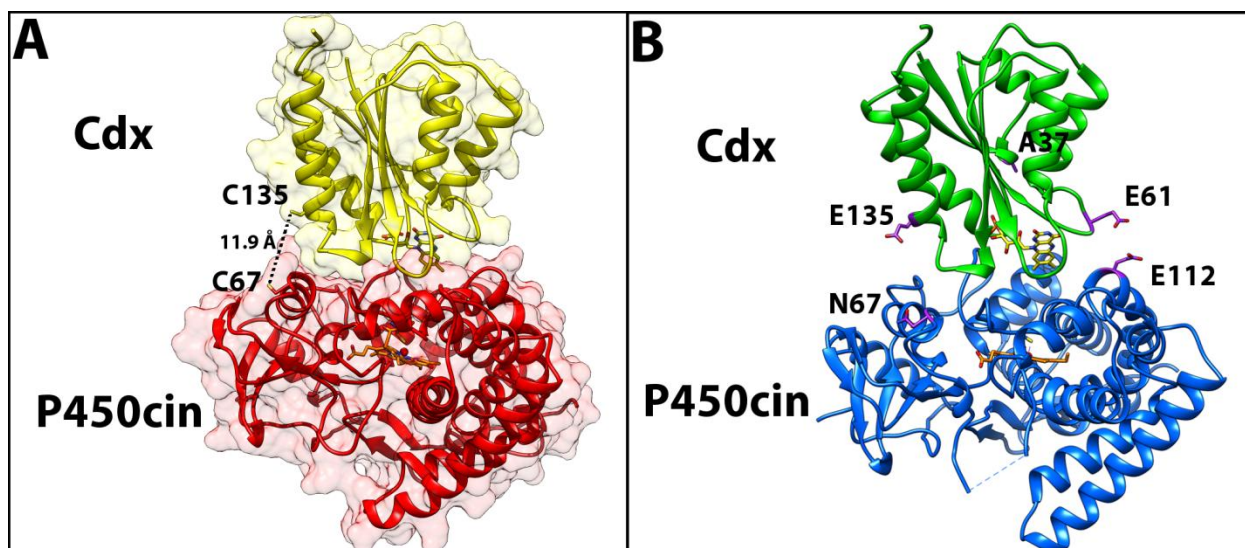
Figure 6.4 – P450cin-Cdx ET complex model
Model is based on BD/MD simulations.[160]

Crosslinking was attempted with four different crosslinkers of different lengths: 8.0 Å, 10.9 Å, 13.0 Å and 17.9 Å, and all of them produced similar yields of complex, including, surprisingly, the 8.0 Å linker (data not shown). The bismaleimdohexane crosslinker (BMH, 13.0 Å) was chosen as optimal based on our model, and gave estimated yields of 45-60% (Figure 6.5A, lane 4). Encouraged by the results, the reaction mixture was purified (see Experimental Procedures section for details) and crystallization attempts were made using a random screening approach and a grid screening approach in a hanging drop vapor diffusion setup at room temperature. Out of over 800 conditions screened, only two hits were obtained (Figure 6.6), both in well solution containing the same precipitant (dibasic ammonium phosphate). Unfortunately, even after extensive attempts at optimization changing drop size, pH, precipitant concentration, free interface diffusion, and seeding, the crystals were never obtained again.
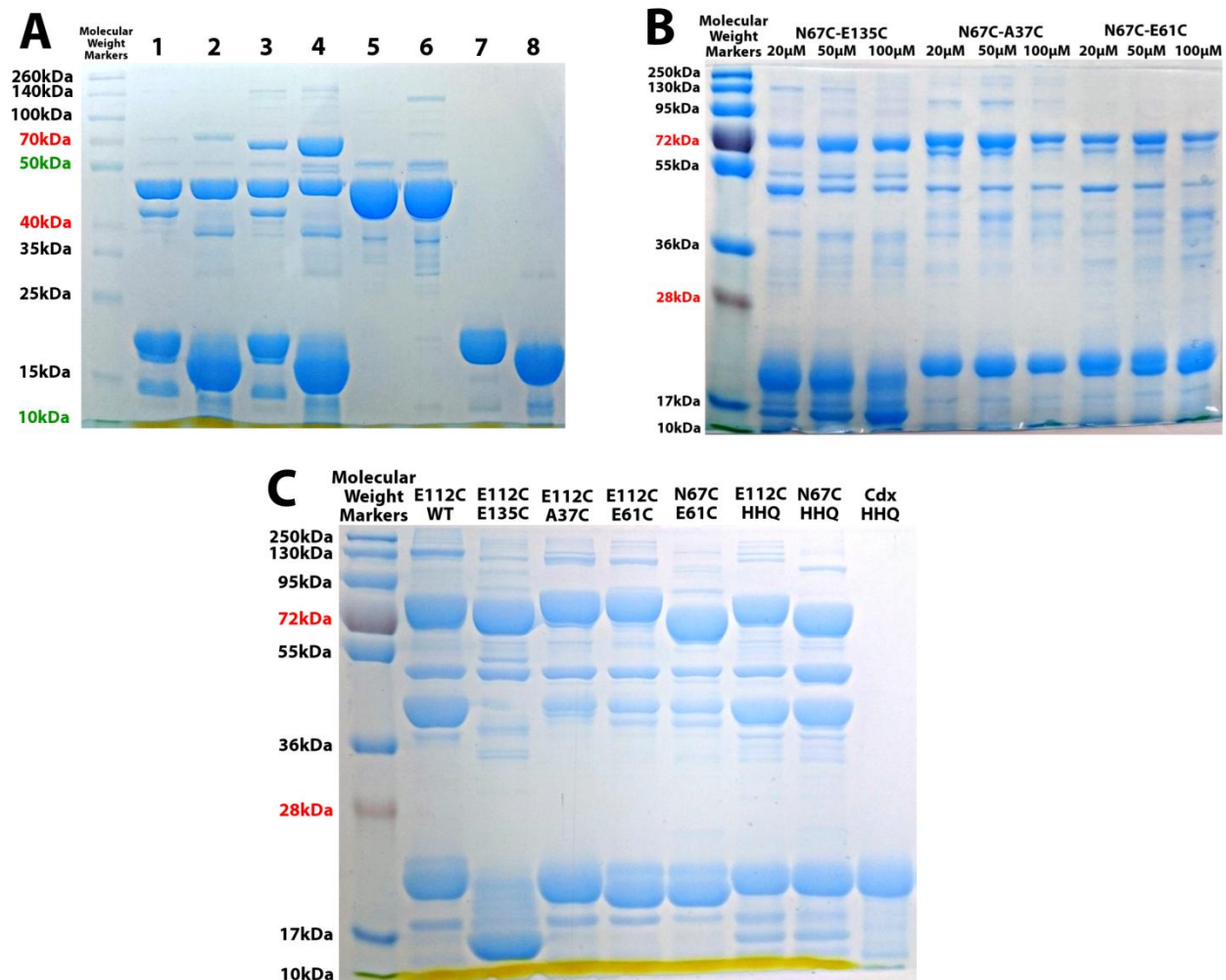
Figure 6.5 – **SDS-PAGE displaying bismaleimide crosslinking results**
(A) Lanes were loaded as follows: 1- Control: P450cin(WT)+Cdx(WT); 2- Control: P450cin(WT)+Cdx(E135C); 3- Control: P450cin(N67C)+Cdx(WT); 4- P450cin(N67C)-Cdx(E135C); 5- P450cin(WT) only; 6-P450cin(N67C) only; 7- Cdx(WT) only; 8-Cdx(E135C) only. (B) Reactions were set up between P450cin(N67C) and three different Cdx mutants, E135C, A37C, and E61C, and with three different concentrations of BMH crosslinker: 20, 50, and 100 μM. (C) Reactions were set up between P450cin(E112C) and three different Cdx mutants, E135C, A37C, and E61C. For brevity, Cdx H34Q/H135Q double mutant is designated as HHQ.
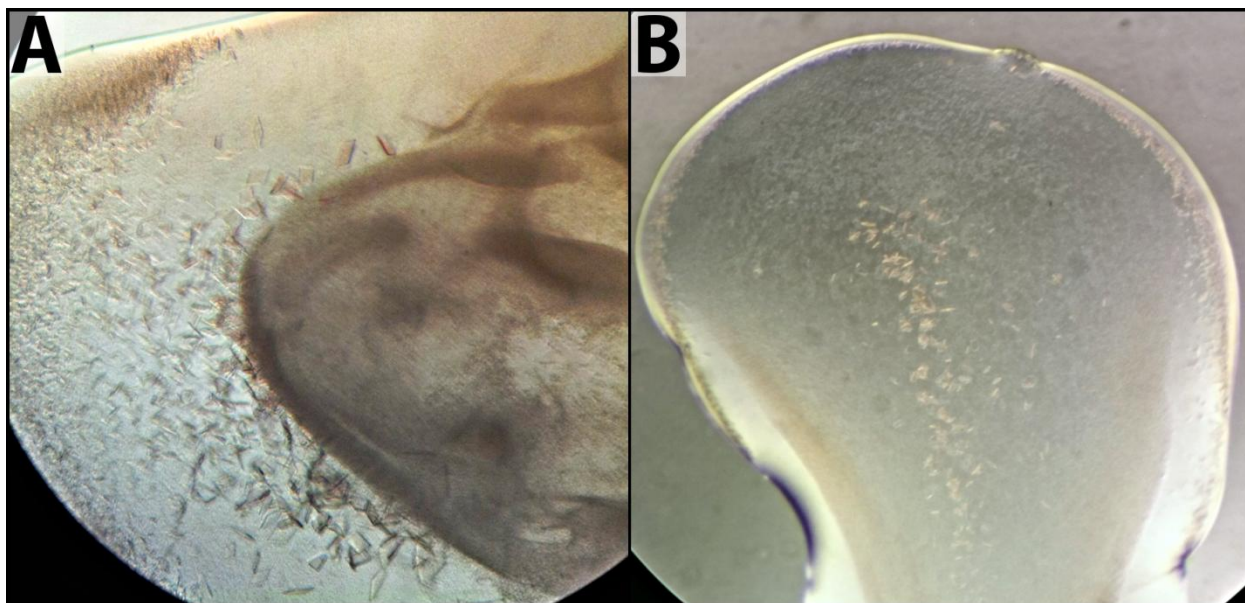
Figure 6.6 – **P450cin(N67C)-Cdx(E135C) crosslinked complex crystal screen hits**
All screens were done in a vapor diffusion setup at room temperature (A) Well solution containing 1.0 M Ammonium phosphate dibasic, 0.1 M Imidazole pH 8.0 and 0.2 M Sodium Chloride. (B) Well solution containing 1.5 M Ammonium phosphate dibasic and 0.1 M Bis-Tris pH 8.5.

The poor crystallization results suggested heterogeneity in the sample, so we next hypothesized that the crosslinking was occuring at two or more sites. We therefore took a different approach to crosslinking that involves generating Cys mutants at different locations on each protein and measuring crosslinking yield. The Cdx A37C, Cdx E61C and P450cin E112C mutants were generated, (see Figure 6.4B for locations) and all of them gave similar yields of complex (Figure 6.5B and C), suggesting non-specific crosslinking. We next set up a crosslinking negative control with P450cin N67C and wild type Cdx, which resulted in a low yield of crosslinked complex (~10%, Figure 6.5A, lane 3). Taken together, our results suggest that another residue on Cdx is the likely source of the crosslink. We extracted each band from a gel, proteolyzed with trypsin and analyzed by liquid chromatography coupled with tandem mass spectrometry (LC-MS/MS) (data not shown). The MS data confirmed that the extracted gel band at ~70 kDa is a mixture of P450cin and Cdx, but all peptide fragments were accounted for, suggesting heterogeneous crosslinking. Tandem MS data was used to sequence our protein

116

fragments, but we were unable to identify a single predicted crosslink. Contrary to the

manufacturer's specifications, we have seen for the P450cam-Pdx complex that BMH can react

with a Histidine amine nitrogen at pH 7.4 (Figure 6.7).[217] We therefore hypothesized that one of

the two Cdx Histidines (His34 or His 125). We turned to site-directed mutagenesis of both His

residues to Gln, but the resulting "HHQ" mutant did not reduce the yield of crosslinked complex

(Figure 6.5C, lanes 7 and 8), suggesting that another residue is involved in the crosslinking. By

process of elimination, the only possible source of crosslink remaining is the C-terminal Cdx

His-tag.
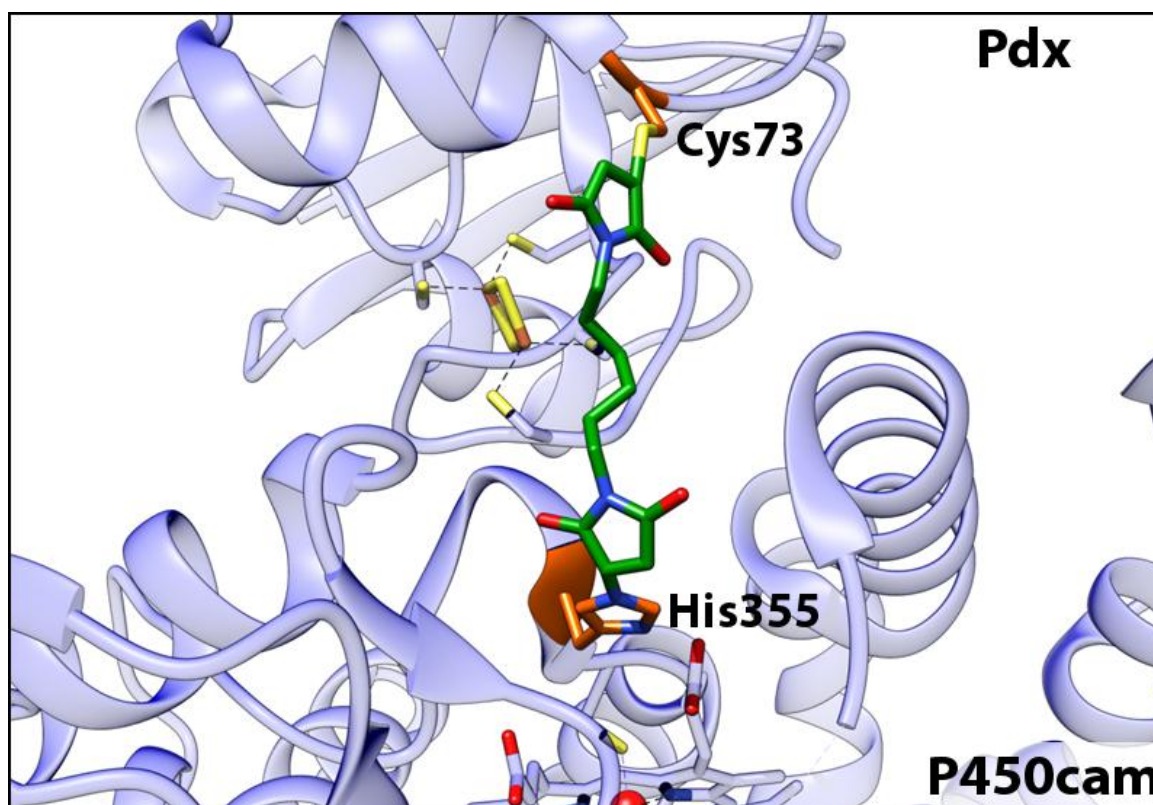
Figure 6.7 – P450cam-Pdx covalent complex with Cys-His crosslink (PDB entry 4JWS)[217]

To address the interference of the uncleavable 6X-His tag, both the Cdx and P450cin

genes were cloned into different constructs (see the experimental procedures section for more

details). The vector used was pCWori with a C-terminal thrombin restriction site that precedes

the 6X-Histidine tag. A cleavable C-terminal 6X-His tag should allow for homogeneous crosslinking and therefore much easier crystallization.

Future Directions

Although a crystal structure of the complex can provide a clear answer as to the potential effector role of Cdx, other biochemical experiments could provide additional clues. We propose three different experiments: the first aims to determine whether the second electron transfer (Step D-E in Figure 1.6) is specific to Cdx by attempting to obtain product turnover using a variety of redox partners from other P450 systems and measuring product formation by gas chromotagrophy coupled to mass spectrometry (GC-MS). Dr. Irina Sevrioukova has provided purified human cytochrome P450 reductase, BM3 reductase, PdR-Pdx, Adrenodoxin reductase-Adrenodoxin and Cytochrome b5 reductase-cytochrome b5, which can all be tested for the ability to transfer the second electron to P450cin.

The second proposed experiment aims to determine if product turnover can occur in the open conformation. The P450cam-Pdx crystal structure had product in 3 of the 4 molecules in the asymmetric unit,[217] indicating that X-ray induced reduction of the heme iron can catalyze product turnover in the open conformation of P450cam. A simple experiment could be done for P450cin in isolation by using crystals of the substrate-free form trapped in the open conformation. These crystals can be soaked in well solution containing substrate, which would make its way to the active site without inducing the large conformational change required to close the active site. These crystals could then be diffracted at the synchrotron that provide the

electrons to see if product formation can occur. Product captured in such an experiment would provide strong corroboration for the importance of the open conformation in the P450cin system.

The third proposed experiment involves testing whether a PCET network is important for P450cin activity. Madrona et al. observed that the P450cin R346A mutant severely reduces enzymatic activity (95% decrease in k_{cat}), and that even a 20-fold increase in enzyme concentration does not restore turnover, indicating that the rate-limiting step has been impaired.[160] Based on these observations, we hypothesize that the mutation did not simply affect complex association/dissociation, but may have affected the PCET event. We propose a double stopped-flow experiment to determine which catalytic step has been affected. The experiment proposed involves 3 drive syringes labeled A-C, containing: (A) Anaerobic P450cin(Fe^{II}) (B) O_2 saturated reaction buffer (C) Anaerobic Cdx (reduced). Driving the solutions contained in A and B into the high-efficiency stopped-flow mixer will form the P450cin-oxy complex, with a high decay rate of 0.08 s^{-1}. Solution C will be then be mixed in rapid succession. We will measure two events, i) Formation of the P450cin-oxy complex (step D in Figure 1.6), evidenced by a red shift from Fe^{II} at 411nm to Fe^{II}-O_2 at 415nm and ii) Relaxation back to the 392nm high-spin state after turnover (step H in Figure 1.6). Altogether, these experiments can provide a solid case for the potential role of Cdx, and hopefully allow us to see if this system is analogous to P450cam.

Conclusions

Even though we have been unsuccessful at obtaining a crystal structure of the P450cin-Cdx complex, we have still established a powerful protocol for determining the likely docking site of an unknown complex. By using site-specific crosslinking combined with a random mutagenesis approach, one can observe the yields of complex and determine the most likely docking site and orientation. This method, combined with trypsinolysis and a mass spectrometry technique such as MALDI-TOF or even LC-MS-MS can elucidate the fragments involved in the crosslinking, thus shedding light on how the two proteins associate. We believe that obtaining a crystal structure of a covalent complex can be achieved in the near future using this technique, as long as crosslinking heterogeneity can be eliminated.

COMMUNICATION BETWEEN THE ZINC AND TETRAHYDROBIOPTERIN BINDING SITES IN NITRIC OXIDE SYNTHASE

Chapter 7

Summary

We begin our analysis of NOS structure by using pterin analogues (ones that mimic the H_4B cofactor structurally) to take a closer look at the NOS dimer and H_4B binding site. Pterin analogues have proven useful in probing the function of H_4B in the past, and can potentially serve as NOS inhibitors and activators. This is useful because, as seen in the NOS introductory chapter, under or over-production of NO can be quite harmful, and NOS activity must therefore be well regulated. An adequate supply of H_4B in cells is therefore crucial to maintain a balanced availability of NO in cells. We have determined the crystal structures of the bovine endothelial NOS dimer oxygenase domain bound to three different pterin analogues, which reveal an intimate structural communication between the H_4B and Zn^{2+} sites that was previously unknown. The binding of one of these compounds, 6-acetyl-2-amino-7,7-dimethyl-7,8-dihydro-4(3H)-pteridinone (**1**), to the pterin site reveals that binding of Zn^{2+} and of **1** are mutually exclusive. Analogue **1** both directly and indirectly disrupts hydrogen bonding between key residues in the Zn^{2+} binding motif, resulting in destabilization of the dimer and in the complete disruption of the Zn^{2+} site. Addition of excess Zn^{2+} stabilizes the Zn^{2+} site at the expense of weakened binding of **1**. The unique structural features of **1** that disrupt the dimer interface are extra methyl groups that extend into the dimer interface and force a slight opening of the dimer, thus resulting in the

disruption of the Zn^{2+} site. The work described in this chapter illustrates a very delicate balance of forces and structure at the dimer interface that must be maintained to properly form the Zn^{2+}, pterin, and substrate binding sites in NOS.

INTRODUCTION

As we have discussed in Chapter 1, mammalian NOSs require the cofactor H_4B[59] to convert L-arginine to L-citrulline and NO.[79, 220] Each of the three NOS isoforms[56] is active only as a homodimer because the pterin binding site is located right at the dimer interface and monomeric NOS does not bind H_4B or the substrate.[60] The dimer interface is formed between two N-terminal heme binding domains and is further stabilized by the coordination of a Zn^{2+} ion ligated to two cysteine thiols from each subunit (ZnS_4) (Figure 7.1).[61-62] All NOS isoforms share a strikingly similar pterin binding pocket with comparable H_4B binding affinities, and cofactor and substrate binding events have been shown to synergistically stabilize the NOS dimer.[221-223] Low-temperature sodium dodecyl sulfate−polyacrylamide gel electrophoresis (SDS−PAGE) and urea dissociation studies indicate that the relative dimer strengths of the three mammalian NOS isoforms decrease in order from eNOS to nNOS to iNOS and that the role of H_4B in dimer stability is less critical in eNOS.[224-225] The structural basis for this disparity, however, is not yet fully understood.
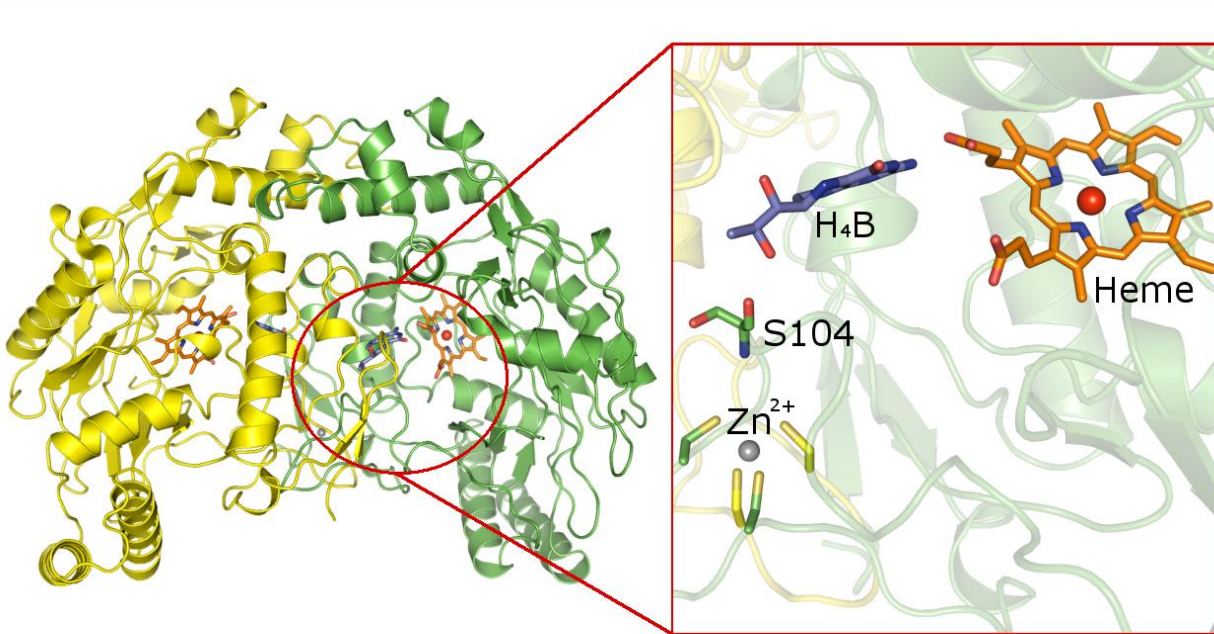
Figure 7.1 – Structure of bovine eNOS dimer in complex with H$_4$B (PDB entry 9NSE)
The Zn^{2+} binding site is located at the dimer interface and ~15 Å from the center of the pterin binding pocket in both molecules A and B of the dimer. Chain A is depiced in green, Chain B is in yellow, pterin in blue, and heme in orange. All molecular graphics shown in the chapter were prepared using PyMOL.[170]

One way of exploring the relationship between dimer stability and H$_4$B binding is to investigate the pterin binding pocket using various pterin analogues. Moreover, inactive pterin analogues could potentially serve as NOS inhibitors[221, 226-228] and have proven to be useful in probing the function of H$_4$B.[229-232] In this study, we have determined the crystal structures of three novel pterin compounds (Figure 7.2) analogous to H$_4$B bound to eNOS, which has unexpectedly provided important insights into the intimate connection among the Zn^{2+}, pterin, and substrate binding sites.
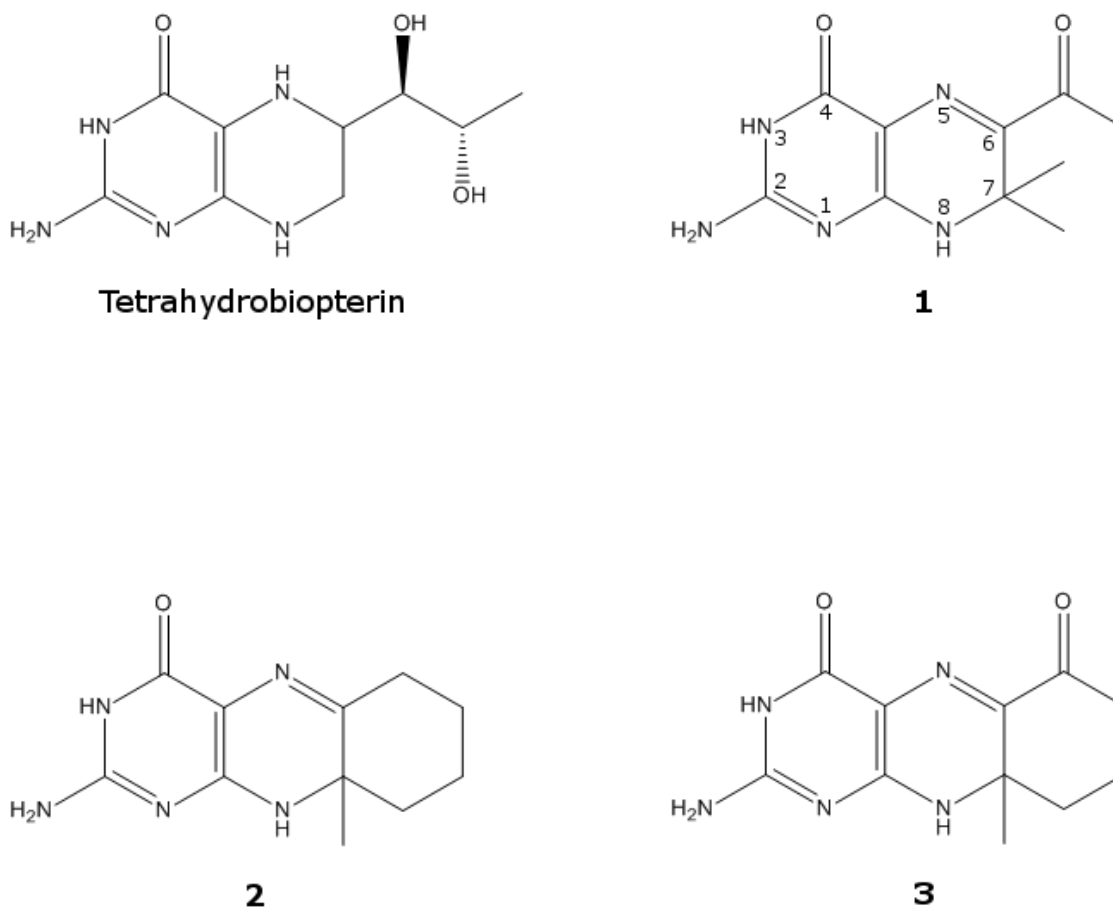
Figure 7.2 – Chemical structures of the pterin compounds.
Compounds **1**, **2** and **3** were designed and synthesized to be the dihydro analogues of NOS cofactor H_4B.

EXPERIMENTAL PROCEDURES

Protein Expression and Purification.

The bovine holo eNOS pCWori construct containing an Amp^R gene and an N-terminal six-His tag was expressed in *Escherichia coli* BL21-(DE3) cells already containing the calmodulin plasmid (with a Chl^R gene), and the cells were then plated on LB agar with ampicillin (100 µg/mL) and chloramphenicol (35 µg/mL). *E. coli* cells inherently lack the

machinery to synthesize H_4B, ensuring that eNOS would remain free of H_4B. A single colony was used to inoculate each 5 mL of LB starter culture (100 μg/mL ampicillin and 35 μg/mL chloramphenicol). The culture was incubated for 8 h at 37 °C with 220 rpm agitation. Each liter of TB medium (100 μg/mL ampicillin and 35 μg/mL chloramphenicol) was inoculated with 2 mL of LB starter culture. The cells were grown at 37 °C with agitation at 220 rpm until the OD_{600} reached 1.0−1.2. Protein expression was then induced by adding 0.5 mM isopropyl β-D-thiogalactoside and 0.4 mM δ-aminolevulinic acid. New doses of ampicillin and chloramphenicol were also added, and cell growth resumed at 25 °C and 100 rpm for 24 h. The cells were then harvested by centrifugation and stored at −80 °C. Cells were thawed and resuspended by being stirred for 3 h at 4 °C in buffer A [50 mM sodium phosphate (pH 7.8), 10% glycerol, 0.5 mM L-Arg, 5 mM β-mercaptoethanol, 0.1 mM phenylmethanesulfonyl fluoride (PMSF), and 200 mM NaCl]. The following protease inhibitors were also added to buffer A before lysis: trypsin inhibitor (5 μg/mL), pepstatin A (1 μg/mL), and leupeptin (1 μg/mL). Cells were lysed by being passed through a microfluidizer at 18K psi (Microfluidics International Co.). The soluble fraction was isolated by centrifugation at 17,000 rpm and 4 °C for 1 h. The crude extract was then loaded onto a Ni^{2+}-nitrilotriacetate column pre-equilibrated with 10 column volumes of buffer A. After being loaded with the crude extract, the column was washed with 10 column volumes of 10 mM imidazole in buffer A before being eluted with a 10 to 200 mM imidazole linear gradient in buffer A. Colored fractions were pooled and loaded onto a 2′,5′-ADP Sepharose column preequilibrated with buffer B [50 mM Tris-HCl (pH 7.8), 10% glycerol, 5 mM β-mercaptoethanol, 0.1 mM PMSF, 0.5 mM L-Arg, and 200 mM NaCl]. The column was then washed with 10 column volumes of buffer B and eluted with 10 mM $NADP^+$ in buffer B. Colored fractions were pooled and concentrated in a 30,000 molecular weight cutoff

(MWCO) Amicon concentrator at 4 °C. The eNOS heme domain used for crystallization was generated by limited trypsinolysis: a 20:1 eNOS:trypsin weight ratio was used for a 1 h incubation at 25 °C. The digested sample was then loaded onto a Superdex 200 column (HiLoad 26/60, GE Healthcare) controlled by an FPLC system and preequilibrated with buffer B to separate the heme domain and flavin-containing fragment generated by the trypsin digest. Fractions were pooled according to an A_{280}/A_{395} spectral ratio of <1.7, and sample homogeneity was determined by SDS−PAGE.

Synthesis of H₂B Analogues.

The preparation of pterin compounds 6-acetyl-2-amino-7,7-dimethyl-7,8-dihydro-4(3H)-pteridinone (**1** in Figure 7.2), 2-amino-9a-methyl-6,7,8,9,9a,10-hexahydrobenzo[g]pteridin-4(3H)-one (**2**), and 2-amino-9amethyl-8,9,9a,10-tetrahydrobenzo[g]pteridine-4,6(3H,7H)-dione (**3**) used in this study has been previously described.[233-234]

Crystal Preparation.

All eNOS heme domain samples were prepared for crystallization by being concentrated to 12 mg/mL in buffer B using a 30,000 MWCO Amicon concentrator. Cocrystallization was conducted by combining protein with 5 mM cofactor and 5 mM L-arginine. Crystals were grown at 4 °C in 18−20% PEG 3,350 (w/v), 250 mM magnesium acetate, 100 mM cacodylate pH 6.25, and 5 mM tris(2-carboxyethyl)-phosphine (TCEP) in a sitting-drop vapor diffusion setup. Freshly grown crystals were passed stepwise through a cryoprotectant solution containing 20% PEG 3350, 10% (v/v) glycerol, 10% (w/v) trehalose, 5% (w/v) sucrose, 5% (w/v) mannitol, 10

mM cofactor, and 5−10 mM L-Arg for 4−6 h at 4 °C before being flash-cooled with liquid nitrogen.

X-ray Diffraction Data Collection, Processing, and Structure Refinement.

Cryogenic (100 K) X-ray diffraction data were collected remotely at the SSRL using the data collection control software Blu-Ice[103] and a crystal mounting robot. An ADSC Q315r CCD detector at beamline 7-1 or a Mar325 CCD detector at beamline 9-2 was used for data collection. Raw data frames were indexed, integrated, and scaled using HKL2000.[235] The binding of H_4B analogues was detected by the initial difference Fourier maps calculated with REFMAC.[129, 168] The pterin molecules were then modeled in COOT[108] and refined using REFMAC. Water molecules were added in REFMAC and checked by COOT. The TLS[169] protocol was implemented in the final stage of refinements with each subunit as one TLS group. The refined structures were validated in COOT before being deposited in the Protein Data Bank. The crystallographic data collection and structure refinement statistics are listed in Table 7.1 with Protein Data Bank (PDB) entry codes included.

data set	1	2	3	1 (+50µM Zinc Acetate)
PDB code	4CUL	4CUM	4CUN	4CVG
radiation source	SSRL BL 7-1	SSRL BL 7-1	SSRL BL 7-1	SSRL BL 9-2
space group	$P2_12_12_1$	$P2_12_12_1$	$P2_12_12_1$	$P2_12_12_1$
unit cell dimensions a, b, c (Å)	57.09, 105.47, 158.25	58.01, 106.49, 156.48	58.87, 106.18, 156.74	57.41, 105.96, 156.53
data resolution (Å) (highest shell)	50.0 - 2.23 (2.31 - 2.23)	88.04 - 2.33 (2.41 - 2.33)	87.9 - 2.48 (2.57 - 2.48)	50.0 - 2.31 (2.39 - 2.31)
X-ray wavelength (Å)	1.13	1.13	1.13	0.98
total observations	208127	184003	140206	164961
unique reflections (highest shell)	47234 (4613)	42159 (4091)	35505 (3482)	42009 (3784)
completeness (%) (highest shell)	99.77 (98.99)	99.53 (97.87)	99.47 (99.63)	97.91 (90.01)
R_{merge} (highest shell)	0.088 (0.884)	0.085 (0.862)	0.078 (0.689)	0.060 (0.690)
I/σ (highest shell)	19.86 (2.01)	22.03 (2.13)	22.85 (2.01)	24.04 (2.07)
redundancy (highest shell)	4.4 (4.4)	4.4 (4.4)	3.9 (3.8)	4.0 (3.9)
B factor, Wilson plot (Å^2)	38.83	44.96	56.81	43.54
no. of protein atoms	6141	6446	6446	6400
no. of heteroatoms	158	169	173	131
no. of waters	279	214	51	231
disordered residues	40-66, 91-120 (A) 40-68, 91-120 (B)	40-66, 110-120 (A) 40-68, 112-120 (B)	40-66, 110-120 (A) 40-68, 112-120 (B)	40-66, 108-120 (A) 40-68, 109-120 (B)
R_{work}/R_{free}	0.165/0.209	0.170/0.227	0.184/0.242	0.155/0.214
rmsd bond length (Å)	0.012	0.017	0.017	0.017
rmsd bond angle (°)	1.47	1.69	1.97	1.83

Table 7.1 – Crystallographic Data and Refinement Statistics

RESULTS AND DISCUSSION

Structural Characterization of the H4B Binding Pocket

As shown in Figure 7.2, the three dihydropterin analogues retain the ring structure of H_4B and introduce variations only in the side chain. Figure 3 shows the electron density of the three dihydropterin analogues bound to eNOS. Analogue **1** (Figure 7.3A) exhibits the strongest and

most well defined electron density. As expected from its structural similarity to H_4B, analogue **1** fits into the pterin binding pocket quite well, maintaining most of the interactions found with H_4B: the π−π stacking with W449, the H-bonds from its 2-aminopyrimidine nitrogens to the heme propionate A, the H-bond from O4 to R367, and the van der Waals contacts with aromatic residues of the other subunits (W76 and F462).

Therefore, it is not surprising that the tetrahydro form of **1** can support the conversion of L-arginine to NO in nNOS.[236] From kinetic studies, the estimated K_D for **1** is 115 μM compared to a value of 1.1 μM for H_4B.[236] However, the two additional H-bonds from the dihydroxypropyl side chain of H_4B to the carbonyls of S104 and F462 are lost in **1**. Unique to **1** is the close contact from one of its methyl groups at the C7 position to the W447 side chain of the other subunit. Both **2** and **3** in the dihydro oxidation state introduce a third cyclohexane ring to replace the H_4B side chain. Although the third ring is tolerated by the pterin binding pocket, the extra methyl group at C7 may generate steric clashes with the protein. As a result, **2** (Figure 7.3B) and **3** (Figure 7.3C) exhibit weaker electron density. Crystals of the eNOS−**3** complex diffract poorly, which we have found correlates well with poor ligand binding. Because **3** is structurally similar to **2** and differs only in the carbonyl O atom on the cyclohexane ring, the additional steric crowding of this oxygen in **3** very likely accounts for why this pterin analogue binds more poorly. Overall, the inability of the three pterin analogues to form hydrogen bonds with S104 and F462 and the steric clashes from their protruding methyl groups may be attributed to a binding affinity that is poorer than that of the native pterin, H_4B.
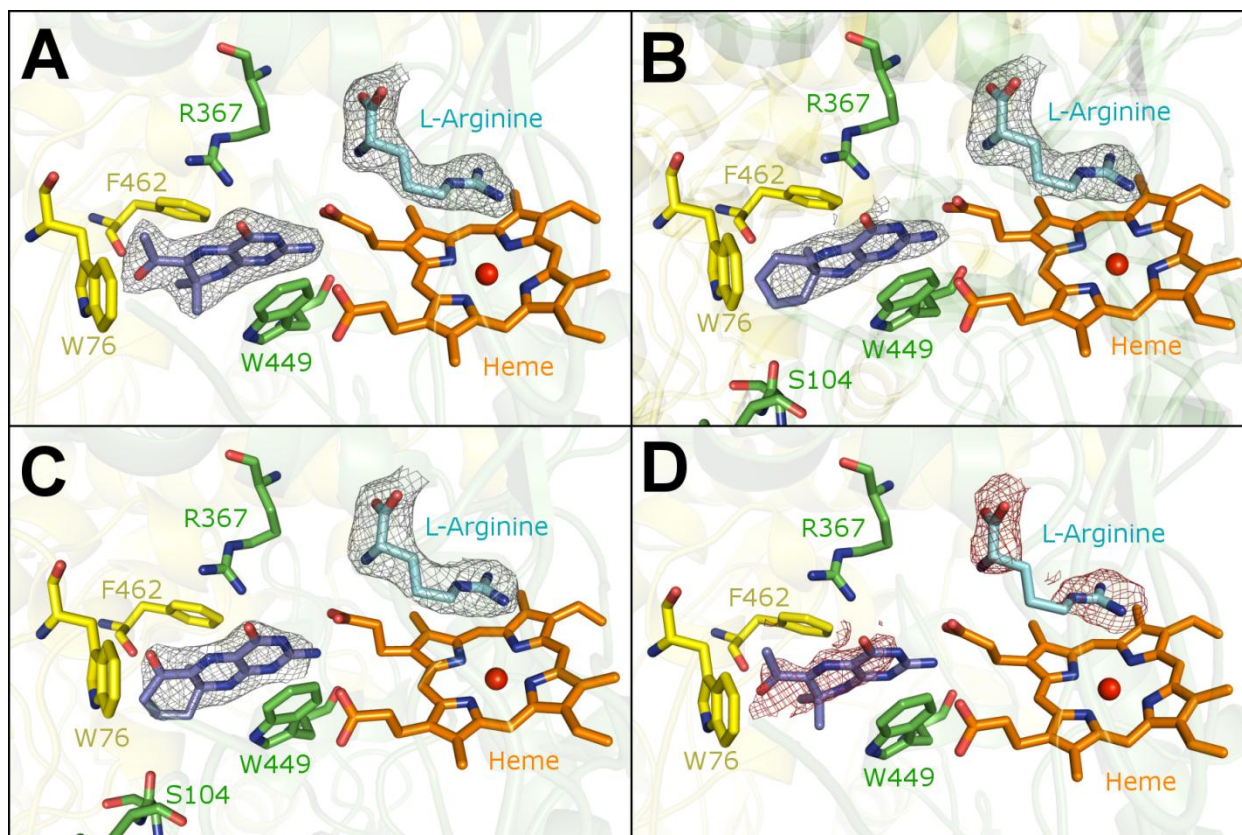
Figure 7.3 – Bovine eNOS active site in complex with each pterin analogue
(A) eNOS in complex with analogue **1** with the $2F_o - F_c$ electron density map contoured at 1.0 σ. The strong density supports binding to the pterin site even though the compound lacks the ability to form a hydrogen bond with Ser104 of Chain A. (B and C) eNOS in complex with **2** and **3**, respectively, with the $2F_o - F_c$ density map contoured at 1.0 σ. The density for **2** is not as strong as that for analogue **1** but supports binding of **2** with the extra methyl facing F462, while the density for **3** is weaker than that for **1** or **2**, yet strong enough to support binding of **3** in the shown orientation. (D) eNOS in complex with analogue 1 as shown in panel A but overlaid with the $2F_o - F_c$ density map calculated using the data collected with a crystal supplemented with 50 μM zinc acetate during the cryoprotectant soaks. The poorly defined pterin and substrate density at best supports partial occupancy. The color scheme is as follows: Chain A is depicted in green, Chain B in yellow, pterin in blue, L-Arginine in cyan and heme in orange.

Disruption of the Zn^{2+} Binding Site

As shown in Figure 7.4, a single Zn^{2+} ion is situated at the dimer interface where it is tetrahedrally coordinated by symmetry-related Cys residues along the dimer axis. The Zn^{2+} is ~15 Å from the center of the pterin binding pocket in both subunits A and B of the dimer. Quite unexpectedly, we found that the binding of **1** completely disrupts the Zn^{2+} binding region, as evidenced by a total lack of electron density for residues 91−109 and the Zn^{2+} (Figure 7.4A). It has been known for some time that both Zn^{2+} and H_4B contribute to dimer stability,[61, 237-238] but

this is the first indication that there is a relatively long-range communication between these two sites. To probe whether the binding of **1** and the binding of Zn^{2+} are mutually exclusive, we soaked crystals of the eNOS−**1** complex in a cryoprotectant solution supplemented with 50 μM Zn acetate. The crystal structure shows that Zn^{2+} binding is restored (Figure 7.4D), while the electron density for **1** and the substrate, L-Arg, are poorly defined (Figure 7.3D). We next soaked crystals at a more moderate Zn acetate concentration of 20 μM. In this case, **1** and L-Arg bind well but the Zn^{2+} site is disordered (data not shown). In contrast, binding of **2** and binding of **3** do not interfere with Zn^{2+} binding (Figure 7.4B,C). The interdependence of pterin and L-Arg binding is well-known and is very likely mediated by the fact H_4B H-bonds to the same heme propionate as the α-amino group of L-Arg (Figure 7.3).[221-223]
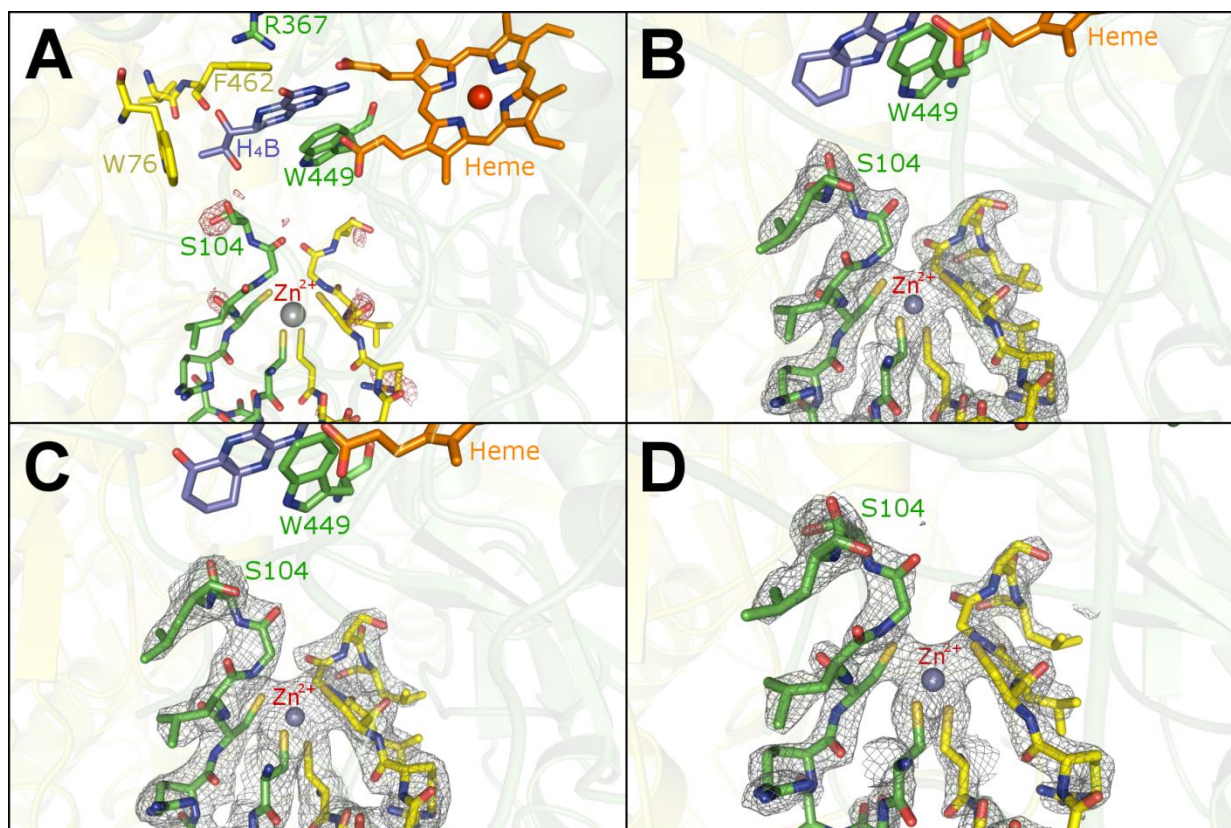
Figure 7.4 – Bovine eNOS-analogue complexes superposed with reference structures

(A) $2F_o$ - F_c electron density map contoured at 1.0 σ of the eNOS-1 complex overlaid on a reference bovine eNOS structure (PDB entry 9NSE) with H_4B bound and an ordered Zn^{2+} site. This is to illustrate the disordered Zn^{2+} site resulting from binding of **1** to the pterin pocket. The lack of electron density spans residues 91-109 in chain A and 91-111 in chain B. (B and C) Zn^{2+} binding site of bovine eNOS in complex with **2** and **3**, respectively. The $2F_o$ - F_c electron density map (1.0 σ) derived from the same eNOS-**1** structure showing poor pterin and substrate density in Fig. 3D. The crystal was soaked in a cryoprotectant solution supplemented with 50 μM zinc acetate. The Zn^{2+} site is fully ordered, while **1** is disordered in the structure.

How Does the Pterin Site Communicate with the Zn^{2+} Site?

These results clearly show that there is a strong long-range communication between the Zn^{2+}, pterin, and substrate binding sites. To explain why, we next conducted a detailed comparison between the eNOS−**1** complex with a disordered Zn^{2+} and the fully ordered eNOS structure with H_4B bound. By superposition of the α-carbon backbone of chains A (Figure 7.5B), we see that chain B has shifted away by a significant distance. For comparison, we next superposed H_4B-bound to H_4B-free eNOS structures (Figure 7.5A) and did the same for bound structures of **2** (Figure 7.5C) and **3** (Figure 7.5D).
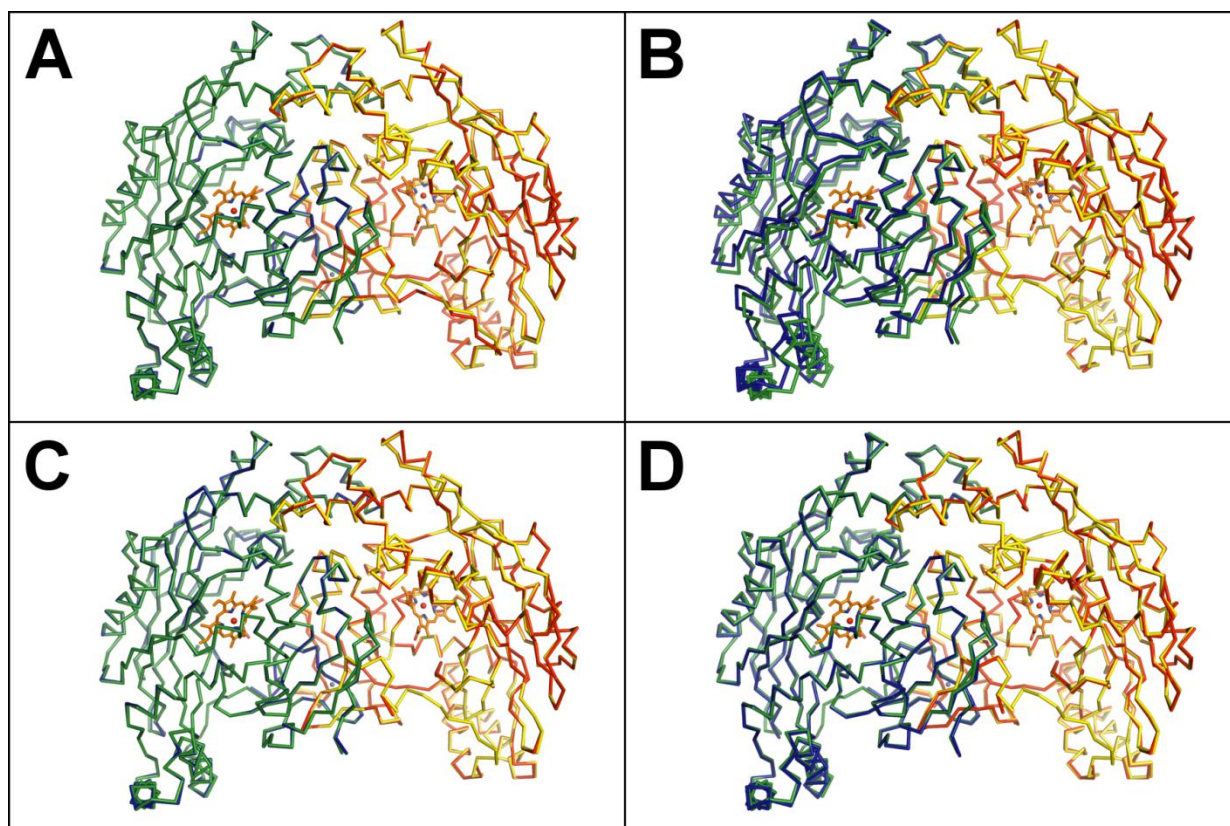
Figure 7.5 – Overall bovine eNOS structure and superpositions

(A) Superposition of the α-carbon backbone of an h4B free (PDB entry 5NSE) on an H4B-bound (PDB entry 9NSE) eNOS heme domain structure. For all four panels, the superposition was conducted in Coot only on chain A of both structures to observe the relative deviation in chain B. (B-D) superposition of an H4B-bound eNOS heme domain (PDB entry 9NSE) with a compound **1**, **2**, and **3** bound structure, respectively. The color scheme is as follows: H4B-bound structure chain A is depicted in yellow and chain B in green. H4B-Free structure, Chain A is depicted in red and chain B in blue.

In these cases, chain B does not move significantly relative to chain A. For the sake of consistency, we superposed the α-carbon backbone of chain B and observed a similar shift in chain A. To further quantify the observation, we calculated the root-mean square deviations (rmsds) of chains A and B for residues 121−482 in each pair of structures. For the eNOS−**1** complex superposed on the basis of only chain A with an H_4B-bound eNOS reference structure (PDB entry 9NSE), the rmsd of chain B is 1.23 Å, compared to the values of 0.27−0.44 Å calculated with the same method against the same reference structure for either an H_4B-free structure or other pterin analogue structures that do not disrupt the Zn^{2+} site (Table 7.2).

134

Structure	PDB code	RMS Deviation (Å)	
		Chain A	Chain B
H4B-free	5NSE	0.165	0.357
Compound 1	4CUL	0.25	1.227
Compound 2	4CUM	0.22	0.27
Compound 3	4CUN	0.309	0.418
Compound 1 (with 50µM Zn Acetate)	4CVG	0.218	0.446

Table 7.2 – Calculation of RMS deviations of α-Carbons
Chain A of each structure was superposed with chain A of H4B-bound eNOS (PDB entry 9NSE) and all RMSDs were calculated using LSQMAN (http://xray.bmc.uu.se/usf/)

A close examination of the eNOS−**1** structure reveals that chain B moves away from chain A because of the methyl groups on C7 of **1** (Figure 7.6B). Accommodating these methyl substituents forces W447 of chain B to shift away from chain A. The shift of W447 is not merely absorbed locally, but instead induces a global change in the entire chain B as a rigid body. The repulsion between the methyl group of **1** and W447 occurs in a symmetrical manner in both subunits, resulting in the slight opening of the dimer interface. The widened dimer interface causes disruption of key backbone contacts between the Cys bearing Zn^{2+} binding hairpin fragment (residues 95−102) that includes contacts between C101 and N468 (Figure 7.6B). Loss of those key interactions leads to the total disordering of the Zn^{2+} binding site. Comparatively, the H_4B-free eNOS structure (Figure 7.6A) and those in complexes with **2** (Figure 7.6C) and **3** (Figure 7.6D) show practically no shift of W447. The extra methyl group in **2** and **3** is not directly pointing to W477, causing no disruption of the dimer interface. In the same way, we also compared the H_4B-bound eNOS structure to the structure of the eNOS−**1** complex supplemented with 50 μM Zn^{2+} giving a restored Zn^{2+} site, and the resulting superposition shows a tighter dimer (Figure 7.7A) and a restored W447 position (Figure 7.7B) at the expense of weakened binding of **1** (Figure 7.3D). It also should be noted that residues directly contacting H_4B, W447, W449, and F462, are conserved in both nNOS and eNOS.
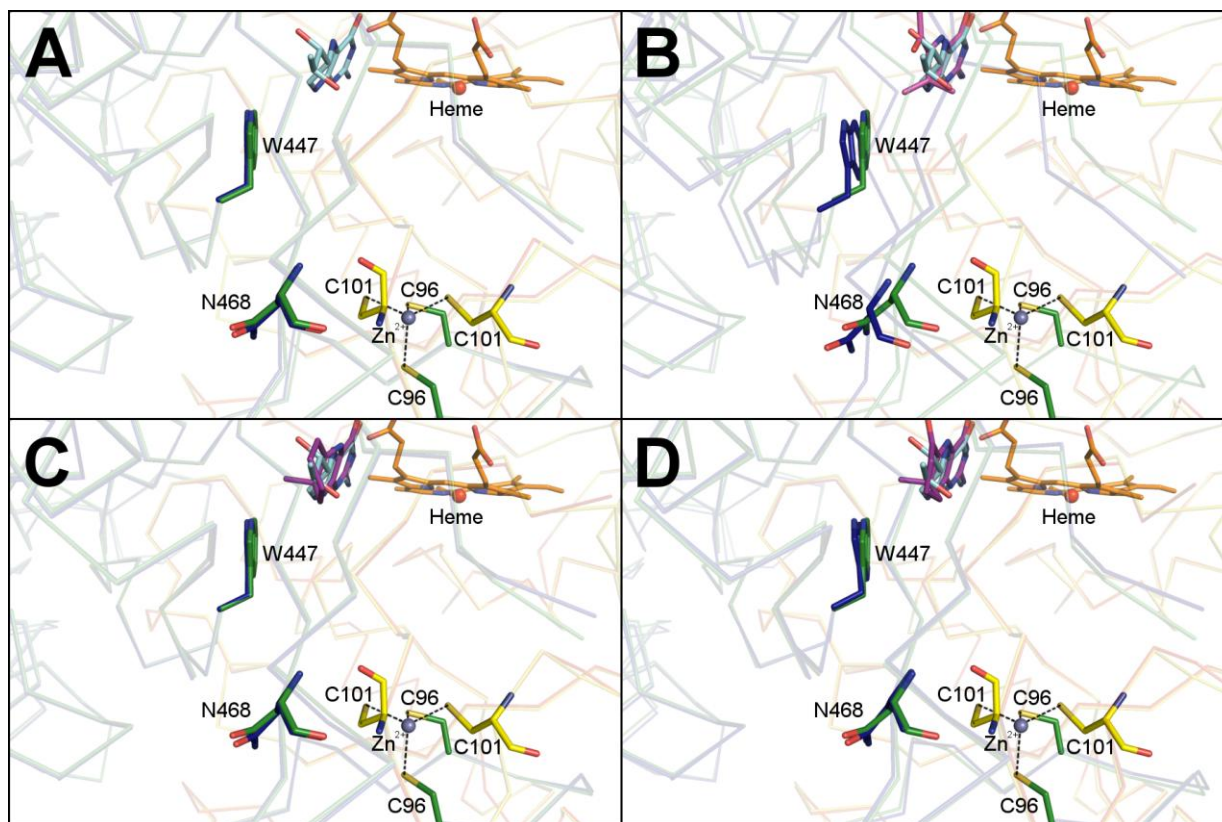
Figure 7.6 – Close-up views based on the same superpositions shown in Figure 7.5
This was done in order to observe the relative structural deviation of W447 of chain B for each pair of structures. (A) eNOS with or without H_4B bound, (B) H_4B vs analogue **1**, (C) H4B vs analogue **2**, and (D) H4B vs analogue **3**. The color scheme is as follows: For the H4B-bound structure, chain A is depicted in yellow, chain B in green. For the H4B-free or pterin analogue-bound structures, chain A is depicted in red and chain B in blue. H4B is cyan, analogue in purple, and heme in orange.
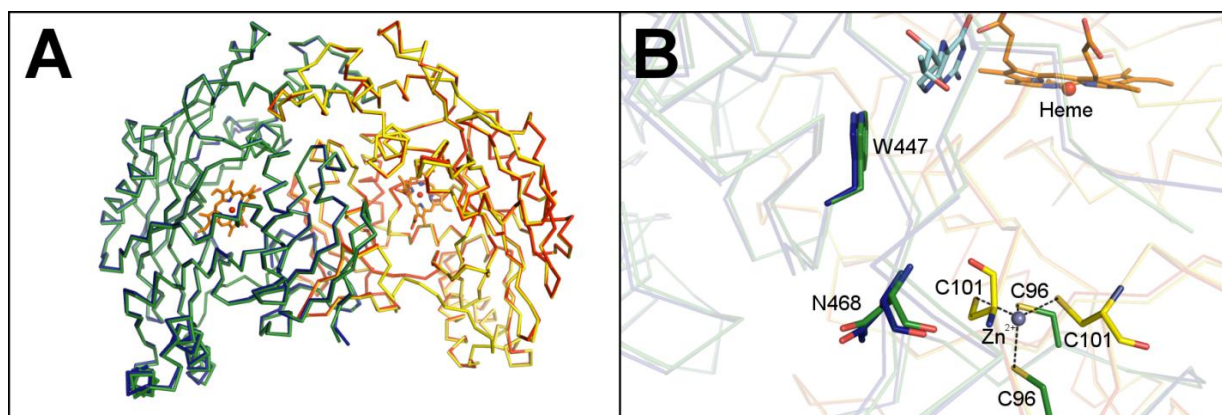
Figure 7.7 – Overall structure and close-up views based on superpositions of zinc supplemented crystal
(A) Superposition of the α-carbon backbone of eNOS heme domains with compound **1** bound, supplemented with 50 μM zinc acetate in a cryosoak, on an H_4B-bound structure (PDB entry 9NSE). The superposition was done only on chain A of both structures to observe the relative deviation in chain B. (B) Close-up view of the Zn^{2+} binding and active sites based on the superposition in panel A for the observation of the relative structural deviation of W447 in chain B. The color scheme for both panels is as follows. For the H_4B-bound form, chain A is depicted in yellow and chain B in green. For the pterin analogue-bound form, chain A is depicted in red and chain B in blue. H_4B is in cyan, the pterin analogue in purple, and the heme in orange.

136

What Does This Communication Reveal about the NOS Dimer?

These results reveal that the eNOS dimer is able to loosen up and expand to accommodate **1**. The side effect is that all hydrogen bonding interactions that stabilize the Zn^{2+} binding site, mainly the two between N468 and C101, are weakened or lost, as shown in Figure 6. This effect being compounded on both chains causes a complete disruption of Zn^{2+} binding and destabilization of the dimer. Previous studies have shown that eNOS has the most stable dimer compared to nNOS and iNOS.[224] To obtain NOS−pterin complexes, it is necessary to purify NOS in the absence of H_4B and only eNOS, not nNOS, is stable enough without H_4B during purification and the proteolysis required to generate the heme domain for crystallization. Two attempts were made to purify nNOS with pterin-free buffer or the buffer supplemented with **1**, but the protein denatured completely upon trypsinolysis required for generating the heme domain. This very likely reflects the fact that the eNOS dimer is more stable than nNOS: it can survive purification without H4B bound and can bind **1** without disruption of the dimer. This also suggests that the combination of intersubunit contacts attributed to the greater dimer strength of eNOS allows it to survive disruption of the Zn^{2+} site without complete disruption of the dimer.

Conclusions

Even though the importance of H_4B in stabilizing the NOS dimer has been known for some time, this study provides the structural basis for the intimate structural communication among H_4B, Zn^{2+}, substrate binding, and dimer stability. It is important to note that zinc-free NOS retains near full catalytic activity, although the dimer is substantially less stable.[238] A number of biochemical studies[237, 239-242] have shown that the main role of the zinc site is to promote H_4B binding, which in turn increases the affinity for the substrate, L-Arg. The study presented here provides a structural basis for this interdependence.

We were fortunate that the additional stability of the eNOS dimer allowed us to probe perturbations at the dimer interface without totally disrupting the dimer, which would

preclude any detailed crystallographic analysis as in the case of nNOS. It is remarkable that the mere addition of the methyl groups in **1** can have such a dramatic effect on the Zn^{2+} site. This underscores the exquisite fine-tuning of interactions that stabilize the NOS dimer and the close interdependence of the Zn^{2+}, pterin, and substrate binding sites.

CHIRAL LINKERS TO IMPROVE SELECTIVITY OF DOUBLE-HEADED NEURONAL NITRIC OXIDE SYNTHASE INHIBITORS

Chapter 8

Summary

We shift gears and dive into the first of five chapters that describes NOS inhibitor design to find alternate therapies to treat neurodegenerative diseases. As we have discussed in section 1.4, overexpression of neuronal NOS has been implicated in many neurodegenerative diseases, which means that a better control of nNOS expression is highly desirable. Dr. Qing Jing and our collaborators in the Silverman group have designed and prepared new double-headed molecules with chiral linkers derived from natural amino acids. One of these compounds, (R)-**6b**, exhibits a K_i of 32 nM against nNOS and is 475-fold more selective for nNOS than eNOS (n/e) and 244-fold more selective for nNOS than iNOS (n/i). We have solved the crystal structures of NOS in a complex with (R)-**6b**, which revealed that the structural basis for the higher n/e selectivity is the aminomethyl moiety of (R)-**6b** that forms H-bonds with the two heme propionates in nNOS, but not in eNOS. This work demonstrates the importance of stereochemistry in this class of molecules, which significantly influences the potency and selectivity of the inhibitors. The structure–activity information also provides a guide for the optimization of the structures of future inhibitors.

The work described in this chapter was primarily designed by Dr. Qing Jing and our collaborators in Dr. Richard Silverman's laboratory. I am a co-author on the mansucript that was published as a result of this collaboration, and my contribution to this work included solving the crystal structures of eNOS in complex with the inhibitors in order to structurally address the potency/specificity issues and help guide the design of future inhibitors. This chapter is an adaptation of a portion of the text and images from our published work.[243]

New concepts:

K_i : Dissociation constant of the enzyme-inhibitor complex. The K_i value is a measure of the inhibitory strength of a particular compound.

INTRODUCTION

We have seen how NO expression is critical in neural and cardiovascular systems, but that overexpression of nNOS and therefore excessive NO production has been implicated in many neurodegenerative diseases.[81-88] Inhibiting nNOS is therefore one way to potentially treat these diseases.[63, 244-245] However, inhibitors must have greater selectivity for nNOS over the other two isoforms, since eNOS is involved in blood flow and pressure control, while iNOS is involved in immune system function. In the past, the Silverman group has developed two compounds, labelled **1** and **2** (Figure 8.1),[246-247] which show high potency against nNOS. Compound **1** exhibits a higher selectivity for nNOS over eNOS and iNOS,[246] but the compound was not ideal since its synthesis is very tedious, making it difficult to optimize. Compound **2** is easier to synthesize, but not as efficient as **1**.[247] In this work, the approach taken is to modify the double-headed inhibitor design of compounds **1** and **2** by adding stereogenic centers, providing chirality to the compounds. Because the inhibitors are based on natural chiral scaffolds, synthesis is simple, making these new compounds easily accessible and ready for further optimization.
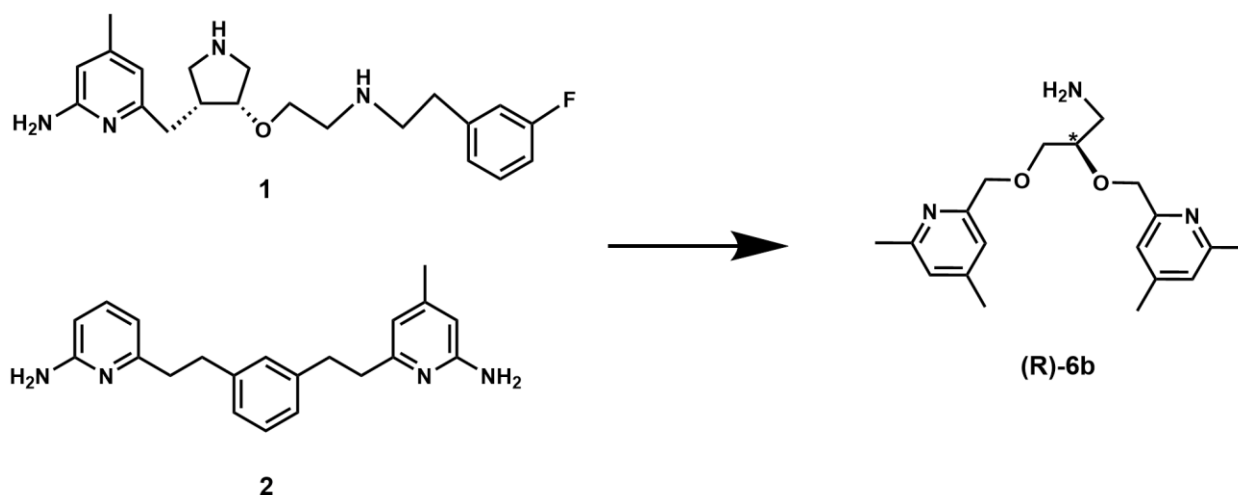
Figure 8.1 – Chemical structures of inhibitors from previous work.

EXPERIMENTAL PROCEDURES

Preparation and Characterization of Compounds and NOS inhibition assays

The syntheses and characterization (^{1}H NMR and ^{12}C NMR) of inhibitors **6, 8, 11, 12** and **16**, as well as the NOS inhibition assays were performed by Prof. Silverman's group, and are described in the manuscript that was published as a result from this collaboration.[243]

Inhibitor Complex Crystal Preparation

The nNOS or eNOS heme domain proteins used for crystallographic studies were produced by limited trypsinolysis from the corresponding full length enzymes and further purified through a Superdex 200 gel filtration column (GE Healthcare) as described in Chapter 7. The nNOS heme domain at 7-9 mg/mL containing 20 mM histidine or the eNOS heme domain at 12 mg/mL containing 2 mM imidazole were used for the sitting drop vapor diffusion crystallization setup under the conditions reported before.[62, 98] Fresh crystals (1-2 day old) were first passed stepwise through cryo-protectant solutions as described[62, 98]and then soaked with 10 mM inhibitor for 4-6 hours at 4 °C before being flash cooled with liquid nitrogen.

X-ray Diffraction Data Collection, Processing, and Structure Refinement

Cryogenic (100 K) X-ray diffraction data were collected remotely at various beamlines at Stanford Synchrotron Radiation Lightsource (SSRL) or Advanced Light Source (ALS) using the data collection control software Blu-Ice4 and a crystal mounting robot. Raw data frames were indexed, integrated, and scaled using HKL2000.[235] The binding of inhibitors was detected by the initial difference Fourier maps calculated with REFMAC.[129, 168] The inhibitor molecules were then modeled in COOT[108] and refined using REFMAC. Disordering in portions of inhibitor

bound in the NOS active site was often observed resulting in poor density quality. However, partial structural features usually could still be visible by lowering the contour level of the $2F_o - F_c$ map to 0.5 σ, which allowed the building of a reasonable model into the disordered regions. Water molecules were added in REFMAC and checked by COOT. The TLS[169] protocol was implemented in the final stage of refinements with each subunit as one TLS group. The omit $F_o - F_c$ density maps were calculated by repeating the last round of TLS refinement with inhibitor coordinate removed from the input PDB file to generate the map coefficients DELFWT and SIGDELFWT. The refined structures were validated in COOT before deposition in the RCSB protein data bank. The crystallographic data collection and structure refinement statistics are summarized in Table 8.1 with PDB accession codes included.

Data Set	nNOS/(S)-**6a**	nNOS/(R)-**6b**	nNOS/(S)-**12**	nNOS/(S,S)-**16b**
		Data Collection		
PDB entry	4K5D	4K5E	4K5F	4K5G
Space group	$P2_12_12_1$	$P2_12_12_1$	$P2_12_12_1$	$P2_12_12_1$
Cell dimensions a, b, c (Å)	52.0 110.9 164.4	52.0 110.7 164.4	51.6 110.7 164.4	52.1 110.7 164.4
Resolution (Å)	2.09 (2.13-2.09)	1.90 (1.93-1.90)	2.20 (2.24-2.20)	1.85 (1.88-1.85)
R_{merge}	0.068 (0.674)	0.054 (0.585)	0.086 (0.755)	0.060 (0.610)
I / σ	19.6 (1.8)	29.9 (2.7)	23.6 (2.1)	24.9 (2.0)
No. unique reflections	56,566	75,781	48,263	80,582
Completeness (%)	99.8 (100.0)	99.2 (99.9)	99.3 (99.7)	98.0 (95.5)
Redundancy	3.6 (3.6)	4.0 (3.9)	4.5 (4.6)	3.9 (3.8)
		Refinement		
Resolution (Å)	2.10	1.90	2.20	1.85
No. reflections used	53,721	71,966	45,779	76,506
R_{work}/R_{free}	0.190/0.233	0.180/0.212	0.192/0.248	0.185/0.219
no. of protein atoms	6659	6670	6659	6681
no. of heteroatoms	177	177	179	179
no. of waters	284	462	148	379
rmsd bond length (Å)	0.011	0.014	0.012	0.011
rmsd bond angle (°)	1.99	1.42	2.09	1.40
Data Set	eNOS/(S)-**6a**	eNOS/(R)-**6b**	eNOS/(S)-**12**	eNOS/(S,S)-**16b**
		Data Collection		
PDB entry	4K5H	4K5I	4K5J	4K5K
Space group	$P2_12_12_1$	$P2_12_12_1$	$P2_12_12_1$	$P2_12_12_1$
Cell dimensions a, b, c (Å)	57.9 106.4 156.9	57.7 106.4 156.7	57.8 106.3 156.7	57.9 106.5 156.7
Resolution (Å)	2.25 (2.29-2.25)	2.08 (2.12-2.08)	2.36 (2.40-2.36)	2.00 (2.03-2.00)
R_{merge}	0.073 (0.670)	0.064 (0.719)	0.071 (0.714)	0.061 (0.665)
I / σ	19.9 (2.5)	25.0 (2.0)	22.1 (2.1)	37.5 (2.2)
No. unique reflections	46732	57767	39788	66497
Completeness (%)	99.5 (100.0)	97.8 (95.1)	97.9 (94.0)	99.8 (99.7)
Redundancy	3.7 (3.7)	4.0 (3.9)	3.9 (3.9)	5.1 (3.9)
		Refinement		
Resolution (Å)	2.10	2.08	2.36	2.00
No. reflections used	44.71	54730	37750	62877
R_{work}/R_{free}	0.155/0.206	0.167/0.208	0.161/0.214	0.179/0.217
no. of protein atoms	6446	6466	6426	6444
no. of heteroatoms	223	203	205	205
no. of waters	339	340	203	335
rmsd bond length (Å)	0.017	0.011	0.012	0.014
rmsd bond angle (°)	1.81	1.45	1.54	1.64

Table 8.1 – Crystallographic data collection and refinement statistics

RESULTS AND DISCUSSION

The inhibitors synthesized and used in this study are shown in Figure 8.2. Starting with compound **8**, which has a 6-atom linker bearing two ether oxygens between the two aminopyridine head groups, our collaborators have introduced either an aminoethyl or aminomethyl tail through a chiral center to generate inhibitors **11** and **6**, respectively. Inhibitor assays were measured against all three NOS isoforms (Table 8.2), and indicate that neither of the two **11** isomers is potent and selective, but that the two **6** isomers show either better potency or better selectivity when compared to **8**. More importantly, the stereochemistry of the chiral center dramatically influences the outcomes: inhibitor (R)**-6b** provides much better characteristics than (S)**-6a** in terms of both potency (32 nM) and selectivity (475 of e/n and 244 of i/n). All of the inhibitors were assayed against the three different isoforms of NOS including rat nNOS, bovine eNOS, and murine macrophage iNOS using L-arginine as a substrate. K_i values are shown in Table 8.2.
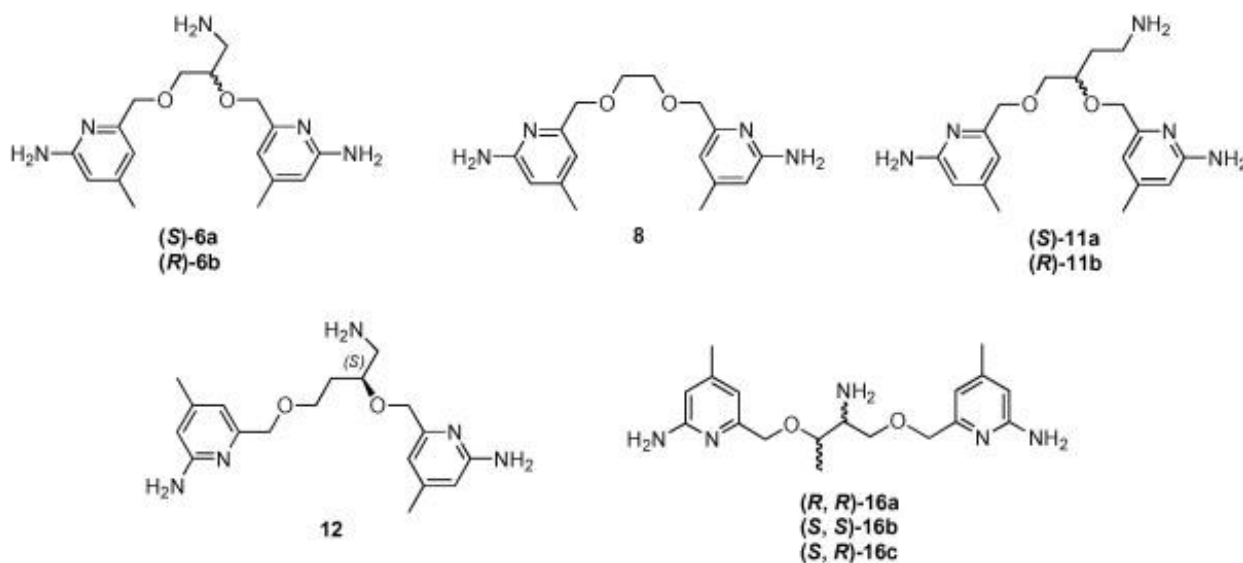
Figure 8.2 – Chemical structures of inhibitors synthesized for this study
Details for the synthesis of compounds is detailed in the published work.[243]

145

Inhibitor	K_i (nM)			Selectivity	
	nNOS	eNOS	iNOS	n/e	n/i
(S)-6a	382	26446	40829	69	107
(S)-6b	32	15213	7821	475	244
8	316	5264	2929	17	9
(S)-11a	1599	92756	53222	58	33
(R)-11b	881	66959	31410	76	35
(S)-12	232	20196	10725	87	46
(R,R)-16a	47	2995	1857	64	39
(S,S)-16b	37	2542	2262	69	61
(S,R)-16c	384	17673	10996	46	28

Table 8.2 – K_i and isoform selectivity values of inhibitors for rat nNOS, bovine eNOS and murine iNOS. IC_{50} values were measured using L-Arginine as a substrate with a standard deviation ± 10%. K_i values were calculated from the IC_{50} values using the equation $K_i = IC_{50}/(1+ [S]/K_M)$ with known K_M values (nNOS, 1.3 μM; iNOS, 8.3 μM; eNOS, 1.7 μM).

To understand the structure–activity relationship of these inhibitors, we determined the crystal structures of both nNOS and eNOS in complex with either (S)-**6a** or (R)-**6b**. As shown in Figure 8.3, (S)-**6a** binds to the active site of nNOS and eNOS in totally

different orientations. In nNOS, it is the aminopyridine with a 3-atom linker from the chiral center that hydrogen bonds to the active site Glu592, while in eNOS the inhibitor is flipped 180°, and the other aminopyridine with the 2-atom linker H-bonds with the active site Glu592 (Figure 8.3B). In nNOS the ether oxygen in the linker forms a weak H-bond (3.2–3.3 Å) with a water molecule that is in turn H-bonded with Glu592 (Figure 8.3A). The aminomethyl group off of the chiral center does not make any strong interactions with the protein, as evidenced by its weaker electron density. In nNOS the second aminopyridine is in position to H-bond with the heme propionate of the pyrrole ring D (propionate D). In eNOS, the aminomethyl nitrogen is in position to form H-bonds with both heme propionates. However, this favorable amino group forces the second aminopyridine ring into position where it cannot make favorable protein interactions and is, therefore, partially disordered with poorly defined density. In summary, these structures show that (S)-**6a** does not gain much binding affinity from its aminomethyl group in

nNOS while the inhibitor loses potential binding contributions from its second aminopyridine in eNOS.

Figure 8.3 – Inhibitor (R)-6a in complex with nNOS and eNOS.
View of the active site of nNOS (A) (PDB entry 4K5D) and eNOS (B) (PDB entry 4K5H) in complex with inhibitor (R)-**6a**. The omit $2F_o$ - F_c density maps for the inhibitor are also shown contoured at 2.5 σ level. Relevant hydrogen bonds are depicted as dashed lines. All molecular graphics shown in this chapter were prepared using PyMOL.[170]

As for (R)-**6b**, despite its chirality, one of the aminopyridines still forms equivalent H-bonds with the active site Glu in eNOS and nNOS (Figure 8.4) of (R)-**6b**. In eNOS, (R)-**6b** binding is much weaker, as seen by the weak electron density, which allows us to model only up to the chiral center, making it difficult to know its exact binding mode in eNOS. The model that best fits the density has the 3-atom linker aminopyridine H-bonded with Glu363, (Figure 8.4), in a similar binding mode to nNOS. The enhanced selectivity that is observed for nNOS (Table 8.2) is probably caused by two main factors. First, when (R)-**6b** binds to nNOS, its binding is stabilized by the aminomethyl nitrogen H-bonding with the heme propionates, but the binding mode in eNOS does not support these H-bonds. Second, in nNOS, the ether oxygen, just like in **6a**, H-bonds with a water that itself is H-bonded to Glu592 (Figure 8.4A), while in eNOS, the ether oxygen bends away from Glu363, preventing any H-bonding interaction with the water

147

molecule next to Glu363. The structures of (S)-**6a** and (R)-**6b** complexed with eNOS and nNOS also provide an explanation for why (S)-**11a** and (R)-**11b** are poor inhibitors (Table 8.2). The bulkier aminoethyl group of **11** would result in steric clashes and the loss of important interactions with the heme propionates.
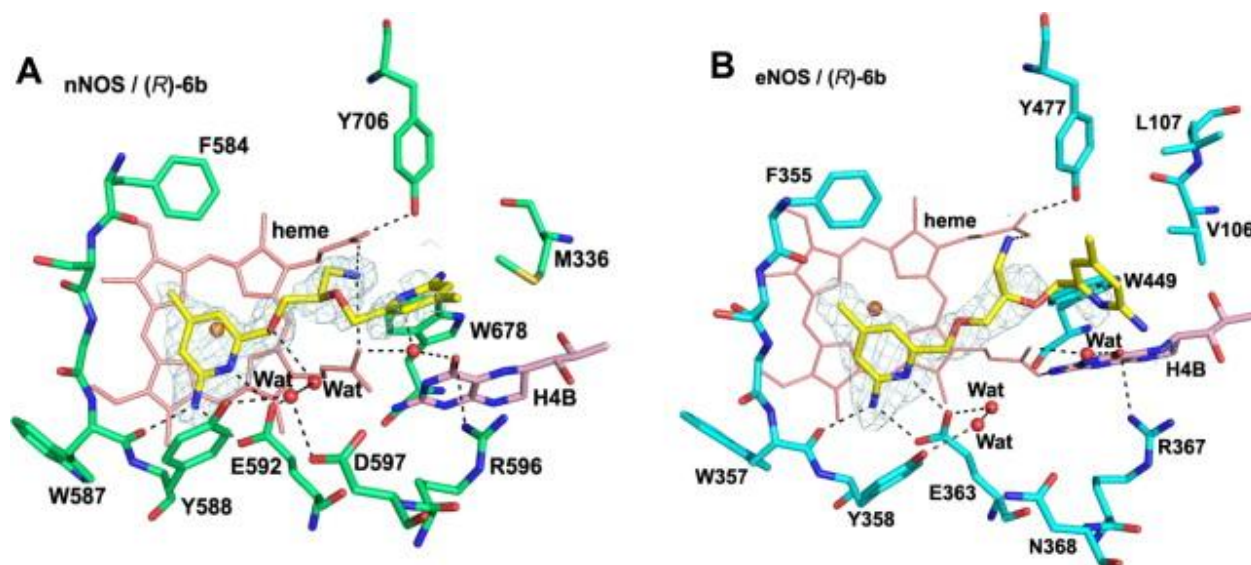
Figure 8.4 – Inhibitor (R)-6b in complex with nNOS and eNOS.
View of the active site of nNOS (A) (PDB entry 4K5E) and eNOS (B) (PDB entry 4K5I) in complex with inhibitor (R)-**6b**. The omit $2F_o$ - F_c density maps for the inhibitor are also shown contoured at 2.5 σ level. Relevant hydrogen bonds are depicted as dashed lines.

Our collaborators extended the 3-atom linker in atoms (R)-**6b** to 4-atoms, making (S)-**12**. Although its stereochemical configuration is (S), compound (S)-**12** has the same stereochemistry as (R)-**6b**, but the chain length modification improves neither potency nor selectivity (Table 8.2). We solved the crystal structure of (S)-**12** complexed to nNOS, which revealed a different binding mode Glu592 (Figure 8.5A). A different aminopyridine head, the one with the 2-atom linker, binds to the heme propionate. In this binding mode, the aminomethyl nitrogen H-bonds with Glu592 and is also about 5.3 Å from Asp597. The position of the aminomethyl is very similar to how dipeptide amide inhibitors bind[248] with the amino group situated between Glu592 and Asp597 for maximum electrostatic stabilization. The other aminopyridine group of (S)-**12** H-

148

bonds to heme propionate D (Figure 8.5A). In eNOS, (S)-**12** binding is flipped (Figure 8.5B) and

the aminopyridine head with a 4-atom linker H-bonds to the analogous Glu363 in eNOS. The

main consequence of this different binding mode is that the second aminopyridine extends

further out of the active site and is disordered. Although the binding mode of (S)-**12** is totally

different with nNOS and eNOS, the selectivity for nNOS over eNOS is only 87. (S)-**12** may gain

some affinity for eNOS from the H-bond between its ether oxygen and the water molecule next

to Glu363 (Figure 8.5B) and possibly some favorable electrostatic interactions between the

aminomethyl and heme propionate D.
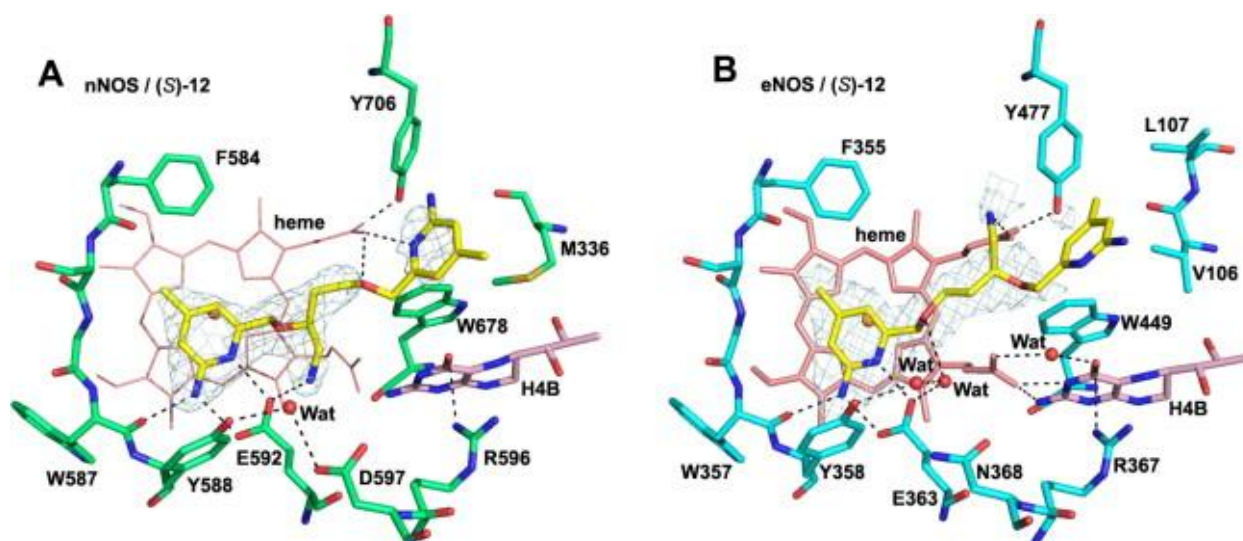
Figure 8.5 – Inhibitor (S)-12 in complex with nNOS and eNOS.
View of the active site of nNOS (A) (PDB entry 4K5F) and eNOS (B) (PDB entry 4K5J) in complex with inhibitor (S)-**12**. The omit $2F_o$ - F_c density maps for the inhibitor are also shown contoured at 2.5 σ level. Relevant hydrogen bonds are depicted as dashed lines.

The next inhibitors that were tested had two chiral centers in the linker between the two

aminopyridine heads, with one center bearing a primary amine and the other a methyl group.

Three of the four possible isomers were synthesized, (R,R)-**16a** and (S,S)-**16b** showing

promising potencies of 47 and 37 nM, respectively. The third isomer, however, (S,R)-**16c**

exhibited a 10-fold decreased affinity (Table 8.2). The crystal structures show an interesting

149

effect of binding of (S,S)-**16b** to nNOS is that the second aminopyridine group H-bonds to heme propionate D causing the Tyr706 to swing out into an alternate rotamer configuration (Figure 8.6A). This does not occur in eNOS-(S,S)-**16b** (Figure 8.6B). Unfortunately, this difference does not increase selectivity for nNOS. The inhibition assays reveal a 69-fold n/e selectivity, indicating that (S,S)-**16b** has a better binding affinity for eNOS than (R)-**6b**, as seen in Table 8.2. These observations suggest that inhibitor binding affinity is highly increased when the amino group of the inhibitor can form strong H-bonds with the heme propionates. In contrast, the observed interaction between the second aminopyridine group of (S,S)-**16b** to heme propionate D does not really increase overall inhibitory potency, as shown by (R)-**6b** binding which lacks these H-bonds (Figure 8.4A), yet maintains strong potency.
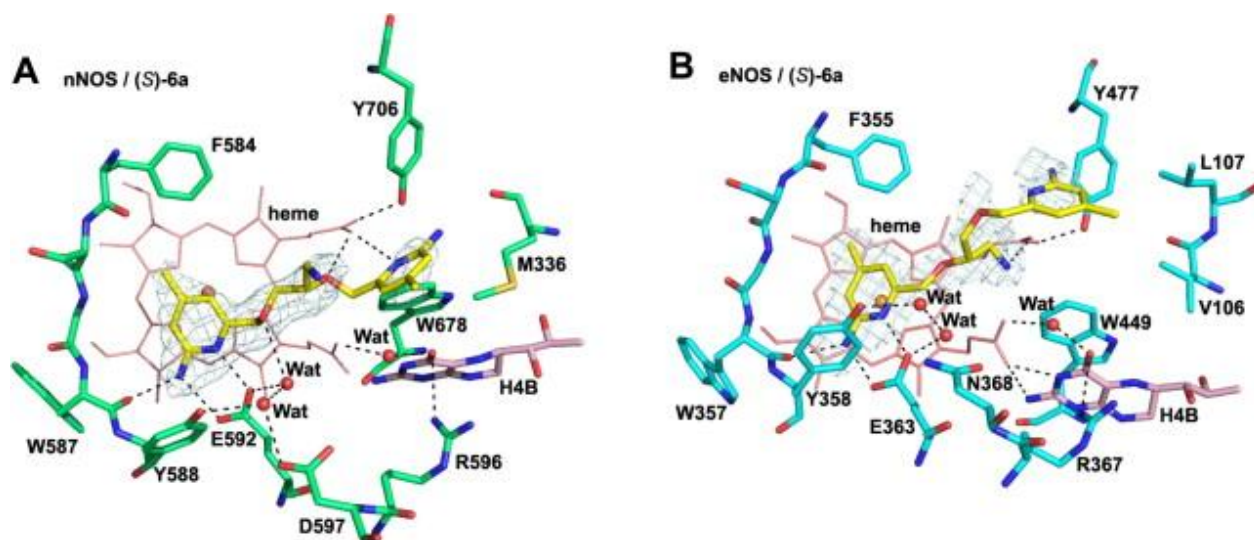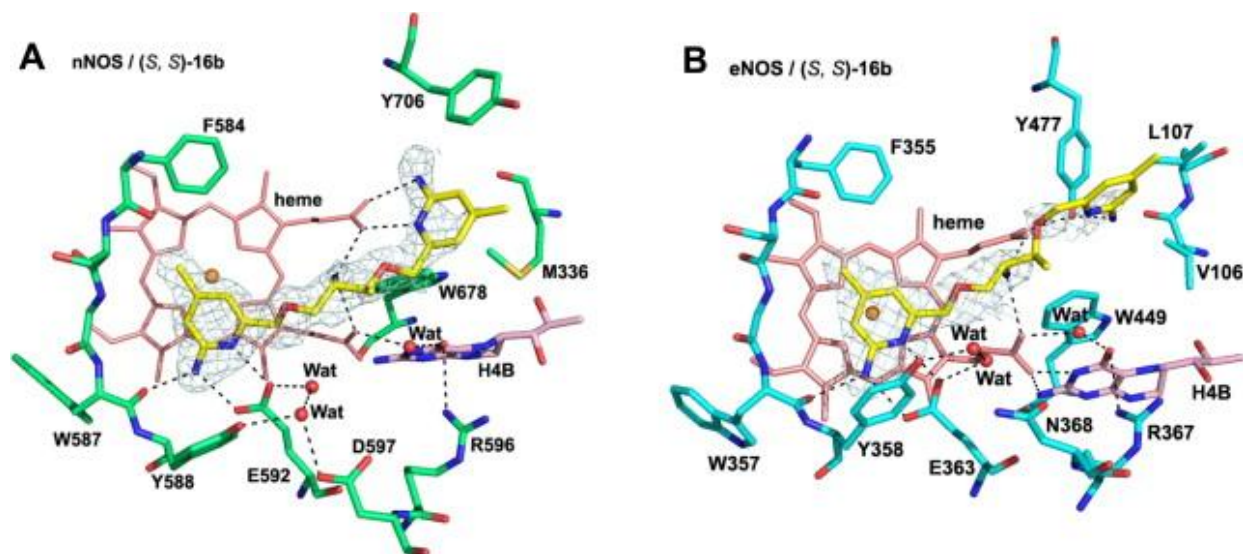

Figure 8.6 – Inhibitor (S,S)-16b isoforms in complex with nNOS and eNOS.
View of the active site of nNOS (A) (PDB entry 4K5F) and eNOS (B) (PDB entry 4K5J) in complex with inhibitor (S)-**12**. The omit $2F_o$ - F_c density maps for the inhibitor are also shown contoured at 2.5 σ level. Relevant hydrogen bonds are depicted as dashed lines.

Conclusions

Our collaborators have designed and synthesized a series of double-headed inhibitors with a chiral linker derived from natural amino acids. This work is beneficial for three main reasons. First, using natural chiral scaffols has made synthesis a much easier task. Second, one of these resulting chiral inhibitors, (R)-**6b**, exhibits high potency of 32 nM and high n/e selectivity of 475-fold and n/i selectivity of 244-fold. Third, the structural work on (R)-**6b** and (S,S)-**16b** reveals that the primary structural requirement for an efficient inhibitor with low nanomolar affinity is strong H-bonding between the inhibitor amine and both heme propionates. The additional interactions between the second aminopyridine group and heme propionate D, unfortunately, showed little improvement in overall potency. These observations can guide the design of future inhibitors with similar features to improve n/e selectivity.

POTENT AND SELECTIVE DOUBLE-HEADED THIOPHENE-2-CARBOXIMIDAMIDE INHIBITORS OF NEURONAL NITRIC OXIDE SYNTHASE FOR THE TREATMENT OF MELANOMA

Chapter 9

Summary

Continuing our efforts to find better nNOS inhibitors, we next look at another strategy for inhibitor design. This novel strategy combines the pharmacokinetically promising thiophene-2-carboximidamide fragment with structural features of potent and selective aminopyridine inhibitors that were previously designed by the Silverman group. We will see how two of these new "hybrid" inhibitors, **13** and **14**, exhibit low nanomolar inhibitory potency (K_i = 5 nM for nNOS) and good isoform selectivities (n/e of 440-fold for **13** and 540-fold for **14**, and n/i of 260-fold for **13** and 340-fold for **14**). The crystal structures of these nNOS−inhibitor complexes reveal a new binding "hot spot" that explains the selectivity of **14** and why converting the secondary to tertiary amine leads to enhanced selectivity. More importantly, these compounds are the first highly potent and selective nNOS inhibitory agents that exhibit excellent *in vitro* efficacy in melanoma cell lines.

The work described in this chapter was primarily designed by Dr. He Huang and our collaborators in Dr. Richard Silverman's laboratory. I am a co-author on the mansucript that

was published as a result of this collaboration, and my contribution to this work included solving the crystal structures of eNOS in complex with the inhibitors in order to structurally address the potency/specificity issues and help guide the design of future inhibitors. This chapter is an adaptation of a portion of the text and multiple images from our published work.[249]

INTRODUCTION

Previous studies done by the Silverman group have shown that NO generated by nNOS also plays an important role in increasing the invasion and proliferation of human melanoma cells.[89] While we have already exhaustively discussed the role of NO in neurodegenerative diseases, these findings suggest that nNOS inhibition may also be therapeutic solution for melanoma. One great challenge is the unwanted inhibition of iNOS and eNOS, which can cause deleterious side-effects,[96-97] which means that we need inhibitors with greater selectivity for nNOS. The Silverman-Poulos collaboration has produced a series of highly potent and selective nNOS small molecule inhibitors based on a 2-aminopyridinomethyl pyrrolidine scaffold (Figure 9.1, compounds **1** and **2**).[100, 246, 250-252] Some showed excellent potency ($K_i < 10$ nM) and greater than 2500-fold n/e selectivity and 700-fold n/i selectivity. The strong potency was structurally explained to be due to the 2-aminopyridine moiety being able to H-bond with both the active site glutamate (Glu592 in nNOS/Glu363 in eNOS) and with the heme propionate in a 180° flipped conformation, depending on the chirality of the pyrrolidine. Based on this observation, previous studies tried to capitalize on these two binding modes by designing a series of symmetric double-headed aminopyridines (e.g., **3** in Figure 9.1),[247, 253] but suffered from poor membrane permeability.[254]

Figure 9.1 – Chemical structures of inhibitors 1 - 3 from previous work. [100, 246-247, 250-253]

In addition to the aminopyridine-based inhibitors, thiophene-2-carboximidamides (Figure 9.2, **4−6**) represent another important class of nNOS inhibitors which were shown to be quite promising.[255-260] Unfortunately, they exhibited lower potency and nNOS selectivity *in vitro* compared to aminopyridine-based inhibitors, and little structural information exists to reveal the binding modes and basis for the low observed efficiency.

Figure 9.2 – Chemical structures of inhibitors 4 - 6 from previous work.[255-260]

The strategy used in this study involved designing hybrid inhibitors that combine the thiophene-2-carboximidamide fragment successful in compounds **4-6** with structural features of

the potent and selective double-headed aminopyridine inhibitors **1-3**. Based on this, a series of compounds (**7-17**) were synthesized by Dr. Huang in the Silverman group (Figure 9.3), and we conducted crystallographic studies to identify the enzyme−inhibitor interactions that promote nNOS-specific inhibition.
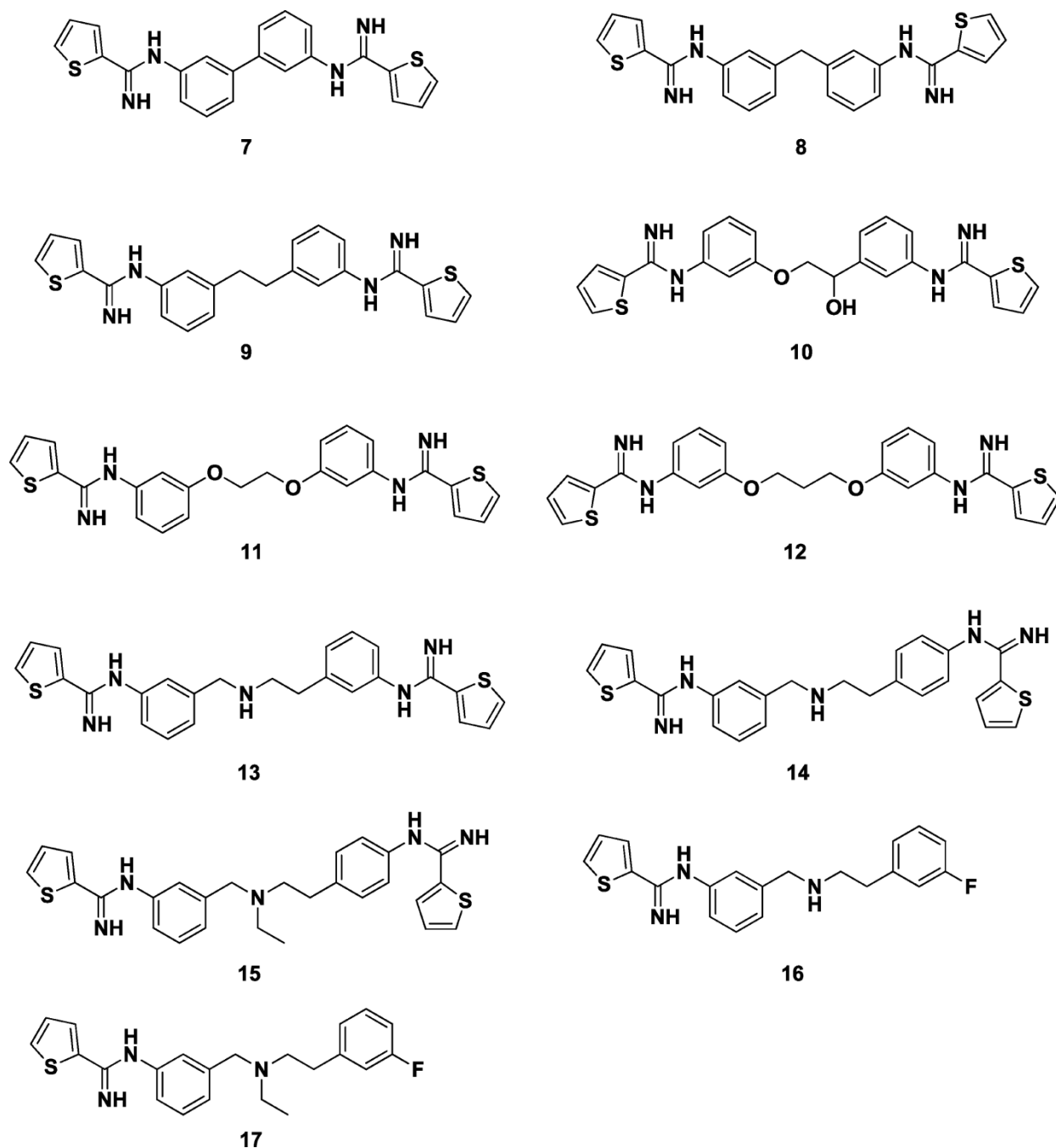
Figure 9.3 – Chemical structures of inhibitors 7 - 17 designed and synthesized for this study.

EXPERIMENTAL PROCEDURES

Preparation and Characterization of Compounds and NOS inhibition assays

The syntheses and characterization (^{1}H NMR and ^{12}C NMR) of inhibitors **7-17**, as well as the NOS inhibition assays were performed by Prof. Silverman's group, and are described in the manuscript that was published as a result from this collaboration.[249]

Inhibitor Complex Crystal Preparation

and

X-ray Diffraction Data Collection, Processing, and Structure Refinement

The nNOS or eNOS heme domain proteins used for crystallographic studies were produced as described in Chapter 8. Chapter 8 also describes the X-ray diffraction data collection, processing and structure refinement protocols that were used. The refined structures were deposited in the RCSB Protein Data Bank. The crystallographic data collection and structure refinement statistics for the eNOS-inhibitor complex structures are summarized in Table 9.1 with PDB accession codes included. All details on the nNOS-inhibitor structures are included in the published manuscript.[249]

Data Set	eNOS-**14**	eNOS-**15**	eNOS-**16**	eNOS-**17**
	Data Collection			
PDB entry	4KCP	4KCQ	4KCR	4KCS
Space group	$P2_12_12_1$	$P2_12_12_1$	$P2_12_12_1$	$P2_12_12_1$
Cell dimensions a, b, c (Å)	57.7, 106.2, 156.8	57.7, 106.4, 156.7	57.6, 106.2, 156.5	57.7, 106.4, 157.1
Resolution (Å)	2.07 (2.11–2.07)	2.03 (2.07–2.03)	2.09 (2.13–2.09)	2.05 (2.09–2.05)
R_{merge}	0.060 (0.712)	0.064 (0.494)	0.059 (0.576)	0.051 (0.528)
I / σ	24.2 (1.9)	26.9 (2.6)	27.3 (2.6)	31.0 (2.9)
No. unique reflections	59332	62254	57743	61246
Completeness (%)	99.1 (99.9)	98.4 (99.7)	99.7 (100.0)	99.2 (100.0)
Redundancy	4.0 (4.0)	3.9 (3.9)	4.0 (4.1)	4.0 (4.0)
	Refinement			
Resolution (Å)	2.07	2.03	2.09	2.05
No. reflections used	56,198	59,095	54,719	58,050
R_{work}/R_{free}	0.166/0.213	0.179/0.224	0.164/0.205	0.168/0.213
no. of protein atoms	6446	6429	6436	6446
no. of heteroatoms	216	223	206	201
no. of waters	305	359	354	350
rmsd bond length (Å)	0.02	0.013	0.011	0.02
rmsd bond angle (°)	2.02	1.63	1.45	2.05

Table 9.1 – Crystallographic data collection and refinement statistics for the eNOS-inhibitor complex structures

RESULTS AND DISCUSSION

Compounds **7−12** were designed with double thiophene-2-carboximidamide heads having diverse flexible linkers. The main difference between the compounds is the chain length, which is used to probe the NOS active site. Table 9.2 shows the results of inhibition assays of compounds **7−12** against all three NOS isoenzymes. The measured K_i values suggest that while **7−10** exhibit at most moderate inhibitory potency, **11** and **12** are the best nNOS inhibitors. Compound **11** also shows outstanding n/i selectivity (513-fold) and good n/e selectivity (105-fold). **12** is structurally similar to **11**, but has one additional methylene group. The extra group greatly reduces the potency and selectivity for nNOS over either eNOS or iNOS.

| Inhibitor no. | K_i (μM) | | | Selectivity | |
	nNOS	eNOS	iNOS	n/e	n/i
7	0.787 ± 0.061	66.4 ± 5.2	177.3 ± 10.9	225	84
8	0.776 ± 0.069	79.0 ± 4.0	133.0 ± 12.4	171	102
9	0.739 ± 0.053	103.8 ± 8.7	66.0 ± 5.8	89	141
10	0.819 ± 0.067	10.1 ± 0.9	5.2 ± 0.4	6	12
11	0.130 ± 0.062	66.8 ± 2.7	13.7 ± 0.7	105	513
12	0.237 ± 0.019	12.6 ± 0.8	4.0 ± 0.3	17	53
13	0.005 ± 0.0005	1.3 ± 0.2	2.2 ± 0.1	440	260
14	0.005 ± 0.0003	1.7 ± 0.1	2.7 ± 0.2	540	340
15	0.049 ± 0.002	14.2 ± 0.8	41.4 ± 2.2	845	290
16	0.011 ± 0.001	1.6 ± 0.07	0.9 ± 0.05	82	145
17	0.073 ± 0.003	12.1 ± 0.74	21.7 ± 1.57	297	166

Table 9.2 – K_i and isoform selectivity values of inhibitors for rat nNOS, bovine eNOS and murine iNOS.

Once again, to determine the structural basis behind the observed potencies/selectivities and to guide future designs, we determined the crystal structures of several inhibitors bound to nNOS and eNOS. Compounds **7** and **9** bind to nNOS with one thiophene-2-carboximidamide head forming two H-bonds with Glu592, while the other head occupies a hydrophobic pocket surrounded by Met336, Leu337, and Tyr706 near the active site entrance (Figure 9.4). The two phenyl rings in **7** are in van der Waals contacts with both heme propionates (Figure 9.4A). In contrast, having a 2-carbon linker between the two phenyl rings in **9** pushes the second phenyl and thiophene-2-carboximidamide head farther away from the heme (Figure 9.4B). The Leu337 side chain must adopt an alternate rotamer to accommodate the longer compound **9**. The second carboximidamide in **9** does not make any direct contacts with the protein, while the one in **7** makes only a weak H-bond with heme propionate D. Therefore, the submicromolar binding affinity is mainly attributed to the first phenyl ring and the thiophene-2-carboximidamide head that tightly anchors the inhibitor to the NOS active site. The structure of **10** (same chain length as **9**) bound to nNOS (data not shown) also supports this conclusion. While the first phenyl ring and thiophene-2-carboximidamide head is clearly shown in the electron density, the remainder of the

compound is disordered, indicating high flexibility and inability to form contacts with the heme propionates. Nevertheless, **10** shares a similar affinity to nNOS as **7** and **9** (Table 9.2).
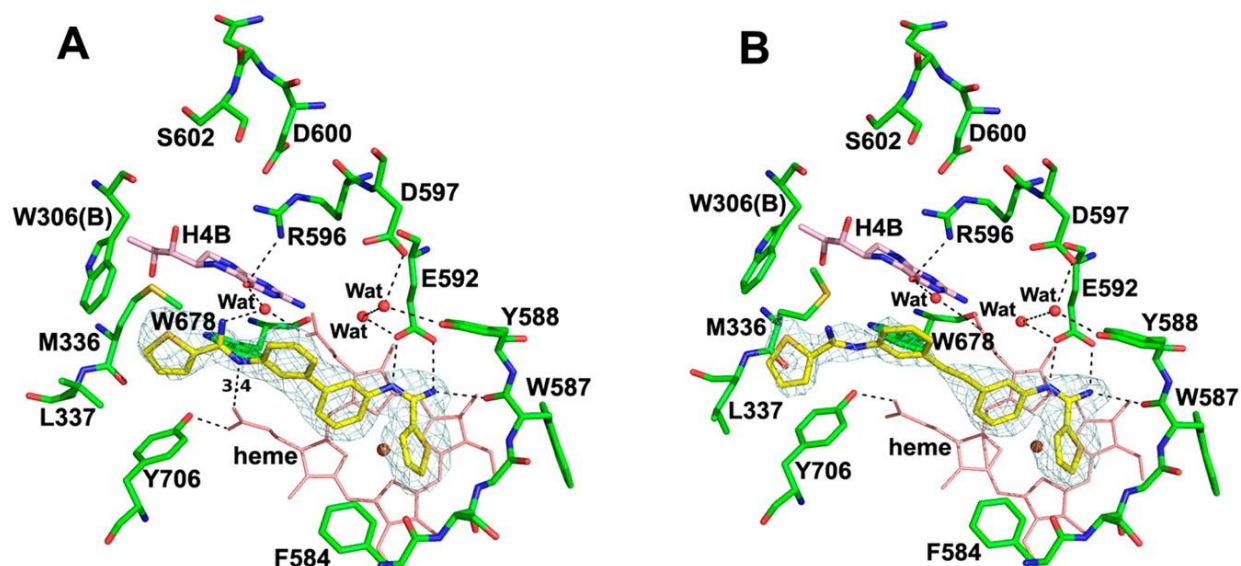
Figure 9.4 – Inhibitors 7 and 9 in complex with nNOS
(A) Active site of nNOS-**7** (PDB entry 4KCH). (B) Active site of nNOS-**9** (PDB entry 4KCI). The omit $2F_o - F_c$ density maps for the inhibitors are shown at a contour level of 2.5 σ. Relevant hydrogen bonds are depicted as dashed lines. Key distances are labeled in Å. All molecular graphics shown in this chapter were prepared using PyMOL.[170]

Next, we look at increasing the chain length. Compounds **11** and **12**, which have a 4- and 5- atom long linker between the two head groups, respectively, exhibit greater potency than the shorter linker variants. (Table 9.2). The nNOS-**11** structure (Figure 9.5A) reveals that the binding mode is similar to **7** and **9**, but the structures reveal four additional interactions that explain the higher measured potency. First, a weak H-bond (3.4 Å) interaction between the central O atom in the linker and Gln478. Second, a new stacking interaction between the phenyl ring and the Arg481 guanidinium group that rotates into position (compared to the native structure). Third, the amine in the second thiophene-2-carboximidamide head finds additional stability in a H-bonding network involving a water molecule, Arg596, Asp600 and Arg603. Fourth, the longer head extends into a pocket that reaches into the other subunit of the dimer, being stabilized by

interactions with several residues. This novel inhibitor binding mode is potentially quite promising, since one of the interactions in nNOS (Ser102), could not form in eNOS (His) or iNOS (Gln), and might explain the higher nNOS selectivity observed for **11**. Compound **12**, with a slightly longer linker (5-atoms), results in a 2-fold lower potency, most likely because the second thiophene-2-carboximidamide head is no longer stabilized.
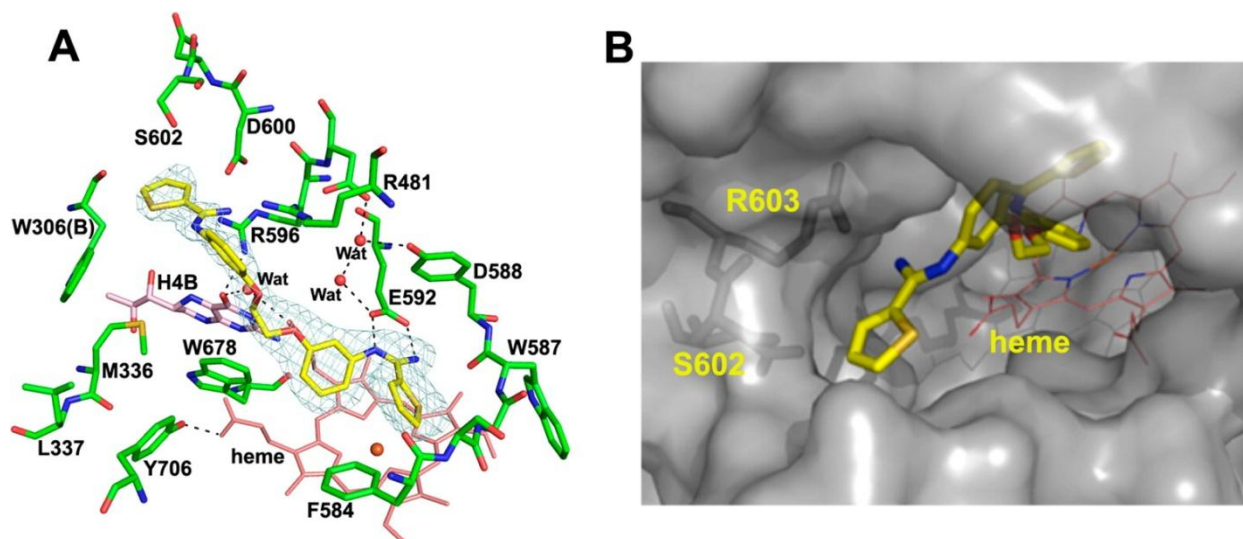
Figure 9.5 – Inhibitor 11 in complex with nNOS
(A) Active site of nNOS-**11** (PDB entry 4KCJ). The omit $2F_o$ - F_c density map for the inhibitor is shown at a contour level of 2.5 σ. Relevant hydrogen bonds are depicted as dashed lines. (B) New pocket "hot spot" around the second thiophene head.

The next inhibitors that we screened were **13** and **14**, which were generated by introducing a nitrogen to the linker portion of compound **11** instead of the two oxygens. This was done to mimic the pyrrolidine nitrogen in inhibitors **1** and **2** that contributed to potency and selectivity due to better electronic stabilization by negatively charged nNOS active site residues. The resulting K_i values for **13** and **14** for nNOS are 5 nM, which is 25-fold more potent than that of **11**, while preserving the good n/e selectivity and improving n/i selectivity. The crystal structures of **13** and **14** bound to nNOS both use the first phenyl ring and thiophene-2-carboximidamide head to anchor the inhibitor to the nNOS active site (Figure 9.6), just like **11**.

The higher binding affinity observed for **13** and **14** is most likely due to the newly introduced amino group that forms H-bonds with the two heme propionates. As for differences between **13** and **14**, the second phenyl group in **13** is meta-bisubstituted, and is able to extend into the same pocket as **11** (Figure 9.6A), while the second phenyl group in **14** is para-bisubstituted, and is disordered in the crystal structure, most likely due to steric hindrance (Figure 9.6B).
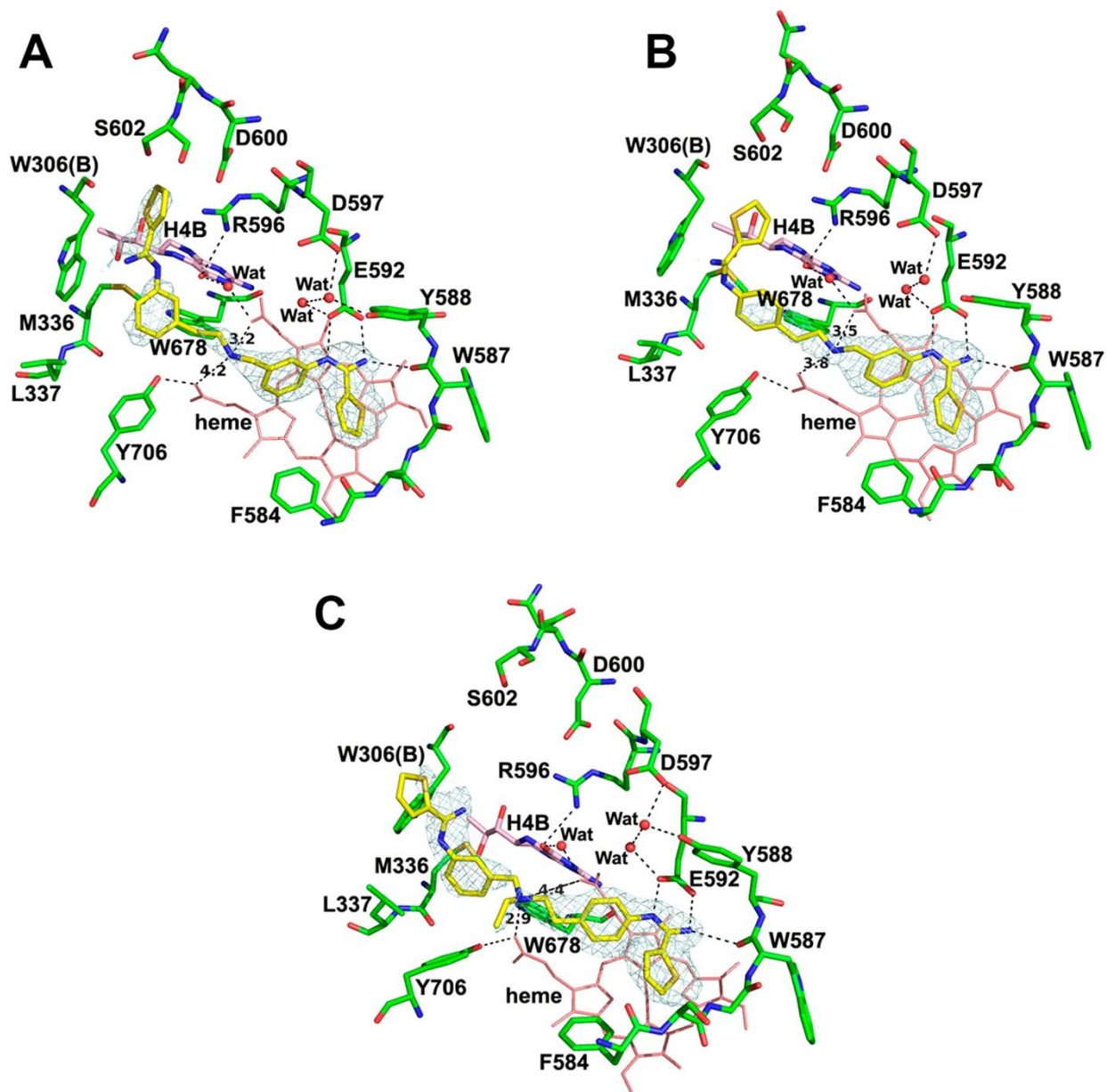
Figure 9.6 – Inhibitors 13, 14 and 15 in complex with nNOS
(A) Active site of nNOS-**13** (PDB entry 4KCK). (B) Active site of nNOS-**14** (PDB entry 4KCL). (C) Active site of nNOS-**15** (PDB entry 4KCM). The omit $2F_o$ - F_c density maps for the inhibitors are shown at a contour level of 2.5 σ. Relevant hydrogen bonds are depicted as dashed lines.

The presence of the amine in the linker of **13** and **14** increases potency, but also introduces a potential hydroxylation site by flavin monooxygenases that could treat it as a substrate.[261] Compound **14** was therefore modified by connecting an ethyl group to the amine nitrogen to generate **15**. While the resulting substitution heavily decreases the potency, but increases n/e selectivity by 845-fold. Unexpectedly, the nNOS-**15** structure reveals that **15** (Figure 9.6C) binds to nNOS a 180° flipped orientation compared to **14** (Figure 9.6B). In this flipped binding mode, the para-bisubstituted phenyl ring and its adjacent thiophene-2-carboximidamide form two H-bonds with Glu592. The lower nNOS inhibitory potency for **15** is likely due to weaker contacts with both heme propionates when compared to **14**.

We next probed the structural basis for the large difference in isoform selectivity in **14** and **15** by solving the structures of eNOS-**14** and eNOS-**15**. The binding mode in eNOS-**14** (Figure 9.7A) is largely the same as the one observed for nNOS-**14**, with the exception that the second head of the inhibitor does not extend into the same pocket as it does in nNOS-**14**, and therefore finds less stabilizing interactions in eNOS. This is most likely due to the presence of His373 in eNOS (Ser602 in nNOS), which has a bulkier side-chain. The inhibitor binding mode observed in the eNOS-**15** structure (Figure 9.7B) is almost the same as the binding seen in the nNOS-**15** structure (Figure 9.6C), suggesting that the 845-fold n/e selectivity of **15** (Table 9.2) is most likely due to stabilization of the second head of the inhibitor. Unfortunately, the position of this thiophene ring is less certain because of poorer density in this region in both the eNOS-**15** and nNOS-**15** structures. We hypothesize that the basis for the different selectivities is likely due to greater hydrophobicity of the pocket in nNOS than eNOS.
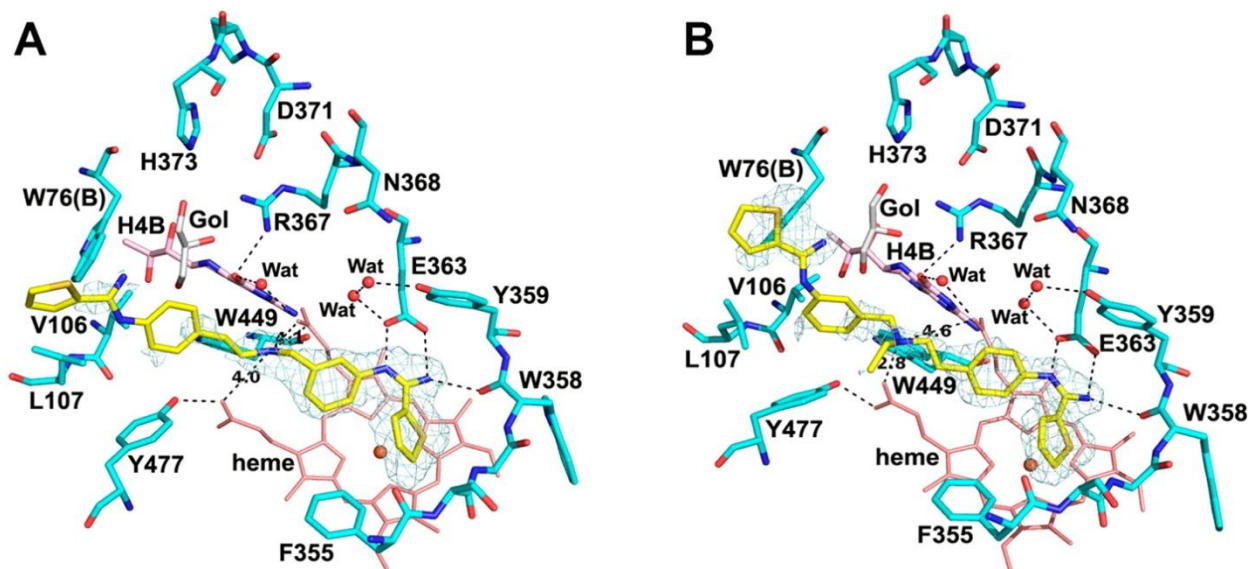
Figure 9.7 – Inhibitors 14 and 15 in complex with eNOS
(A) Active site of eNOS-**14** (PDB entry 4KCP). (B) Active site of eNOS-**15** (PDB entry 4KCQ). The omit $2F_o - F_c$ density maps for the inhibitors are shown at a contour level of 2.5 σ. Relevant hydrogen bonds are depicted as dashed lines and key distances are labeled in Å.

Finally, compounds **16** and **17** were designed to explore whether the addition of the tertiary amine can also improve selectivity for mono-thiophene-2-carboximidamide inhibitors instead of the double headed ones we have used so far. For both, the thiophene-2-carboximidamide head was replaced by a fluorobenzene since some success has been achieved by using fluorine in other compounds.[262] Compared to **14**, compound **16** exhibits lower inhibitory potency and drastically lower n/e selectivity. As for **17**, which is generated by adding an ethyl group to the central amine nitrogen of **16**, assays show enhanced n/e selectivity, but decreased inhibitory potency. The reason for decreased potency may be the shorter length of the compound, which can no longer extend into the pocket. Regardless, attaching an ethyl group to the secondary amine does achieve higher n/e selectivity for these compounds, which can be considered a success. Detailed interactions of **16** and **17** in nNOS and eNOS are shown in Figure 9.8.
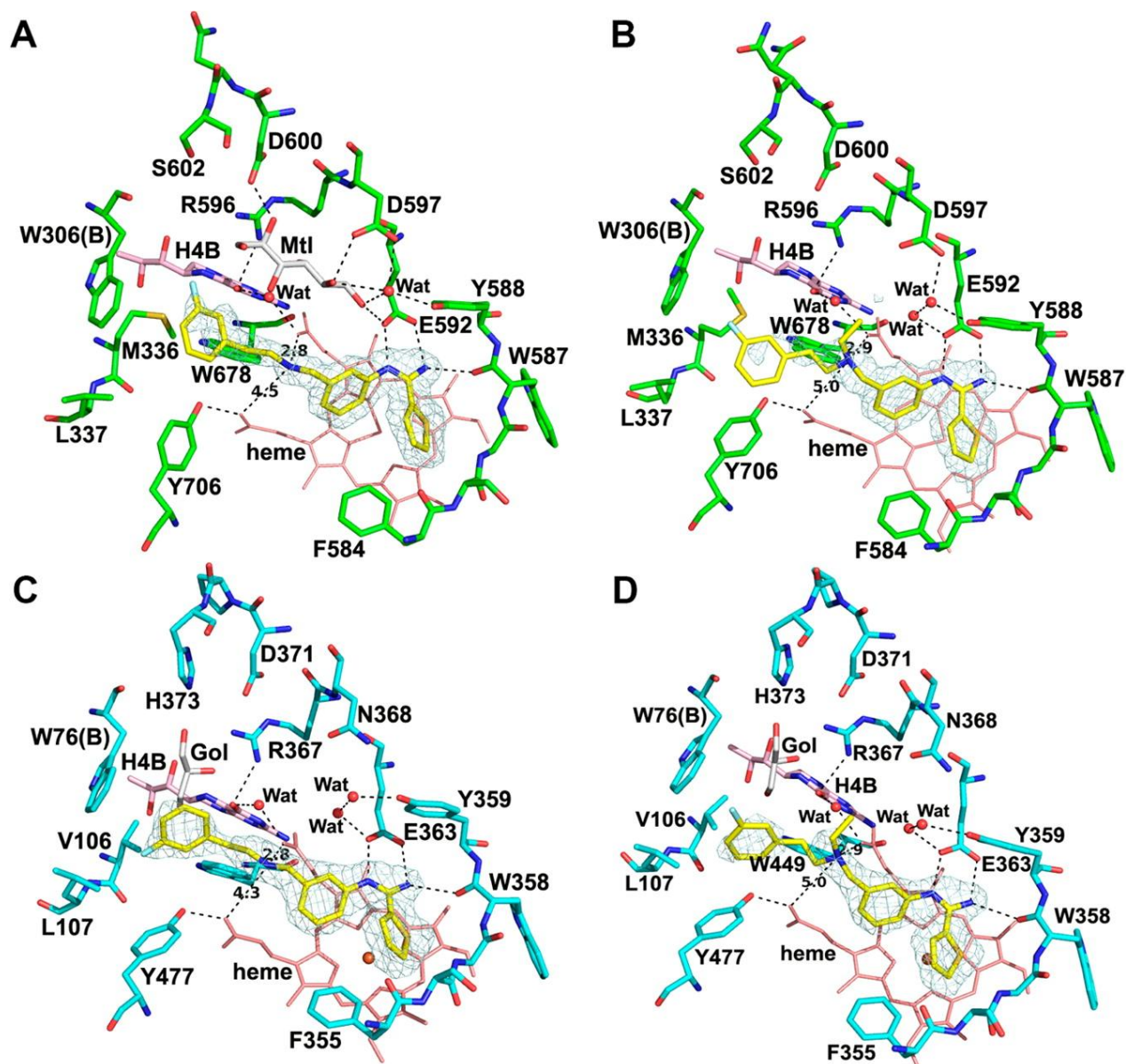
Figure 9.8 – Inhibitors 16 and 17 in complex with nNOS and eNOS
(A) Active site of nNOS-**16** (PDB entry 4KCN). (B) Active site of nNOS-**17** (PDB entry 4KCO). (C) Active site of eNOS-**16** (PDB entry 4KCR). (D) Active site of eNOS-**17** (PDB entry 4KCS). The omit 2F_o - F_c density maps for the inhibitors are shown at a contour level of 2.5 σ. Relevant hydrogen bonds are depicted as dashed lines and key distances are labeled in Å.

Given the enzyme potency of **13** and **14**, our collaborators next tested whether these inhibitors were effective in melanoma cell lines. In previous work,[89] the Silverman group showed that nNOS is associated with the proliferation of melanoma and that nNOS inhibitors that reduce intracellular NO levels can successfully inhibit the proliferation. Assays on inhibitors **13** and **14** designed for this study exhibited potent antimelanoma activity *in vitro*, which is encouraging. Unfortunately, the compounds also inhibited proliferation in primary normal cells. Nevertheless, the results are still promising and suggest that potent and selective nNOS inhibition offers an interesting therapeutic route to treat melanoma patients that is worth exploring further. For more details on the results of these experiments, please refer to the published manuscript.[249]

Conclusions

nNOS inhibitors were designed using a hybrid strategy that uses features from previously designed inhibitors. These novel inhibitors essentially combine the thiophene-2-carboximidamide fragment with structural features from double-headed aminopyridine inhibitors. Two of the compounds, **13** and **14**, show excellent potency (5 nM) and good selectivities for nNOS over the other isozymes. Moreover, the crystal structures have uncovered a new hydrophobic pocket near Ser602 in nNOS that may help in the design of future inhibitors that improve isozyme selectivity. Finally, attaching an ethyl group to the amine of the inhibitor was also shown to improve isozyme selectivity. Most excitingly, the Silverman group was able to achieve good cellular activity in two melanoma cell lines by using compounds **13** and **14**. Overall, these inhibitors pave the way for the design of potent inhibitors that are more selective for the nNOS isoform.

SIMPLIFIED 2-AMINOQUINOLINE-BASED SCAFFOLD FOR POTENT AND SELECTIVE NEURONAL NITRIC OXIDE SYNTHASE INHIBITION

Chapter 10

Summary

In this third chapter that describes our efforts to find better nNOS inhibitors, we explore another strategy for inhibitor design. This strategy uses 2-aminoquinoline-based scaffolds to try to preserve the strong inhibitory potency of inhibitors that are L-arginine mimetics, while also having chemical properties that increase permeability of the blood-brain barrier. Dr. Maris Cinelli and our collaborators in the Silverman group have prepared and assayed a series of such compounds. Two of these compounds, **7** and **15**, with a 7-substituted 2-aminoquinoline, were shown to have high inhibitory potency and high selectivity for nNOS over the other isoforms. The greatest achievement in this study is that Compounds **7** and **15** were tested in a Caco-2 assay and exhibit good membrane permeability, suggesting that this approach to inhibitor design is extremely promising.

The work described in this chapter was primarily designed by Dr. Maris Cinelli and our collaborators in Dr. Richard Silverman's laboratory. I am a co-author on the mansucript that was published as a result of this collaboration, and my contribution to this work included solving the crystal structures of eNOS in complex with the inhibitors in order to structurally address the potency/specificity issues and help guide the design of future inhibitors. This chapter is an adaptation of a portion of the text and multiple images from our published work.[263]

New concepts?

Caco-2 assay : The Caco-2 cell line is a human intestinal epithelial line. Assays using Caco-2 lipid monolayers approximate a compound's permeabililty in the gastrointestinal tract, as well as in the blood–brain barrier.[264-266]

The Silverman-Poulos collaboration has produced a series of nNOS inhibitors by using fragment hopping[267] and subsequent structure-based optimization[251] to produce compounds **1** and **2** (Figure 10.1). These compounds are highly potent inhibitors that are selective for nNOS. Compound **1** was even shown to reverse a hypoxic-ischemic brain damage phenotype in newborn rabbit kits and prevents cerebral palsy when administered intravenously to the mother.[268]
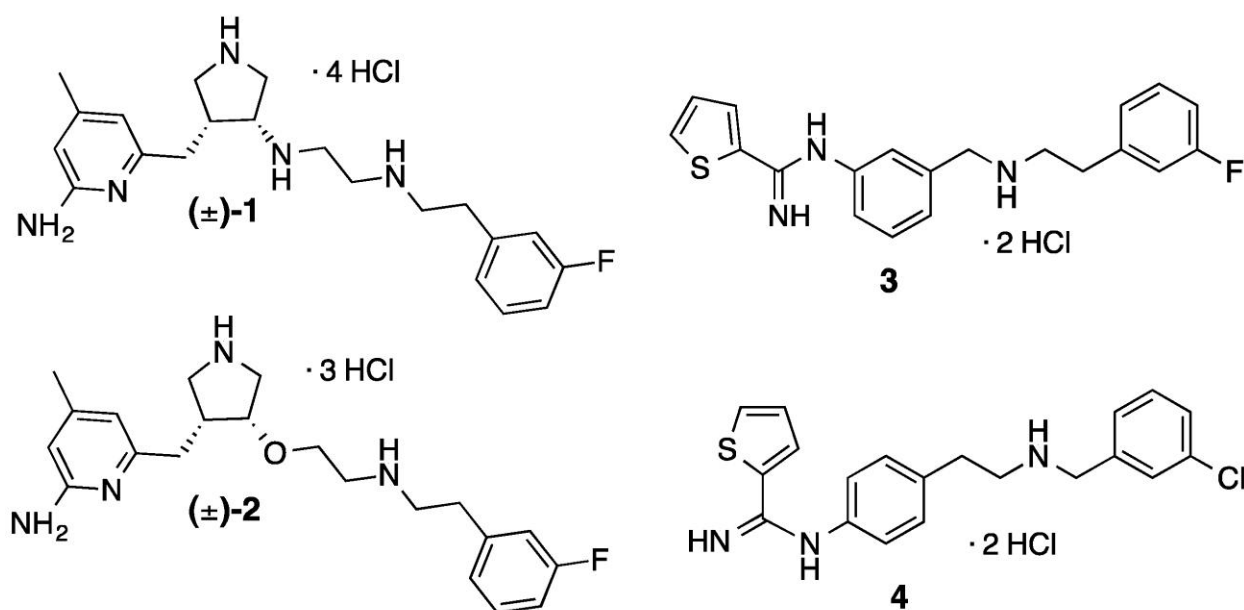
Figure 10.1 – Chemical structures of previous nNOS inhibitors that are mentioned in this chapter.

Although these compounds have been effective *in vitro*, **1** and **2** are nevertheless not optimal for therapeutic application, because their high polarity and hydrophillicity make it impossible to cross the blood-brain barrier, where it needs to inhibit nNOS *in vivo*.[269-270] Many attempts to improve the bioavailability of these types of compounds have been made, but resulted in either diminished potency or selectivity. The chiral scaffolds of **1** and **2** are also difficult (>12 steps) to prepare, which from a clinical standpoint, makes them less desirable than simpler scaffolds, such as **3** (compound **16** in Chapter 9),[249] and compound **4** synthesized by

AstraZeneca (AR-R17477). However, simpler scaffolds are also not optimal, as they have lower isoform selectivities, **3** suffers from poor Caco-2 permeability, and **4** is much less potent in cell-based assays[271] than against isolated enzymes, probably because the amidine moiety is charged at physiological pH.

In this chapter, we look at a different approach made by the Silverman group to address the membrane permeability and difficult synthesis of **3**. They hypothesized that replacing the amidine group of a molecule such as **3** with another arginine isostere would improve nNOS inhibitor design, while allowing the use of a simpler scaffold. This replacement group would be stable, weakly basic (pK_a between 6 and 8), and possess as few hydrogen-bond donors as possible. The 2-aminoquinoline group, with a pK_a of 7.3,[272] is an ideal candidate to replace the amidine group, due to its similarity in structure and pK_a to the aminopyridines of **1** and **2**. Using a 2-aminoquinoline group is also a sound approach based on three studies by Jaroch et al. that use dihydroaminoquinolines as nNOS inhibitors,[273-275] and also since the 2-aminoquinoline-based BACE1 inhibitors have been shown to have high cellular activity and good blood–brain barrier permeability in a rat model.[276]

Therefore, compound **5** was produced as a hybrid between **3** and 2-aminoquinoline. Several other modifications were then made to this scaffold (Figure 10.2) in an effort to probe the hydrophobic pocket at the end of the substrate access channel in nNOS discussed in Chapter 9, Figure 9.3A and C). Contact between an inhibitor and the residues lining this pocket has been shown to increase selectivity for nNOS over the other two isoforms.[277-278] Preliminary docking studies and crystallography indicated that elongation of the chain between the aminoquinoline

system and the distal fluorophenyl ring of **5**, moving the position of the secondary amine, or a combination of both, might provide the right length and orientation to reach this hydrophobic pocket. Compounds **6** to **9** were synthesized in order to determine the optimal chain length and nitrogen position (Figure 10.2). Additionally, computer modeling done by the Silverman group suggested that the placement of the "tail" of the inhibitor at position 6 of the aminoquinoline system (instead of position 7) may be more effective; and so synthesized compounds **10**–**13** (Figure 10.2) to test this hypothesis. Finally, 7-substituted compounds **14** to **16** were designed with different halogens and substitutions (Figure 10.2) based on previous studies[246, 267] that show that different halogen and substitution patterns on the noncoordinating aryl ring can increase potency and selectivity. All of the compounds mentioned were assayed against purified rat nNOS, and select compounds were assayed against eNOS, iNOS, and human nNOS, and for cellular permeability in a Caco-2 model.
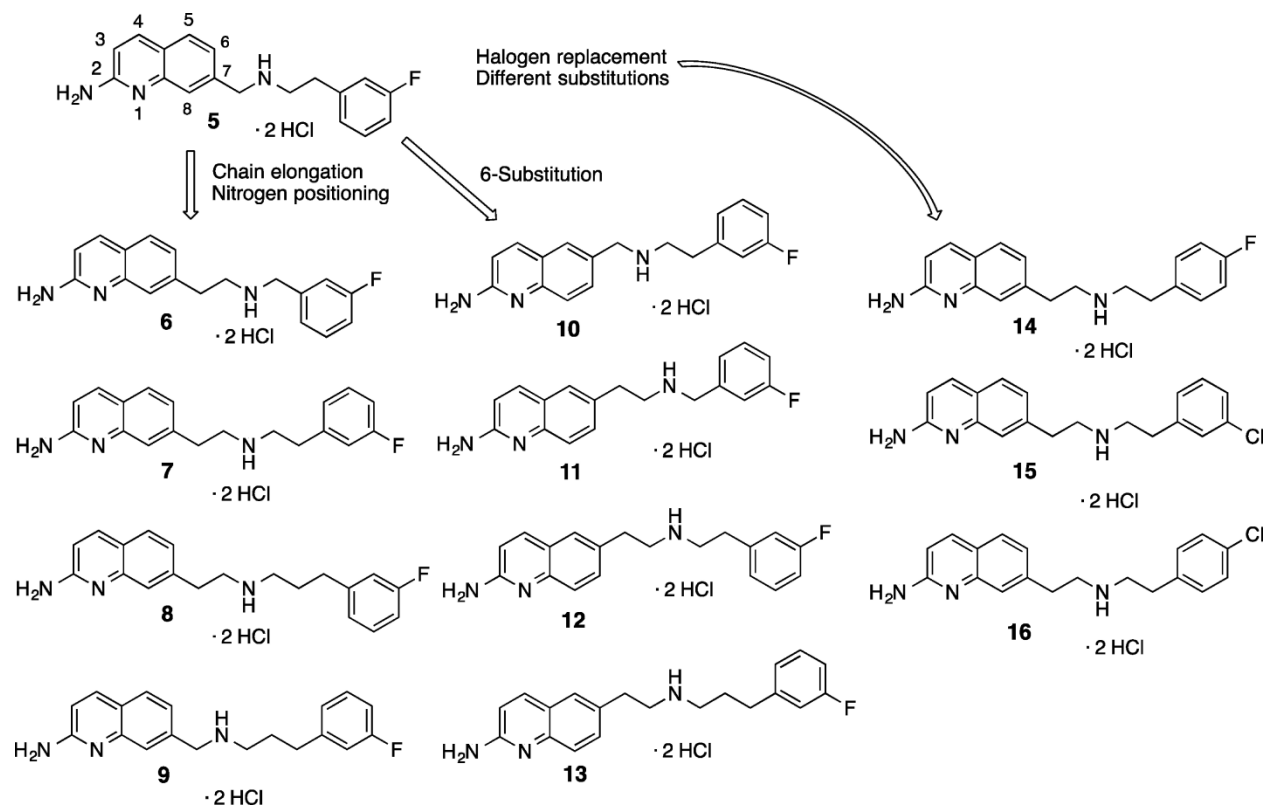
Figure 10.2 – Chemical structures and design strategy of nNOS inhibitors prepared in this study

171

EXPERIMENTAL PROCEDURES

Preparation and Characterization of Compounds, NOS inhibition assays and cellular

permeability assays

The syntheses and characterization (^{1}H NMR and ^{12}C NMR) of inhibitors, as well as the NOS inhibition and cell permeability assays were performed by Prof. Silverman's group, and are described in the manuscript that was published as a result of this collaboration.[263]

Inhibitor Complex Crystal Preparation

and

X-ray Diffraction Data Collection, Processing, and Structure Refinement

The nNOS or eNOS heme domain proteins used for crystallographic studies were produced as described in Chapter 8. Chapter 8 also describes the X-ray diffraction data collection, processing and structure refinement details. The refined structures were deposited in the RCSB Protein Data Bank. The crystallographic data collection and structure refinement statistics for the NOS-inhibitor complex structures are summarized in Table 10.1 with PDB accession codes included. For additional details, please refer to the published manuscript.[263]

Data Set	nNOS-**5**	nNOS-**6**	nNOS-**7**	nNOS-**8**
Data Collection				
PDB entry	4CAM	4CAN	4CDT	4CAO
Space group	$P2_12_12_1$	$P2_12_12_1$	$P2_12_12_1$	$P2_12_12_1$
Cell dimensions a, b, c (Å)	51.9, 111.1, 165.9	51.9, 111.3, 164.6	52.4, 111.8, 165.5	52.1, 111.5, 165.2
Detector	pixel array	pixel array	CCD	pixel array
Resolution (Å)	1.83 (1.93–1.83)	1.91 (2.01-1.91)	2.03 (2.07 -2.03)	1.98 (2.09-1.98)
R_{merge}	0.065 (1.815)	0.065 (1.638)	0.108 (0.799)	0.067 (1.366)
$CC_{1/2}$	99.9 (82.0)	99.9 (68.0)	99.9 (73.2)	99.9 (72.3)
I / σ	16.8 (1.3)	16.6 (1.2)	15.2 (1.1)	15.7 (1.3)
No. unique reflections	83,395	74,375	62,187	66,671
Completeness (%)	99.7 (99.8)	99.7 (99.7)	96.2 (83.6)	99.5 (98.4)
Redundancy	5.9 (6.0)	5.5 (5.6)	3.6 (2.6)	5.5 (5.5)
Refinement				
Resolution (Å)	1.83	1.91	2.00	1.98
No. reflections used	80,402	71,150	58,610	63,725
R_{work}/R_{free}	0.194/0.230	0.196/0.239	0.196/0.249	0.196/0.236
no. of protein atoms	6691	6671	6649	6649
no. of heteroatoms	173	173	185	187
no. of waters	317	247	183	179
rmsd bond length (Å)	0.011	0.013	0.016	0.015
rmsd bond angle (°)	1.44	1.56	1.88	2.20

Data Set	nNOS-**9**	nNOS-**15**	eNOS-**5**	eNOS-**7**
Data Collection				
PDB entry	4CAP	4CAQ	4CAR	4CFT
Space group	$P2_12_12_1$	$P2_12_12_1$	$P2_12_12_1$	$P2_12_12_1$
Cell dimensions a, b, c (Å)	51.8, 110.8, 165.2	52.1, 111.3, 165.2	57.8, 106.3, 156.7	57.8, 106.5, 156.9
Detector	pixel array	CCD	CCD	CCD
Resolution (Å)	2.06 (2.17-2.06)	1.95 (1.98-1.95)	2.05 (2.09-2.05)	1.80 (1.83-1.80)
R_{merge}	0.075 (1.580)	0.076 (1.000)	0.081 (0.704)	0.076 (0.713)
CC 1/2	99.9 (61.2)	n/a (71.7)	n/a	n/a (63.4)
I / σ	15.1 (1.2)	20.0 (1.2)	22.7 (2.1)	33.3
No. unique reflections	57,966	69,050	60,520	91,304
Completeness (%)	99.2 (99.2)	97.4 (97.6)	98.6 (95.4)	99.5 (97.2)
Redundancy	5.5 (5.2)	3.7 (3.6)	4.0 (3.9)	4.9 (3.3)
Refinement				
Resolution (Å)	2.06	1.95	2.05	1.80
No. reflections used	56,215	65,544	57,345	86,440
R_{work}/R_{free}	0.185/0.235	0.186/0.228	0.154/0.198	0.165/0.192
no. of protein atoms	6675	6658	6446	6429
no. of heteroatoms	175	174	199	198
no. of waters	218	262	386	325
rmsd bond length (Å)	0.017	0.011	0.019	0.01
rmsd bond angle (°)	2.32	1.45	1.97	1.38

Table 10.1 – Crystallographic data collection and refinement statistics

RESULTS AND DISCUSSION

Compounds **5–16** were assayed against purified rat nNOS, bovine eNOS, and murine macrophage iNOS using the hemoglobin capture assay, as previously described.[254, 279] The apparent K_i values and isoform selectivities are summarized in Table 10.2, and previously measured values for compounds **1**, **2**, **3** and **4** are included for comparative purposes.

Inhibitor no.	K_i (µM)			Selectivity	
	nNOS	iNOS	eNOS	n/i	n/e
1	0.014	4.1	28	293	2000
2	0.007	5.8	19.2	807	2676
3	0.011	1.6	0.9	149	82
4	0.035	5.0	3.5	143	100
5	0.075	9.14	0.485	124	6.2
6	0.254	24.5	7.77	97	30
7	0.049	44	11.16	899	228
8	0.164	31.9	7.25	194	44
9	0.06	32.3	3.69	538	62
10	>5.7	NT	NT	ND	ND
11	>5.7	NT	NT	ND	ND
12	>5.7	NT	NT	ND	ND
13	4.37	NT	NT	ND	ND
14	0.183	51.2	8.86	280	37
15	0.066	28.4	7.24	431	110
16	0.212	19.2	9.89	91	47

Table 10.2 – K_i and isoform selectivity values of inhibitors for rat nNOS, bovine eNOS and murine iNOS. K_i values were calculated from the IC_{50} values. All experimental standard error values are less than 14% and all correlation coefficients are >0.81. NT = not tested; ND = not determined.

Compound **5** has potent nNOS inhibitory activity (74 nM) and high n/i selectivity (124-fold), but has poor n/e selectivity (around 6-fold). The crystal structures of **5** bound to both nNOS and eNOS (Figure 10.3a and b, respectively) indicate that the bound conformation of **5** is virtually identical in both isoforms. In both cases, the aminoquinoline acts as an arginine mimic and interacts with the active site glutamate as arginine does (Glu592 in nNOS (PDB entry 1OM4); Glu363 in eNOS (PDB entry 2NSE),[62] while the secondary amine sits between the heme propionates, making H-bonds to both. To simultaneously establish hydrogen bonds between the aminoquinoline and Glu592, as well as between the secondary amine and both heme propionates,

the rigid quinoline plane must tilt significantly from the heme plane. The fluorophenethyl moiety, as predicted from the short linker length, does not quite reach the hydrophobic pocket (Figure 10.3) consisting of Tyr706, Leu337, Met336, and Trp306 in nNOS (Tyr477, Leu107, Val106, and Trp76 in eNOS). Contact with these residues has been shown to improve potency and isoform selectivity.[277-278] Similar to the crystal structure of **3** (Chapter 9, Figure 9.8A and C), these contacts are absent in **5**, thus explaining the poor n/e selectivity.
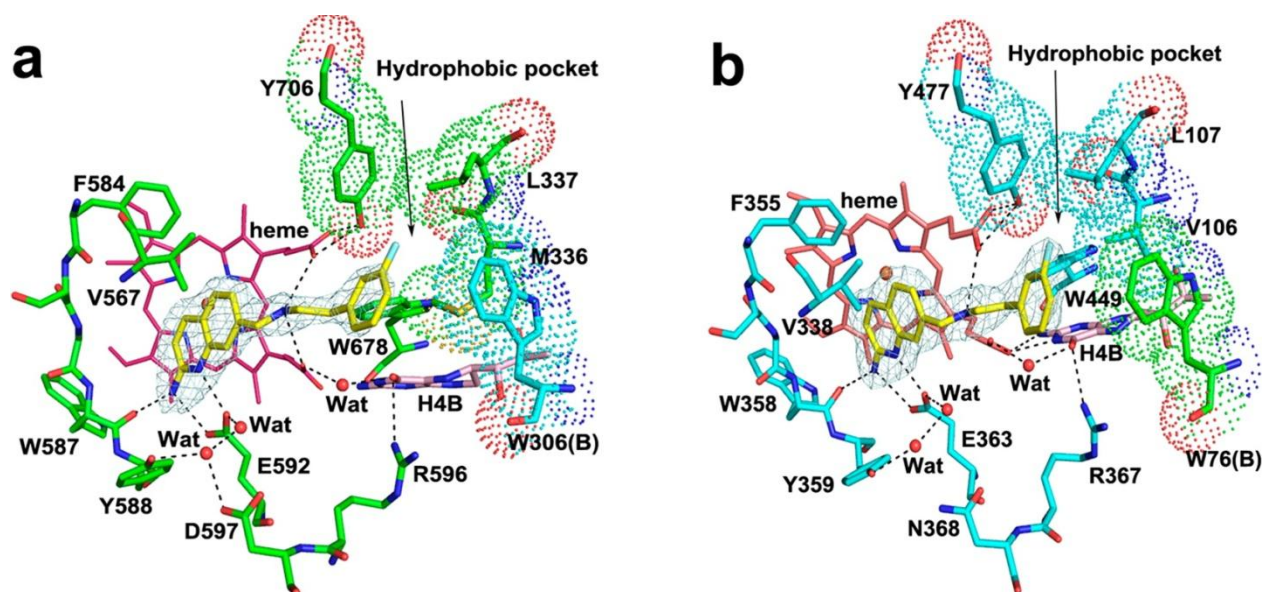
Figure 10.3 –Crystal structures of inhibitor 5 bound to nNOS and eNOS
(a) Active site of nNOS-**5** complex (b) Active site of eNOS-**5** complex. The omit $F_o – F_c$ density map for the inhibitor is shown at the 2.5 σ contour level. Major hydrogen bonds are shown as dashed lines. In each panel, the four residues that line a hydrophobic pocket are highlighted by a dot surface representation. While residues in chain A of nNOS (a) and eNOS (b) are colored green and cyan, respectively, the residue from chain B (second monomer in the homodimeric structure) is distinguished by a different color. The same color scheme is used in the other figures in this chapter. All molecular graphics shown in this chapter were prepared using PyMOL.[170]

For aminoquinoline compounds **6-9**, the chain was elongated by adding extra methylene groups on either side of the amine group. Two factors affect the potency of the inhibitors in this series of compounds: the linker length and the position of the amine group. The structure of the nNOS-**6** complex (Figure 10.4a) reveals that placing two carbons between the quinoline and the amine weakens the interaction with the heme propionates (more than 3.6 Å distance), leading to increased flexibility as evidenced by the disordered fluorophenethyl tail in the structure of **6** and

lower potency compared to **5**. Superposition of nNOS-**5** and nNOS-**6** (Figure 10.4b) reveals that the absence of H-bonding interactions between the amine of **6** and the heme propionates allows the quinoline to assume a more parallel orientation relative to the heme than observed in the structure of **5**. However, since the 4-atom linker of **5** and **6** is not long enough to bring the fluorophenyl ring in contact with the hydrophobic pocket (Figure 10.3), the majority of the stabilization results from hydrogen bonds between the aminoquinoline and the linker amine. Therefore, **5**, with an extra hydrogen bond, is a stronger inhibitor than **6**.
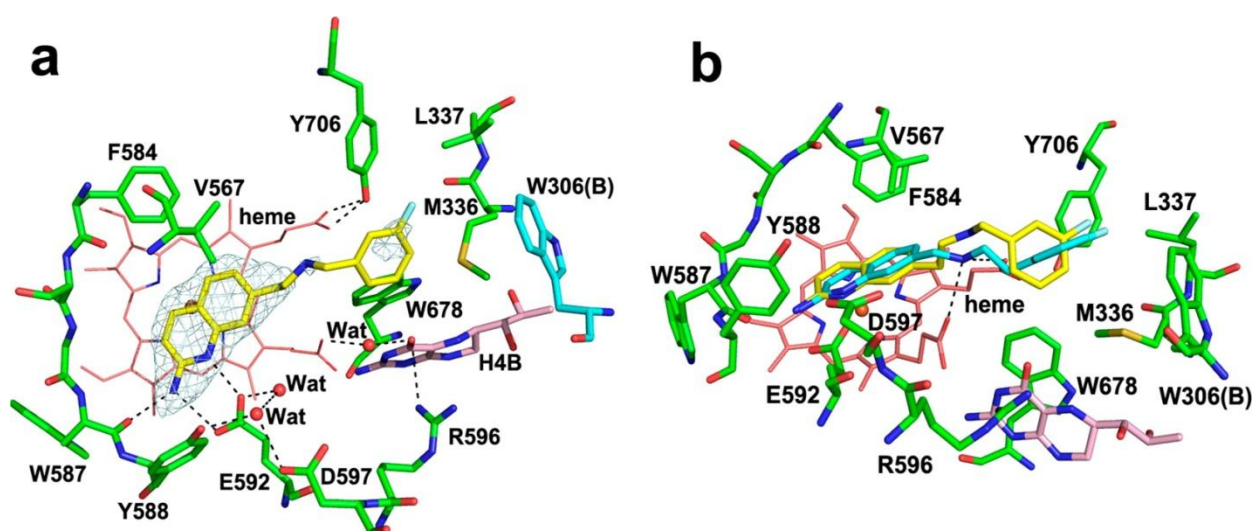
Figure 10.4 –Crystal structures of inhibitor 6 bound to nNOS
(a) Active site of nNOS-**6** complex. The omit $F_o - F_c$ density map for the inhibitor is shown at the 2.5 σ contour level. The fluorophenyl tail is partially disordered with weaker density. (b) Overaly of **5** (cyan) and **6** (yellow) in nNOS. The different tilt angles of the aminoquinoline ring relative to the heme plane is in part related to whether hydrogen bonds (dashed lines) from the heme propionates to the linker amine are present (**5**) or absent (**6**).

In general, compounds with shorter linkers (**5** and **6**) were found to have lower nNOS inhibitory activity than compounds with longer linkers (**7** and **9**, Table 10.2). The data suggest that the ideal chain length is five atoms between the quinoline and fluorophenyl groups. The omit electron density map reveals a disordered fluorophenyl tail for compound **7** (Figure 10.5a), suggesting that the lack of a strong secondary amine–heme propionate loosens the tail, making it more flexible. This is made more evident when compared to binding of compound **9**, which shows an amine–propionate interaction and a well ordered fluorophenyl tail. Compounds **7** and **9**

exhibit very similar nNOS inhibitiory potency (Table 10.2), suggesting that the position of the amine nitrogen is not a crucial factor in potency for these inhibitors that have longer linkers. This is most likely because the hydrophobic pocket in nNOS provides additional stabilization that compensates for the weakened H-bond between the amine and the propionates. The structure of nNOS-**9** (Figure 10.5b) shows numerous favorable hydrophobic contacts between the fluorophenyl group and the nonpolar residues at the far end of the substrate access channel, Tyr706, Leu337, Met336, and Trp306 of the other monomer. Although the tail of **7** (Figure 10.5a) is more disordered than that of **9** (Figure 10.5b), these hydrophobic contacts exist with **7** as well. Therefore, when the linker is long enough to allow contact between the fluorophenyl ring and the hydrophobic pocket, the strong combined stabilization from both the hydrophobic interactions and the aminoquinoline–Glu592 interaction may outweigh any lack of interaction between the secondary amine and heme propionates.
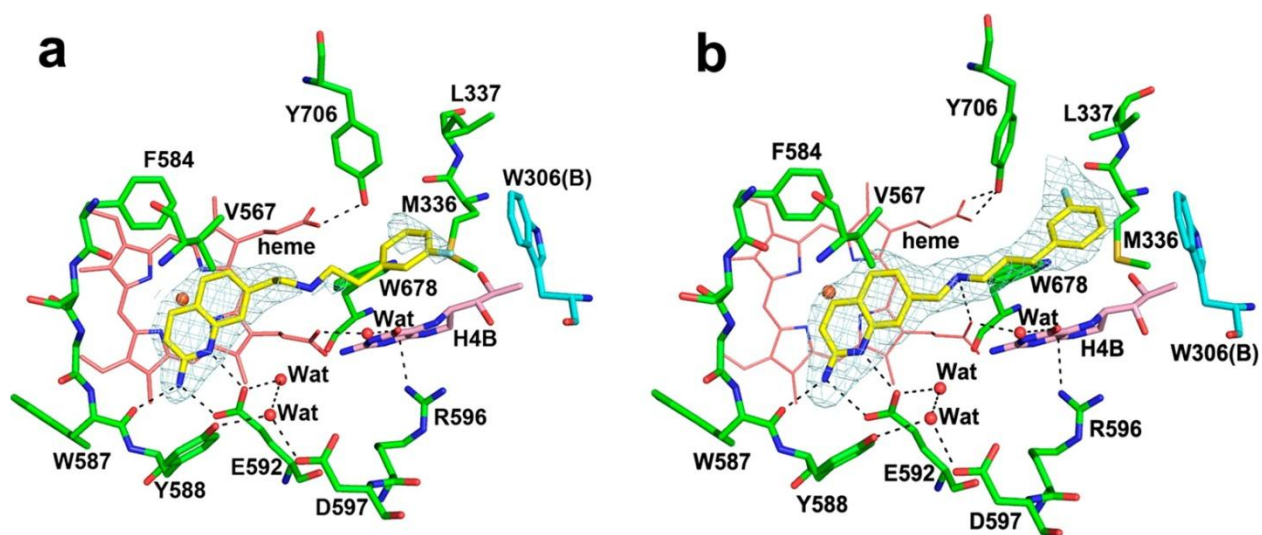
Figure 10.5 –Crystal structures of inhibitor 7 and 9 bound to nNOS
(a) Active site structure of nNOS-**7** complex. (b) Active site structure of nNOS-**9** complex. The omit $F_o – F_c$ density map for the inhibitor is shown at the 2.5 σ contour level. Density for the fluorophenyl tail of **7** is weak, indicating partial disorder. Major hydrogen bonds are depicted as dashed lines.

Compound **8**, with six atoms between the quinoline and fluorophenyl group has a lower inhibitory potency compared to **7** or **9**, suggesting that a chain length longer than five atoms

reduces efficiency. The crystal structure of nNOS-**8** (Figure 10.6a) shows that the fluorophenyl ring of **8** makes hydrophobic contacts similar to those of **7** and **9**, but assumes a kinked conformation compared to nNOS-**9** (Figure 10.5b). This kinked conformation seen in nNOS-**8** may cause unfavorable torsional strain in the linker region upon binding, accounting for the reduced potency.
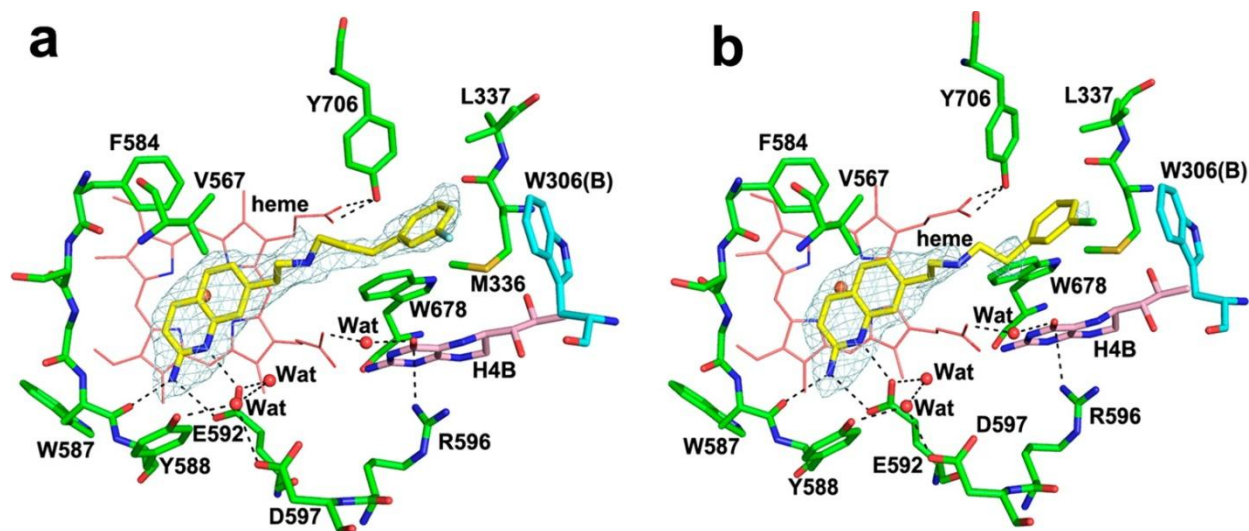
Figure 10.6 – Crystal structures of inhibitor 8 and 15 bound to nNOS
(a) Active site structure of nNOS-**8** complex. (b) Active site structure of nNOS-**15** complex. The omit $F_o - F_c$ density map for the inhibitor is shown at the 2.5 σ contour level. The chlorophenyl tail of **15** is partially disordered. Major hydrogen bonds are depicted as dashed lines.

The 2-amnioquinoline group itself has been shown to exhibit weak iNOS inhibitory activity (1.7 μM).[280] Our results corroborate these findings and also show that 7-substituted 2-aminoquinolines are generally very poor iNOS inhibitors. Compounds **7**, **9**, and **15** have K_i values of 44 μM, 32.3 μM, and 28.4 μM, respectively, and **7** has nearly 900-fold n/i selectivity, which is significantly higher than those of **1**–**4**. The reason for this poor inhibition and much much greater nNOS selectivity could be partly due to contact with the hydrophobic pocket. Murine iNOS contains a polar Asn115 instead of Leu337 of nNOS, which would weaken binding of a hydrophobic group. Also, the iNOS active site is smaller and more rigid compared to nNOS,[277] which may explain why binding of the aminoquinoline is less favored. What about

n/e selectivity? Higher n/e selectivity is exhibited by compounds whose binding are stabilized by H-bonds between the center pyrrolidine ring and Asp597 in nNOS (Asn369 in eNOS).[250] In other cases, n/e selectivity can also be increased by tighter π-stacking with Tyr706 of nNOS than with the analogous Tyr477 of eNOS.[250] While no clear π-stacking interactions are visible in the nNOS crystal structures of **6**, **7**, **8**, or **9**, other hydrophobic contacts may contribute to n/e selectivity for aminoquinolines. The binding mode of the aminoquinoline portion is identical in the structure of nNOS-**7** (Figure 10.5a) or eNOS-**7** (Figure 10.7) and does not contribute to isoform selectivity. What we do notice, however, is that the length of the linker in **7** allows the fluorophenyl ring to come into close hydrophobic contact with the Met336 residue in nNOS (Val106 in eNOS). Also, the side chain of Tyr706 in nNOS rotates by about 60° and is able to make better nonbonded contacts with the tail of **7**, which does not seem to occur for Tyr477 in eNOS (Figure 10.7). These observations may also explain why **7** is more selective than **9**.
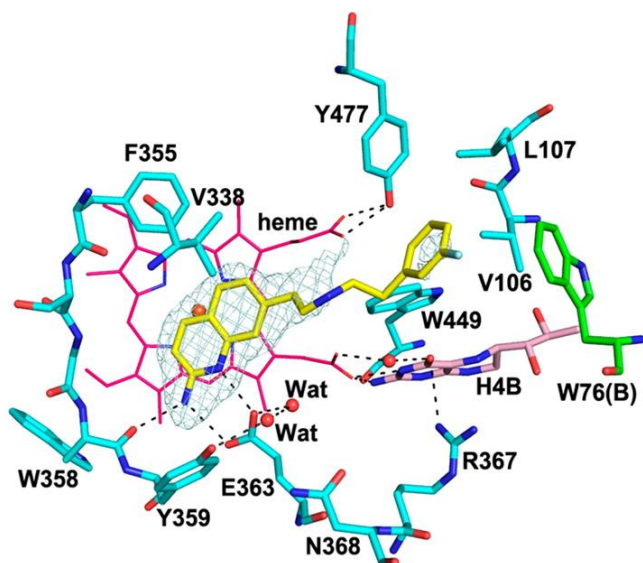
Figure 10.7 –Crystal structure of inhibitor 7 bound to eNOS
(a) Active site structure of eNOS-**7** complex. The omit $F_o - F_c$ density map for the inhibitor is shown at the 2.5 σ contour level. Density for the fluorophenethyl tail of **7** is weaker, indicating the tail is partially disordered. Major hydrogen bonds are depicted as dashed lines.

While 7-substituted aminoquinolines (**5**–**9** and **14**–**16**) are all highly potent against nNOS, the analogous 6-substituted aminoquinolines **10**–**13** have low potency, regardless of chain length or nitrogen position. The crystal structures of the 2-aminoquinoline compounds reveal that the lower potency for 6-substituted compounds is due to steric clash that would be caused by the large Val567 and Phe584 residues and heme propionates if it were to bind in the same mode as 7-substituted compounds.

The fluorine in **7** was replaced with a bulkier chlorine to make compound **15**. The larger group has little effect on nNOS inhibitory potency or isoform selectivity. Structurally, the binding mode of **15** to nNOS (Figure 10.6b) is very similar to that of **7** (Figure 10.5a). Without a strong interaction between the amine and the heme propionates, the chlorophenethyl tail is partially disordered but can still be located based on partial density when contoured at 0.5 σ. In this model, the chlorine atom is not pointing directly into the hydrophobic pocket, so the switch between chlorine and fluorine should not significantly alter contacts with the enzyme. As for the position of the fluorine or chlorine group, the 4-position results in lower potency in both cases (compounds **14** and **16**), probably because of steric clashes of the 4-substituent with Met336 and Leu337 in the hydrophobic pocket.

Finally, compounds **7** and **15** were assayed by the Silverman group in a Caco-2 monolayer permeability assay. This assay is an approximation of both a compound's ability to penetrate the epithelium of the GI tract as well as the blood–brain barrier.[264-266] The results showed that both compounds **7** and **15** displayed good membrane permeability, with **15**

exhibiting more permability than **4** and **7**. For more details on the Caco-2 asssay and results, please refer to the published manuscript.[263]

Conclusions

The Silverman-Poulos collaboration has once again furthered the search for a potent, selective and permeable nNOS inhibitor. In this chapter, we have seen how a novel series of simplified 2-aminoquinolines designed by Dr. Cinelli to preserve the potency and selectivity of arginine mimetics while having reduced polarity and increased hydrophobicity, therefore increasing their bioavailability. Inhibition assays and structural data have revealed that 7-substituted 2-aminoquinolines with a chain length of five atoms between the aminoquinoline and aryl ring are highly potent and selective inhibitors of nNOS. We have solved the crystal structures which reveal the binding mode of these inhibitors to the NOS active sites and provide a structural basis for the different observed potencies and selectivities. The aminoquinoline portion is stabilized by two H-bonds to the active site Glu592, while the aryl rings are stabilized in a hydrophobic pocket on the far end of the substrate access channel. Since this pocket is more hydrophobic for nNOS than eNOS, compounds **7** and **15** were able to make just the right contacts, thus exhibiting higher n/e selectivity. Finally, results from permeability assays have confirmed that compounds **7** and **15** are quite promising, which provides a direction for future nNOS inhibitor development that involves fragment hopping and tweaking of 7-substituted-2-aminoquinolines.

NITRIC OXIDE SYNTHASE INHIBITORS THAT INTERACT WITH BOTH HEME PROPIONATE AND TETRAHYDROBIOPTERIN SHOW HIGH ISOFORM SELECTIVITY

Chapter 11

Summary

In this fourth chapter describing efforts to develop better nNOS inhibitors, we explore another strategy for inhibitor design. The approach described in this chapter is to develop inhibitors that are stabilized by interactions both in the substrate L-Arginine binding pocket, as well with cofactor H_4B. To address this, Dr. Soosung Kang and our collaborators in the Silverman group developed a series of six α-amino functionalized aminopyridine derivatives (**3-8**). Compound **8R** was identified as exhibiting the highest inhibitory potency against nNOS (K_i = 24 nM), and highest isoform selectivity, with 273-fold higher n/i selectivity, and 2822-fold higher n/e selectivity. Free energy calculations reveal that the much greater selectivity is most likely due to the electrostatic environment that stabilize binding of **8R**. Once again, the results disccused in this chapter offers a new route for inhibitor design that appears quite promising.

The work described in this chapter was primarily designed by Dr. Soosung Kang and our collaborators in Dr. Richard Silverman's laboratory. I am a co-author on the mansucript that was published as a result of this collaboration, and my contribution to this work included solving the crystal structures of eNOS in complex with the inhibitors in order to structurally address the potency/specificity issues and help guide the design of future inhibitors. This chapter is an adaptation of a portion of the text and multiple images from our published work.[281]

New concepts?

Binding free-energy: For an inhibitor, the thermodynamic free-energy change (ΔG) that occurs when an inhibitor binds to a target protein and forms a protein-inhibitor complex. This value is useful to predict whether a particular molecule will be a potent inhibitor.

INTRODUCTION

The inhibitor design approach used in this chapter takes advantage of several structural features of NOS. To recap, H4B forms tight H-bonds with heme propionate A and is stabilized by residues from both subunits of the dimer, stabilizing the dimer as a whole.[224, 282] Since additional stability will increase inhibitory potency, the strategy employed in this study is to design inhibitors that interact with the active site while also making contact with residues in the pterin binding pocket, which has been successful in the past. Our collaborators in the Silverman group have therefore prepared a new series of inhibitors that simplify synthesis while maintaining the crucial interactions that stabilize inhibitor binding in nNOS. A series of six double headed 2-aminopyridine compounds (Figure 11.1) were therefore prepared with various amino functional groups and stereochemistries. Compounds **3** to **5**, with a central α amino group were synthesied first and their crystal structures in a complex with nNOS guided the synthesis of compounds **6-8**, which have a central methylamino group. Once again, these inhibitors were probed using inhibitory assays against all three NOS isoforms and by X-ray crystallography to provide a structural basis for the observed potencies and selectivities.
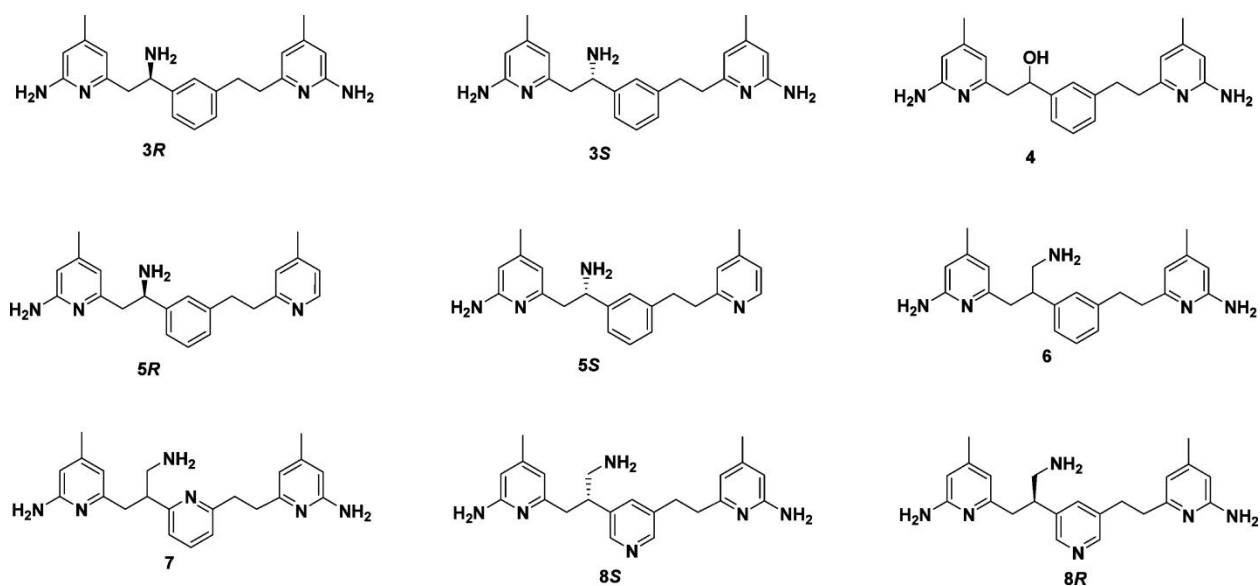
Figure 11.1 – Chemical structures of nNOS inhibitors prepared in this study

EXPERIMENTAL PROCEDURES

Preparation and Characterization of Compounds, NOS inhibition assays

and MM-PBSA compuational calculations

The syntheses and characterization (^{1}H NMR and ^{12}C NMR) of inhibitors, the NOS inhibition assays, as well as the computational calculations were performed by Prof. Silverman's group, and are described in the manuscript that was published as a result of this collaboration.[281]

Inhibitor Complex Crystal Preparation

and

X-ray Diffraction Data Collection, Processing, and Structure Refinement

The nNOS or eNOS heme domain proteins used for crystallographic studies were produced as described in Chapter 8. Chapter 8 also describes the X-ray diffraction data collection, processing and structure refinement details. The refined structures were deposited in the RCSB Protein Data Bank. The crystallographic data collection and structure refinement statistics for the eNOS-inhibitor complex structures are summarized in Table 11.1 with PDB accession codes included. For statistics on the nNOS-inhibitor structures and other details, please refer to the published manuscript.[281]

Data Set	eNOS-**3R**	eNOS-**5S**	eNOS-**8R**	eNOS-**8S**
	Data Collection			
PDB entry	4CTY	4CTZ	4CU0	4CU1
Space group	$P2_12_12_1$	$P2_12_12_1$	$P2_12_12_1$	$P2_12_12_1$
Cell dimensions a, b, c (Å)	57.8, 106.5, 156.8	58.0, 106.7, 158.4	57.9, 106.4, 156.9	57.3, 105.2, 155.0
Resolution (Å)	2.30 (2.34-2.30)	2.00 (2.03-2.00)	2.09 (2.13-2.09)	1.90 (1.93-1.90)
R_{merge}	0.090 (0.761)	0.058 (0.566)	0.063 (0.703)	0.085 (>1.000)
I / σ	15.7 (1.9)	34.8 (2.2)	26.1 (2.1)	28.5 (1.2)
No. unique reflections	43,670	65,590	57,825	74,481
Completeness (%)	98.9 (99.8)	98.5 (100.0)	99.3 (100.0)	99.0 (99.8)
Redundancy	3.7 (3.7)	4.1 (4.3)	3.6 (3.6)	4.7 (4.2)
	Refinement			
Resolution (Å)	2.30	2.01	2.09	1.90
No. reflections used	41,276	62,115	55,687	70,704
R_{work}/R_{free}	0.161/0.219	0.165/0.205	0.166/0.214	0.170/0.205
no. of protein atoms	6454	6446	6438	6438
no. of heteroatoms	207	197	193	200
no. of waters	333	271	291	295
rmsd bond length (Å)	0.015	0.019	0.019	0.011
rmsd bond angle (°)	1.72	1.97	1.96	1.55

Table 11.1 – Crystallographic data collection and refinement statistics for the eNOS-inhibitor complex structures

RESULTS AND DISCUSSION

The inhibitory assays were performed by our collaborators in the Silverman group and the values are reported in Table 11.2. Enantiomers **3S** and **3R**, with α-amino group and two symmetric aminopyridine head groups, as well as compound **4**, with α-hydroxyl group instead, exhibited good potencies, with K_i values around 100 nM. Enantiomers **5S and 5R**, also α-amino tailed but with two asymmetric head groups, exhibited the lowest potencies to nNOS with K_i values of 903 and 4370 nM, respectively.

The remaining compounds **6**, **7** and **8**, with a central α-aminomethyl and two aminopyridine head groups, showed improved potency by up to 5-fold compared to the other compounds, with **8** having the lowest K_i of 30 nM. The most encouraging results are the excellent isoform selectivities, especially for compounds **7** and **8**, with over one hundred-fold n/i selectivities, up to 138-fold for **7** and several hundred-fold n/e selectivities, as high as 1072-fold for **7** and 544-fold

for **8**. This suggests that although the α-aminomethyl group does not result in much improved potency against nNOS, it does greatly improve selectivity.

| Inhibitor | Ki (nM) | | | Selectivity | |
	nNOS	iNOS	eNOS	n/i	n/e
3S	0.144	17.670	70.900	123	492
3R	0.122	15.620	14.390	128	118
4	0.070	5.990	3.610	86	52
5S	0.903	>100	328	>110	363
5R	4.370	>100	1049	>22	240
6	0.053	1.894	4.770	36	90
7	0.123	17.916	133.174	138	1072
8	0.030	2.810	16.0	95	544
8S	0.070	4.386	19.417	105	276
8R	0.024	6.629	68.520	273	2822

Table 11.2 – K_i and isoform selectivity values of inhibitors for rat nNOS, bovine eNOS and murine iNOS.

Based on the promising results obtained with compound **8**, each enantiomer was assayed separately. Compound **8R** showed excellent potency (K_i = 24 nM) for nNOS, a 273-fold n/i selectivity and a 2822-fold n/e selectivity, meaning that **8R** has the highest n/e selectivity in this series of inhibitors. Human nNOS (HnNOS) has a slightly different hydrophobic pocket than rat nNOS (Leu336 is His342 in HnNOS), and in this series of double-headed inhibitiors, the second headgroup extends and is stabilized by interactions with residues in this hydrophobic pocket. Therefore, compound **8** was also assayed against HnNOS and exhibited excellent inhibitory potency, with a K_i value of 90 nM.

We determined the crystal structures of nNOS in complex with the inhibitors in order to provide a structural basis for the measured values. We started with **3S**, **3R**, **4**, and **5**, all of which have a central α-amino group. Both **3S** and **3R** are able to bind nNOS with both aminopyridine heads, the first head H-bonding with Glu592 and the second with the heme propionate D (Figure 11.2). The central α-amino group helps stabilize the double-headed binding. Interestingly, the

binding orientation of **3** is dependent on the chirality leading to different positions for the α-amine. The α-amino group of **3S** is next to the aminopyridine that H-bonds with Glu592 and points downward to the heme (Figure 11.2A), while the α-amino group of **3R** is on the side of the aminopyridine that H-bonds with the heme propionate D (Figure 11.2B).

Compound **4**, with a hydroxyl group replacing the central α-amino group can no longer achieve a double-headed binding (Figure 11.2C). Instead, the aminopyridine H-bonds with Glu592 and the second aminopyridine is no longer H-bonding with the protein, as evidenced by the weak density for that portion of the molecule. Crystal structures of nNOS-**5** reveals the basis for the poor observed potency. Its aminopyridine is able to bind similarly to the other compounds, but the 4-methylpyridine head is not stabilized by any interaction, as evidenced by the poor electron density (Figure 11.2D). The α-amino nitrogen is also able to H-bond with Glu592, but this causes the phenyl ring to bend toward the heme in a kinked orientation.
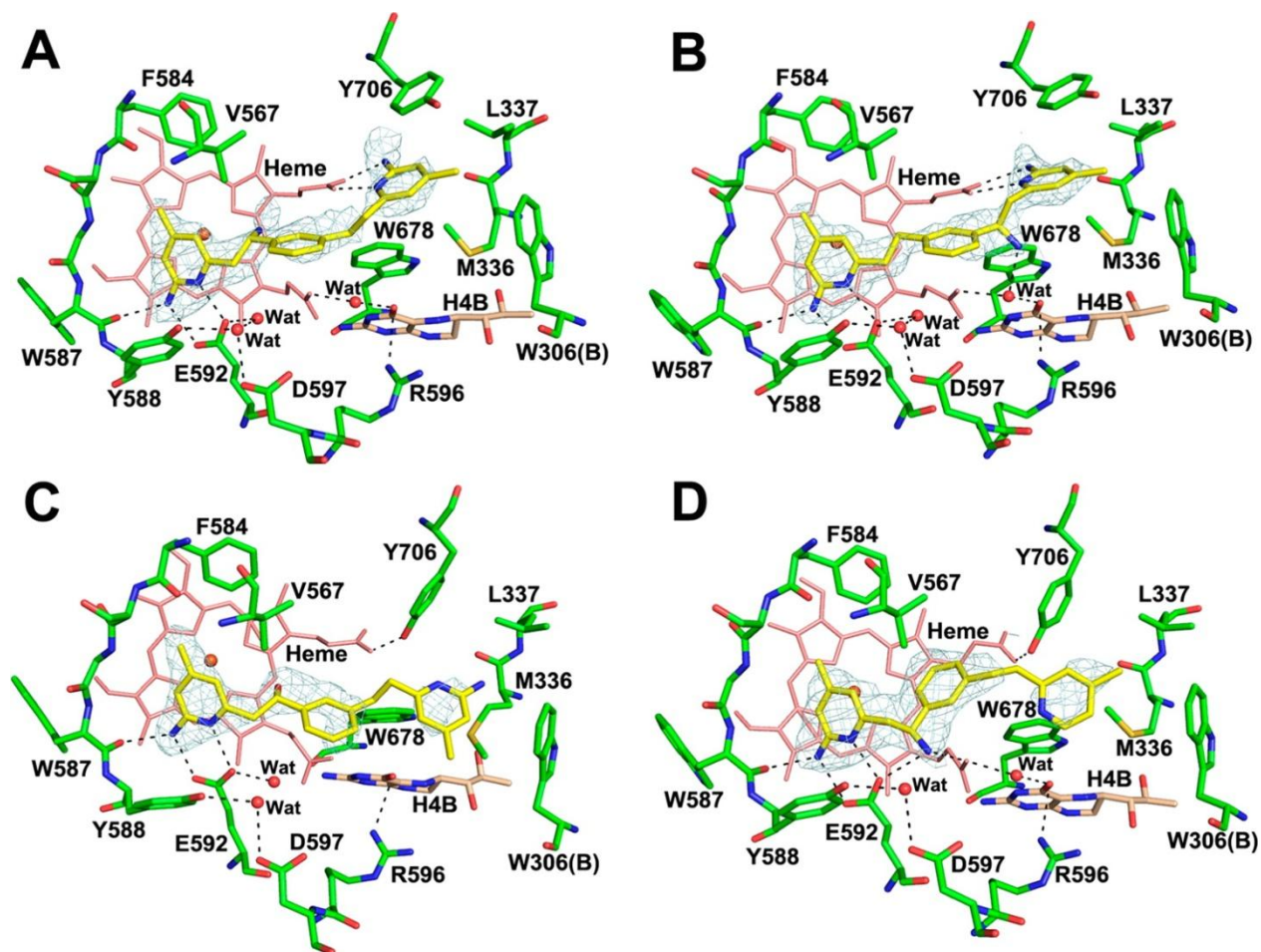
Figure 11.2 –Crystal structure of inhibitors 3,4 and 5 bound to nNOS
Active site structure of the (A) nNOS-**3S** complex, (B) nNOS-**3R** complex, (C) nNOS-**4** complex, (D) nNOS-**5** or **-5S** complex. The omit $F_o - F_c$ density map for the inhibitor is shown at the 2.5 σ contour level. Density for the tail portions of **4** and **5** is weaker, indicating the tail is partially disordered. Major hydrogen bonds are depicted as dashed lines. All molecular graphics shown in this chapter were prepared using PyMOL.[170]

To probe the structural basis for n/e selectivity, we determined the crystal structures of

3S, **3R**, and **5S** bound to eNOS. In the eNOS-**3S** structure (data not shown), the density was so

poor that only one aminopyridine could be modeled H-bonding to Glu363, with the rest of the

compound being disordered, which prevented us from obtaining a fully refined structure.

Clearly, eNOS-**3S** cannot have the same double-headed binding mode as nNOS-**3S**, which

explains the good n/e selectivity. The eNOS-**3R** structure, however, reveals that this enantiomer

is able to bind in a double-headed mode (Figure 11.3A), similar to nNOS-3R, which explains

why the n/e selectivity for 3R is not as high as for 3S (although it remains over 100-fold n/e selectivity). The structure of eNOS-**5S** (Figure 11.3B) reveals a different binding mode than for nNOS-**5S**, where the α-amino group does not directly H-bond with Glu363, but to a water that links the two groups. This places the α-amino group of the inhibitor near Glu592 and Asp597 for additional electrostatic stabilization. In eNOS, Asp597 is replaced with Asn368, which explains the 363-fold higher n/e selectivity measured for **5S** (Table 11.2).
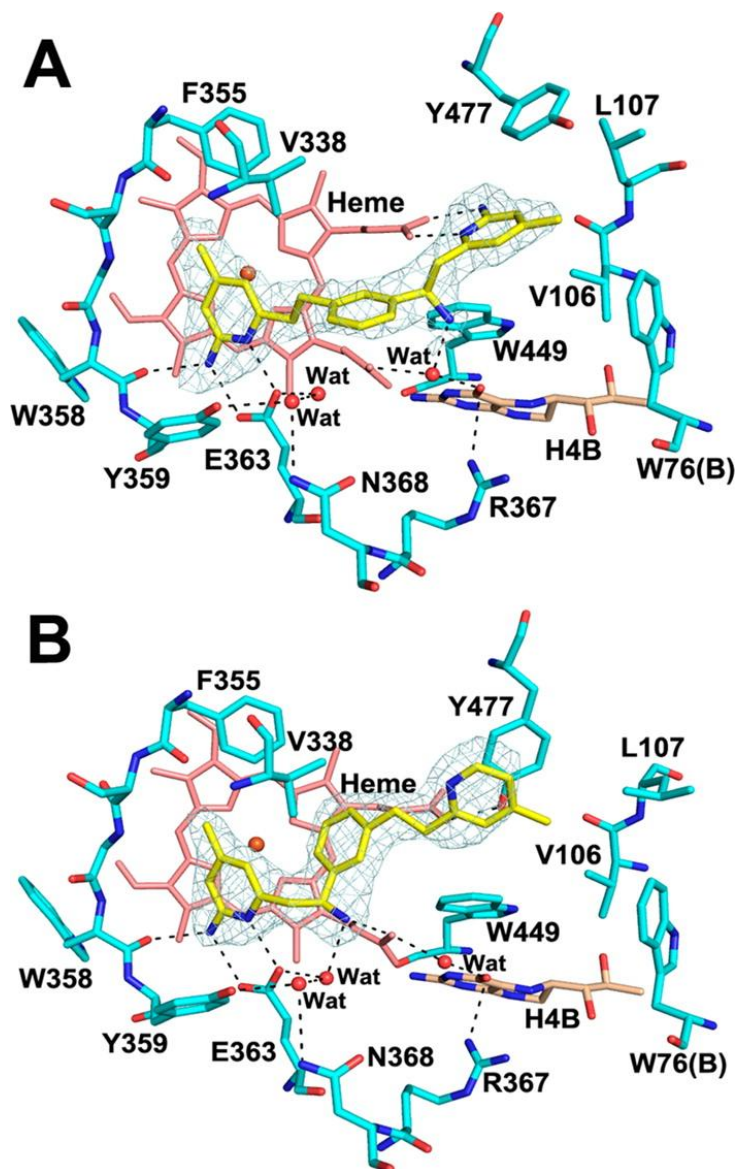
Figure 11.3 – Crystal structure of inhibitors 3R and 5S bound to eNOS
Active site structure of the (A) eNOS-**3R** complex, (B) nNOS-**5S** complex. The omit $F_o - F_c$ density map for the inhibitor is shown at the 2.5 σ contour level. Major hydrogen bonds are depicted as dashed lines.

The next compounds **6**, **7**, and **8** had an aminomethyl group replacing the amine (Figure 11.1). The crystal structures of **6** and **8** bound to nNOS showed that they share a similar double-headed binding mode (Figure 11.4), and that the R-enantiomer is the one that binds the active site. The inhibitory assays indicated that 6 and 8 indeed have improved potency (Table 11.2). The structure of nNOS-**6R** (Figure 11.4A) shows a similar binding mode to nNOS-**3R** (Figure 11.2B), with the newly added aminomethyl group H-bonding with both H_4B and heme propionate A. This increased stabilization explains the 2-fold increase in potency compared to **3**. The structure of nNOS-**8** (Figure 11.4B) shows that the pyridine ring forms H-bonds with the solvent waters and with Gln478. The added stability compared to nNOS-**6R** explains why **8** exhibits greater potency.

Crystal structure of nNOS-**7** (Figure 11.4C) shows preferred binding of the **7S**-enantiomer over the **7R**, in a 180° flipped orientation compared to **8** (Figure 11.4B). Even though this flipped orientation negatively affects inhibitory potency when compared to **6** or **8**, it does result in an improved selectivity for the nNOS isoform. We tried to probe the basis for n/e isoform selectivity, but were unfortunately unable to obtain a good structure of eNOS-**7**, because the electron density for the inhibitor was too weak, indicating weak binding. Based on the structure of eNOS-5S (Figure 11.4B) the poor binding of **7** is most likely due to a lack of H-bonding interactions between its aminomethyl group and Glu363.
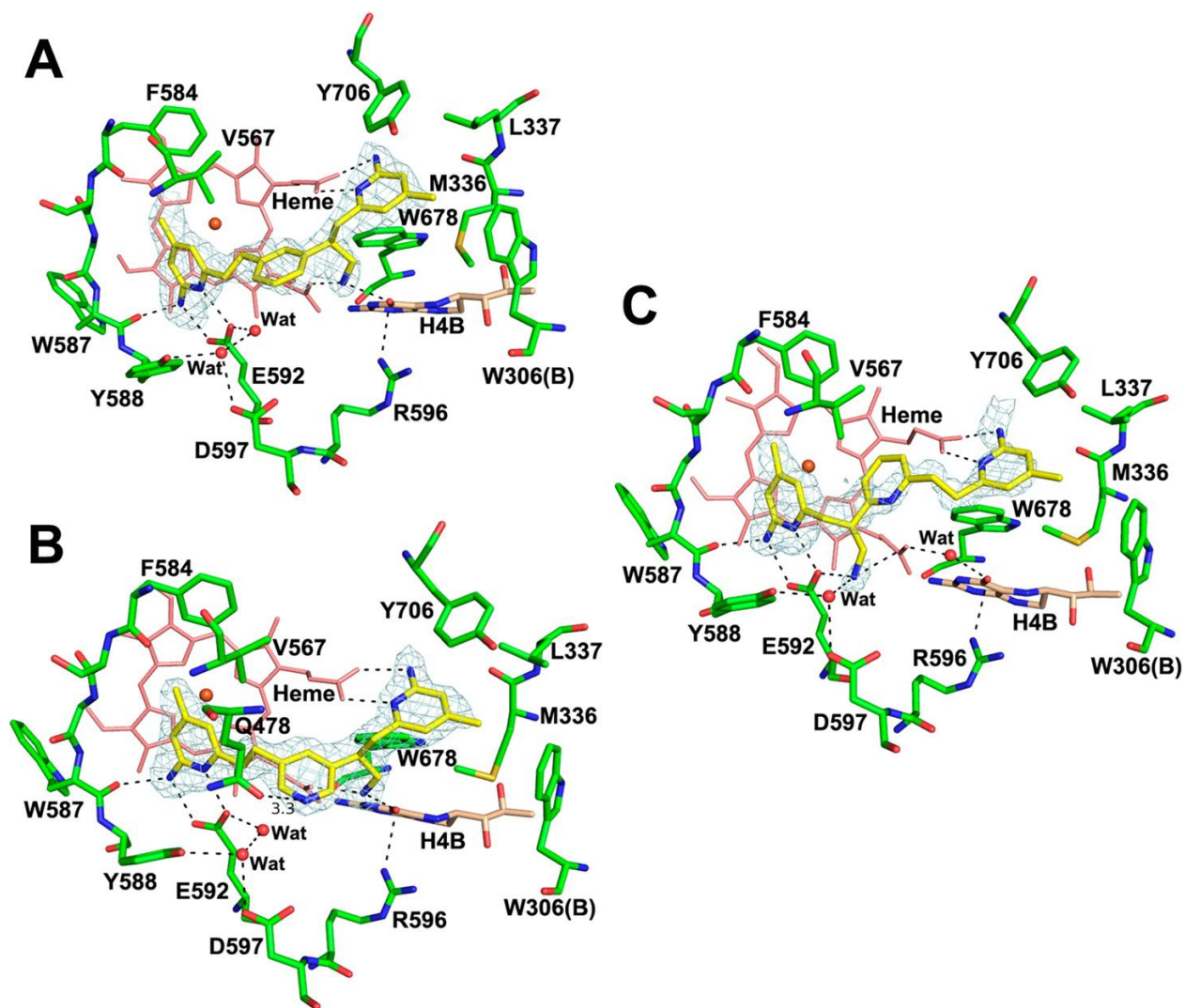
Figure 11.4 – Crystal structure of inhibitors 6, 7 and 8 bound to nNOS
Active site structure of the (A) eNOS-**6** or **6R** complex, (B) nNOS-**8** or **8R** complex. (C) nNOS-**7 or 7S** complex. The omit $F_o – F_c$ density map for the inhibitor is shown at the 2.5 σ contour level. Major hydrogen bonds are depicted as dashed lines.

Since compound **8** exhibits the best nNOS inhibitory potency in this series of inhibitors, the next step was to probe the role and contribution of chirality. Dr. Kang therefore prepared enantiopure compounds **8S** and **8R**, which revealed that the **8R** enantiomer gives the best inhibitory potency against nNOS (24 nM) and an excellent 2822-fold n/e selectivity (Table 11.2). Crystal structures of nNOS with both enantiomers show similar double-headed binding modes, and confirms that the nNOS-**8** structure is really **8R** (Figure 11.4B). On the other hand, the

192

nNOS-**8S** structure (Figure 11.5A) shows slight variations, mostly around the chiral center, and a stronger H-bond between the center pyridine group of **8S** and Gln478. As for the structural basis for n/e selectivity, the eNOS-**8S** structure (Figure 11.5B) reveals a one-headed binding mode, with the second aminopyridine exhibiting weak electron density, unable to find a stable H-bond with the heme propionate D. Unfortunately, the eNOS-**8R** structure did not reveal an obvious structural basis for the impressive n/e selectivity we observe (Figure 11.5C). The Silverman group therefore used a computational approach to determine the basis for such high n/e selectivity by calculating and comparing the ΔG of binding to nNOS and eNOS. The results indicate that the selectivity difference arises from more favorable electrostatic interactions in nNOS than eNOS. For additional details, please refer to the published work.[281]
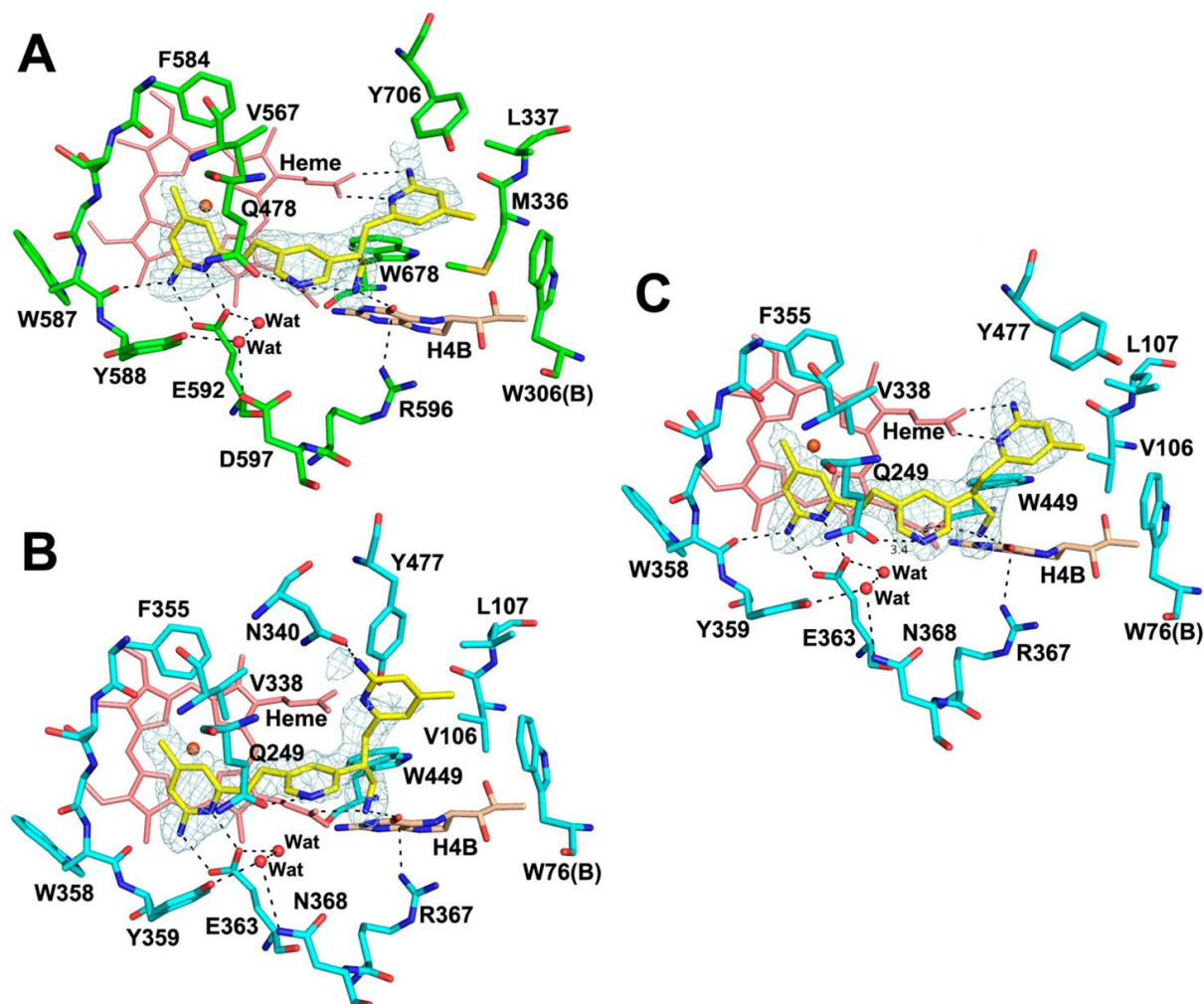
Figure 11.5 – Crystal structure of inhibitors 8S bound to eNOS and of 8S and 8R bound to nNOS
Active site structure of the (A) eNOS-**8S** complex, (B) nNOS-**8S** complex. (C) nNOS-**8R** complex. The omit $F_o - F_c$ density map for the inhibitor is shown at the 2.5 σ contour level. Major hydrogen bonds are depicted as dashed lines.

Conclusions

Inhibitors were designed based on the strategy that interactions both in the substrate ʟ-Arginine binding pocket, as well as with cofactor H_4B would result in increased potency. To this end, a series of six α-amino or aminomethyl aminopyridine derivatives **3**-**8** were synthesized. Compounds with symmetric double-heads, such as **3** and **4** exhibited much greater potency than **5** with the asymmetric head. Only inihbitors with a central aminomethyl group were able to replace a solvent water, making direct H-bonds with H_4B and heme propionate A, which results

in increased isoform selectivity. Out of all the inhibitors in this series, **8R** exhibited the highest inhibitory potency against rat nNOS, with a K_i of 24 nM and highest isoform selectivity, with 273-fold higher n/i selectivity, and excellent 2822-fold higher n/e selectivity. **8R** also showed good potency against human nNOS, with a K_i of 90 nM. Although the binding modes of **8R** to nNOS and eNOS were practically identical, a free energy calculation revealed that the basis for the high n/e selectivity is most likely due to different active site electrostatic environments in nNOS and eNOS. Taken together, the work described in this chapter provides a guide for the design of future inhibitors to further improve isoform selectivity.

NOVEL 2,4-DISUBSTITUTED PYRIMIDINES AS POTENT, SELECTIVE, AND CELL PERMEABLE INHIBITORS OF NEURONAL NITRIC OXIDE SYNTHASE

Chapter 12

Summary

In this fifth and final chapter discussing my contribution to the Poulos-Silverman collaboration, we take another approach to inhibitor design in order to improve bioavailability. The strategy used involves using a 2-imidazolylpyrimidine head combined with features from previous inhibitors. Crystal structures reveal that these inhibitors are stabilized by interactions in the same hydrophobic pocket as previously described, thus exhibiting strong inhibitory potency and isoform selectivity. Most interestingly, compound **9** exhibited good permeability, increasing its potential as a bioavailable therapeutic.

The work described in this chapter was primarily designed by Dr. Paramita Mukherjee and our collaborators in Dr. Richard Silverman's laboratory. I am a co-author on the mansucript that was published as a result of this collaboration, and my contribution to this work included solving the crystal structures of eNOS in complex with the inhibitors in order to structurally address the potency/specificity issues and help guide the design of future inhibitors. This chapter is an adaptation of a portion of the text and multiple images from our published work.[283]

New concepts?

Type I vs Type II heme ligand: Type I binding occurs when a ligand binds to the active site without directly coordinating the heme, but often displaces a water molecule already coordinated to the heme, thus shifting its spin state from hexacoordinated low spin to pentacoordinated high spin. Type II binding occurs when a ligand directly coordinates the iron, replacing the sixth ligand and increasing the low spin character of the iron.

INTRODUCTION

2-aminopyridine based scaffolds discussed in Chapters 8 to 11 exhibit high potency and isoform selectivity, but unfortunately suffer from poor blood-brain barrier permeability, usually due to the hydrophilic, polar properties of these inhibitors. In Chapter 11, we very promising improvements made with 2-aminopyridine based compounds which exhibited good membrane permeability (Chapter 11, compounds **7** and **15**, Figure 11.2). The approach described in this chapter uses the same scaffold, but explores the potential of inhibitors that can directly coordinate the heme iron, as opposed to simply occupying the active site pocket without direct coordination. While imidazole (pK_a = 6.9) binds weakly to nNOS (IC$_{50}$ of 200 μM), 1-phenylimidazole shows a much more potent IC$_{50}$ of 25 μM.[284] Therefore, in order to improve cellular permeability while retaining inhibitory potency and isoform selectivity, compound **5** was designed as a hybrid with a 2-aminopyridine scaffold and an imidazole moiety that can directly coordinate the heme iron, making it a type II heme ligand. Then, **5** was further modified by exploring the effect of the length of the linker between the two heads, the number of secondary amines, and various substitutions on the aromatic rings, to generate compounds **6**-**20**. Figure 12.1 summarizes the different nNOS inhibitors designed in this study.
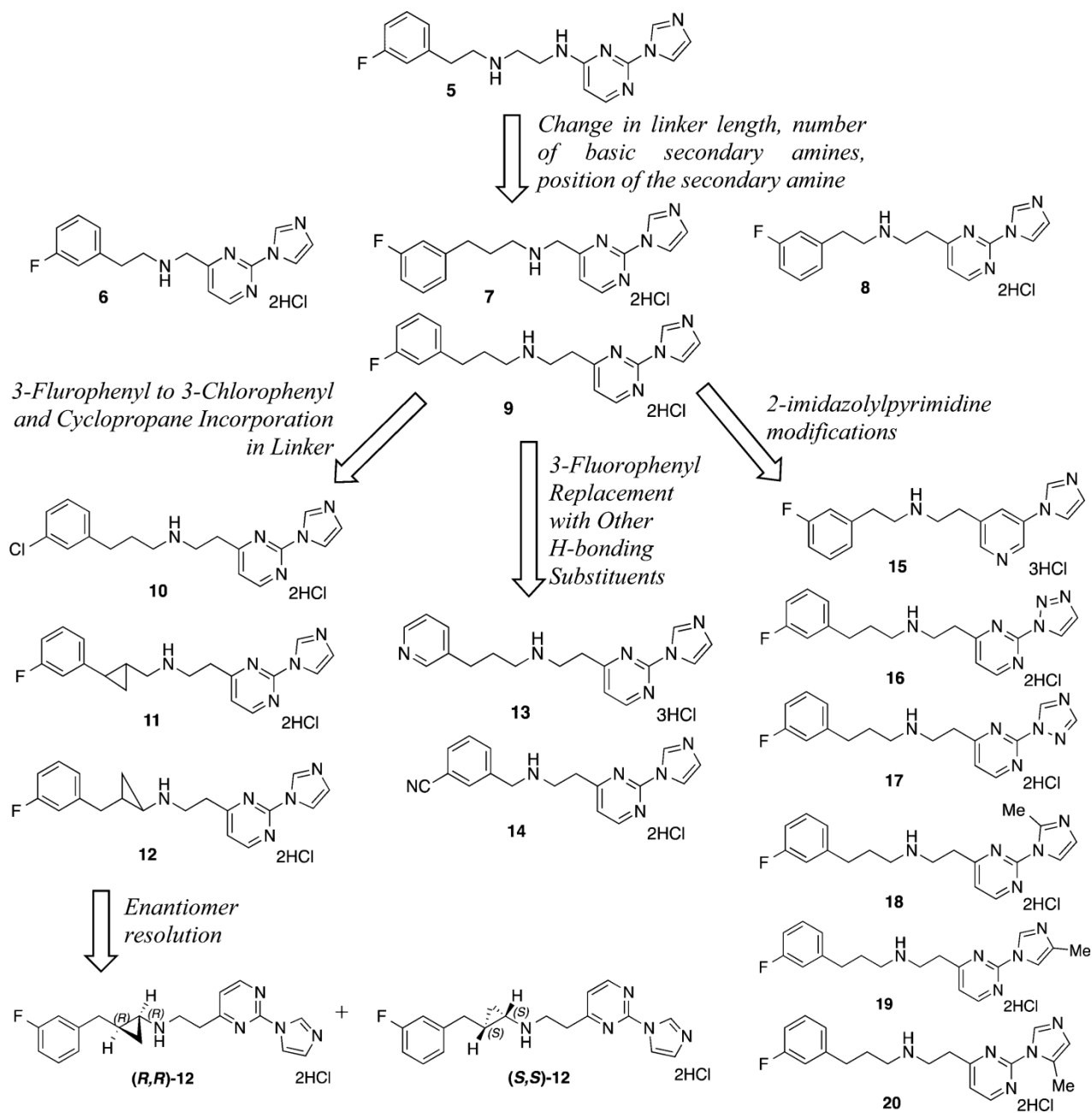
Figure 12.1 – Chemical structures and design strategy of nNOS inhibitors prepared in this study

EXPERIMENTAL PROCEDURES

Preparation and Characterization of Compounds, NOS inhibition assays and cellular

permeability assays

The syntheses and characterization (^{1}H NMR and ^{12}C NMR) of inhibitors, as well as the NOS inhibition and cell permeability assays were performed by Prof. Silverman's group, and are described in the manuscript that was published as a result of this collaboration.[283]

Inhibitor Complex Crystal Preparation

and

X-ray Diffraction Data Collection, Processing, and Structure Refinement

The nNOS or eNOS heme domain proteins used for crystallographic studies were produced as described in Chapter 8. Chapter 8 also describes the X-ray diffraction data collection, processing and structure refinement details. The refined structures were deposited in the RCSB Protein Data Bank. The crystallographic data collection and structure refinement statistics for the eNOS-inhibitor complex structures are summarized in Table 12.1 with PDB accession codes included. For statistics of nNOS-inhibitor structures and other details, please refer to the published manuscript.[283]

Data Set	eNOS-**5**	eNOS-**8**	eNOS-**9**	eNOS-**10**
	Data Collection			
PDB entry	4D33	4D34	4D35	4D36
Space group	$P2_12_12_1$	$P2_12_12_1$	$P2_12_12_1$	$P2_12_12_1$
Cell dimensions a, b, c (Å)	56.9 105.1 154.4	58.2 106.6 156.6	57.6 105.9 157.0	57.9 106.4 156.6
Detector	CCD	Pixel Array	CCD	Pixel Array
Resolution (Å)	2.09 (2.14-2.09)	2.25 (2.37-2.25)	2.18 (2.28-2.18)	2.05 (2.13-2.05)
Rmerge	0.120 (0.984)	0.092 (2.327)	0.071 (1.044)	0.100 (2.818)
$CC_{1/2}$	n/a (0.541)	0.999 (0.438)	0.998 (0.652)	0.999 (0.272)
I/σ	18.0 (0.9)	14.0 (0.8)	11.6 (1.2)	12.3 (0.6)
No. unique reflections	55,431	47,016	50,670	61,300
Completeness (%)	99.8 (100.0)	99.6 (98.7)	98.8 (89.4)	99.1 (90.6)
Redundancy	4.8 (4.5)	5.8 (5.5)	3.9 (3.3)	5.4 (4.7)
	Refinement			
Resolution (Å)	2.09	2.25	2.18	2.05
No. reflections used	55,539	46,558	50,568	59,626
R_{work}/R_{free}	0.172/0.209	0.176/0.231	0.185/0.240	0.168/0.214
no. of protein atoms	6438	6452	6446	6446
no. of heteroatoms	217	193	203	203
no. of waters	288	173	195	353
rmsd bond length (Å)	0.014	0.014	0.016	0.008
rmsd bond angle (°)	1.76	1.69	1.88	1.14
Data Set	eNOS-**11**	eNOS-**12**	eNOS-**14**	eNOS-**20**
	Data Collection			
PDB entry	4D37	4D38	4D39	4D3A
Space group	$P2_12_12_1$	$P2_12_12_1$	$P2_12_12_1$	$P2_12_12_1$
Cell dimensions a, b, c (Å)	58.2 106.3 156.6	57.8 106.0 156.3	57.8 106.1 156.3	57.6 105.9 156.0
Detector	CCD	CCD	CCD	CCD
Resolution (Å)	2.10 (2.19-2.10)	2.30 (2.42-2.30)	2.00 (2.05-2.00)	2.25 (2.29-2.25)
Rmerge	0.091 (1.502)	0.129 (2.333)	0.132 (2.221)	0.081 (1.338)
$CC_{1/2}$	0.998 (0.426)	0.997 (0.251)	0.997 (0.222)	0.999 (0.435)
I/σ	8.6 (0.9)	7.7 (0.7)	8.2 (0.7)	15.2 (1.1)
No. unique reflections	57,273	43,431	65,857	45,581
Completeness (%)	99.4 (99.4)	99.7 (100.0)	99.6 (95.8)	99.0 (97.4)
Redundancy	4.9 (5.0)	4.9 (4.9)	5.1 (5.0)	4.1 (4.2)
	Refinement			
Resolution (Å)	2.10	2.30	2.00	2.25
No. reflections used	57,167	43,331	65,523	45,504
R_{work}/R_{free}	0.182/0.229	0.174/0.230	0.172/0.222	0.162/0.210
no. of protein atoms	6423	6418	6446	6458
no. of heteroatoms	197	197	217	205
no. of waters	351	249	499	390
rmsd bond length (Å)	0.008	0.008	0.008	0.008
rmsd bond angle (°)	1.14	1.15	1.15	1.10

Table 12.1 – Crystallographic data collection and refinement statistics for the eNOS-inhibitor complex structures

Inhibitor no.	K_i (µM)					Selectivity	
	RnNOS	eNOS	iNOS	HnNOS	n/e	n/e	R/HnNOS
5	0.368	40	6.4	NT	109	17	
6	8.7	NT	NT	NT			
7	2.7	90	10.5	NT	33	4	
8	0.138	4	1.1	0.758	30	8	5.5
9	0.019	4.95	0.77	0.193	260	41	10.1
10	0.032	8.1	0.91	0.125	253	28	3.9
11	0.056	4	1.9	0.359	71	34	6.4
12	0.04	14.5	2.9	0.358	363	73	8.9
(R,R)-12	0.018	10.32	2.14	0.137	573	119	7.6
(S,S)-12	0.15	40	3	0.873	267	20	5.8
13	0.054	10.9	1.8	0.125	202	33	2.3
14	0.183	10.5	3.4	0.138	57	19	0.75
15	5.5	NT	NT	NT			
16	60	NT	NT	NT			
17	27	NT	NT	NT			
18	11.5	NT	NT	NT			
19	81	NT	NT	NT			
20	0.06	15.4	24	0.303	257	400	5

Table 12.2 – K_i and isoform selectivity values of inhibitors for rat nNOS (RnNOS), bovine eNOS, murine iNOS and human nNOS (HnNOS).

As done in previous chapters, *in vitro* assays were performed on all inhibitors and the results are summarized in Table 12.2. The starter inhibitor **5** exhibited good inhibitory potency against nNOS, with a K_i of 368 nM. We determined the crystal structure of nNOS-**5** (Figure 12.2A), which showed that the imidazole head does coordinate the heme iron, as intended, and that the flexible linker extends toward the hydrophobic pocket.Three additional observations can be made. First, there is a gap between the imidazole and Glu592, which becomes filled with a water molecule, second, the amine next to the pyrimidine ring H-bonds with heme propionate A, and third, the central amine H-bonds the water that itself is H-bonded to H_4B. This also represents the first structure of nNOS with a type II imidazole-based heme-bound inhibitor. The eNOS-**5** crystal structure (Figure 11.2B) reveals the basis for the 100-fold n/e selectivity observed. The fluorine atom in the tail does not extend into the hydrophobic pocket like in

nNOS, and thus is not stabilized by van der Waals contact in the pocket. This is most likely because a stiffer Val106 in eNOS replaces Met336, and sterically prevents the inhibitor tail from extending into the pocket. This also causes the amine in the linker to H-bond with heme propionate D.

Figure 12.2 – Crystal structure of inhibitor 5 bound to nNOS and eNOS
Active site structure of the (A) nNOS-**5** complex, (B) eNOS-**5** complex. The omit $F_o - F_c$ density map for the inhibitor is shown at the 2.5 σ contour level. Major hydrogen bonds are depicted as dashed lines and the heme pyrrole rings are labeled in order to identify the propionate positions. All molecular graphics shown in this chapter were prepared using PyMOL.[170]

Compounds **6**-**9** were designed in order to improve interactions beyond the active site. **6** was designed with a shorter 4-atom linker in order to avoid the twisting of methylene units seen in **5**. These inhibitors were also assayed (Table 12.2),which revealed that both the position of the secondary amine and the length of the linker are crucial to inhibitor potency and selectivity. Inhibitors **6** and **7** had very low potencies, likely due to the position of the secondary amine in the chain. The structure of nNOS-**7** (Figure 12.3A) reveals that the secondary amine can no longer H-bond with either of the heme propionates.

Figure 12.3 – Crystal structure of inhibitors 7 and 8 bound to nNOS
Active site structure of the (A) nNOS-**7** complex, (B) nNOS-**8** complex. The omit $F_o - F_c$ density map for the inhibitor is shown at the 2.5 σ contour level. Major hydrogen bonds are depicted as dashed lines.

Compound **8** and **9**, where the position of the secondary amine is one carbon further away from the pyrimidine than for **6** and **7**, results in much improved potency. The structure of nNOS-**8** (Figure 12.3B) reveals that this amine position allows the inhibitor to H-Bond with both heme propionates, explaining the additional stability. Unfortunately, the 5-atom linker of **8** is too short for the tail of the fluorophenyl ring to comfortably extend into the hydrophobic pocket. The structure of nNOS-**9** (Figure 12.4A) shows that a 6-atom linker is the minimum chain length required for the fluorophenyl tail to extend into the hydrophobic pocket. This also results in **9** being one of the most potent inhibitors in this series of 2-imidazolylpyrimidine inhibitors, with a K_i of 19 nM. Compound **9** also exhibited 260-fold n/e selectivity, which the structure of eNOS-**9** (Figure 12.4B) revealed is most likely due to the different interactions in the hydrophobic pocket of the different isoforms. As we have said, Val106 in eNOS replaces Met336 in nNOS, which results in less stabilizing contacts in the eNOS pocket, and thus poorer eNOS binding.
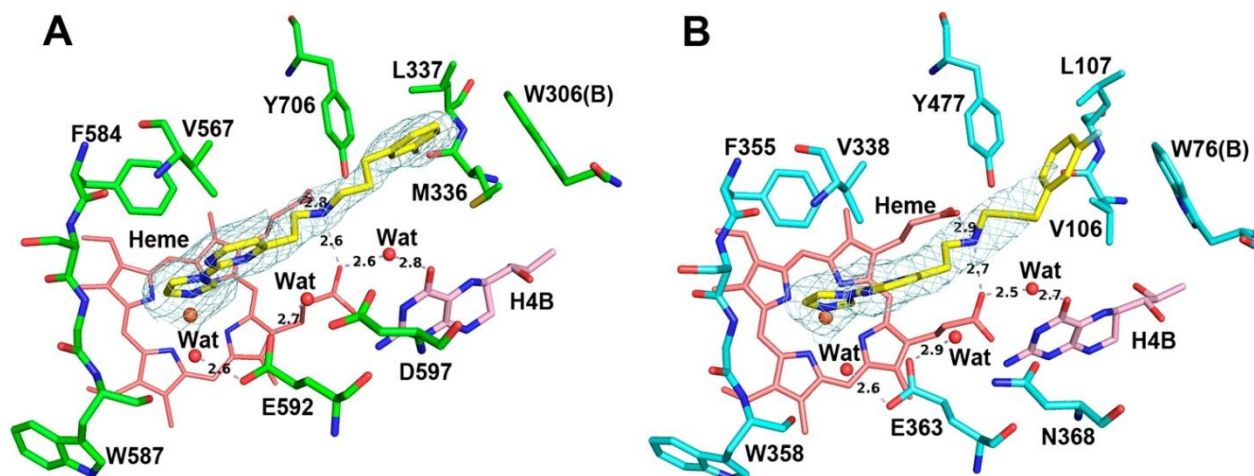
Figure 12.4 – Crystal structure of inhibitor 9 bound to nNOS and eNOS
Active site structure of the (A) nNOS-**9** complex, (B) eNOS-**9** complex. The omit $F_o – F_c$ density map for the inhibitor is shown at the 2.5 σ contour level. Major hydrogen bonds are depicted as dashed lines.

Since halogen replacements have been shown to enhance inhibitory potency and selectivity caused by enhanced contacts between the inhibitor and residues in the hydrophobic pocket,[246, 277] compound **10** was designed with a chlorophenyl ring instead of the fluorophenyl ring of **9**. Unfortunately, this resulted in a slightly reduced inhibitory potency of 32 nM (K_i of 9 is 19 nM). The nNOS-**10** structure (Figure 12.5A) reveals that the poorer inhibitory potency is caused by the bulkier chlorine atom, which is too large to comfortably fit in the hydrophobic pocket. This is even worse for the eNOS-**10** structure (Figure 12.5B), where the chlorophenyl ring does not extend into the pocket at all.
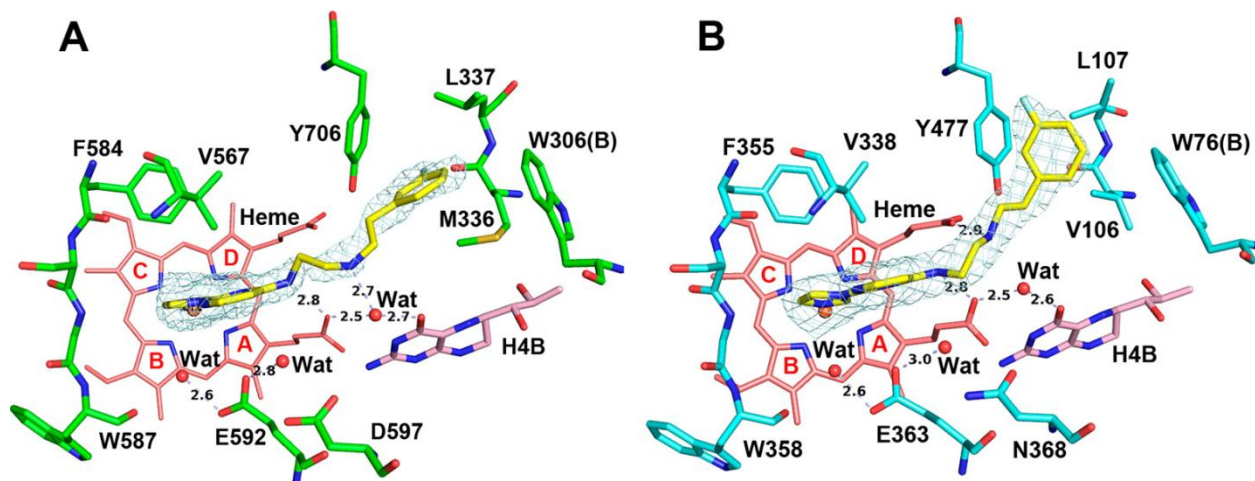
Figure 12.5 – Crystal structure of inhibitor 10 bound to nNOS and eNOS
Active site structure of the (A) nNOS-**10** complex, (B) eNOS-**10** complex. The omit $F_o – F_c$ density map for the inhibitor is shown at the 2.5 σ contour level. Major hydrogen bonds are depicted as dashed lines.

Although compound **9** exhibits excellent n/e selectivity, it's n/i selectivity is rather low. Compounds **11** and **12** were designed with a cyclopropane ring to attempt to sterically weaken binding in the more rigid iNOS active site. This strategy was successful for **12**, which saw its n/i selectivity improved from 41- to 73-fold and the highest n/e selectivity (363-fold) for this series of inhibitors. The crystal structures of both **11** and **12** in nNOS (Figure 12.6) show that the cyclopropane ring provides additional rigidity to the linker, causing the fluorophenyl ring to no longer be able to extend as far into the hydrophobic pocket compared to **9**, which explains the lower nNOS potency. The higher n/e selectivity is explained in the eNOS-**11** and eNOS-**12** structures (Figure 12.7), which reveal that the fluorophenyl tail is not able to enter the pocket, thus reducing its stabilizing contacts. This effect is even more pronounced for eNOS-**12**. All of the structures reveal preferential binding of the (R,R) enantiomer of **11** and **12**. To probe this further, each enantiomer of **12** was isolated and assayed (Table 12.2), which confirmed the structural observations. The (R,R) enantiomer exhibited a K_i of 18 nM (150 nM for the (S,S) enantiomer) and 119-fold n/i selectivity (20-fold for the (S,S) enantiomer).
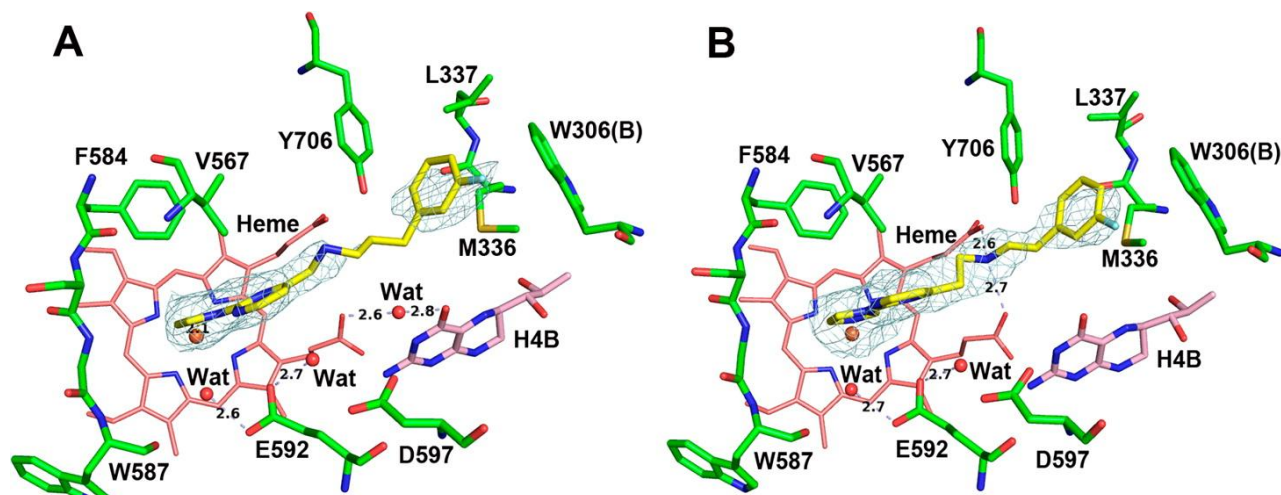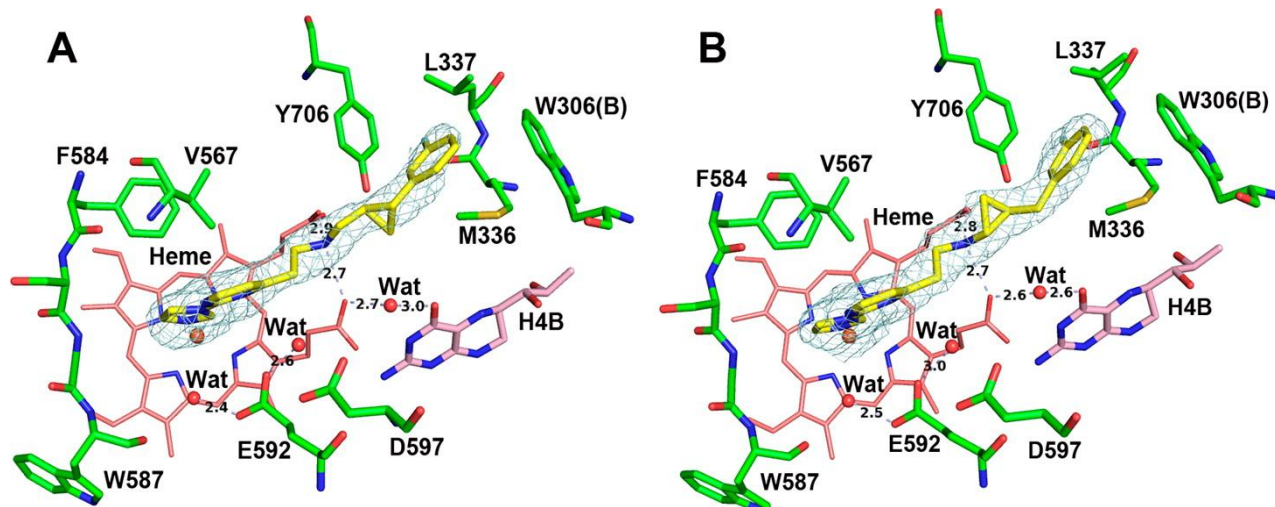
Figure 12.6 – Crystal structure of inhibitors 11 and 12 bound to nNOS
Active site structure of the (A) nNOS-**11** complex, (B) nNOS-**12** complex. For both inhibitors, (R,R) is the only enantiomer that binds. The omit $F_o – F_c$ density map for the inhibitor is shown at the 2.5 σ contour level. Major hydrogen bonds are depicted as dashed lines.
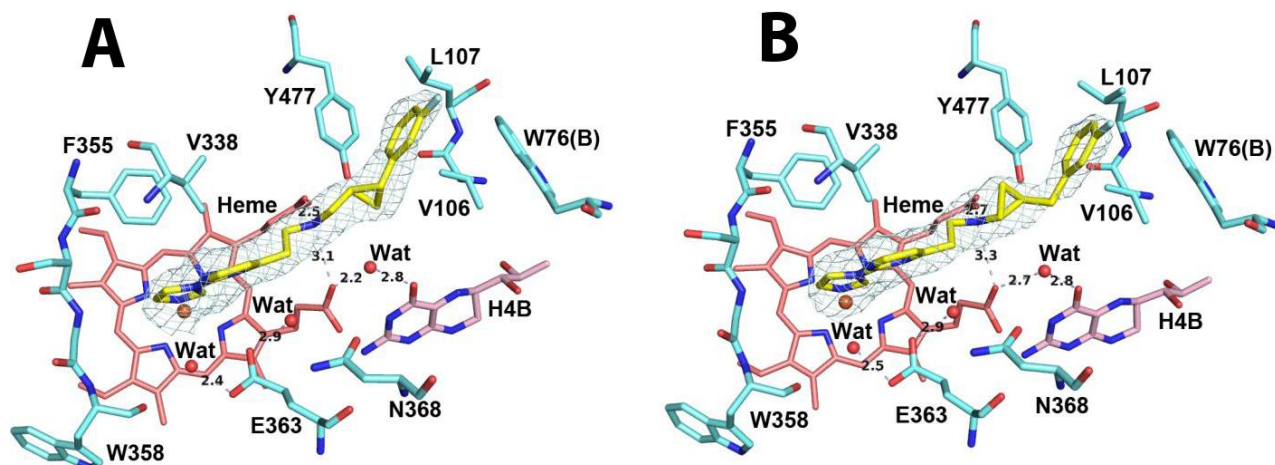
Figure 12.7 – Crystal structure of inhibitors 11 and 12 bound to eNOS
Active site structure of the (A) eNOS-**11** complex, (B) eNOS-**12** complex. For both inhibitors, (R,R) is the only enantiomer that binds. The omit $F_o – F_c$ density map for the inhibitor is shown at the 2.5 σ contour level. Major hydrogen bonds are depicted as dashed lines.

In human nNOS, His342 replaces Leu337 in the hydrophobic pocket, which adds hydrophilicity to the pocket and may affect the potency of inhibitors that utilize this binding mode. Since HnNOS crystal structures are now being solved at higher resolution,[285] the compounds were also assayed against HnNOS. Compounds **9**–**12** exhibited good potency against HnNOS, and similar selectivities. Compounds **13** and **14** were designed with smaller and polar

207

aromatic ends in order to better fit in the slightly more hydrophilic pocket of HnNOS. Compound **13** Showed good potency against HnNOS, with a K_i of 125 nM. The HnNOS-**13** structure (Figure 12.8A) confirms that the added nitrogen in the pyridine ring H-bonds with His342, finding additional stability, while the RnNOS-**13** structure (Figure 12.8B) shows that the ring is disordered.
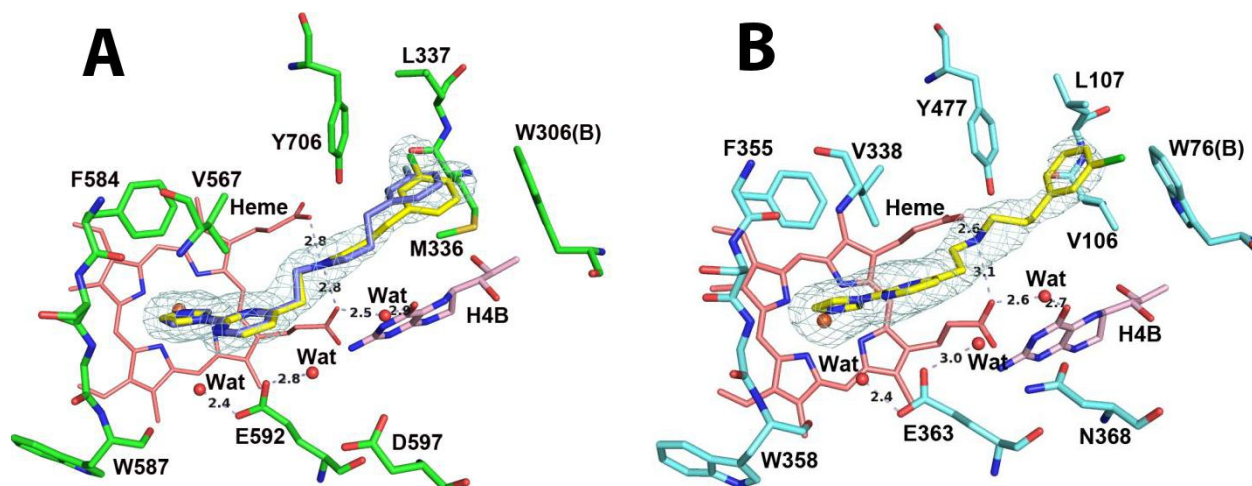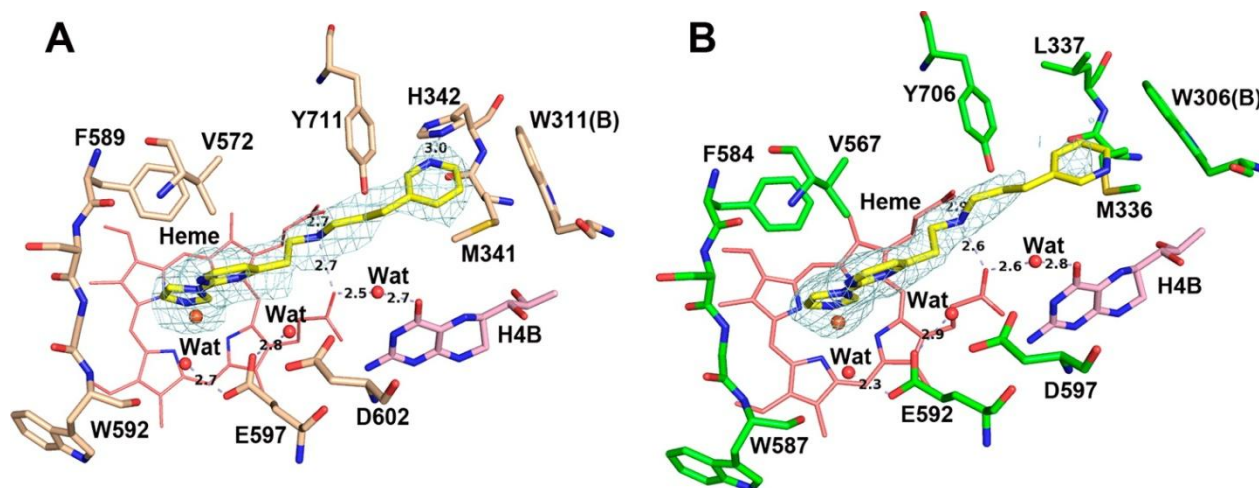

Figure 12.8 – Crystal structure of inhibitor 13 bound to HnNOS and RnNOS
Active site structure of the (A) HnNOS-**13** complex, (B) RnNOS-**13** complex. The omit $F_o - F_c$ density map for the inhibitor is shown at the 2.5 σ contour level. Major hydrogen bonds are depicted as dashed lines.

Compound **14**, with a more polar cyanophenyl ring and shorter 4-atom linker, is the first inhibitor that exhibited a better inhibitory potency against HnNOS (138 nM) than RnNOS (183 nM). The structural basis for higher selectivity for the human enzyme is shown in the crystal structure of RnNOS-**14** (Figure 12.9A), in which the shorter linker of **14** prevents the cyanophenyl ring from extending into the hydrophobic pocket, but appears to be ideally positioned to be stabilized in HnNOS by an H-bond between the cyanophenyl nitrogen and His342.

The last compounds investigated in this study were **15**-**20** which were designed with variations in the 2-imidazolylpyrimidine portion of the scaffold, based on preliminary docking

studies. Unfortunately, compounds **15**-**19** exhibited very poor inhibition against nNOS (the lowest K_i was 5.5 μM!). Compound **20**, with a 5-methyl attached to the 2-imidazolylpyrimidine, was the only exception, exhibiting excellent potency against RnNOS (K_i of 60 nM), great 257-fold n/e selectivity and excellent 400-fold n/i selectivity. The crystal structure of nNOS-**20** (Figure 12.9A) suggests that the additional methyl group sticking out in the active site pocket would most likely cause steric hindrance in the smaller and more rigid iNOS active site pocket. While for eNOS-**20** (Figure 12.9B), binding of the inhibitor is weakened by lack of stabilizing interactions in the hydrophobic pocket.
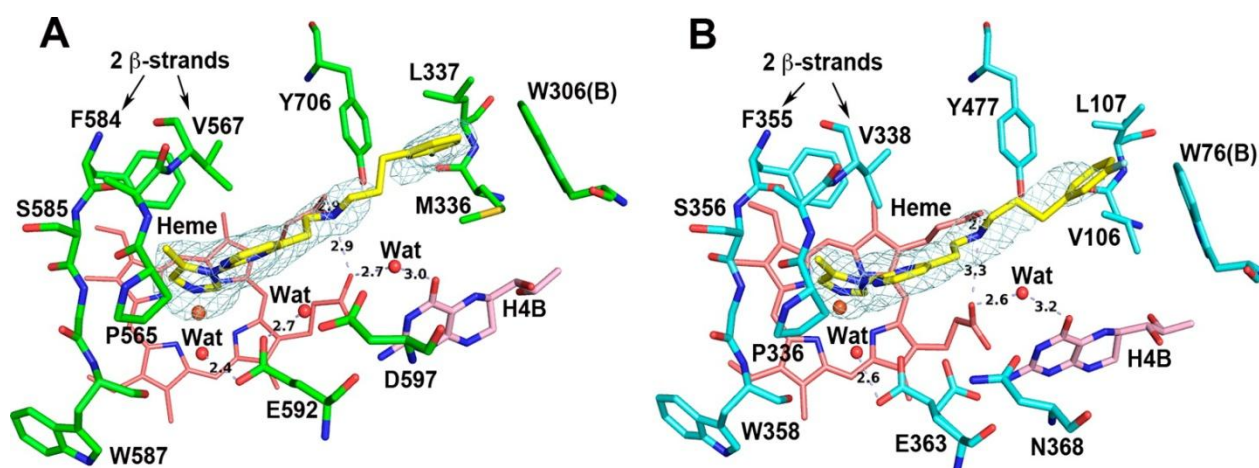
Figure 12.9 – Crystal structure of inhibitor 20 bound to RnNOS and eNOS
Active site structure of the (A) RnNOS-**20** complex, (B) eNOS-**20** complex. The omit $F_o - F_c$ density map for the inhibitor is shown at the 2.5 σ contour level. Major hydrogen bonds are depicted as dashed lines.

Finally, compound **9** was assayed by the Silverman group in a Caco-2 monolayer permeability assay. The results showed that **9** displayed good cellular permeability, which was quite encouraging. For more details on the Caco-2 assay results, see the published manuscript.[283]

Conclusions

This chapter describes the rational design of nNOS inhibitors based on 2,4-disubstituted pyrimidine scaffolds designed as type II ligands that directly coordinate the heme iron. The crystal structures of these inhibitors reveal that the ideal binding mode involves direct heme coordination by the 2-imidazolylpyrimidine portion of the inhibitors, as well as stabilization of the tail portion in the hydrophobic pocket at the end of the substrate access channel. Overall, compounds, **9**, **12**, and **13** exhibitied excellent binding affinity in the low nanomolar range, good isoform selectivity, and good Caco-2 permeability, which provides a step further in the design of potent and selective nNOS inhibitors that are also bioavailable.

FINAL CONCLUSIONS

Chapter 13

Heme proteins are essential in all facets of biological life, where they perform a vast number of different functions, including oxygen storage and transport, electron transfer, catalysis, immune system defense, xenobiotic detoxification, and cell signaling. The outstanding property that defines all of these proteins is the heme prosthetic group, which is able to drive this wide array of different functions depending on the protein environment in which it is found. The architecture of the protein scaffold can stabilize heme binding in a variety of ways and therefore tune the activity of the heme group in three main ways: the chemical properties of the axial ligands that coordinate the heme iron, the layout of the active site pocket, and the solvent-exposed surface residues that play a role in protein-protein recognition. The central thesis of this dissertation revolved around expanding our understanding of the structure-function relationship in heme proteins and to do this, we have investigated a variety of fascinating heme protein systems.

We started with heme peroxidases, enzymes that convert H_2O_2 to water, and saw that one such peroxidase, expressed by the parasitic protozoa *L. major*, is actually a cytochrome c peroxidase, similar to the well studied yeast CcP which was thought for a long time to be unique in its use of cytochrome c as a substrate. Much insight has been gained from studying the similarities and differences between the LmP and CcP systems. We have confirmed that each discrete step that outlines the CcP mechanism applies to LmP as well, and in the process discovered insights about LmP that are not shared with CcP, such as the crucial role of specific

ionic interactions in this protein-redox partner complex. Steady-state and single turnover kinetics now provide us a clear understanding of the overall mechanism of LmP catalysis. We have found that k_{cat} for LmP remains relatively constant at all ionic strengths and that association and dissociation events are not limiting at any ionic strength in LmP, but rather that the intramolecular electron transfer reaction from $Fe^{IV}=O;Trp$ to $Fe^{III}-OH;Trp^{\cdot+}$ is the limiting event at all ionic strengths. This intramolecular rate-limiting step at steady-state exhibits a strong deuterium solvent isotope effect, making LmP an excellent system to probe the reduction of CmpII in more detail than was previously possible with CcP. By taking advantage of the easy kinetics in LmP and coupling them to X-ray crystallography, we are able to confirm that the mechanism of CmpI formation and subsequent CmpII reduction involves a water-mediated proton transfer. This would not have been easy without the usefulness of X-ray free electron lasers (XFELs) that were able to capture the structure of CcP CmpI with a oxoferryl center, therefore highlighting the usefulness of XFELS as an excellent tool to capture the crystal structures of proteins with virtually no X-ray damage or reduction of their transition metal center. We have also found that the LmP-LmCytc complex is quite different from CcP-Cytc, and depends much more on finely tuned charge complementarity. This property is best exemplified in two main observations: first, breaking a single ion pair has a dramatic effect on the association of the complex, and second, the multiple charges on helix A, which is adjacent to the docking site, are crucial to redox-partner recognition and association events which are transient and not directly observable in the crystal structures.

It is unfortunate that a CcP found in a parasite did not prove to be a useful therapeutic target. However, the identification of LmPP, a very similar heme enzyme from the same

organism that does not catalyze the detoxification of H_2O_2, but instead of $ONOO^-$, has proven to be one of the most interesting projects to work on. The project had been abandoned before a clear mechanism could be determined because of a lack of structural corroboration. We revived the project, and were able to clone, express, purify, crystallize and solve the 1.76 Å crystal structure of the LmPP enzyme. This achievement has opened new avenues for determining the mechanism of catalysis. Our results confirm that the active site is composed of a Cys/His ligated heme, that the presence of a strong H-bond between proximal His ligand and nearby Glu side chain appears prepared to stabilize a higher iron oxidation state, suggesting a role in catalysis, and that the distal pocket with Val and Arg residues is equipped to catalyze the isomerisation of peroxynitrite to nitrate. Based on these observations, we were able to propose a potential mechanism, which awaits future testing. We were also able to propose a possible biological role for the coordinatively saturated heme iron: to protect the active site from other reactive molecules that could disable transition metal catalysis and to tune reactivity to $ONOO^-$ only. We hope that future experiments can confirm whether the proposed mechanism is correct.

We then shifted gears and tackled one of the most fascinating enzymes in biology, cytochrome P450. With over 35,000 different P450s identified, P450s are one of the largest enzyme superfamilies. The previously confirmed effector role of Pdx in the P450cam system compels us to ask whether this feature is unique to P450cam or not. We thus began a study on the P450cin system from *Citrobacter braakii* and used a site-specific crosslinking protocol with bismaleimide crosslinkers in order to crystallize the covalent P450cin-Cdx complex. Even though we were unsucessful, we were still able to probe the strengths and weakenesses of the technique and derive a useful protocol for future crosslinking experiments that eliminate

heterogeneity. Altogether, we are convinced that this method can be successful in determining the docking site and orientation of the redox partners, and is definitely worth pursuing in order to determine the crystal structure of the P450cin-Cdx complex.

The final heme enzyme we studied was NOS, to which we dedicated the last six chapters. The three mammalian NOS isoforms are involved in signal transduction cascades that control blood flow/pressure, as well as signaling between neurons and immune system response. Since controlling NO production is critical to proper physiology, we first probed the binding of H_4B analogues in NOS, which allowed us to understand which features of the compound stabilizes its binding in the pterin site to design better NOS activators. In the process, we discovered a potential basis for the difference in dimer strengths between the three mammalian isoforms and discovered a previously unknown communication between the H_4B and Zn^{2+} binding sites that highlights the delicate balance of forces in the protein structure. While NOS activation is sometimes desired, excessive production of NO has been linked to a large number of neurodegenerative diseases, promoting efforts to design NOS inhibitors. Our group has been collaborating with the Silverman group to design potent, selective, and bioavailable NOS inhibitors to better regulate NO production in neuronal cells. This collaboration has been quite fruitful, and I have been fortunate to be a part of. The combined efforts from both research groups have yielded a large library of NOS inhibitors with high inhibitory potencies, isoform selectivities and promising bioavailability, validating multiple strategies for nNOS inhibitor design and paving the way forward to produce real therapeutic solutions.

Closing remarks

Heme enzymes undoubtedly serve an indispensable role in the fields of biochemistry, enzymology and X-ray crystallography, and have consistently emphasized the importance of structure-function relationships in all of biology. The ease of purification, accessibility of spectroscopic techniques and X-ray crystallography of heme enzymes has made their study incredibly attractive, and has allowed the field to grow immensely. A number of related biological fields would be at a serious detriment if effort had not been placed on obtaining a clearer understanding of the basic biochemistry of heme proteins. While research efforts spent on better understanding structure-function relationships don't always have quite the same appeal as biomedical research, it is still a worthwhile pursuit that has provided a foundational understanding of biochemistry and consequently has greatly driven other fields of biology further. There is still much unknown, and the sheer number of heme enzymes with vastly different functions being discovered each day is staggering, leaving much more to be done in order to further our understanding of these biological functions and consequently, of how nature is ordered.

REFERENCES

1. McIntosh, J. A., Farwell, C. C., and Arnold, F. H. (2014) Expanding P450 catalytic reaction space through evolution and engineering, *Curr Opin Chem Biol 19*, 126-134.

2. Poulos, T. L., Freer, S. T., Alden, R. A., Edwards, S. L., Skogland, U., Takio, K., Eriksson, B., Xuong, N., Yonetani, T., and Kraut, J. (1980) The crystal structure of cytochrome c peroxidase, *J Biol Chem 255*, 575-580.

3. Volkov, A. N., Nicholls, P., and Worrall, J. A. (2011) The complex of cytochrome c and cytochrome c peroxidase: the end of the road?, *Biochim Biophys Acta 1807*, 1482-1503.

4. Coulson, A. F., and Yonetani, T. (1972) Oxidation of cytochrome c peroxidase with hydrogen peroxide: identification of the "endogenous donor", *Biochem Biophys Res Commun 49*, 391-398.

5. Sivaraja, M., Goodin, D. B., Smith, M., and Hoffman, B. M. (1989) Identification by ENDOR of Trp191 as the free-radical site in cytochrome c peroxidase compound ES, *Science 245*, 738-740.

6. Geren, L., Hahm, S., Durham, B., and Millett, F. (1991) Photoinduced electron transfer between cytochrome c peroxidase and yeast cytochrome c labeled at Cys 102 with (4-bromomethyl-4'-methylbipyridine)[bis(bipyridine)]ruthenium2+, *Biochemistry 30*, 9450-9457.

7. Hahm, S., Durham, B., and Millett, F. (1992) Photoinduced electron transfer between cytochrome c peroxidase and horse cytochrome c labeled at specific lysines with (dicarboxybipyridine)(bisbipyridine)ruthenium(II), *Biochemistry 31*, 3472-3477.

8. Hahm, S., Miller, M. A., Geren, L., Kraut, J., Durham, B., and Millett, F. (1994) Reaction of horse cytochrome c with the radical and the oxyferryl heme in cytochrome c peroxidase compound I, *Biochemistry 33*, 1473-1480.

9. Liu, R. Q., Hahm, S., Miller, M., Durham, B., and Millett, F. (1995) Photooxidation of Trp-191 in cytochrome c peroxidase by ruthenium-cytochrome c derivatives, *Biochemistry 34*, 973-983.

10. Miller, M. A., Liu, R. Q., Hahm, S., Geren, L., Hibdon, S., Kraut, J., Durham, B., and Millett, F. (1994) Interaction domain for the reaction of cytochrome c with the radical and the oxyferryl heme in cytochrome c peroxidase compound I, *Biochemistry 33*, 8686-8693.

11. Pappa, H. S., Tajbaksh, S., Saunders, A. J., Pielak, G. J., and Poulos, T. L. (1996) Probing the cytochrome c peroxidase-cytochrome c electron transfer reaction using site specific cross-linking, *Biochemistry 35*, 4837-4845.

12. Roe, J. A., and Goodin, D. B. (1993) Enhanced oxidation of aniline derivatives by two mutants of cytochrome c peroxidase at tryptophan 51, *J Biol Chem 268*, 20037-20045.

13. Liu, R. Q., Miller, M. A., Han, G. W., Hahm, S., Geren, L., Hibdon, S., Kraut, J., Durham, B., and Millett, F. (1994) Role of methionine 230 in intramolecular electron transfer between the oxyferryl heme and tryptophan 191 in cytochrome c peroxidase compound II, *Biochemistry 33*, 8678-8685.

14. Miller, M. A. (1996) A complete mechanism for steady-state oxidation of yeast cytochrome c by yeast cytochrome c peroxidase, *Biochemistry 35*, 15791-15799.

15. Welinder, K. G. (1992) Superfamily of plant, fungal and bacterial peroxidases, *Current Opinion in Structural Biology 2*, 388-393.

16.   Dolphin, D., Forman, A., Borg, D., Fajer, J., and Felton, R. (1971) Compounds I of catalase and horse radish peroxidase: π-cation radicals, *Proceedings of the National Academy of Sciences 68*, 614-618.

17.   Adak, S., and Datta, A. K. (2005) Leishmania major encodes an unusual peroxidase that is a close homologue of plant ascorbate peroxidase: a novel role of the transmembrane domain, *Biochemical Journal 390*, 465-474.

18.   Jasion, V. S., and Poulos, T. L. (2012) Leishmania major peroxidase is a cytochrome c peroxidase, *Biochemistry 51*, 2453-2460.

19.   Dolai, S., Yadav, R. K., Datta, A. K., and Adak, S. (2007) Effect of thiocyanate on the peroxidase and pseudocatalase activities of Leishmania major ascorbate peroxidase, *Biochimica et Biophysica Acta (BBA)-General Subjects 1770*, 247-256.

20.   Yadav, R. K., Dolai, S., Pal, S., and Adak, S. (2008) Role of tryptophan-208 residue in cytochrome c oxidation by ascorbate peroxidase from Leishmania major-kinetic studies on Trp208Phe mutant and wild type enzyme, *Biochimica et Biophysica Acta (BBA)-Proteins and Proteomics 1784*, 863-871.

21.   Jasion, V. S., Polanco, J. A., Meharenna, Y. T., Li, H., and Poulos, T. L. (2011) Crystal structure of Leishmania major peroxidase and characterization of the compound I tryptophan radical, *Journal of Biological Chemistry 286*, 24608-24615.

22.   Jasion, V. S., Doukov, T., Pineda, S. H., Li, H., and Poulos, T. L. (2012) Crystal structure of the Leishmania major peroxidase–cytochrome c complex, *Proceedings of the National Academy of Sciences 109*, 18390-18394.

23.   Pelletier, H., and Kraut, J. (1992) Crystal structure of a complex between electron transfer partners, cytochrome c peroxidase and cytochrome c, *Science 258*, 1748-1755.

24.   Pal, S., Yadav, R. K., and Adak, S. (2012) Role of K+ binding residues in stabilization of heme spin state of Leishmania major peroxidase, *Biochimica et Biophysica Acta (BBA)-Proteins and Proteomics 1824*, 1002-1007.

25.   Pettersen, E. F., Goddard, T. D., Huang, C. C., Couch, G. S., Greenblatt, D. M., Meng, E. C., and Ferrin, T. E. (2004) UCSF Chimera—a visualization system for exploratory research and analysis, *Journal of computational chemistry 25*, 1605-1612.

26.   Pal, S., Dolai, S., Yadav, R. K., and Adak, S. (2010) Ascorbate peroxidase from Leishmania major controls the virulence of infective stage of promastigotes by regulating oxidative stress, *PloS one 5*, e11271.

27.   Garfinkel, D. (1958) Studies on pig liver microsomes. I. Enzymic and pigment composition of different microsomal fractions, *Archives of biochemistry and biophysics 77*, 493-509.

28.   Klingenberg, M. (1958) Pigments of rat liver microsomes, *Archives of biochemistry and biophysics 75*, 376-386.

29.   Omura, T., and Sato, R. (1964) The carbon monoxide-binding pigment of liver microsomes. I. Evidence for its hemoprotein nature, *J Biol Chem 239*, 2370-2378.

30.   Lamb, D. C., Lei, L., Warrilow, A. G., Lepesheva, G. I., Mullins, J. G., Waterman, M. R., and Kelly, S. L. (2009) The first virally encoded cytochrome p450, *Journal of virology 83*, 8266-8269.

31.   Nelson, D. (Last Accessed on 02/10/2016) Cytochrome P450 Stats, http://drnelson.uthsc.edu/P450.stats.Aug2013.png.

32. Guengerich, F. P., and Munro, A. W. (2013) Unusual cytochrome P450 enzymes and reactions, *Journal of Biological Chemistry 288*, 17065-17073.

33. Narhi, L. O., and Fulco, A. J. (1987) Identification and characterization of two functional domains in cytochrome P-450BM-3, a catalytically self-sufficient monooxygenase induced by barbiturates in Bacillus megaterium, *Journal of Biological Chemistry 262*, 6683-6690.

34. Shumyantseva, V. V., Bulko, T. V., and Archakov, A. I. (2005) Electrochemical reduction of cytochrome P450 as an approach to the construction of biosensors and bioreactors, *Journal of inorganic biochemistry 99*, 1051-1063.

35. Perera, R., Jin, S., Sono, M., and Dawson, J. H. (2007) Cytochrome P450-catalyzed hydroxylations and epoxidations, *Metal Ions in Life Sciences 3*, 319-359.

36. Dawson, J. H., Holm, R., Trudell, J. R., Barth, G., Linder, R. E., Bunnenberg, E., Djerassi, C., and Tang, S. (1976) Magnetic circular dichroism studies. 43. Oxidized cytochrome P-450. Magnetic circular dichroism evidence for thiolate ligation in the substrate-bound form. Implications for the catalytic mechanism, *Journal of the American Chemical Society 98*, 3707-3709.

37. Sono, M., and Dawson, J. (1982) Formation of low spin complexes of ferric cytochrome P-450-CAM with anionic ligands. Spin state and ligand affinity comparison to myoglobin, *Journal of Biological Chemistry 257*, 5496-5502.

38. Sono, M., Andersson, L., and Dawson, J. H. (1982) Sulfur donor ligand binding to ferric cytochrome P-450-CAM and myoglobin. Ultraviolet-visible absorption, magnetic circular dichroism, and electron paramagnetic resonance spectroscopic investigation of the complexes, *Journal of Biological Chemistry 257*, 8308-8320.

39. Liu, H. I., Sono, M., Kadkhodayan, S., Hager, L. P., Hedman, B., Hodgson, K. O., and Dawson, J. H. (1995) X-ray Absorption Near Edge Studies of Cytochrome P-450-CAM, Chloroperoxidase, and Myoglobin DIRECT EVIDENCE FOR THE ELECTRON RELEASING CHARACTER OF A CYSTEINE THIOLATE PROXIMAL LIGAND, *Journal of Biological Chemistry 270*, 10544-10550.

40. Higuchi, T., Shimada, K., Maruyama, N., and Hirobe, M. (1993) Heterolytic oxygen-oxygen bond cleavage of peroxy acid and effective alkane hydroxylation in hydrophobic solvent mediated by an iron porphyrin coordinated by thiolate anion as a model for cytochrome P-450, *Journal of the American Chemical Society 115*, 7551-7552.

41. Adachi, S., Nagano, S., Ishimori, K., Watanabe, Y., Morishima, I., Egawa, T., Kitagawa, T., and Makino, R. (1993) Roles of proximal ligand in heme proteins: replacement of proximal histidine of human myoglobin with cysteine and tyrosine by site-directed mutagenesis as models for P-450, chloroperoxidase, and catalase, *Biochemistry 32*, 241-252.

42. Groves, J. T., McClusky, G. A., White, R. E., and Coon, M. J. (1978) Aliphatic hydroxylation by highly purified liver microsomal cytochrome P-450. Evidence for a carbon radical intermediate, *Biochemical and biophysical research communications 81*, 154-160.

43. Haniu, M., Tanaka, M., Yasunobu, K., and Gunsalus, I. (1982) Amino acid sequence of the Pseudomonas putida cytochrome P-450. I. Sequences of tryptic and clostripain peptides, *Journal of Biological Chemistry 257*, 12657-12663.

44. Haniu, M., Armes, L., Yasunobu, K., Shastry, B., and Gunsalus, I. (1982) Amino acid sequence of the Pseudomonas putida cytochrome P-450. II. Cyanogen bromide peptides, acid cleavage peptides, and the complete sequence, *Journal of Biological Chemistry 257*, 12664-12671.

45. Katagiri, M., Ganguli, B., and Gunsalus, I. (1968) A soluble cytochrome P-450 functional in methylene hydroxylation, *Journal of Biological Chemistry 243*, 3543-3546.

46. Poulos, T. L., Finzel, B. C., and Howard, A. J. (1987) High-resolution crystal structure of cytochrome P450cam, *Journal of molecular biology 195*, 687-700.

47. Poulos, T. L., Finzel, B., Gunsalus, I., Wagner, G. C., and Kraut, J. (1985) The 2.6-A crystal structure of Pseudomonas putida cytochrome P-450, *Journal of Biological Chemistry 260*, 16122-16130.

48. Tyson, C. A., Lipscomb, J. D., and Gunsalus, I. (1972) The roles of putidaredoxin and P450cam in methylene hydroxylation, *Journal of Biological Chemistry 247*, 5777-5784.

49. Sligar, S., Debrunner, P., Lipscomb, J., Namtvedt, M., and Gunsalus, I. (1974) A role of the putidaredoxin COOH-terminus in P-450cam (cytochrome m) hydroxylations, *Proceedings of the National Academy of Sciences 71*, 3906-3910.

50. Lipscomb, J. D., Sligar, S., Namtvedt, M., and Gunsalus, I. (1976) Autooxidation and hydroxylation reactions of oxygenated cytochrome P-450cam, *Journal of Biological Chemistry 251*, 1116-1124.

51. Moncada, S., Palmer, R., and Higgs, E. (1991) Nitric oxide: physiology, pathophysiology, and pharmacology, *Pharmacological reviews 43*, 109-142.

52. Nathan, C. F., and Hibbs, J. B. (1991) Role of nitric oxide synthesis in macrophage antimicrobial activity, *Current opinion in immunology 3*, 65-70.

53. Ischiropoulos, H., Zhu, L., and Beckman, J. S. (1992) Peroxynitrite formation from macrophage-derived nitric oxide, *Archives of biochemistry and biophysics 298*, 446-451.

54. Griffith, O. W., and Stuehr, D. J. (1995) Nitric oxide synthases: properties and catalytic mechanism, *Annual review of physiology 57*, 707-734.

55. Arnold, W. P., Mittal, C. K., Katsuki, S., and Murad, F. (1977) Nitric oxide activates guanylate cyclase and increases guanosine 3′: 5′-cyclic monophosphate levels in various tissue preparations, *Proceedings of the National Academy of Sciences 74*, 3203-3207.

56. Knowles, R. G., and Moncada, S. (1994) Nitric oxide synthases in mammals, *Biochemical Journal 298*, 249.

57. Peterson, J. A., and Prough, R. A. (1986) Cytochrome P-450 reductase and cytochrome b5 in cytochrome P-450 catalysis, In *Cytochrome P-450*, pp 89-117, Springer.

58. Murataliev, M. B., Feyereisen, R., and Walker, F. A. (2004) Electron transfer by diflavin reductases, *Biochimica et Biophysica Acta (BBA)-Proteins and Proteomics 1698*, 1-26.

59. Hevel, J. M., White, K. A., and Marletta, M. A. (1991) Purification of the inducible murine macrophage nitric oxide synthase. Identification as a flavoprotein, *Journal of Biological Chemistry 266*, 22789-22791.

60. Crane, B. R., Arvai, A. S., Gachhui, R., Wu, C., Ghosh, D. K., Getzoff, E. D., Stuehr, D. J., and Tainer, J. A. (1997) The structure of nitric oxide synthase oxygenase domain and inhibitor complexes, *Science 278*, 425-431.

61. Li, H., Raman, C., Glaser, C. B., Blasko, E., Young, T. A., Parkinson, J. F., Whitlow, M., and Poulos, T. L. (1999) Crystal Structures of Zinc-free and-bound Heme Domain of Human Inducible Nitric-oxide Synthase IMPLICATIONS FOR DIMER STABILITY AND COMPARISON WITH ENDOTHELIAL NITRIC-OXIDE SYNTHASE, *Journal of Biological Chemistry 274*, 21276-21284.

62. Raman, C., Li, H., Martásek, P., Král, V., Masters, B. S. S., and Poulos, T. L. (1998) Crystal structure of constitutive endothelial nitric oxide synthase: a paradigm for pterin function involving a novel metal center, *Cell 95*, 939-950.

63. Alderton, W. K., Cooper, C. E., and Knowles, R. G. (2001) Nitric oxide synthases: structure, function and inhibition, *Biochemical Journal 357*, 593-615.

64. Bredt, D. S., Hwang, P. M., Glatt, C. E., Lowenstein, C., Reed, R. R., and Snyder, S. H. (1991) Cloned and expressed nitric oxide synthase structurally resembles cytochrome P-450 reductase, *Nature 351*, 714-718.

65. White, K. A., and Marletta, M. A. (1992) Nitric oxide synthase is a cytochrome P-450 type hemoprotein, *Biochemistry 31*, 6627-6631.

66. McMillan, K., Bredt, D. S., Hirsch, D. J., Snyder, S. H., Clark, J. E., and Masters, B. (1992) Cloned, expressed rat cerebellar nitric oxide synthase contains stoichiometric amounts of heme, which binds carbon monoxide, *Proceedings of the National Academy of Sciences 89*, 11141-11145.

67. Garcin, E. D., Bruns, C. M., Lloyd, S. J., Hosfield, D. J., Tiso, M., Gachhui, R., Stuehr, D. J., Tainer, J. A., and Getzoff, E. D. (2004) Structural basis for isozyme-specific regulation of electron transfer in nitric-oxide synthase, *Journal of Biological Chemistry 279*, 37918-37927.

68. Xia, C., Misra, I., Iyanagi, T., and Kim, J.-J. P. (2009) Regulation of interdomain interactions by calmodulin in inducible nitric-oxide synthase, *Journal of Biological Chemistry 284*, 30708-30717.

69. Zhang, J., Martásek, P., Paschke, R., Shea, T., Masters, B. S. S., and Kim, J.-J. P. (2001) Crystal structure of the FAD/NADPH-binding domain of rat neuronal nitric-oxide synthase Comparisons with NADPH-cytochrome P450 oxidoreductase, *Journal of Biological Chemistry 276*, 37506-37513.

70. Crane, B. R., Arvai, A. S., Ghosh, D. K., Wu, C., Getzoff, E. D., Stuehr, D. J., and Tainer, J. A. (1998) Structure of nitric oxide synthase oxygenase dimer with pterin and substrate, *Science 279*, 2121-2126.

71. Fischmann, T. O., Hruza, A., Da Niu, X., Fossetta, J. D., Lunn, C. A., Dolphin, E., Prongay, A. J., Reichert, P., Lundell, D. J., and Narula, S. K. (1999) Structural characterization of nitric oxide synthase isoforms reveals striking active-site conservation, *Nature Structural & Molecular Biology 6*, 233-242.

72. Abu-Soud, H. M., and Stuehr, D. J. (1993) Nitric oxide synthases reveal a role for calmodulin in controlling electron transfer, *Proceedings of the National Academy of Sciences 90*, 10769-10772.

73. Siddhanta, U., Presta, A., Fan, B., Wolan, D., Rousseau, D. L., and Stuehr, D. J. (1998) Domain Swapping in Inducible Nitric-oxide Synthase ELECTRON TRANSFER OCCURS BETWEEN FLAVIN AND HEME GROUPS LOCATED ON ADJACENT SUBUNITS IN THE DIMER, *Journal of Biological Chemistry 273*, 18950-18958.

74. Vogel, H. J. (1994) Calmodulin: a versatile calcium mediator protein, *Biochemistry and cell biology 72*, 357-376.

75. Cho, H. J., Xie, Q., Calaycay, J., Mumford, R. A., Swiderek, K. M., Lee, T. D., and Nathan, C. (1992) Calmodulin is a subunit of nitric oxide synthase from macrophages, *The Journal of experimental medicine 176*, 599-604.

76. Wei, C.-C., Wang, Z.-Q., Wang, Q., Meade, A. L., Hemann, C., Hille, R., and Stuehr, D. J. (2001) Rapid kinetic studies link tetrahydrobiopterin radical formation to heme-dioxy reduction and arginine hydroxylation in inducible nitric-oxide synthase, *Journal of Biological Chemistry 276*, 315-319.

77. Bec, N., Gorren, A. F., Mayer, B., Schmidt, P. P., Andersson, K. K., and Lange, R. (2000) The role of tetrahydrobiopterin in the activation of oxygen by nitric-oxide synthase, *Journal of inorganic biochemistry 81*, 207-211.

78. Santolini, J., Meade, A. L., and Stuehr, D. J. (2001) Differences in three kinetic parameters underpin the unique catalytic profiles of nitric-oxide synthases I, II, and III, *Journal of Biological Chemistry 276*, 48887-48898.

79. Marletta, M. A. (1993) Nitric-Oxide Synthase Structure and Mechanism, *Journal of Biological Chemistry 268*, 12231-12234.

80. Stuehr, D. J., and Griffith, O. W. (2006) Mammalian nitric oxide synthases, *Advances in Enzymology and Related Areas of Molecular Biology, Volume 65*, 287-346.

81. Dawson, V. L., and Dawson, T. M. (1996) Nitric oxide neurotoxicity, *Journal of chemical neuroanatomy 10*, 179-190.

82. Li, H., and Förstermann, U. (2000) Nitric oxide in the pathogenesis of vascular disease, *The Journal of pathology 190*, 244-254.

83. Comini, L., Boraso, A., Bachetti, T., Bernocchi, P., Pasini, E., Bastianon, D., Curello, S., Terracciano, C. M., Ceconi, C., and Ferrari, R. (2005) Effects of endotoxic shock on neuronal NOS and calcium transients in rat cardiac myocytes, *Pharmacological research 51*, 409-417.

84. Smith, S., Man, C., Yip, P., Tang, E., Chapman, A., and Meldrum, B. (1996) Anticonvulsant effects of 7-nitroindazole in rodents with reflex epilepsy may result from L-arginine accumulation or a reduction in nitric oxide or L-citrulline formation, *British journal of pharmacology 119*, 165-173.

85. Ramachandran, R., Ploug, K. B., Hay-Schmidt, A., Olesen, J., Jansen-Olesen, I., and Gupta, S. (2010) Nitric oxide synthase (NOS) in the trigeminal vascular system and other brain structures related to pain in rats, *Neuroscience letters 484*, 192-196.

86. Dorheim, M.-A., Tracey, W. R., Pollock, J. S., and Grammas, P. (1994) Nitric oxide synthase activity is elevated in brain microvessels in Alzheimer′s disease, *Biochemical and biophysical research communications 205*, 659-665.

87. Giasson, B. I., Duda, J. E., Murray, I. V., Chen, Q., Souza, J. M., Hurtig, H. I., Ischiropoulos, H., Trojanowski, J. Q., and Lee, V. M.-Y. (2000) Oxidative damage linked to neurodegeneration by selective α-synuclein nitration in synucleinopathy lesions, *Science 290*, 985-989.

88. Norris, P., Waldvogel, H., Faull, R., Love, D., and Emson, P. (1996) Decreased neuronal nitric oxide synthase messenger RNA and somatostatin messenger RNA in the striatum of Huntington's disease, *Neuroscience 72*, 1037-1047.

89. Yang, Z., Misner, B., Ji, H., Poulos, T. L., Silverman, R. B., Meyskens, F. L., and Yang, S. (2013) Targeting nitric oxide signaling with nNOS inhibitors as a novel strategy for the therapy and prevention of human melanoma, *Antioxidants & redox signaling 19*, 433-447.

90. Bian, K., and Murad, F. (2003) Nitric oxide (NO)--biogeneration, regulation, and relevance to human diseases, *Frontiers in bioscience: a journal and virtual library 8*, d264-278.

91. Holden, J. K., Li, H., Jing, Q., Kang, S., Richo, J., Silverman, R. B., and Poulos, T. L. (2013) Structural and biological studies on bacterial nitric oxide synthase inhibitors, *Proceedings of the National Academy of Sciences 110*, 18127-18131.

92. Van Sorge, N. M., Beasley, F. C., Gusarov, I., Gonzalez, D. J., von Köckritz-Blickwede, M., Anik, S., Borkowski, A. W., Dorrestein, P. C., Nudler, E., and Nizet, V. (2013) Methicillin-resistant Staphylococcus aureus bacterial nitric-oxide synthase affects antibiotic sensitivity and skin abscess development, *Journal of Biological Chemistry 288*, 6417-6426.

93. Matter, H., and Kotsonis, P. (2004) Biology and chemistry of the inhibition of nitric oxide synthases by pteridine-derivatives as therapeutic agents, *Medicinal research reviews 24*, 662-684.

94. Peterlin Masic, L. (2006) Arginine mimetic structures in biologically active antagonists and inhibitors, *Current medicinal chemistry 13*, 3627-3648.

95. Hobbs, A. J., Higgs, A., and Moncada, S. (1999) Inhibition of nitric oxide synthase as a potential therapeutic target, *Annual Review of Pharmacology and Toxicology 39*, 191-220.

96. Villanueva, C., and Giulivi, C. (2010) Subcellular and cellular locations of nitric oxide synthase isoforms as determinants of health and disease, *Free Radical Biology and Medicine 49*, 307-316.

97. Olesen, J. (2010) Nitric oxide-related drug targets in headache, *Neurotherapeutics 7*, 183-190.

98. Li, H., Shimizu, H., Flinspach, M., Jamal, J., Yang, W., Xian, M., Cai, T., Wen, E. Z., Jia, Q., and Wang, P. G. (2002) The novel binding mode of N-alkyl-N'-hydroxyguanidine to neuronal nitric oxide synthase provides mechanistic insights into NO biosynthesis, *Biochemistry 41*, 13868-13875.

99. Poulos, T. L., and Li, H. (2012) Structural basis for isoform-selective inhibition in nitric oxide synthase, *Accounts of chemical research 46*, 390-398.

100. Silverman, R. B. (2009) Design of selective neuronal nitric oxide synthase inhibitors for the prevention and treatment of neurodegenerative diseases, *Accounts of chemical research 42*, 439-451.

101. Mauk, M. R., Ferrer, J. C., and Mauk, A. G. (1994) Proton linkage in formation of the cytochrome c-cytochrome c peroxidase complex: electrostatic properties of the high-and low-affinity cytochrome binding sites on the peroxidase, *Biochemistry 33*, 12609-12614.

102. Hahm, S., Geren, L., Durham, B., and Millett, F. (1993) Reaction of cytochrome c with the radical in cytochrome c peroxidase compound I, *Journal of the American Chemical Society 115*, 3372-3373.

103. McPhillips, T. M., McPhillips, S. E., Chiu, H.-J., Cohen, A. E., Deacon, A. M., Ellis, P. J., Garman, E., Gonzalez, A., Sauter, N. K., and Phizackerley, R. P. (2002) Blu-Ice and the Distributed Control System: software for data acquisition and instrument control at macromolecular crystallography beamlines, *Journal of synchrotron radiation 9*, 401-406.

104. Battye, T. G. G., Kontogiannis, L., Johnson, O., Powell, H. R., and Leslie, A. G. (2011) iMOSFLM: a new graphical interface for diffraction-image processing with MOSFLM, *Acta Crystallographica Section D: Biological Crystallography 67*, 271-281.

105. Evans, P. R., and Murshudov, G. N. (2013) How good are my data and what is the resolution?, *Acta Crystallographica Section D: Biological Crystallography 69*, 1204-1214.

106. McCoy, A. J., Grosse-Kunstleve, R. W., Adams, P. D., Winn, M. D., Storoni, L. C., and Read, R. J. (2007) Phaser crystallographic software, *Journal of applied crystallography 40*, 658-674.

107. Adams, P. D., Mustyakimov, M., Afonine, P. V., and Langan, P. (2009) Generalized X-ray and neutron crystallographic analysis: more accurate and complete structures for biological macromolecules, *Acta Crystallographica Section D: Biological Crystallography 65*, 567-573.

108. Emsley, P., and Cowtan, K. (2004) Coot: model-building tools for molecular graphics, *Acta Crystallographica Section D: Biological Crystallography 60*, 2126-2132.

109. Wang, K., Mei, H., Geren, L., Miller, M. A., Saunders, A., Wang, X., Waldner, J. L., Pielak, G. J., Durham, B., and Millett, F. (1996) Design of a ruthenium-cytochrome c derivative to measure electron transfer to the radical cation and oxyferryl heme in cytochrome c peroxidase, *Biochemistry 35*, 15107-15119.

110. Bhaskar, B., Immoos, C. E., Shimizu, H., Sulc, F., Farmer, P. J., and Poulos, T. L. (2003) A novel heme and peroxide-dependent tryptophan–tyrosine cross-link in a mutant of cytochrome c peroxidase, *Journal of molecular biology 328*, 157-166.

111. Mei, H., Wang, K., McKee, S., Wang, X., Waldner, J. L., Pielak, G. J., Durham, B., and Millett, F. (1996) Control of formation and dissociation of the high-affinity complex between cytochrome c and cytochrome c peroxidase by ionic strength and the low-affinity binding site, *Biochemistry 35*, 15800-15806.

112. Coulson, A. F., Erman, J. E., and Yonetani, T. (1971) Studies on cytochrome c peroxidase XVII. Stoichiometry and mechanism of the reaction of compound ES with donors, *Journal of Biological Chemistry 246*, 917-924.

113. Casadei, C. M., Gumiero, A., Metcalfe, C. L., Murphy, E. J., Basran, J., Teixeira, S. C., Schrader, T. E., Fielding, A. J., Ostermann, A., and Blakeley, M. P. (2014) Neutron cryo-crystallography captures the protonation state of ferryl heme in a peroxidase, *Science 345*, 193-197.

114. Poulos, T. L., and Kraut, J. (1980) The stereochemistry of peroxidase catalysis, *Journal of Biological Chemistry 255*, 8199-8205.

115. Harris, H., Fisher, K., and Dance, I. (2001) Coordination and dehydrogenation of PH3 by 23 transition metal ions in the gas phase: FTICR experiments and density functional interpretations, *Inorganic chemistry 40*, 6972-6982.

116. Derat, E., Shaik, S., Rovira, C., Vidossich, P., and Alfonso-Prieto, M. (2007) The effect of a water molecule on the mechanism of formation of compound 0 in horseradish peroxidase, *Journal of the American Chemical Society 129*, 6346-6347.

117. Pearl, N. M., Jacobson, T., Meyen, C., Clementz, A. G., Ok, E. Y., Choi, E., Wilson, K., Vitello, L. B., and Erman, J. E. (2008) Effect of Single-Site Charge-Reversal Mutations on the Catalytic Properties of Yeast Cytochrome c Peroxidase: Evidence for a Single, Catalytically Active, Cytochrome c Binding Domain†, *Biochemistry 47*, 2766-2775.

118. Vidossich, P., Fiorin, G., Alfonso-Prieto, M., Derat, E., Shaik, S., and Rovira, C. (2010) On the role of water in peroxidase catalysis: a theoretical investigation of HRP compound I formation, *The Journal of Physical Chemistry B 114*, 5161-5169.

119. Berglund, G. I., Carlsson, G. H., Smith, A. T., Szöke, H., Henriksen, A., and Hajdu, J. (2002) The catalytic pathway of horseradish peroxidase at high resolution, *Nature 417*, 463-468.

120. Meharenna, Y. T., Doukov, T., Li, H., Soltis, S. M., and Poulos, T. L. (2010) Crystallographic and Single-Crystal Spectral Analysis of the Peroxidase Ferryl Intermediate, *Biochemistry 49*, 2984-2986.

121. Poulos, T. L. (2014) Heme enzyme structure and function, *Chemical reviews 114*, 3919-3962.

122. Green, M. T. (2006) Application of Badger's rule to heme and non-heme iron-oxygen bonds: An examination of ferryl protonation states, *Journal of the American Chemical Society 128*, 1902-1906.

123. Chreifi, G., Hollingsworth, S. A., Li, H., Tripathi, S., Arce, A. P., Magaña-Garcia, H. I., and Poulos, T. L. (2015) Enzymatic Mechanism of Leishmania major Peroxidase and the Critical Role of Specific Ionic Interactions, *Biochemistry 54*, 3328-3336.

124. Meharenna, Y. T., Oertel, P., Bhaskar, B., and Poulos, T. L. (2008) Engineering Ascorbate Peroxidase Activity into Cytochrome c Peroxidase†‡, *Biochemistry 47*, 10324-10332.

125. Cohen, A. E., Ellis, P. J., Miller, M. D., Deacon, A. M., and Phizackerley, R. P. (2002) An automated system to mount cryo-cooled protein crystals on a synchrotron beamline, using compact sample cassettes and a small-scale robot, *Journal of applied crystallography 35*, 720-726.

126. Cohen, A. E., Soltis, S. M., González, A., Aguila, L., Alonso-Mori, R., Barnes, C. O., Baxter, E. L., Brehmer, W., Brewster, A. S., and Brunger, A. T. (2014) Goniometer-based femtosecond crystallography with X-ray free electron lasers, *Proceedings of the National Academy of Sciences 111*, 17122-17127.

127. Kabsch, W. (2014) Processing of X-ray snapshots from crystals in random orientations, *Acta Crystallographica Section D: Biological Crystallography 70*, 2204-2216.

128. Vagin, A., and Teplyakov, A. (1997) MOLREP: an automated program for molecular replacement, *Journal of applied crystallography 30*, 1022-1025.

129. Murshudov, G. N., Skubák, P., Lebedev, A. A., Pannu, N. S., Steiner, R. A., Nicholls, R. A., Winn, M. D., Long, F., and Vagin, A. A. (2011) REFMAC5 for the refinement of macromolecular crystal structures, *Acta Crystallographica Section D: Biological Crystallography 67*, 355-367.

130. Papagrigoriou, E., Gingras, A. R., Barsukov, I. L., Bate, N., Fillingham, I. J., Patel, B., Frank, R., Ziegler, W. H., Roberts, G. C., and Critchley, D. R. (2004) Activation of a vinculin-binding site in the talin rod involves rearrangement of a five-helix bundle, *The EMBO journal 23*, 2942-2951.

131. Kabsch, W. (2010) Xds, *Acta Crystallographica Section D: Biological Crystallography 66*, 125-132.

132. Winn, M. D., Ballard, C. C., Cowtan, K. D., Dodson, E. J., Emsley, P., Evans, P. R., Keegan, R. M., Krissinel, E. B., Leslie, A. G., and McCoy, A. (2011) Overview of the CCP4 suite and current developments, *Acta Crystallographica Section D: Biological Crystallography 67*, 235-242.

133. Smart, O. S., Womack, T. O., Flensburg, C., Keller, P., Paciorek, W., Sharff, A., Vonrhein, C., and Bricogne, G. (2012) Exploiting structure similarity in refinement: automated NCS and target-structure restraints in BUSTER, *Acta Crystallographica Section D: Biological Crystallography 68*, 368-380.

134. Harris, D. L., and Loew, G. H. (2001) Proximal ligand effects on electronic structure and spectra of compound I of peroxidases, *Journal of Porphyrins and Phthalocyanines 5*, 334-344.

135. Bashford, D., and Gerwert, K. (1992) Electrostatic calculations of the pK a values of ionizable groups in bacteriorhodopsin, *Journal of molecular biology 224*, 473-486.

136. Warshel, A., Sussman, F., and King, G. (1986) Free energy of charges in solvated proteins: microscopic calculations using a reversible charging process, *Biochemistry 25*, 8368-8372.

137. Mongan, J., Case, D. A., and McCAMMON, J. A. (2004) Constant pH molecular dynamics in generalized Born implicit solvent, *Journal of computational chemistry 25*, 2038-2048.

138. Swails, J. M., York, D. M., and Roitberg, A. E. (2014) Constant pH replica exchange molecular dynamics in explicit solvent using discrete protonation states: Implementation, testing, and validation, *Journal of chemical theory and computation 10*, 1341-1352.

139. Bonagura, C. A., Bhaskar, B., Shimizu, H., Li, H., Sundaramoorthy, M., McRee, D. E., Goodin, D. B., and Poulos, T. L. (2003) High-resolution crystal structures and spectroscopy of native and compound I cytochrome c peroxidase, *Biochemistry 42*, 5600-5608.

140. Poulos, T. L., and Kraut, J. (1980) A hypothetical model of the cytochrome c peroxidase. cytochrome c electron transfer complex, *Journal of Biological Chemistry 255*, 10322-10330.

141. Behan, R. K., and Green, M. T. (2006) On the status of ferryl protonation, *Journal of inorganic biochemistry 100*, 448-459.

142. Mukai, M., Nagano, S., Tanaka, M., Ishimori, K., Morishima, I., Ogura, T., Watanabe, Y., and Kitagawa, T. (1997) Effects of concerted hydrogen bonding of distal histidine on active site structures of horseradish peroxidase. Resonance Raman studies with Asn70 mutants, *Journal of the American Chemical Society 119*, 1758-1766.

143. Terner, J., Palaniappan, V., Gold, A., Weiss, R., Fitzgerald, M. M., Sullivan, A. M., and Hosten, C. M. (2006) Resonance Raman spectroscopy of oxoiron (IV) porphyrin π-cation radical and oxoiron (IV) hemes in peroxidase intermediates, *Journal of inorganic biochemistry 100*, 480-501.

144. Hashimoto, S., Tatsuno, Y., and Kitagawa, T. (1986) Resonance Raman evidence for oxygen exchange between the FeIV= O heme and bulk water during enzymic catalysis of horseradish peroxidase and its relation with the heme-linked ionization, *Proceedings of the National Academy of Sciences 83*, 2417-2421.

145. Fields, J. B., Hollingsworth, S. A., Chreifi, G., Heyden, M., Arce, A. P., Magaña-Garcia, H. I., Poulos, T. L., and Tobias, D. J. (2015) "Bind and Crawl" Association Mechanism of Leishmania major Peroxidase and Cytochrome c Revealed by Brownian and Molecular Dynamics Simulations, *Biochemistry 54*, 7272-7282.

146. Kang, C., Ferguson-Miller, S., and Margoliash, E. (1977) Steady state kinetics and binding of eukaryotic cytochromes c with yeast cytochrome c peroxidase, *Journal of Biological Chemistry 252*, 919-926.

147. Pielak, G. J., and Wang, X. (2001) Interactions between yeast iso-1-cytochrome c and its peroxidase, *Biochemistry 40*, 422-428.

148. Brittain, T., Kidd, R. D., and Baker, E. N. (2002) Electron transfer between cytochrome b 5 and some oxidised haemoglobins: the role of ionic strength, *Journal of inorganic biochemistry 88*, 328-334.

149. Cruz-Gallardo, I., Díaz-Moreno, I., Díaz-Quintana, A., and Miguel, A. (2012) The cytochrome f–plastocyanin complex as a model to study transient interactions between redox proteins, *FEBS letters 586*, 646-652.

150. De Rienzo, F., Gabdoulline, R. R., Menziani, M. C., De Benedetti, P. G., and Wade, R. C. (2001) Electrostatic analysis and Brownian dynamics simulation of the association of plastocyanin and cytochrome f, *Biophysical journal 81*, 3090-3104.

151. Furukawa, Y., Matsuda, F., Ishimori, K., and Morishima, I. (2002) Investigation of the electron-transfer mechanism by cross-linking between Zn-substituted myoglobin and cytochrome b 5, *Journal of the American Chemical Society 124*, 4008-4019.

152. Gabdoulline, R. R., and Wade, R. C. (2001) Protein-protein association: investigation of factors influencing association rates by Brownian dynamics simulations, *Journal of molecular biology 306*, 1139-1155.

153. Gabdoulline, R. R., and Wade, R. C. (2009) On the contributions of diffusion and thermal activation to electron transfer between Phormidium laminosum plastocyanin and cytochrome f: Brownian dynamics simulations with explicit modeling of nonpolar desolvation interactions and electron transfer events, *Journal of the American Chemical Society 131*, 9230-9238.

154. Gross, E. L. (2007) A Brownian dynamics computational study of the interaction of spinach plastocyanin with turnip cytochrome f: the importance of plastocyanin conformational changes, *Photosynthesis research 94*, 411-422.

155. Gross, E. L., and Pearson, D. C. (2003) Brownian dynamics simulations of the interaction of Chlamydomonas cytochrome f with plastocyanin and cytochrome c 6, *Biophysical journal 85*, 2055-2068.

156. Grove, T. Ž., Ullmann, G. M., and Kostić, N. M. (2012) Simultaneous true, gated, and coupled electron-transfer reactions and energetics of protein rearrangement, *Journal of inorganic biochemistry 106*, 143-150.

157. Keinan, S., Nocek, J. M., Hoffman, B. M., and Beratan, D. N. (2012) Interfacial hydration, dynamics and electron transfer: multi-scale ET modeling of the transient [myoglobin, cytochrome b5] complex, *Physical Chemistry Chemical Physics 14*, 13881-13889.

158. Lin, J., and Beratan, D. N. (2005) Simulation of electron transfer between cytochrome C2 and the bacterial photosynthetic reaction center: Brownian dynamics analysis of the native proteins and double mutants, *The Journal of Physical Chemistry B 109*, 7529-7534.

159. Long, H., Chang, C. H., King, P. W., Ghirardi, M. L., and Kim, K. (2008) Brownian dynamics and molecular dynamics study of the association between hydrogenase and ferredoxin from Chlamydomonas reinhardtii, *Biophysical journal 95*, 3753-3766.

160. Madrona, Y., Hollingsworth, S. A., Tripathi, S., Fields, J. B., Rwigema, J.-C. N., Tobias, D. J., and Poulos, T. L. (2014) Crystal structure of cindoxin, the P450cin redox partner, *Biochemistry 53*, 1435-1446.

161. Moreno-Beltrán, B., Díaz-Quintana, A., González-Arzola, K., Velázquez-Campoy, A., Miguel, A., and Díaz-Moreno, I. (2014) Cytochrome c 1 exhibits two binding sites for cytochrome c in plants, *Biochimica et Biophysica Acta (BBA)-Bioenergetics 1837*, 1717-1729.

162. Nocek, J. M., Sishta, B. P., Cameron, J. C., Mauk, A. G., and Hoffman, B. M. (1997) Cyclic electron transfer within the [Zn-myoglobin, cytochrome b 5] complex, *Journal of the American Chemical Society 119*, 2146-2155.

163. Northrup, S. H., Boles, J. O., and Reynolds, J. (1988) Brownian dynamics of cytochrome c and cytochrome c peroxidase association, *Science 241*, 67-70.

164. Northrup, S. H., Thomasson, K. A., Miller, C. M., Barker, P. D., Eltis, L. D., Guillemette, J. G., Mauk, A. G., and Inglis, S. C. (1993) Effects of charged amino acid mutations on the bimolecular kinetics of reduction of yeast iso-1-ferricytochrome c by bovine ferrocytochrome b5, *Biochemistry 32*, 6613-6623.

165. Pearson, D. C., and Gross, E. L. (1998) Brownian dynamics study of the interaction between plastocyanin and cytochrome f, *Biophysical journal 75*, 2698-2711.

166. Xiong, P., Nocek, J. M., Vura-Weis, J., Lockard, J. V., Wasielewski, M. R., and Hoffman, B. M. (2010) Faster interprotein electron transfer in a [myoglobin, b5] complex with a redesigned interface, *Science 330*, 1075-1078.

167. Zöllner, A., Pasquinelli, M. A., Bernhardt, R., and Beratan, D. N. (2007) Protein phosphorylation and intermolecular electron transfer: a joint experimental and computational study of a hormone biosynthesis pathway, *Journal of the American Chemical Society 129*, 4206-4216.

168. Murshudov, G. N., Vagin, A. A., and Dodson, E. J. (1997) Refinement of macromolecular structures by the maximum-likelihood method, *Acta Crystallographica Section D: Biological Crystallography 53*, 240-255.

169. Winn, M., Isupov, M., and Murshudov, G. N. (2001) Use of TLS parameters to model anisotropic displacements in macromolecular refinement, *Acta Crystallographica Section D: Biological Crystallography 57*, 122-133.

170. DeLano, W. L. (2002) The PyMOL molecular graphics system.

171. Hoare, C. A., and Wallace, F. G. (1966) Developmental stages of trypanosomatid flagellates: a new terminology.

172. Ferrer-Sueta, G., and Radi, R. (2009) Chemical biology of peroxynitrite: kinetics, diffusion, and radicals, *ACS Chemical Biology 4*, 161-177.

173. Fridovich, I. (1995) Superoxide radical and superoxide dismutases, *Annual review of biochemistry 64*, 97-112.

174. Huie, R. E., and Padmaja, S. (1993) The reaction of NO with superoxide, *Free radical research communications 18*, 195-199.

175. Koppenol, W., Moreno, J., Pryor, W. A., Ischiropoulos, H., and Beckman, J. (1992) Peroxynitrite, a cloaked oxidant formed by nitric oxide and superoxide, *Chemical research in toxicology 5*, 834-842.

176. Tsai, J.-H. M., Harrison, J. G., Martin, J. C., Hamilton, T. P., van der Woerd, M., Jablonsky, M. J., and Beckman, J. S. (1994) Role of Conformation of peroxynitrite Anion (ONOO-) with its stability and toxicity, *Journal of the American Chemical Society 116*, 4115-4116.

177. Tsai, H.-H., Hamilton, T. P., Tsai, J.-H. M., and Beckman, J. S. (1995) Ab initio studies of peroxynitrite anion-water complexes, *Structural Chemistry 6*, 323-332.

178. Lo, W. J., Lee, Y. P., Tsai, J. H. M., Tsai, H. H., Hamilton, T. P., Harrison, J. G., and Beckman, J. S. (1995) Infrared absorption of cis-and trans-alkali-metal peroxynitrites (MOONO, M= Li, Na, and K) in solid argon, *The Journal of chemical physics 103*, 4026-4034.

179. Lo, W.-J., Lee, Y.-P., Tsai, J.-H. M., and Beckman, J. S. (1995) Ultraviolet absorption spectra of cis and trans potassium peroxynitrite (KOONO) in solid argon, *Chemical physics letters 242*, 147-152.

180. Pryor, W. A., and Squadrito, G. L. (1995) The chemistry of peroxynitrite: a product from the reaction of nitric oxide with superoxide, *American Journal of Physiology-Lung Cellular and Molecular Physiology 268*, L699-L722.

181. Crow, J. P., Beckman, J. S., and McCord, J. M. (1995) Sensitivity of the essential zinc-thiolate moiety of yeast alcohol dehydrogenase to hypochlorite and peroxynitrite, *Biochemistry 34*, 3544-3552.

182. Castro, L., Rodriguez, M., and Radi, R. (1994) Aconitase is readily inactivated by peroxynitrite, but not by its precursor, nitric oxide, *Journal of Biological Chemistry 269*, 29409-29415.

183. Hausladen, A., and Fridovich, I. (1994) Superoxide and peroxynitrite inactivate aconitases, but nitric oxide does not, *Journal of Biological Chemistry 269*, 29405-29408.

184. Radi, R., Beckman, J. S., Bush, K. M., and Freeman, B. A. (1991) Peroxynitrite oxidation of sulfhydryls. The cytotoxic potential of superoxide and nitric oxide, *Journal of Biological Chemistry 266*, 4244-4250.

185. Quijano, C., ALVAREZ, B., GATTI, R. M., AUGUSTO, O., and Rafael, R. (1997) Pathways of peroxynitrite oxidation of thiol groups, *Biochemical Journal 322*, 167-173.

186. Ramezanian, M. S., Padmaja, S., and Koppenol, W. H. (1996) Nitration and hydroxylation of phenolic compounds by peroxynitrite, *Chemical research in toxicology 9*, 232-240.

187.   Ischiropoulos, H., Zhu, L., Chen, J., Tsai, M., Martin, J. C., Smith, C. D., and Beckman, J. S. (1992) Peroxynitrite-mediated tyrosine nitration catalyzed by superoxide dismutase, *Archives of biochemistry and biophysics 298*, 431-437.

188.   Beckmann, J. S., Ye, Y. Z., Anderson, P. G., Chen, J., Accavitti, M. A., Tarpey, M. M., and White, C. R. (1994) Extensive nitration of protein tyrosines in human atherosclerosis detected by immunohistochemistry, *Biological chemistry Hoppe-Seyler 375*, 81-88.

189.   Douki, T., Cadet, J., and Ames, B. N. (1996) An adduct between peroxynitrite and 2'-deoxyguanosine: 4, 5-dihydro-5-hydroxy-4-(nitrosooxy)-2'-deoxyguanosine, *Chemical research in toxicology 9*, 3-7.

190.   Cadet, J., Delatour, T., Douki, T., Gasparutto, D., Pouget, J.-P., Ravanat, J.-L., and Sauvaigo, S. (1999) Hydroxyl radicals and DNA base damage, *Mutation Research/Fundamental and Molecular Mechanisms of Mutagenesis 424*, 9-21.

191.   Radi, R., Beckman, J. S., Bush, K. M., and Freeman, B. A. (1991) Peroxynitrite-induced membrane lipid peroxidation: the cytotoxic potential of superoxide and nitric oxide, *Archives of biochemistry and biophysics 288*, 481-487.

192.   Forman, H. J., and Torres, M. (2002) Reactive oxygen species and cell signaling: respiratory burst in macrophage signaling, *American journal of respiratory and critical care medicine 166*, S4-S8.

193.   Iyengar, R., Stuehr, D. J., and Marletta, M. A. (1987) Macrophage synthesis of nitrite, nitrate, and N-nitrosamines: precursors and role of the respiratory burst, *Proceedings of the National Academy of Sciences 84*, 6369-6373.

194.   Bose, M., Saha, R., Santara, S. S., Mukherjee, S., Roy, J., and Adak, S. (2012) Protection against peroxynitrite by pseudoperoxidase from Leishmania major, *Free Radical Biology and Medicine 53*, 1819-1828.

195.   Saha, R., Bose, M., and Adak, S. (2013) Mutation of Val90 to His in the pseudoperoxidase from Leishmania major enhances peroxidase activity, *Biochimica et Biophysica Acta (BBA)-Proteins and Proteomics 1834*, 651-657.

196.   Saha, R., Bose, M., Sen Santara, S., Roy, J., and Adak, S. (2013) Identification of Proximal and Distal Axial Ligands in Leishmania major Pseudoperoxidase, *Biochemistry 52*, 8878-8887.

197.   Terwilliger, T. C., Adams, P. D., Read, R. J., McCoy, A. J., Moriarty, N. W., Grosse-Kunstleve, R. W., Afonine, P. V., Zwart, P. H., and Hung, L.-W. (2009) Decision-making in structure solution using Bayesian estimates of map quality: the PHENIX AutoSol wizard, *Acta Crystallographica Section D: Biological Crystallography 65*, 582-601.

198.   Terwilliger, T. C., Grosse-Kunstleve, R. W., Afonine, P. V., Moriarty, N. W., Zwart, P. H., Hung, L.-W., Read, R. J., and Adams, P. D. (2008) Iterative model building, structure refinement and density modification with the PHENIX AutoBuild wizard, *Acta Crystallographica Section D: Biological Crystallography 64*, 61-69.

199.   Poulos, T. (1988) Heme enzyme crystal structures, *Advances in inorganic biochemistry 7*, 1.

200.   Herold, S., Kalinga, S., Matsui, T., and Watanabe, Y. (2004) Mechanistic studies of the isomerization of peroxynitrite to nitrate catalyzed by distal histidine metmyoglobin mutants, *Journal of the American Chemical Society 126*, 6945-6955.

201. Yi, J., Heinecke, J., Tan, H., Ford, P. C., and Richter-Addo, G. B. (2009) The distal pocket histidine residue in horse heart myoglobin directs the O-binding mode of nitrite to the heme iron, *Journal of the American Chemical Society 131*, 18119-18128.

202. Radi, R. (2013) Peroxynitrite, a stealthy biological oxidant, *Journal of Biological Chemistry 288*, 26464-26472.

203. Trujillo, M., and Radi, R. (2002) Peroxynitrite reaction with the reduced and the oxidized forms of lipoic acid: new insights into the reaction of peroxynitrite with thiols, *Archives of biochemistry and biophysics 397*, 91-98.

204. Madrona, Y., Tripathi, S., Li, H., and Poulos, T. L. (2012) Crystal structures of substrate-free and nitrosyl cytochrome P450cin: Implications for O2 activation, *Biochemistry 51*, 6623-6631.

205. Meharenna, Y. T., Li, H., Hawkes, D. B., Pearson, A. G., De Voss, J., and Poulos, T. L. (2004) Crystal structure of P450cin in a complex with its substrate, 1, 8-cineole, a close structural homologue to D-camphor, the substrate for P450cam, *Biochemistry 43*, 9487-9494.

206. Scott, E. E., He, Y. A., Wester, M. R., White, M. A., Chin, C. C., Halpert, J. R., Johnson, E. F., and Stout, C. D. (2003) An open conformation of mammalian cytochrome P450 2B4 at 1.6-Å resolution, *Proceedings of the National Academy of Sciences 100*, 13196-13201.

207. Scott, E. E., White, M. A., He, Y. A., Johnson, E. F., Stout, C. D., and Halpert, J. R. (2004) Structure of Mammalian Cytochrome P450 2B4 Complexed with 4-(4-Chlorophenyl) imidazole at 1.9-Å Resolution INSIGHT INTO THE RANGE OF P450 CONFORMATIONS AND THE COORDINATION OF REDOX PARTNER BINDING, *Journal of Biological Chemistry 279*, 27294-27301.

208. Lee, Y.-T., Wilson, R. F., Rupniewski, I., and Goodin, D. B. (2010) P450cam visits an open conformation in the absence of substrate, *Biochemistry 49*, 3412-3419.

209. Shimada, H., Nagano, S., Hori, H., and Ishimura, Y. (2001) Putidaredoxin–cytochrome P450cam interaction, *Journal of inorganic biochemistry 83*, 255-260.

210. Unno, M., Christian, J. F., Sjodin, T., Benson, D. E., Macdonald, I. D., Sligar, S. G., and Champion, P. M. (2002) Complex Formation of Cytochrome P450cam with Putidaredoxin EVIDENCE FOR PROTEIN-SPECIFIC INTERACTIONS INVOLVING THE PROXIMAL THIOLATE LIGAND, *Journal of Biological Chemistry 277*, 2547-2553.

211. Nagano, S., Shimada, H., Tarumi, A., Hishiki, T., Kimata-Ariga, Y., Egawa, T., Suematsu, M., Park, S.-Y., Adachi, S.-i., and Shiro, Y. (2003) Infrared spectroscopic and mutational studies on putidaredoxin-induced conformational changes in ferrous CO-P450cam, *Biochemistry 42*, 14507-14514.

212. Tosha, T., Yoshioka, S., Takahashi, S., Ishimori, K., Shimada, H., and Morishima, I. (2003) NMR Study on the Structural Changes of Cytochrome P450cam upon the Complex Formation with Putidaredoxin FUNCTIONAL SIGNIFICANCE OF THE PUTIDAREDOXIN-INDUCED STRUCTURAL CHANGES, *Journal of Biological Chemistry 278*, 39809-39821.

213. Tosha, T., Yoshioka, S., Ishimori, K., and Morishima, I. (2004) L358P Mutation on Cytochrome P450cam Simulates Structural Changes upon Putidaredoxin Binding THE STRUCTURAL CHANGES TRIGGER ELECTRON TRANSFER TO OXY-P450CAM FROM ELECTRON DONORS, *Journal of Biological Chemistry 279*, 42836-42843.

214. Shiro, Y., Iizuka, T., Makino, R., Ishimura, Y., and Morishima, I. (1989) Nitrogen-15 NMR study on cyanide (C15N-) complex of cytochrome P-450cam. Effects of d-camphor and putidaredoxin on the iron-ligand structure, *Journal of the American Chemical Society 111*, 7707-7711.

215.	Pochapsky, S. S., Pochapsky, T. C., and Wei, J. W. (2003) A model for effector activity in a highly specific biological electron transfer complex: The cytochrome P450cam-putidaredoxin couple, *Biochemistry 42*, 5649-5656.

216.	Zhang, W., Pochapsky, S. S., Pochapsky, T. C., and Jain, N. U. (2008) Solution NMR structure of putidaredoxin–cytochrome P450cam complex via a combined residual dipolar coupling–spin labeling approach suggests a role for Trp106 of putidaredoxin in complex formation, *Journal of molecular biology 384*, 349-363.

217.	Tripathi, S., Li, H., and Poulos, T. L. (2013) Structural basis for effector control and redox partner recognition in cytochrome P450, *Science 340*, 1227-1230.

218.	Hawkes, D. B., Adams, G. W., Burlingame, A. L., de Montellano, P. R. O., and De Voss, J. J. (2002) Cytochrome P450cin (CYP176A), isolation, expression, and characterization, *Journal of Biological Chemistry 277*, 27725-27732.

219.	Madrona, Y., Hollingsworth, S. A., Khan, B., and Poulos, T. L. (2013) P450cin active site water: implications for substrate binding and solvent accessibility, *Biochemistry 52*, 5039-5050.

220.	Stuehr, D. J., and Griffith, O. W. (1992) Mammalian nitric oxide synthases, *Advances in Enzymology and Related Areas of Molecular Biology, Volume 65*, 287-346.

221.	Presta, A., Siddhanta, U., Wu, C., Sennequier, N., Huang, L., Abu-Soud, H. M., Erzurum, S., and Stuehr, D. J. (1998) Comparative functioning of dihydro-and tetrahydropterins in supporting electron transfer, catalysis, and subunit dimerization in inducible nitric oxide synthase, *Biochemistry 37*, 298-310.

222.	Klatt, P., Schmid, M., Leopold, E., Schmidt, K., Werner, E. R., and Mayer, B. (1994) The pteridine binding site of brain nitric oxide synthase. Tetrahydrobiopterin binding kinetics, specificity, and allosteric interaction with the substrate domain, *Journal of Biological Chemistry 269*, 13861-13866.

223.	KLÖSCH, B., VÖLKER, C., GORREN, A. C., SESSA, W. C., WERNER, E. R., KUKOVETZ, W. R., SCHMIDT, K., and MAYER, B. (1997) Characterization of bovine endothelial nitric oxide synthase as a homodimer with down-regulated uncoupled NADPH oxidase activity: tetrahydrobiopterin binding kinetics and role of haem in dimerization, *Biochemical Journal 323*, 159-165.

224.	Panda, K., Rosenfeld, R. J., Ghosh, S., Meade, A. L., Getzoff, E. D., and Stuehr, D. J. (2002) Distinct dimer interaction and regulation in nitric-oxide synthase types I, II, and III, *Journal of Biological Chemistry 277*, 31020-31030.

225.	Venema, R. C., Ju, H., Zou, R., Ryan, J. W., and Venema, V. J. (1997) Subunit Interactions of Endothelial Nitric-oxide Synthase COMPARISONS TO THE NEURONAL AND INDUCIBLE NITRIC-OXIDE SYNTHASE ISOFORMS, *Journal of Biological Chemistry 272*, 1276-1282.

226.	Werner, E. R., PITTERS, E., SCHMIDT, K., WACHTER, H., WERNER-FELMAYER, G., and MAYER, B. (1996) Identification of the 4-amino analogue of tetrahydrobiopterin as a dihydropteridine reductase inhibitor and a potent pteridine antagonist of rat neuronal nitric oxide synthase, *Biochemical Journal 320*, 193-196.

227.	Mayer, B., Wu, C., Gorren, A. C., Pfeiffer, S., Schmidt, K., Clark, P., Stuehr, D. J., and Werner, E. R. (1997) Tetrahydrobiopterin binding to macrophage inducible nitric oxide synthase: heme spin shift and dimer stabilization by the potent pterin antagonist 4-amino-tetrahydrobiopterin, *Biochemistry 36*, 8422-8427.

228.	Pfeiffer, S., GORREN, C. A., PITTERS, E., SCHMIDT, K., WERNER, R. E., and MAYER, B. (1997) Allosteric modulation of rat brain nitric oxide synthase by the pterin-site enzyme inhibitor 4-aminotetrahydrobiopterin, *Biochemical Journal 328*, 349-352.

229. Schmidt, P. P., Lange, R., Gorren, A. C., Werner, E. R., Mayer, B., and Andersson, K. K. (2001) Formation of a protonated trihydrobiopterin radical cation in the first reaction cycle of neuronal and endothelial nitric oxide synthase detected by electron paramagnetic resonance spectroscopy, *JBIC Journal of Biological Inorganic Chemistry 6*, 151-158.

230. Gorren, A. C., SCHRAMMEL, A., RIETHMÜLLER, C., SCHMIDT, K., KOESLING, D., WERNER, E. R., and MAYER, B. (2000) Nitric oxide-induced autoinhibition of neuronal nitric oxide synthase in the presence of the autoxidation-resistant pteridine 5-methyltetrahydrobiopterin, *Biochemical Journal 347*, 475-484.

231. Riethmüller, C., Gorren, A. C., Pitters, E., Hemmens, B., Habisch, H.-J., Heales, S. J., Schmidt, K., Werner, E. R., and Mayer, B. (1999) Activation of neuronal nitric-oxide synthase by the 5-methyl analog of tetrahydrobiopterin Functional evidence against reductive oxygen activation by the pterin cofactor, *Journal of Biological Chemistry 274*, 16047-16051.

232. Hevel, J. M., and Marletta, M. A. (1992) Macrophage nitric oxide synthase: relationship between enzyme-bound tetrahydrobiopterin and synthase activity, *Biochemistry 31*, 7160-7165.

233. Al-Hassan, S. S., Cameron, R. J., Curran, A. W., Lyall, W. J., Nicholson, S. H., Robinson, D. R., Stuart, A., Suckling, C. J., Stirling, I., and Wood, H. C. (1985) Specific inhibitors in vitamin biosynthesis. Part 7. Syntheses of blocked 7, 8-dihydropteridines via α-amino ketones, *Journal of the Chemical Society, Perkin Transactions 1*, 1645-1659.

234. Cameron, R., Nicholson, S. H., Robinson, D. H., Suckling, C. J., and Wood, H. C. (1985) Specific inhibitors in vitamin biosynthesis. Part 8. Syntheses of some functionalised 7, 7-dialkyl-7, 8-dihydropterins, *Journal of the Chemical Society, Perkin Transactions 1*, 2133-2143.

235. Otwinowski, Z., and Minor, W. (1997) [20] Processing of X-ray diffraction data collected in oscillation mode, *Methods in enzymology 276*, 307-326.

236. Suckling, C. J., Gibson, C. L., Huggan, J. K., Morthala, R. R., Clarke, B., Kununthur, S., Wadsworth, R. M., Daff, S., and Papale, D. (2008) 6-Acetyl-7, 7-dimethyl-5, 6, 7, 8-tetrahydropterin is an activator of nitric oxide synthases, *Bioorganic & medicinal chemistry letters 18*, 1563-1566.

237. Miller, R. T., Martásek, P., Raman, C., and Masters, B. S. S. (1999) Zinc Content of Escherichia coli-expressed Constitutive Isoforms of Nitric-oxide Synthase ENZYMATIC ACTIVITY AND EFFECT OF PTERIN, *Journal of Biological Chemistry 274*, 14537-14540.

238. Hemmens, B., Goessler, W., Schmidt, K., and Mayer, B. (2000) Role of bound zinc in dimer stabilization but not enzyme activity of neuronal nitric-oxide synthase, *Journal of Biological Chemistry 275*, 35786-35791.

239. Chen, P.-F., Tsai, A.-L., and Wu, K. K. (1995) Cysteine 99 of endothelial nitric oxide synthase (NOS-III) is critical for tetrahydrobiopterin-dependent NOS-III stability and activity, *Biochemical and biophysical research communications 215*, 1119-1129.

240. Ghosh, D. K., Wu, C., Pitters, E., Moloney, M., Werner, E. R., Mayer, B., and Stuehr, D. J. (1997) Characterization of the inducible nitric oxide synthase oxygenase domain identifies a 49 amino acid segment required for subunit dimerization and tetrahydrobiopterin interaction, *Biochemistry 36*, 10609-10619.

241. Martásek, P., Miller, R. T., Liu, Q., Roman, L. J., Salerno, J. C., Migita, C. T., Raman, C., Gross, S. S., Ikeda-Saito, M., and Masters, B. S. S. (1998) The C331A mutant of neuronal nitric-oxide synthase is defective in arginine binding, *Journal of Biological Chemistry 273*, 34799-34805.

242. Rodríguez-Crespo, I., Moënne-Loccoz, P., Loehr, T. M., and Ortiz de Montellano, P. R. (1997) Endothelial nitric oxide synthase: modulations of the distal heme site produced by progressive N-terminal deletions, *Biochemistry 36*, 8530-8538.

243. Jing, Q., Li, H., Chreifi, G., Roman, L. J., Martásek, P., Poulos, T. L., and Silverman, R. B. (2013) Chiral linkers to improve selectivity of double-headed neuronal nitric oxide synthase inhibitors, *Bioorganic & medicinal chemistry letters 23*, 5674-5679.

244. Southan, G. J., and Szabó, C. (1996) Selective pharmacological inhibition of distinct nitric oxide synthase isoforms, *Biochemical pharmacology 51*, 383-394.

245. Babu, B. R., and Griffith, O. W. (1998) Design of isoform-selective inhibitors of nitric oxide synthase, *Current opinion in chemical biology 2*, 491-500.

246. Ji, H., Li, H., Martásek, P., Roman, L. J., Poulos, T. L., and Silverman, R. B. (2009) Discovery of highly potent and selective inhibitors of neuronal nitric oxide synthase by fragment hopping, *Journal of medicinal chemistry 52*, 779-797.

247. Xue, F., Fang, J., Delker, S. L., Li, H., Martásek, P., Roman, L. J., Poulos, T. L., and Silverman, R. B. (2011) Symmetric double-headed aminopyridines, a novel strategy for potent and membrane-permeable inhibitors of neuronal nitric oxide synthase, *Journal of medicinal chemistry 54*, 2039-2048.

248. Flinspach, M. L., Li, H., Jamal, J., Yang, W., Huang, H., Hah, J.-M., Gómez-Vidal, J. A., Litzinger, E. A., Silverman, R. B., and Poulos, T. L. (2004) Structural basis for dipeptide amide isoform-selective inhibition of neuronal nitric oxide synthase, *Nature Structural & Molecular Biology 11*, 54-59.

249. Huang, H., Li, H., Yang, S., Chreifi, G., Martásek, P., Roman, L. J., Meyskens, F. L., Poulos, T. L., and Silverman, R. B. (2014) Potent and selective double-headed thiophene-2-carboximidamide inhibitors of neuronal nitric oxide synthase for the treatment of melanoma, *Journal of medicinal chemistry 57*, 686-700.

250. Delker, S. L., Ji, H., Li, H., Jamal, J., Fang, J., Xue, F., Silverman, R. B., and Poulos, T. L. (2010) Unexpected binding modes of nitric oxide synthase inhibitors effective in the prevention of a cerebral palsy phenotype in an animal model, *Journal of the American Chemical Society 132*, 5437-5442.

251. Ji, H., Delker, S. L., Li, H., Martásek, P., Roman, L. J., Poulos, T. L., and Silverman, R. B. (2010) Exploration of the active site of neuronal nitric oxide synthase by the design and synthesis of pyrrolidinomethyl 2-aminopyridine derivatives, *Journal of medicinal chemistry 53*, 7804-7824.

252. Huang, H., Ji, H., Li, H., Jing, Q., Labby, K. J., Martásek, P., Roman, L. J., Poulos, T. L., and Silverman, R. B. (2012) Selective monocationic inhibitors of neuronal nitric oxide synthase. Binding mode insights from molecular dynamics simulations, *Journal of the American Chemical Society 134*, 11559-11572.

253. Huang, H., Li, H., Martásek, P., Roman, L. J., Poulos, T. L., and Silverman, R. B. (2013) Structure-guided design of selective inhibitors of neuronal nitric oxide synthase, *Journal of medicinal chemistry 56*, 3024-3032.

254. Labby, K. J., Xue, F., Kraus, J. M., Ji, H., Mataka, J., Li, H., Martásek, P., Roman, L. J., Poulos, T. L., and Silverman, R. B. (2012) Intramolecular hydrogen bonding: a potential strategy for more bioavailable inhibitors of neuronal nitric oxide synthase, *Bioorganic & medicinal chemistry 20*, 2435-2443.

255. Ramnauth, J., Speed, J., Maddaford, S. P., Dove, P., Annedi, S. C., Renton, P., Rakhit, S., Andrews, J., Silverman, S., and Mladenova, G. (2011) Design, Synthesis, and Biological Evaluation of 3, 4-Dihydroquinolin-2 (1 H)-one and 1, 2, 3, 4-Tetrahydroquinoline-Based Selective Human Neuronal Nitric Oxide Synthase (nNOS) Inhibitors, *Journal of medicinal chemistry 54*, 5562-5575.

256. Ramnauth, J., Renton, P., Dove, P., Annedi, S. C., Speed, J., Silverman, S., Mladenova, G., Maddaford, S. P., Zinghini, S., and Rakhit, S. (2012) 1, 2, 3, 4-tetrahydroquinoline-based selective human neuronal nitric oxide synthase (nNOS) inhibitors: Lead optimization studies resulting in the identification of N-(1-(2-(methylamino) ethyl)-1, 2, 3, 4-tetrahydroquinolin-6-yl) thiophene-2-carboximidamide as a preclinical development candidate, *Journal of medicinal chemistry 55*, 2882-2893.

257. Annedi, S. C., Ramnauth, J., Cossette, M., Maddaford, S. P., Dove, P., Rakhit, S., Andrews, J. S., and Porreca, F. (2012) Novel, druglike 1, 7-disubstituted 2, 3, 4, 5-tetrahydro-1H-benzo [b] azepine-based selective inhibitors of human neuronal nitric oxide synthase (nNOS), *Bioorganic & medicinal chemistry letters 22*, 2510-2513.

258. Renton, P., Speed, J., Maddaford, S., Annedi, S. C., Ramnauth, J., Rakhit, S., and Andrews, J. (2011) 1, 5-Disubstituted indole derivatives as selective human neuronal nitric oxide synthase inhibitors, *Bioorganic & medicinal chemistry letters 21*, 5301-5304.

259. Annedi, S. C., Maddaford, S. P., Mladenova, G., Ramnauth, J., Rakhit, S., Andrews, J. S., Lee, D. K., Zhang, D., Porreca, F., and Bunton, D. (2011) Discovery of N-(3-(1-methyl-1, 2, 3, 6-tetrahydropyridin-4-yl)-1 H-indol-6-yl) thiophene-2-carboximidamide as a selective inhibitor of human neuronal nitric oxide synthase (nNOS) for the treatment of pain, *Journal of medicinal chemistry 54*, 7408-7416.

260. Mladenova, G., Annedi, S. C., Ramnauth, J., Maddaford, S. P., Rakhit, S., Andrews, J. S., Zhang, D., and Porreca, F. (2012) First-in-class, dual-action, 3, 5-disubstituted indole derivatives having human nitric oxide synthase (nNOS) and norepinephrine reuptake inhibitory (NERI) activity for the treatment of neuropathic pain, *Journal of medicinal chemistry 55*, 3488-3501.

261. Ziegler, D. M., Ansher, S. S., Nagata, T., Kadlubar, F. F., and Jakoby, W. B. (1988) N-Methylation: potential mechanism for metabolic activation of carcinogenic primary arylamines, *Proceedings of the National Academy of Sciences 85*, 2514-2517.

262. Hodgetts, K. J., Combs, K. J., Elder, A. M., and Harriman, G. C. (2010) The role of fluorine in the discovery and optimization of CNS agents: modulation of drug-like properties, *Annual Reports in Medicinal Chemistry 45*, 429-448.

263. Cinelli, M. A., Li, H., Chreifi, G., Martásek, P., Roman, L. J., Poulos, T. L., and Silverman, R. B. (2014) Simplified 2-aminoquinoline-based scaffold for potent and selective neuronal nitric oxide synthase inhibition, *Journal of medicinal chemistry 57*, 1513-1530.

264. Lohmann, C., Hüwel, S., and Galla, H.-J. (2002) Predicting blood-brain barrier permeability of drugs: evaluation of different in vitro assays, *Journal of drug targeting 10*, 263-276.

265. Stewart, B. H., Chan, O. H., Lu, R. H., Reyner, E. L., Schmid, H. L., Hamilton, H. W., Steinbaugh, B. A., and Taylor, M. D. (1995) Comparison of intestinal permeabilities determined in multiple in vitro and in situ models: relationship to absorption in humans, *Pharmaceutical research 12*, 693-699.

266. Yee, S. (1997) In vitro permeability across Caco-2 cells (colonic) can predict in vivo (small intestinal) absorption in man—fact or myth, *Pharmaceutical research 14*, 763-766.

267. Ji, H., Stanton, B. Z., Igarashi, J., Li, H., Martásek, P., Roman, L. J., Poulos, T. L., and Silverman, R. B. (2008) Minimal pharmacophoric elements and fragment hopping, an approach directed at molecular diversity and isozyme selectivity. Design of selective neuronal nitric oxide synthase inhibitors, *Journal of the American Chemical Society 130*, 3900-3914.

268. Ji, H., Tan, S., Igarashi, J., Li, H., Derrick, M., Martásek, P., Roman, L. J., Vásquez-Vivar, J., Poulos, T. L., and Silverman, R. B. (2009) Selective neuronal nitric oxide synthase inhibitors and the prevention of cerebral palsy, *Annals of neurology 65*, 209-217.

269.   Veber, D. F., Johnson, S. R., Cheng, H.-Y., Smith, B. R., Ward, K. W., and Kopple, K. D. (2002) Molecular properties that influence the oral bioavailability of drug candidates, *Journal of medicinal chemistry 45*, 2615-2623.

270.   Seelig, A. (2007) The role of size and charge for blood–brain barrier permeation of drugs and fatty acids, *Journal of molecular neuroscience 33*, 32-41.

271.   Fang, J., and Silverman, R. B. (2009) A cellular model for screening neuronal nitric oxide synthase inhibitors, *Analytical biochemistry 390*, 74-78.

272.   Dewick, P. M. (2006) *Essentials of organic chemistry: for students of pharmacy, medicinal chemistry and biological chemistry*, John Wiley & Sons.

273.   Jaroch, S., Hölscher, P., Rehwinkel, H., Sülzle, D., Burton, G., Hillmann, M., and McDonald, F. M. (2002) Dihydroquinolines as novel n-NOS inhibitors, *Bioorganic & medicinal chemistry letters 12*, 2561-2564.

274.   Jaroch, S., Rehwinkel, H., Hölscher, P., Sülzle, D., Burton, G., Hillmann, M., McDonald, F. M., and Miklautz, H. (2004) Fluorinated dihydroquinolines as potent n-NOS inhibitors, *Bioorganic & medicinal chemistry letters 14*, 743-746.

275.   Jaroch, S., Hölscher, P., Rehwinkel, H., Sülzle, D., Burton, G., Hillmann, M., and McDonald, F. M. (2003) Dihydroquinolines with amine-containing side chains as potent n-NOS inhibitors, *Bioorganic & medicinal chemistry letters 13*, 1981-1984.

276.   Cheng, Y., Judd, T. C., Bartberger, M. D., Brown, J., Chen, K., Fremeau Jr, R. T., Hickman, D., Hitchcock, S. A., Jordan, B., and Li, V. (2011) From fragment screening to in vivo efficacy: optimization of a series of 2-aminoquinolines as potent inhibitors of beta-site amyloid precursor protein cleaving enzyme 1 (BACE1), *Journal of medicinal chemistry 54*, 5836-5857.

277.   Fedorov, R., Vasan, R., Ghosh, D. K., and Schlichting, I. (2004) Structures of nitric oxide synthase isoforms complexed with the inhibitor AR-R17477 suggest a rational basis for specificity and inhibitor design, *Proceedings of the National Academy of Sciences of the United States of America 101*, 5892-5897.

278.   Xue, F., Li, H., Fang, J., Roman, L. J., Martásek, P., Poulos, T. L., and Silverman, R. B. (2010) Peripheral but crucial: A hydrophobic pocket (Tyr 706, Leu 337, and Met 336) for potent and selective inhibition of neuronal nitric oxide synthase, *Bioorganic & medicinal chemistry letters 20*, 6258-6261.

279.   Hevel, J. M., and Marletta, M. A. (1994) [25] Nitric-oxide synthase assays, *Methods in enzymology 233*, 250-258.

280.   Hagmann, W. K., Caldwell, C. G., Chen, P., Durette, P. L., Esser, C. K., Lanza, T. J., Kopka, I. E., Guthikonda, R., Shah, S. K., and MacCoss, M. (2000) Substituted 2-aminopyridines as inhibitors of nitric oxide synthases, *Bioorganic & medicinal chemistry letters 10*, 1975-1978.

281.   Kang, S., Tang, W., Li, H., Chreifi, G., Martásek, P., Roman, L. J., Poulos, T. L., and Silverman, R. B. (2014) Nitric oxide synthase inhibitors that interact with both heme propionate and tetrahydrobiopterin show high isoform selectivity, *Journal of medicinal chemistry 57*, 4382-4396.

282.   Li, H., and Poulos, T. L. (2005) Structure–function studies on nitric oxide synthases, *Journal of inorganic biochemistry 99*, 293-305.

283.   Mukherjee, P., Li, H., Sevrioukova, I., Chreifi, G., Martásek, P., Roman, L. J., Poulos, T. L., and Silverman, R. B. (2014) Novel 2, 4-disubstituted pyrimidines as potent, selective, and cell-permeable inhibitors of neuronal nitric oxide synthase, *Journal of medicinal chemistry 58*, 1067-1088.

284.   Wolff, D. J., Datto, G. A., Samatovicz, R. A., and Tempsick, R. A. (1993) Calmodulin-dependent nitric-oxide synthase. Mechanism of inhibition by imidazole and phenylimidazoles, *Journal of Biological Chemistry 268*, 9425-9429.

285.   Li, H., Jamal, J., Plaza, C., Pineda, S. H., Chreifi, G., Jing, Q., Cinelli, M. A., Silverman, R. B., and Poulos, T. L. (2014) Structures of human constitutive nitric oxide synthases, *Acta Crystallographica Section D: Biological Crystallography 70*, 2667-2674.